Adventurer Gabriel Beyersdorff silhouetted against the nightly glow from one of Ambrym volcano’s active lava lakes.

Elucidating magmatic drivers and eruptive behaviours of persistently active volcanoes

A thesis presented for fulfilment of the requirements for the degree of Doctor of Philosophy.

by

Chris Firth

B.EnvSc (Hons) Macquarie University

Department of Earth and Planetary Science
Macquarie University

October 2015

In memory of
Douglas Charley

CONTENTS

Statement of Originality

The work presented here is the result of my own original research, except where acknowledged in the text. It has not been submitted to any other university or institution.

Chris Firth

ACKNOWLEDGEMENTS

I am gratefully indebted to many people for their assistance with this project. Firstly I must thank people who helped during fieldwork in Vanuatu. In particular I would like to acknowledge the assistance of Douglas Charley who showed me around Yasur on my first trip there in 2011. I am also grateful to Brad Ambrose for collecting samples for me from Marum's Lava Lake in 2014 and to the BBC for funding my fieldwork on both Ambrym and Yasur that year, in return for help with their documentary. The hospitality of the locals on both Tanna and Ambrym was fantastic. Everyone was always happy to help and did everything with a smile, even if it was raining or we were being pelted by ash or suffocated by volcanic gas. More than that I appreciate everyone showing me around, telling me the local stories over kava, and always offering me crazy bush tucker, like fresh honeycomb or slow-cooked flying fox. In particular I must thank my hosts and guides, Phillip, Kelson and Joseph on Tanna and Willy and George on Ambrym. I must also acknowledge the Vanuatu Geohazards Observatory for giving me permission to conduct fieldwork and collect samples. I am also grateful to Clement Gaildry for collecting additional samples in 2012, which he later passed on to me.

Many people have also assisted me in the laboratory. I am grateful to David Adams and Kevin Grant for support while I was using the SEM and EMP, and to Will Powell for assistance on the LA-ICP-MS. Thanks to the ever-busy Peter Wieland for running XRF analyses for me, supplying me with acid (HCl, not LSD!) and for helping fix problems with things like fume-hoods and mass spectrometers. For the latter I must also thank Norm Pearson. Michael Tuner offered invaluable help teaching me how to use the MC-ICP-MS and helping me tune it when it was playing up (which seemed to be every other day). I am grateful to Ian Smith at the University of Auckland for analysing samples for me when the wait at Macquarie was too long. Thanks too to Alan Hogg and Fiona Petchey at the University of Waikato for running radiocarbon analyses for me.

I must acknowledge constructive reviews of the manuscripts contained within this thesis by Nicole Métrich, Sharon Allen, Alex Nichols, Geoff Kilgour and a number of other anonymous reviewers.

Most of all, I must thank my co-authors and supervisors, Heather Handley, Shane Cronin and Simon Turner, as well as Michael Turner (who missed out on the title of supervisor), who offered invaluable discussions, constructive comments and ready answers, as well as lots of red handwriting across my many drafts. These suggestions undoubtedly made this a better piece of work. More than suggestions, however, I am grateful for their unwavering support and trust that I would do things well, especially when I lacked that belief myself.

Lastly I must thank my friends and family for their continued love and support.

ABSTRACT

Yasur and Ambrym volcanoes, which are located within the Vanuatu Arc, are amongst the most regularly active in the world, with both experiencing ongoing eruption throughout their historical record. They offer a natural laboratory for understanding magmatic processes that sustain persistent volcanic activity. Furthermore, both volcanoes have experienced higher magnitide eruptions within their history, albeit with different frequency-magnitude relationships. Over a dozen eruptions of VEI 2-3 have been experienced at Ambrym throughout the past century, while at Yasur eruptions of VEI 5 or more have ocurred at intervals of ~10-25 kyr. These allow the relationship between low-magnitude, persistent activity and higher magnitude, explosive and effusive eruptions to be explored. Both of these motivating themes are primarily investigated by petrological and geochemical means, including mineral, tephra and whole rock major element analysis and whole rock trace element and Sr, Nd, Hf and U-series isotope analysis. This geochemical data is recociled with historical and geological records of eruptive behvaiour to link changes in magmatic processes with variations in eruptive activity.

At Yasur, persistent volcanic activity, which takes the form of regular Strombolian eruptions, has been maintained for at least 600 years. Throughout this period basaltic trachy-andesitic magmas (SiO_2 ~ 56 wt.%) have been erupted at a constant output rate of 410-480 m^3 day^{-1}. The invaraiance of magma composition and output rate through this time suggest that processes of magma replenishment, fractionation and tapping are in equilibrium. Magma replenishment events are estimated to occur at intervals of years, on the basis of thermal and gas output models. Elevated gas fluxes show that an open conduit connects the shallow plumbing system with the surface. Gas fluxes at both volcanoes cannot be reconciled with magma output rates, suggesting that large volumes of magma remain un-erupted. These are likley stored within the magmatic system as a resident magma or a crystal mush. Uranium-series isotopes reval otherwise cryptic interaction between this component and ascending magmas during persistent activity. Less frequent, high magnitude eruptions show greater evidence for interaction between an ascending magma and a resident magma/mush component. Volcanic rocks from these eruptions display diverse petrology, including mineral disequilbrium textures, such as resorbed and skeletal phenocrysts. At Ambrym, effusive eruptions from the central vents show evidence

for mixing between replenishment and residual magmas, while at Yasur, such is less frequent, but involves wholesale rejuvination of a stored crystal mush leading to catatsophic, ignimbrite-producing, caldera-forming eruptions. Fissure-fed lavas erupted from Ambrym's flanks show no evidence for interaction with stored magmas, suggesting they have by-passed the shallow plumbing system, avoiding this component. As such, stored magmas resulting from persistent activity likley reside at depths of ~1-2 km. MELTS models suggest a similar scenario for Yasur. Sr, Nd and Hf isotopes show no evidence for assimilation with other crustal components at either volcano. Combined, these observations demonstrate the role of persistent activity within the magmatic system as a whole. They raise the possibility that persistent volcanic activity is responsible for the generation of crystal mushes beneath these volcanoes, and that such a component plays a significant role in higher magnitude eruptions.

INTRODUCTION

On the morning of 16th October 1894, Commander Purey-Cust, in charge of the Royal Navy vessel *HMS Dart* rounded the western point of Ambrym Island, in what was then called the New Hebrides, now Vanuatu. The waters here are deep and clear, a vibrant indigo. Flying fish skylark and seabirds swoop. Local islanders troll for tuna and wahu and sharks, lines trailing from outrigger canoes, and in the distance, the island's forested hills stumble up from palm-shadowed, black sand beaches. These tropical pleasantries remain unremarked in Purey-Cust's account, however. Instead he relates the presence of a vast and violent cloud rising over the centre of the island, plumes of smoke smudging the closer hills and tongues of lava boiling the sea where they emerged from burnt ravines. Ambrym volcano was erupting (Purey-Cust 1896).

The paroxysmal eruption of Krakatau, a decade earlier, fortified public and scientific interest in volcanoes (e.g. Forbes 1884; Verbeek 1884). Thus, Purey-Cust's account of the 1894 Ambrym eruption was well received when it was presented at a meeting of the Royal Geographical Society on his return to London in 1896. In response, the society's president, Sir Clements Markham, observed, *"The more we know of* [Vanuatu's volcanoes], *and the more details we obtain regarding their nature, and the periods of eruption, the more likely are we some day to come to a knowledge of the causes of these fearful devastations in the New Hebrides and elsewhere along that line of volcanic activity"* (Purey-Cust 1896).

Over the ensuing century significant advances in the fields of earth science (e.g. Wegener 1912; Benioff 1949; Wilson 1963), and particularly geochemistry (e.g. Bowen 1915; 1928; Ringwood 1974; DePaolo and Wasserburg 1977; O'Hara 1977; Dupre and Allegre 1983; Plank and Langmuir 1993; Pearce and Peate 1995; Hawkesworth et al. 2004; Davidson et al. 2005) and volcanology (e.g. Sparks et al. 1973; Walker 1973; Giggenbach et al. 1975; McGuire 1991; Francis and Rothery 2000; Lowe 2011; Cashman and Sparks 2013; Heiken 2013 and references therein) have provided a both a framework to understand volcanism within the Vanuatu Arc, as well as suite of techniques to investigate it further. When compared with many volcanically active regions, the Vanuatu Arc, and indeed the wider south-west Pacific region, remains poorly understood. Five of the most active volcanoes in Italy (namely Etna, Vulcano, Stromboli, Vesuvius and Campi Flegrei) have been the focus of at least 1500 scientific publications. In contrast, the roughly 10,000 km long subduction system running from New Zealand to New

Guinea (Fig 1.1), which hosts at least 60 active volcanoes, has mustered only a third of that number. Of these, less than fifty papers are concerned with the volcanoes in the Vanuatu Arc. These figures do not belie the global importance of volcanism in the south-west Pacific, however. This region contributes >20% of global volcanic SO_2 emissions (Halmer et al. 2002; McGonigle et al. 2004; Bani et al. 2012; McCormick et al. 2012), of which the Vanuatu Arc is the greatest emitter (Bani et al. 2012). High SO_2 fluxes are a reliable indicator of the presence of magma during volcanic unrest (Oppenheimer et al. 2011) and around half of global SO_2 emissions result from degassing at persistently erupting volcanoes (Halmer et al. 2002). Thus the high volcanic gas flux from this region can be taken as an indicator of sustained magmatic activity. By no means, however, are persistent eruptions the only manifestation of volcanic unrest in this area. Significant numbers of caldera systems and associated ignimbrite deposits have been identified within the region (Lowder and Carmichael 1970; Hemming 1974; Monzier et al. 1994; Robin et al. 1994; 1995; Smith et al. 2003; Allen 2005; Caulfield et al. 2011; McKee 2015), attesting to the role of low-frequency, high magnitude eruptions. The most recent of these caldera-forming eruptions (i.e. <2 kyr) are recorded by ice-core records from Greenland and Antarctica and frost-rings in bristlecone pines from the USA, confirming to their global climatic impact (e.g. Gao et al. 2006; Witter and Self 2007; McKee et al. 2015). Thus the south-west Pacific region, and Vanuatu in particular, represents a globally significant zone of volcanism that remains poorly studied and little understood. Further work in this region will not only benefit local and regional hazard planning but will undoubtedly contribute to many of the fundamental questions of volcano science.

The collection of papers presented here address one such issue, investigating persistently active volcanism with a focus on two volcanoes in the Vanuatu Arc. Humans have long understood that certain volcanoes maintain eruptive behaviour for decades, centuries or longer, with descriptions of such activity at Stromboli dating from the time of the Greeks, Romans and Arabs (e.g. Strabo, Pliny, Ibn Hawqal: Rosi et al. 2000). Such behaviour sets these volcanoes (Fig. 1.2) apart from those displaying 'typical' volcanic activity, with long periods of repose interspersed with episodes of violent eruption. Typical persistent activity, which can take the form of active lava lakes (e.g. Le Guern et al. 1979; Tazieff 1994; Harris et al. 1999; Oppenheimer et al. 2004; Witter et al. 2004; Calkins et al. 2008), regular Strombolian eruptions (e.g. Dibble et al. 2008; Bani et al. 2013; Gaudin et al. 2014; Gurioli et al. 2014) and continued degassing (e.g. Allard et al. 1994; Gauthier et al. 2000; Shinohara and Witter 2005; Aiuppa et al.

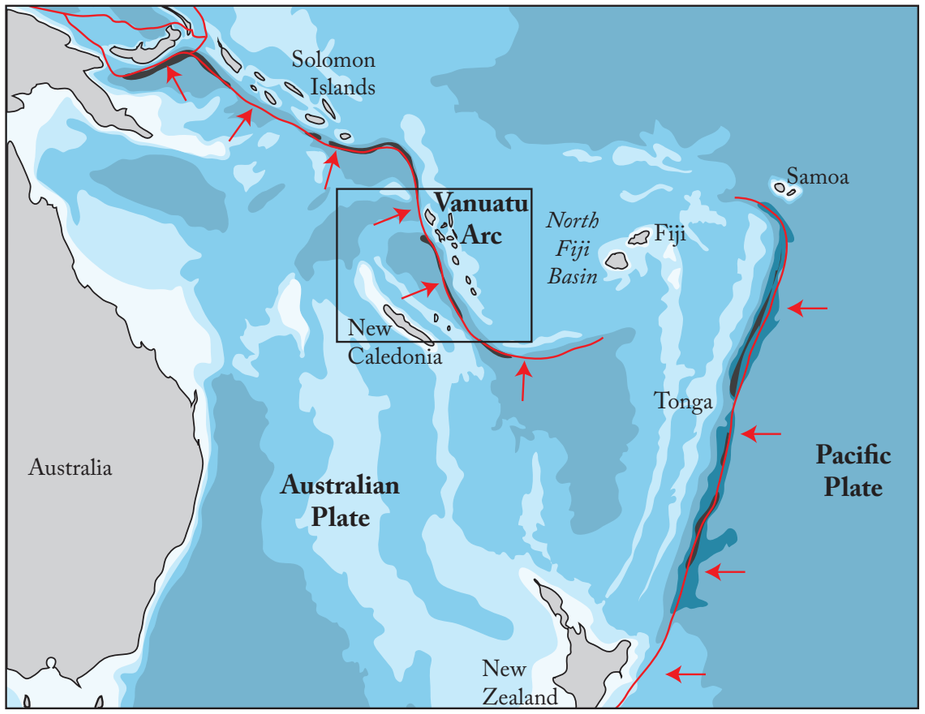

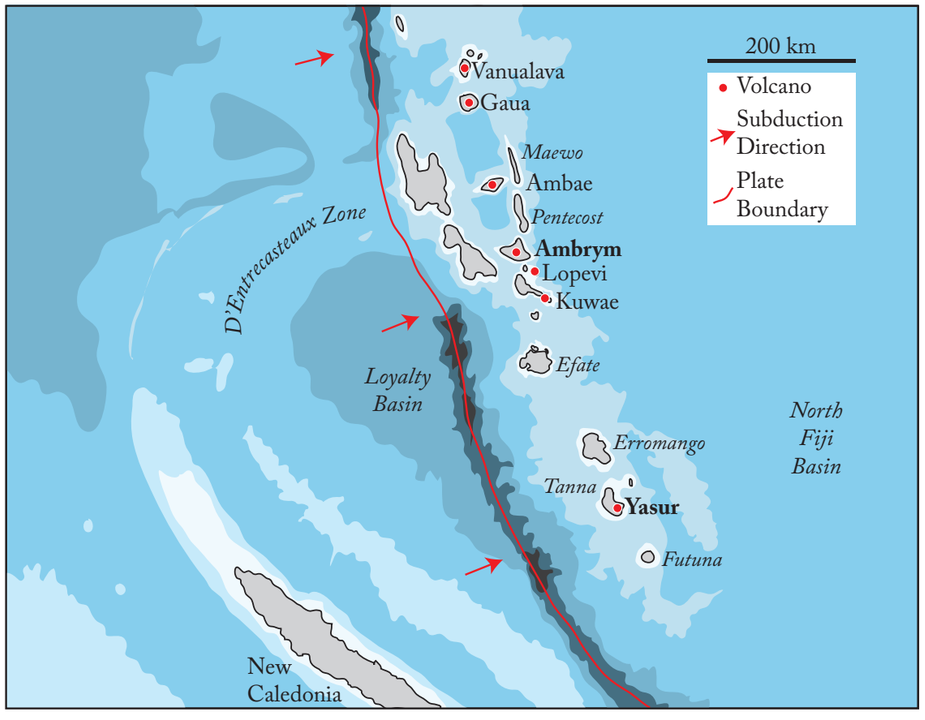

Fig. 1.1 Upper: Map of the south-west Pacific region, showing location and tectonic configuration of the Vanuatu Arc. The square shows the area blown up in the lower map. Lower: Map of the Vanuatu Arc, showing location of active volcanoes. The bathymetric contour interval for both maps is 1000 m.

2006; 2010; Allard et al. 2008; Sawyer et al. 2008; Ilanko et al. 2015) poses a range of hazards. Elevated gas fluxes from these volcanoes are a major global contributor of volatile species, such as H_2O, CO_2 and SO_2 (e.g. Halmer et al. 2002; Oppenheimer et al. 2011). Gas and ash emissions also cause local impacts, including chronic health issues and agricultural disturbance (e.g. Nairn et al. 1988; Cronin and Sharp 2002; Allibone et al. 2012; van Manen 2014). Many of these volcanoes are prone to fluctuations in eruptive behaviour, with 'normal', lower-magnitude activity punctuated by episodes of more violent unrest (e.g. Andronico and Pistolesi 2010; Global Volcanism Program 2015). These pose a significant hazard for local communities (e.g. Tazieff 1977; Favalli et al. 2009; Rosi et al. 2013) as well as increasing numbers of tourists, who are drawn to these volcanoes by their spectacular, yet relatively benign activity (e.g. Heggie 2009; Erfurt-Cooper 2011). Furthermore, the geological records from many persistently active volcanoes display evidence for occasional high-magnitude Plinian-style eruptions (e.g. Bice 1985; Houghton et al. 2004; Allen 2005; Silva Parejas et al. 2010; Lohmar et al. 2012). As such, thorough hazard management plans and focused monitoring networks are important for these volcanoes. Such hazard mitigation measures must be underpinned by a comprehensive understanding of the magmatic processes driving persistent activity and their relationship with higher magnitude eruptions. These two topics form the focus of the following thesis which aims to understand the duration of persistent eruptive activity, the processes that sustain it and time-scales over which they operate, and the importance of such activity within the wider magmatic system. These questions are approached by combining geochemistry with physical volcanology in order to reconcile the surface expression of volcanic activity with the sub-surface processes that sustain it.

This body of work takes the form of four papers, divided into three main themes. The first theme examines the volcanological record of Yasur, a scoria cone on the island of Tanna, at the southern end of the Vanuatu Arc (Fig. 1.1). Yasur displays eruptive behaviour involving regular Strombolian blasts that expel lava bombs, as well as ash and gas (Fig. 1.3). Recently much attention has focused upon observations of current eruptive behaviour at Yasur, through gas monitoring (Oppenheimer et al. 2006; Bani and Lardy 2007; Bani et al. 2012), seismic studies (Nabyl et al. 1997; Kremers et al. 2013), thermal infrared sensing (Bani et al. 2013), pyroclast velocimetry (Gaudin et al. 2014) and laboratory examination of eruptive products (Metrich et al. 2011; Kremers et al. 2012). While this is beginning to produce a cohesive understanding of eruptive behaviour now, little is understood about how long this behaviour has persisted

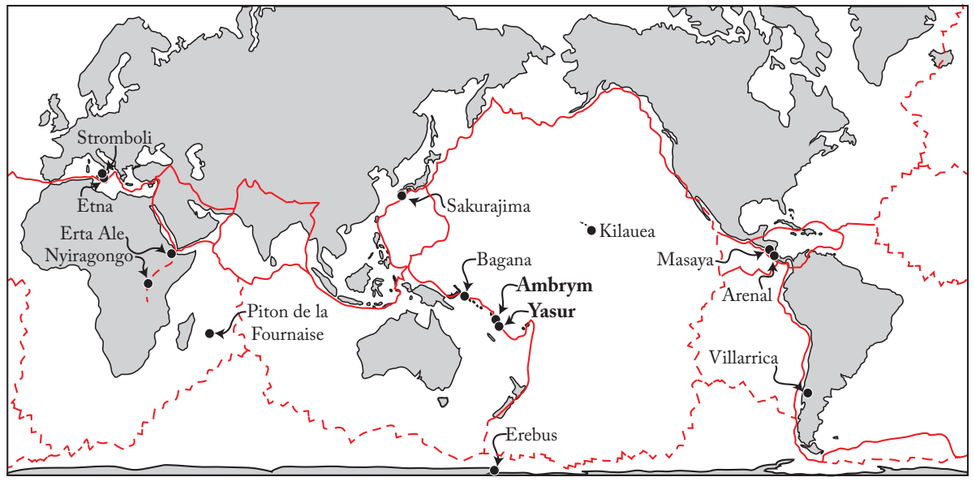

Fig. 1.2 Global map showing the location of notable persistently active volcanoes. Red lines delineate plate boundaries, with full lines representing convergent margins and dashed lines representing divergent margins.

and what variability, both in terms of eruptive behaviour and erupted magma chemistry, is apparent. Simple mass balance calculations require that persistent tapping of a magma chamber must be offset by persistent replenishment. The steady-state operation of these processes is expected to chemically buffer the magma chamber, meaning that the eruptive products should be compositionally invariant (e.g. O'Hara 1977; Albarede 1985; Pyle 1992; Hughes and Hawkesworth 1999; O'Neill and Jenner 2012; Lee et al. 2014). While this has been modelled extensively, the invariability of magma chemistry during long-lived persistent eruptions remains poorly observed. Tephra records with a high temporal resolution are preserved at Yasur, allowing potential covariance of magma chemistry and eruptive behaviour to be investigated over the full duration of persistent activity. This forms the motivation behind Chapter 1, which uses tephra stratigraphy to constrain a detailed history of eruptive behaviour at Yasur over the last 2.5 ka. It shows that the current episode of persistent activity has lasted ~600-800 years, with very limited variations in eruption dynamics, magma output rate and magma chemistry.

Yasur sits within the wider Yenkahe Caldera, which measures approximately 6 by 4 km. This feature was excavated during two successive Plinian eruptions over the last 50 kyr. Both emplaced significant ignimbrite sheets over much of southern Tanna (Robin et al. 1994; Allen 2004). Metrich et al. (2011) showed that the most recent of these, the Siwi Ignimbrite, is derived from the same magmatic system as current eruptive products from Yasur. Nevertheless, the full

relationship between these two vastly different eruptive regimes remains poorly understood. This is addressed in Chapter 2, which aims to elucidate how this magmatic system can host both relatively benign low magnitude eruptions as well as occasional catastrophic, ignimbrite-producing blasts. Were these caldera-forming eruptions unusual, or are they a repeated feature of this system? The Yenkahe Caldera is experiencing some of the highest rates of caldera-uplift in the world (~156 mm yr^{-1}) and this has been interpreted as evidence for magma renewal (Chen et al. 1995; Merle et al. 2013; Brothelande et al. in press). As such, it is a pertinent time to understand how these high-magnitude eruptions fit within the system as whole.

Recently Cooper and Kent (2014) proposed that magmas may be stored at near-solidus conditions for tens to hundreds of thousands of years prior to eruption. This has fortified the standing of a growing body of work that argues for the rapid (days to years) remobilisation of crystal mush bodies as a trigger for large, ignimbrite eruptions (e.g. Bachmann and Bergantz 2006; Martin et al. 2008; Burgisser and Bergantz 2011; Druitt et al. 2012; Huber et al. 2012; Parmigiani et al. 2014). Such a scenario has been used to explain high magnitude silicic eruptions, such as the Fish Canyon Tuff (Bachmann and Bergantz 2003) and Kos Plateau Tuff (Bachmann 2010), as well as eruptions from volcanoes such as Taupo (Charlier et al. 2005), Mt St Helens (Cashman and Blundy 2013) and Mt Hood (Cooper and Kent 2014). Nevertheless, this scenario remains un-tested for rarer, mafic-intermediate ignimbrites. The Yasur/Yenkahe system offers an unparalleled opportunity to investigate whether this hypothesis is applicable to mafic/intermediate magmatic systems and if so, how it can be reconciled with models of persistently active volcanism, such as that seen at Yasur today.

The interplay of persistent activity and higher magnitude eruptions is again addressed in the second theme of this thesis, which focuses on Ambrym volcano, in the centre of the Vanuatu Arc (Fig. 1.1). Like Yasur, Ambrym hosts long-lived persistent activity, however unlike Yasur, deviations to higher-magnitude eruptions occur at intervals of decades, rather than millennia. This difference in frequency/magnitude relationship offers an important comparison with the Yasur/Yenkahe system.

Ambrym volcano displays a variety of eruptive styles, including various forms of effusive and explosive activity (Fig. 1.4). The past and present eruptive behaviour of Ambrym has been explored through examination of volcanic deposits (e.g. Nemeth and Cronin 2008; Nemeth and Cronin 2011; Polacci et al. 2012) as well as gas (Bani et al. 2009; Bani et al. 2012; Allard et al. 2015) and seismic studies (Carniel et al. 2003; Legrand et al. 2005; Rouland et al. 2009),

Fig. 1.3 Yasur. (a) Eroded tephra deposits within 'Lake Siwi' on the north-west side of Yasur. The volcano is visible on the upper right of the image. (b) An ash-rich strombolian blast at Yasur on the 30th August 2014. Note the gas plume coming from both vents. This image is looking to the north-east from the southern side of the crater rim. (c) A large cow-pat bomb erupted from Yasur during heightened activity in 2010. This was ~400 m south of the crater rim. (d) A 1.3 second exposure of a strombolian blast at Yasur on the evening of 9th May 2011. The trajectories of volcanic bombs are marked by trails of light. This image was taken from a similar location to (b).

however few attempts have been made to link magmatic processes with eruptive behaviour through geochemical means. Geochemical studies on Ambrym have primarily focused upon long-term evolution trends throughout the history of the volcano, or else, investigated the most primitive magmas and melt inclusions to understand partial melting processes (Robin et al. 1993; Picard et al. 1995; Sorbadere et al. 2013). A detailed understanding of the shallow plumbing system of the volcano and the magmatic processes operating within it remains largely unknown, although recent work by Allard et al. (2015) using gas flux and melt inclusion data goes some way to rectify this. Beyond the implications for hazard assessment, this is invaluable knowledge, as Ambrym is one of only a handful of volcanoes to have hosted active lava lakes throughout recent decades (e.g. Mallick 1970; Global Volcanism Program 1991; 1996; 1998; 2009). Lava lakes are a remarkable and unique phenomena that have received surprisingly little research attention (Tazieff 1994; Harris et al. 1999; Witham and Llewellin 2006; Stovall et al.

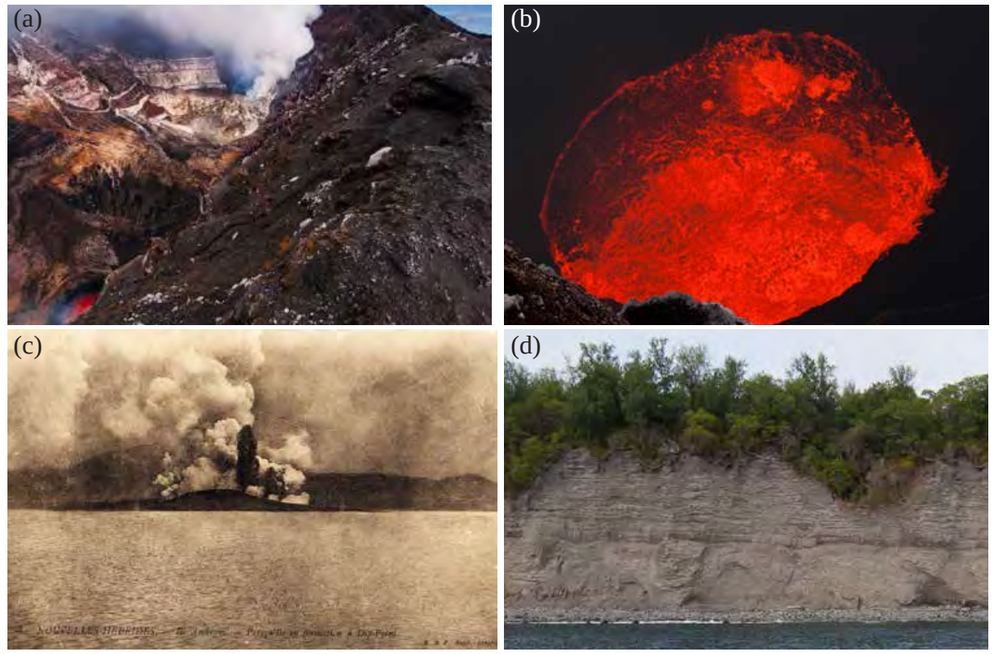

Fig. 1.4 Ambrym. (a) View into Marum cone, one of two active vents on Ambrym. The crater is ~500 m deep and 1 km long. Note the lava lake in the bottom left of the image and the dense gas plume eminating from the back of the crater. (b) Close-up of the lava lake in Marum vent on Ambrym. (c) Historical image of the 1913 flank eruption at Ambrym, showing phreatomagmatic blasts that created a tuff ring at dip-point. (d) Eroded outer wall of the Dip Point tuff ring created during the 1913 eruption (see image c).

2009). While lava lakes on Mt Erebus (e.g. Calkins et al. 2008; Davies et al. 2008; Kelley et al. 2008; Oppenheimer et al. 2009) and at Erta Ale (Le Guern et al. 1979; Oppenheimer and Yirgu 2002; Oppenheimer et al. 2004) have been the focus of some research, those on Ambrym remain relatively un-explored. Factors contributing to the transition from lava lake activity to more explosive eruptions have remained unclear, however these are investigated in Chapter 3 through geochemical examination of historical eruptive products. As well as lava lake activity, two additional styles of eruptive behaviour have been recorded over the past century at Ambrym, with each style associated with eruption of petrologically and geochemically distinct lavas. Such distinctions result from different magma ascent and storage conditions.

Having set the stage with two prime examples of persistently active volcanoes, the final theme of this thesis examines magmatic processes that maintain such activity and the timescales over which they operate. This is achieved through the application of a suite of models to datasets from Yasur and Ambrym and their comparison with other persistently active volcanoes such as Stromboli (e.g. Landi et al. 2004; Allard et al. 2008; Francalanci et al. 2012; Bragagni et al.

2014), Villarrica (e.g. Witter et al. 2004; Palma et al. 2008; Sawyer et al. 2011; Lohmar et al. 2012; Richardson et al. 2014) and Erebus (Kelley et al. 2008; Oppenheimer et al. 2009; Sims et al. 2013; Ilanko et al. 2015). Much of what is known about this style of volcanic activity comes from numerical models that aim to recreate processes occurring in the volcanic conduit (e.g. Kazahaya et al. 1994; Stevenson and Blake 1998) or magma reservoir (e.g. O'Hara 1977; Albarede 1985; Pyle 1992; Albarede 1993; Hughes and Hawkesworth 1999; Annen et al. 2008; O'Neill and Jenner 2012; Lee et al. 2014). Application of these models to volcanic datasets remains relatively limited, however (e.g. Francalanci et al. 1999; Witter et al. 2004; Burton et al. 2007; Stix 2007; Annen et al. 2008). Here a variety of models, relying on gas flux, whole-rock uranium-series isotope ratios and thermal modelling, are used to investigate the time-scales of magma replenishment at Yasur. Magma replenishment is often cited as a trigger for increased eruptive activity (e.g. Corsaro et al. 2007), and so better understanding of the timescales of replenishment will inform hazard monitoring programs, which use seismic and gas data as proxies for this process (e.g. Tilling 2008). In addition, by testing these models against real datasets (and against each other), their accuracy can be gauged, allowing refinement of both the models and our understanding of the processes they aim to recreate.

So, over a century after the Vanuatu arc was first proposed as a natural laboratory to investigate volcanic processes, this thesis illuminates the role of persistently active volcanism within the arc and the important function these volcanoes can play in elucidating magmatic processes, there and elsewhere.

Yasur’s evening fireworks display

Theme 1:

Yasur Volcano

and the

Yenkahe Caldera

1. The Eruptive History and Chemical Stratigraphy of a Post–Caldera, Steady-State Volcano: Yasur, Vanuatu

Chris W. Firth[1*], Heather K. Handley[1], Shane J. Cronin[2], Simon P. Turner[1]

[1] GEMOC, Department of Earth and Planetary Sciences, Macquarie University, Sydney, NSW 2109, Australia

[2] INR, Massey University, Palmerston North, New Zealand

Manuscript submitted to
Bulletin of Volcanology

Submitted: 17th January 2014

Published: 7th June 2014

Please note that this manuscipt was written before the others in this collection and some ideas, principally those associated with the Siwi Ignimbrite, have evolved since this paper was published

The persistent activity of Yasur volcano, a post-caldera, scoria cone in the southern Vanuatu Arc, along with the uniformity exhibited by its eruptive products, indicate that it is a "steady-state" volcano. This implies that rates of magma replenishment and tapping are in equilibrium. Examination of recently exposed tephra sequences suggests that Strombolian-style activity at Yasur has persisted in its current form for the last 630-850 years. Eruption of tephra with uniform grain size and texture throughout this period indicates invariant eruption magnitude and style. Based on tephra accumulation rates, a uniform, time-averaged eruption flux of ~410-480 m^3 d^{-1} is estimated. Major and trace element analyses of glass shards and mineral grains from these tephra deposits show limited variation in magma composition throughout that time, consistent with a chemically-buffered magma reservoir and models for steady-state volcanism. Similarly, mineral crystallisation temperature estimates are within error, suggesting the magma reservoir has retained a constant temperature through this time, while pressure estimates suggest shallow crystallisation. Eruptions appear to be driven by gas release, with small fluctuations in magma chemistry and eruptive behaviour governed by perturbations in volatile flux. This period of steady-state activity was preceded by ~600 years of higher magnitude, lower frequency eruptions during which less evolved compositions were erupted. Variation between these two styles of eruptive behaviour may be explained by a shift from a periodically closed to fully open conduit, allowing more regular magma release and changes to degassing regimes. New radiocarbon ages suggest a period of irregular eruptive behaviour extending > 1400 yr B.P. Overall, a transition from an irregular to a very steady magmatic system has occurred over the past ~ 2 kyr. Previously determined tectonic indicators for caldera resurgence in the area, suggest revived magma replenishment after a hiatus following the caldera-forming Siwi Eruption. This replenishment, while now driving constant activity, has not yet manifest itself in variations in composition or style/magnitude of eruptions.

INTRODUCTION

Worldwide, a number of volcanoes have displayed persistent activity throughout their historical records (e.g. Stromboli and Kilauea). This is attributed to feeding by a steady-state magma reservoir, which is replenished and tapped at equal rates, sustaining eruptions over periods of tens to thousands of years (O'Hara 1977, Albarede 1985). O'Hara (1977) recognised that such equilibrium may also buffer magma composition, permitting it to erupt chemically homogeneous magmas over long periods. Steady-state activity is typically manifest by persistent Hawaiian or Strombolian explosions, continued lava effusion and endogenous growth through magmatic intrusion (Francis et al. 1993). In this sense, it is amongst the most benign forms of volcanic unrest. The prevalence and longevity of such volcanic systems, however, makes them a notable contributor to global rates of volcanism. It has been postulated that mid-ocean ridge volcanism, which produces much of Earth's crust, operates in steady-state (Albarede 1985, O'Neill and Jenner 2012). Steady-state volcanic systems also contribute significant volumes of sulphur and other volcanic gasses to the atmosphere affecting global gas fluxes (e.g. Oppenheimer et al. 2011) and generating chronic health impacts on surrounding populations

(e.g. Alibone et al. 2012). While numerical models have predicted how steady-state behaviour should affect magma compositions, few real-world examples have been examined in detail to identify variability within such systems. The missing data is key to elucidating the magmatic processes that drive steady-state volcanism.

Yasur is a persistently-active basaltic trachy-andesite volcano located on the island of Tanna, in Vanuatu (Fig 2.1). It is thought to have existed in a near-constant state of eruption for at least 300 years (Eissen et al. 1991). The volcano sits within the Yenkahe Caldera, the result of a voluminous, mafic-intermediate eruption, which produced the > 20 kyr B.P. Siwi Ignimbrite (Nairn et al. 1988; Robin et al. 1994). Like many volcanoes in the South Pacific, Yasur's historical record began in the late 18th Century, with intermittent accounts by passing explorers and missionaries comprising much of the record until reliable, continuous monitoring began in the mid-20th Century. To fill this gap and as a basis for hazard planning, detailed examination of tephra sequences is needed to understand the long-term eruptive behaviour of this volcano and elucidate processes occurring within the plumbing and storage systems.

In 2000 a breakout flood from a shallow lake (Lake Siwi) downwind of Yasur exposed a new continuous tephra record that is examined here to clarify the history of post-caldera volcanism within the Yenkahe Caldera. Of particular interest is whether persistent activity at Yasur is a result of steady-state conditions in the magma reservoir. Through detailed stratigraphic and geochemical analysis of Yasur's tephra deposits an understanding of the variability in both eruptive behaviour and magma composition is developed and used to investigate the equilibrium between magma supply and eruption. Lastly, efforts are made to understand both the temporal and source relationships between the caldera-forming eruption and current, post-caldera volcanism.

Volcanic activity within the Yenkahe Caldera Area

Yasur marks the current manifestation of volcanism on Tanna Island (Fig. 2.1). The island consists of Pliocene to Recent basaltic to andesitic volcanic rocks, accompanied by reef limestone. The most recent phase of volcanism is focused in the south-eastern corner of the island and includes the large, caldera-forming Siwi eruption as well as ongoing post-caldera volcanism, including activity at Yasur itself (Fig. 2.1) (Carney and McFarlane 1979). The Late Pleistocene-Holocene Siwi eruption has been linked with the formation of a 4 km-wide caldera and emplacement of a voluminous mafic/intermediate ignimbrite, resulting from collapse of the

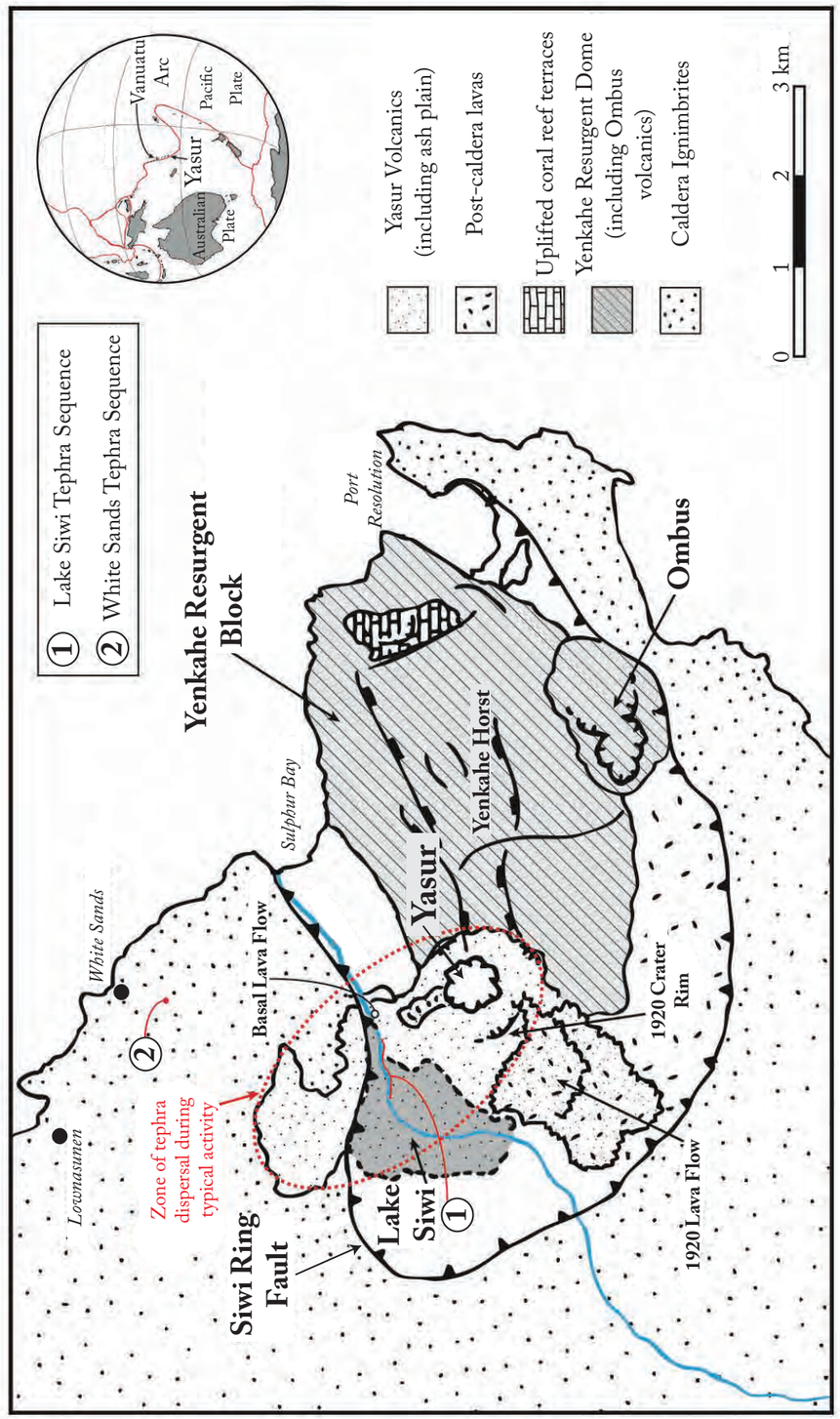

Fig. 2.1 Simplified geological map of south-east Tanna, showing location of tephra sequences and the relationship of Yasur to the Yenkahe Block and Siwi Caldera. Modified after Carney and McFarlane (1979).

eruption column (Nairn et al. 1988; Robin et al. 1994; Allen 2004).

Post-caldera unrest has resulted in a combination of uplift and volcanism. The fault-bounded Yenkahe Resurgent Dome, measuring approximately 3 km by 5 km lies at the center of the caldera (Fig. 2.1) and has undergone rapid uplift through the past millennium (Merle et al. 2013). Chen et al. (1995) used emerged coral reef terraces on the dome to estimate a time-averaged uplift rate of 156 mm yr^{-1} – amongst the highest rates of ground deformation observed worldwide in volcanic caldera complexes. Uplift rates for the Yenkahe Dome are two orders of magnitude greater than the regional uplift rate of 1.6 mm yr^{-1} (Neef et al. 2003), suggesting that uplift is driven by replenishment of an underlying magma reservoir (Chen et al. 1995; Métrich et al. 2011; Merle et al. 2013). Recent post-caldera volcanism has centered on the edges of the Yenkahe Resurgent Dome, apparently influenced by faults associated with this feature (Merle et al. 2013).

Nairn et al. (1988) report that several Holocene cones existed on the Yenkahe Dome, the most recent being Yasur, which has been active for at least 800 years. Yasur is a morphologically simple scoria cone, with a central crater containing three vents that represent the exposed upper opening of magma conduits (Oppenheimer et al. 2006). The earliest historical records of activity at Yasur were provided by the explorers Cook (1777) and D'Entrecasteaux (Labillardiere 1800). Local oral histories record a ~500 m shift in vent location to the north east following an effusive eruption in 1920 A.D, during which lava flowed south and west from the crater, likely choking the vent (D. Charley pers. comm.). Campbell (1888) records Yasur's height as 700 ft (~213 m), consistent with the rim of the 1920 crater, which is still visible on the south-west side of the volcano. This suggests that the edifice may have grown over 100 m in height during the last century, to its present height of 361 m.

Current activity at Yasur consists of regular, small Strombolian explosions from at least three separate vents with distinct activity cycles. Each explosion lasts a few seconds with variable intervals of minutes to tens of minutes in between. The volcano typically expels black, scoriaceous, plagioclase-phyric lava bombs to heights of tens to hundreds of metres above the crater rim. Ash and lapilli are usually dispersed to the north-west of the volcano, as a result of the prevailing trade winds. These finer-grained volcanic deposits can affect human health (Cronin and Sharp 2002; Allibone et al 2012) as well as vegetation, especially coffee plantations in the centre of the island (Nairn et al. 1988). Lava lakes have appeared sporadically at Yasur, likely resulting from high magma levels within the conduit (GVN Bulletin 1990). The volcano

is continuously degassing, with an estimated output of ~15 000 ton d^{-1}, primarily consisting of H_2O, SO_2 and CO_2 (Métrich et al. 2011). All reports suggest that this style of activity has persisted throughout the historical record (Campbell 1888; Eissen et al. 1991). Only one reference to any break in eruptive activity throughout this period has been made, suggesting that the volcano was quiet for a period of some weeks during the early 20th century (Frater 1917).

Continuous seismic monitoring since 1993 shows a cyclical pattern in activity, with periods of intense eruption followed by intervals when explosions are less powerful and less frequent (GVN Bulletin 1999). Heightened activity, such as that in 1994 and 2004, is typically accompanied by extensive ash fall and expulsion of bombs well beyond the crater rim (D. Charley pers. comm.). During such activity tephra is dispersed more widely and affects much of Tanna (e.g. July 1999 eruption: GVN Bulletin 1999). A correlation between heightened activity and heavy rainfall has also been noted throughout the historical record (e.g.. Cook 1777; Campbell 1888) and was observed at the volcano in 2011. This is likely to result from infiltration of meteoric water along faults in the Yenkahe Dome and subsequent interaction with Yasur's magma body. Volatilisation of the water increases the volume of gas in the conduit, driving more vigorous eruption.

Models of open-vent systems, such as Yasur, suggest that the magma reservoir is connected to the surface by a conduit, in which degassing drives magma convection. As buoyant, volatile-rich magmas ascend the conduit, decreased pressure allows soluble gasses to exsolve (Stevenson and Blake 1998). Periodic coalescence of exsolved gasses into slugs and their eventual release to the atmosphere is the main driver of Strombolian activity, such as that seen at Yasur (Oppenheimer et al. 2006). Gas exsolution also drives convective overturn within the conduit, as degassed magma is denser and thus sinks, returning toward the magma reservoir. Rheological differences between the un-degassed and degassed magma limit mixing (Stevenson and Blake 1998). Mingling between undegassed magma and material slumped from the crater walls is thought to occur at Yasur (Kremers et al. 2012).

ANALYTICAL METHODS

To investigate the eruptive history of Yasur, two previously undescribed tephra sequences were examined and logged: one at Lake Siwi, on the ash plain, that provides a high resolution record of activity over the past centuries and a second, more distal site at White Sands, which preserves a longer record of higher magnitude eruptive events (Fig. 2.1). Samples were collected

from both sites for geochemical analysis and radiocarbon dating.

Thirty-three tephra samples from the Lake Siwi sequence and eleven samples from the White Sands sequence were collected for chemical analysis. Samples were dry-sieved and a split of the 250-125 μm grain size fraction from each sample was mounted in epoxy resin and polished for single grain analysis. Major element concentrations of glass shards and phenocrysts, hosted within groundmass or a glass matrix, were analysed using a Cameca SX 100 electron microprobe at the Geochemical Analysis Unit (GAU) at Macquarie University. Initial analysis of the glass shards were conducted using a focused 1 μm beam, as well as defocused 10 μm and 20 μm beams to determine the effects of Na-loss. The focused 1 μm beam returned the most reliable results, so was chosen for the remainder of the analyses. All analyses were carried out with a beam energy of 15 KeV and a beam current of 20 nA. Backscatter images were used to avoid visible microlites and other irregularities within the glass. Accuracy and precision were estimated from replicate analyses of appropriate mineral standards. Analyses with totals outside the range 100 ± 2 % were discarded as being unreliable.

Selected trace elements (Sc, V, Rb, Sr, La, Yb) were analysed on a sub-set of ten samples from both sites using the same polished grainmounts as the major element analyses. Trace elements were chosen to reflect a range in compatibility with the mineral assemblage seen at Yasur. Trace element concentrations were determined by LA-ICP-MS at the GAU, using an excimer laser operating at 9.45 J cm^{-2} and 5 Hz, with a spot size of 50 μm. Trace element concentrations were measured on an Agilent 7700 ICP-MS. USGS reference glass BCR-2 was analysed as an unknown to assess accuracy (values are presented in Table 4 for comparison). Data reduction was completed with the software package GLITTER (van Achterbergh et al. 2001), using NIST 610 glass and Ca as internal and external standards respectively.

Organic material for radiocarbon dating was scarce in both sequences and no radiocarbon dates were obtained for the Lake Siwi sequence. Two small charcoal samples were collected from the base of the White sands sequence and dated by Beta Analytic Inc. using accelerator mass spectrometry (AMS). The relative youth of both sequences precluded the use of conventional radiometric dating methods, such as $^{39}Ar/^{40}Ar$.

TEPHRA STRATIGRAPHY

Tephra deposits are thickest to the north-west of Yasur as a result of the prevailing south-easterly trade winds. Directly adjacent to this side of the volcano a large ash plain has formed.

Tephra from all but the smallest eruptions is deposited here. With greater distance from the volcano, only tephra from the largest eruptions is found in the tephra sequence. Above ~3 km in altitude, the prevailing wind direction shifts to the west, meaning that tephra from the largest eruptions may have been dispersed along different axes.

The Lake Siwi Sequence

The ash plain sequence preserves a >15.3 m-thick section of poorly consolidated tephra which was deposited in Lake Siwi, a semi-permanent, shallow lake covering ~100 Ha (Kanas et al. 2000). The lake provided a stable depositional environment for tephra. It was formed by impounding of the Siwi River by a lava flow that is now exposed at the basin outlet. Heavy rainfall in 2000 A.D. caused the lake to overflow, triggering catastrophic erosion and flooding the settlement downstream at Sulphur Bay (Kanas et al. 2000). As the lake rapidly drained, severe erosion cut through the lake-fill tephra deposits, with subsequent erosion deepening and extending the channel. The exposed, ash-dominated tephra sequence provides a detailed record of day-to-day variations in eruptive behaviour throughout the last $10^2 – 10^3$ years. This previously undescribed sequence offers an unparalleled opportunity to investigate the constancy of eruptions from Yasur over this time period.

Subsequent to the lake drainage, the main dispersal fan of tephra from Yasur is a denuded “ash-plain”, located NE of the volcano (Fig. 2.1). Constant emission of acid gas and fine ash from Yasur under the prevailing SE trade winds (Harrison & Luther 1990) has caused stunting and denudation of vegetation as well as contamination of water and crops (Cronin and Sharp, 2002). At the NE edge of the ash plain, dunes have accumulated against encroaching vegetation. Nearer to Yasur, flat-lying sequences previously preserved below the shallow lake are now exposed to wind erosion.

The sampled Lake Siwi sequence is located ~1.5 km west of Yasur’s crater and lies at an elevation of ~ 50 m a.s.l. in a formerly lake-covered location. Samples were collected along a ~1.2 km semi-continuous river-bank exposure, oriented perpendicular to the tephra fan dispersal axis (Fig. 2.1). The stratigraphy and thickness of tephras vary little across this transect. The tephra sequence is predominantly composed of cm-scale ash beds with sharp contacts (Fig. 2.2). The median diameter (Mdϕ) of the tephra ranges from 0.16 to 3.03ϕ, with rare lapilli beds reaching Md values of -3.27ϕ (Fig. 2.2). No systematic trends in grain size are apparent with depth. Instead, Fig 2.2 shows grain size fluctuates regularly between Mdϕ values

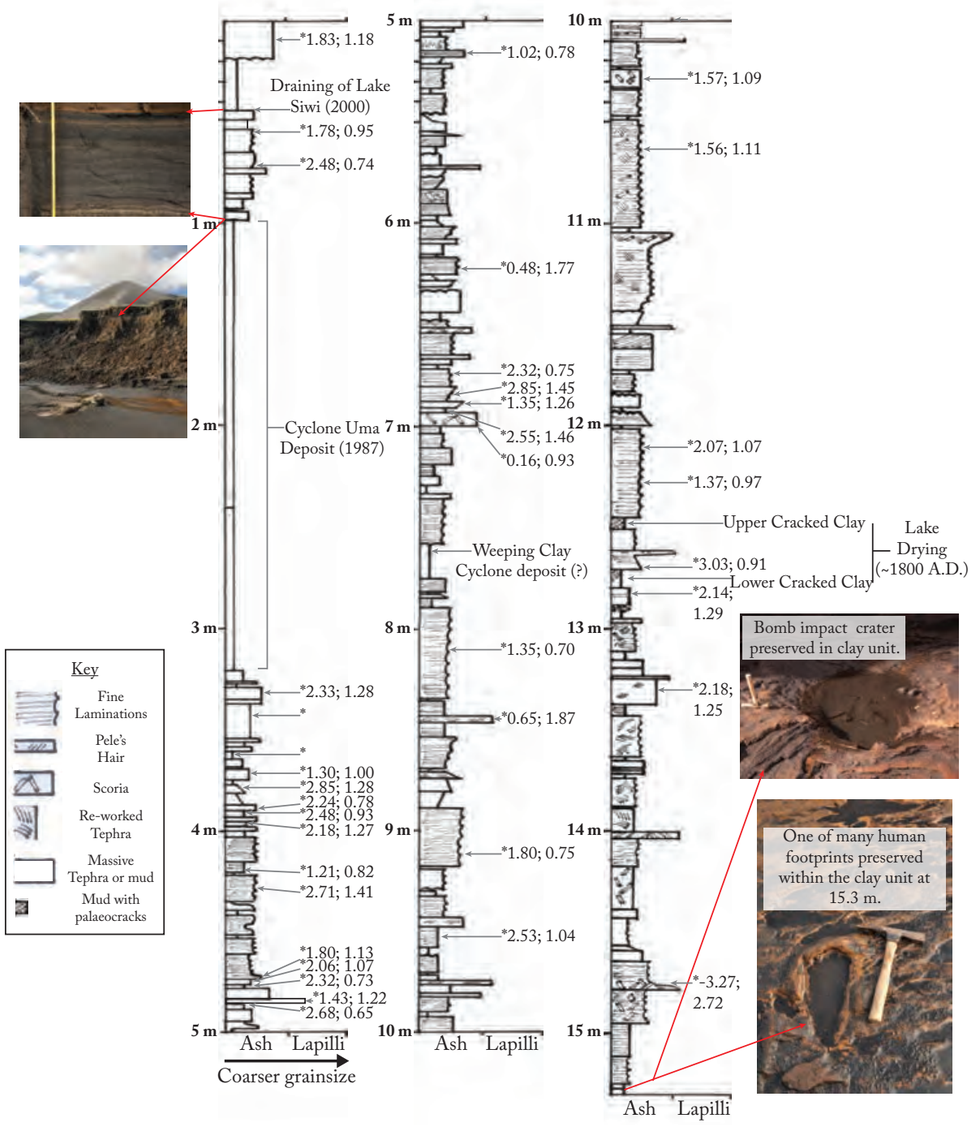

Fig. 2.2 Stratigraphic section of the Lake Siwi Tephra Sequence (19°31.349'S 169°26.234'E), showing variation in grain size with depth. Beds from which samples were collected for geochemical analysis are shown by *. Where measured, grain size data (Mdϕ; σϕ) is also shown. Photos on the left show the detailed tephra beds and position of the tephra sequence relative to the volcano. Photos on the right show a bomb sag and human footprints preserved in the base of the tephra sequence.

of ~1ϕ and >2.5ϕ. Many beds display very fine internal laminations, defined by variations in grain size. Beds are typically well sorted with σϕ ranging from 0.65 to 1.87ϕ, consistent with an airfall origin. No relationship between sorting and grain size is evident, with the exception of the coarsest, lapilli-rich layers which are more poorly sorted, with σ up to 2.72ϕ. A single

lava bomb (> 50 cm in diameter) was found at the base of the sequence, lying within a well-preserved impact crater, suggesting it remained where it had landed following eruption (Fig. 2.2).

The ash consists almost exclusively of juvenile clasts, including black, tachylitic glass shards, scoria and Pele's Hair. Lithic content was negligible in all samples examined. Juvenile clasts are highly angular and contain numerous sub-rounded to elongate vesicles (Fig. 2.3a and b). Pele's Hair is present intermittently throughout the sequence and is generally accumulated in thin (cm-scale) lenticular beds. The shape of these beds suggests that the Pele's Hair accumulated in zones of minor currents within the lake. Similar pockets of recently erupted Pele's Hair are blown into hollows on the ash plain, by the wind. Crystal fragments are also common. These are dominated by plagioclase along with small clinopyroxene crystals and rare olivine. The abundance and size of these phases corresponds with that of the phenocryst assemblages observed in bombs and lava flows erupted from Yasur. The lapilli-sized clasts most commonly consists of juvenile scoriaceous material.

The depositional environment of Lake Siwi may have influenced tephra preservation. Wavy bedforms and low-angle cross-beds occur in rare, isolated units, predominantly in the lower portion of the sequence. These probably represent high inflows into the newly-formed lake, associated with flood and storms. In most locations, however, evidence of tephra remobilisation and reworking is minor. Low-density pumice may have floated and deposited separately from the bulk tephra, but little evidence of this was found. Boygle (1999) suggests that wind can alter deposition patterns in lacustrine tephra deposits, both through blowing floating tephra along the surface and also through its production of waves and currents. Most beds examined, however, are planar and flat-lying with sedimentary characteristics of undisturbed, primary airfall, suggesting that they provide a reliable, high-resolution tephra record for Yasur.

Five non-volcanogenic mud layers are interbedded within the sequence. Two of these represent fluvial inflows (Cyclone Uma Mud: 1-3.2 m depth; and Weeping Clay: 7.5-7.6 m depth; Fig. 2.2), possibly associated with cyclones or other high-rainfall events. There is no evidence for erosion of the underlying tephra units, suggesting that the sites studied were away from the main flow axis associated with these floods. The remaining three thin (<5 cm) mud units (Upper & Lower Cracked Clay: 12.5 m and 12.8 m depth; Footprint Clay: 15.2 m depth; Fig. 2.2) preserve palaeo-cracks that suggest the lake periodically dried up. Tephra preservation following each of these periods may have been significantly different, as finer-grained tephra

would be more easily reworked either by wind or surface runoff.

Preserved on the upper surface of the lowermost mud horizon are a series of 'fossil' human footprints (Fig. 2.2). In places, the prints are partly covered by overlying tephra beds, indicating that they are syndepositional features. Prints from multiple individuals were discerned, including at least one child. They show that a group of people walked from east to west across the lake bed. The footprints may provide a maximum age constraint for the sequence, since humans are proposed to have arrived in southern Vanuatu ~ 2.5 ka (Hurles et al. 2003).

At the eastern end of the ash plain, the ash sequence overlies a ~4m thick lava flow, which was responsible for impounding the Siwi River. The surface of the lava has a ropy texture, however, in some parts tubes have formed, with an outer rind covering ornate pressure ridges beneath. The latter suggests the lava flow originated in the vicinity of Yasur. Much of the flow remains buried beneath overlying tephra deposits and further interpretation of its origin is not possible. The lava contains abundant plagioclase phenocrysts in a black, aphanitic groundmass with numerous vesicles.

The White Sands Sequence

A ~5.30 m-thick sequence of lapilli and ash, inter-bedded with thin, weathered palaeosols (Fig. 2.4) was examined in a cleaned road cutting near the settlement of White Sands, ~3.2 km north of Yasur. This location is located slightly off-axis of the prevailing low-level wind-direction and out of the zone of vegetation denudation caused by ongoing gas release and acid rain (Fig. 2.1). The upper 1.2 m of the sequence is composed of beds of medium to coarse ash (Mdϕ 2.4ϕ). Beneath this, a 1 m-thick sequence of lapilli units occurs (Mdϕ <1ϕ), with each individual bed displaying a weathered upper contact, grading into unweathered tephra beneath. The remainder of the sequence is predominantly composed of fine ash, including three thick beds of ≥25 cm each, as well as occasional beds of fine lapilli. Overall, the tephra units at White Sands are coarser than at the Lake Siwi site, with an average Mdϕ of 0.4ϕ (compared with 1.75ϕ for Lake Siwi) and are also more poorly sorted (σϕ = 1.0 to 3.4ϕ) (Fig.2.4).

The lapilli within the White Sands Site consists of dark-grey to dark-brown high and low density scoria and spatter fragments. Low density scoria are more prevalent in this sequence than at Lake Siwi. Fine scoria, blocky and bubble wall glass shards (Fig. 2.3c and d) and fine, fibrous Pele's Hair are common in many of the ash units. Scanning electron microscopy reveals high microlite contents in the glass shards preserved at the base of the sequence (Fig. 2.3e). As

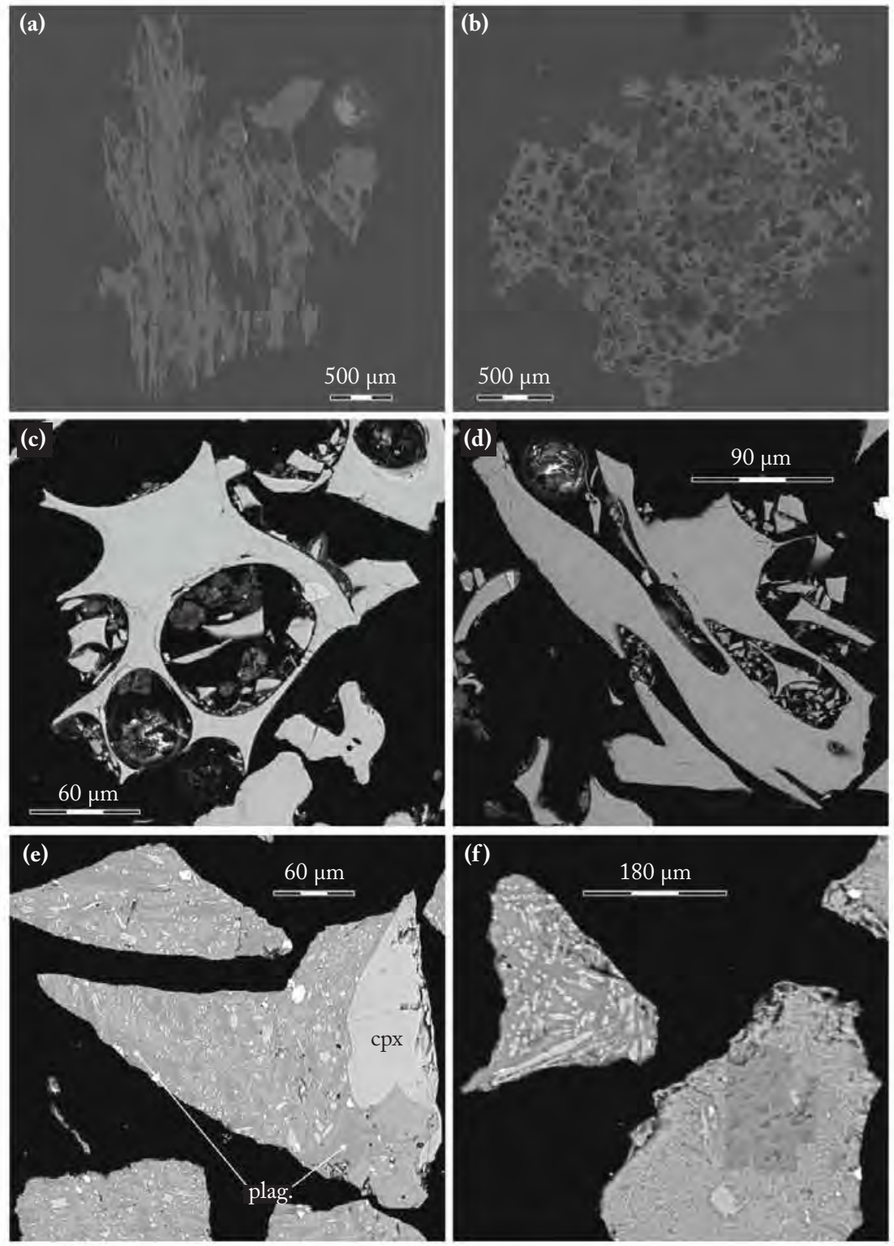

Fig. 2.3 BSE Images showing variation in glass shard morphology between samples. Scoriaceous glass shards with elongate (a) and rounded (b) vesicles from the Lake Siwi sequence. (c) Glass shard displaying elongate vesicles found at ~2.5 m depth in the White Sands sequence. (d) Bubble wall glass shard with rounded vesicles from 2 m depth in the White Sands sequence. (e) Crystal rich glass shards from the base of the White Sands sequence. Compare with the lack of both microlites and phenocrysts in (c) and (d). (f) Microlitic glass shards from ~ 0.75 m depth in the Lake Siwi sequence.

with the Lake Siwi tephras, lithic content is very low.

The tephra beds mantle the topography and show little evidence for re-working, apart from a single erosional unconformity, where the fallout layers immediately above it mantle the irregular surface. This raises the possibility that part of the tephra record is missing at this site.

Dating and correlation

Charcoal samples from the White Sands site returned disparate ages. One sample, from 3.7 m depth, returned an age of zero years, likely due to slash and burn agriculture. Another charcoal sample from the middle of the sequence (Fig. 2.4) returned a calibrated date of 344-524 A.D. (Table 2.1). Further stratigraphic constraints were applied through correlation of the White Sands and Lake Siwi sequences with two tephra sequences described by Nairn et al. (1988) (Fig. 2.5): a distal deposit at Lownasunen, ~ 4 km NNW of Yasur (Fig. 2.1), from which they obtained two radiocarbon ages (Table 2.1), and a proximal deposit on the northern shore of Lake Siwi. The latter differs from the Lake Siwi sequence presented here as it was recorded prior to the catastrophic erosion of 2000, which has exposed a much more detailed stratigraphic record of more recent events.

Further time constraints can be placed on the Lake Siwi sequence through possible correlation of the major mud deposits with records of environmental conditions. The thickest mud unit, a > 1.5 m-thick massive clay deposit extending down from a depth of 1 m (Fig. 2.2), is attributed to a flood event associated with Cyclone Uma in 1987 (D. Charley pers. comm.). Using the depth of tephra deposited between this event and the lake opening in 2000 a crude accumulation rate can be calculated. Historical records suggest that Yasur's eruption rate remained roughly constant between 1987 and 2000 and 58 cm of ash was deposited. This is equivalent to an accumulation rate of 4.5 cm yr^{-1}. Applying this accumulation rate to the whole 15.30 m thick sequence, accounting for 1.85 m of non-volcanogenic, alluvial material, suggests that the tephra sequence records the deposits of eruptions since ~1688 A.D. This age is discordant with radiocarbon dates from a previous examination of a similar sequence downstream that returned corrected ages of 9 and 25 kyr B.P. (Kelley 2008). Stratigraphic correlation between these and the samples described here is not possible. However, the older dates likely represent stratigraphically lower deposits, possibly from another vent, that may be separated by an unconformity.

The radiocarbon date from the White Sands site suggests the sequence records at least 1650

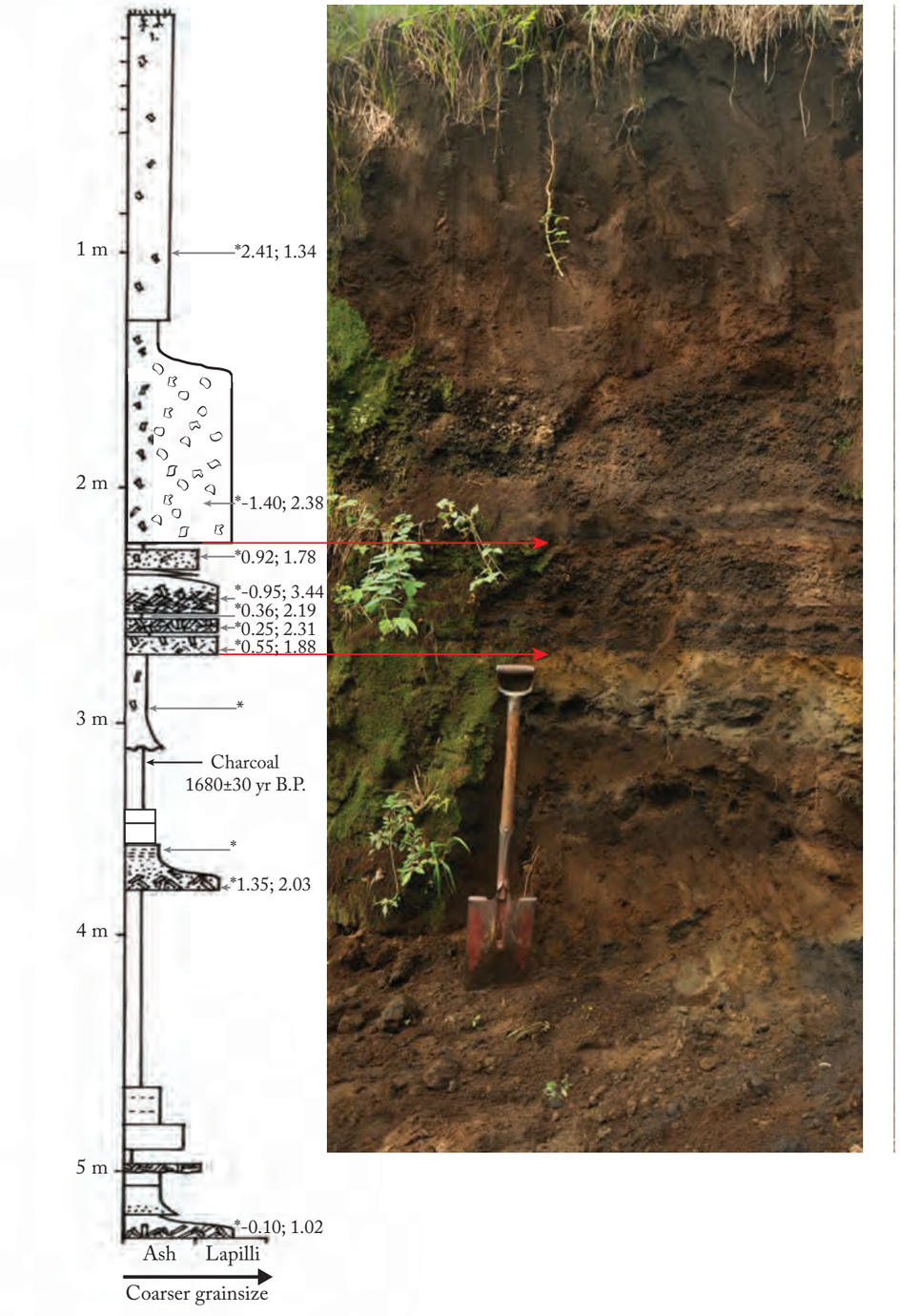

Fig. 2.4 Stratigraphic section of the White Sands Tephra Sequence (19°30.027'S 169°27.083'E), showing variation in grain size with depth. Beds from which samples were collected for geochemical analysis are shown by *. Where measured, grain size data (Mdϕ; σϕ) is also shown. The photo alongside shows the upper part of the sequence and is to the same scale.

Table 2.1. Radiocarbon dates from Yasur tephra sequences

Sample Number	Location	Depth (m)	Conventional Age	Corrected Age
Charcoal 2.1	White Sands	3.2	1680 +/- 30	344-524 A.D.
Charcoal 2.2	White Sands	3.7	0	-
12/1*	Lownasunen	~1.3	804 +/- 56	1162-1383 A.D.
12/3*	Lownasunen	~1.8	1409 +/- 80	539-876 A.D.

Age corrections use shcal 13 correction from Hogg et al. (2013)
*Dates from Nairn et al. (1988)

years of tephra deposition. This time interval is supported by correlation with the Lownasunen site of Nairn et al (1988).

TEPHRA CHEMISTRY

Glass Shard and Whole-Rock Major Element Compositions

New whole-rock data for two lava flows and two lava bombs (one from the Lake Siwi tephra sequence and one recent) (Table 2.2) display a limited compositional range (SiO_2: 55.19 – 56.58 wt.%, MgO: 2.47 – 3.40 wt.%). This is consistent with previously published whole-rock data for Yasur (e.g. Nairn et al. 1988; Métrich et al. 2011; Kremers et al. 2012).

Glass shards from the Lake Siwi Sequence are characterised by trachy-andesitic liquid compositions, with SiO_2 contents ranging from 54.3 to 62.0 wt.% (Table 2.3). The shards show higher SiO_2 contents and a wider compositional range than whole-rock data. This is a common feature of andesitic systems, as glass is a residual phase.

Most major element contents in glass shards from Yasur's tephra deposits display sub-horizontal trends when plotted against SiO_2 (Fig. 2.6). Shallow, negative correlations are observed between MgO and CaO versus SiO_2 in the Lake Siwi samples. Samples from this tephra sequence also display the greatest range in composition. A cluster of samples from the White Sands sequence display noticeably higher MgO and CaO contents than other samples from both sequences. Magnesium numbers in tephras from both sequences are low, ranging from 11.4 to 36.9.

The SiO_2 contents of the glass shards, when plotted against depth, varies between each of the sequences (Fig. 2.7a and b). Data from the Lake Siwi site show an essentially constant composition through time, with the range of each sample falling within the 1σ variation for the

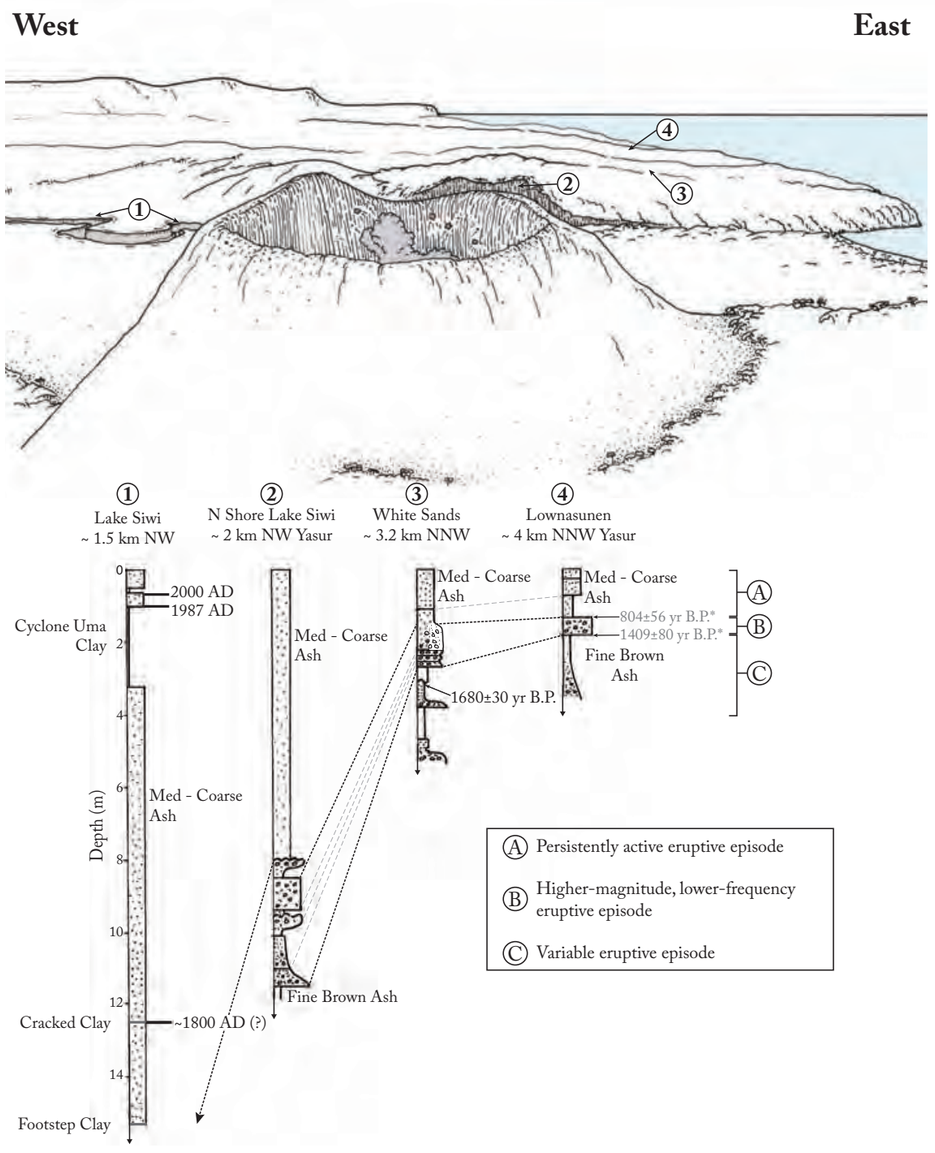

Fig. 2.5 Correlation between the Lake Siwi and White Sands sequences and those of Nairn et al. (1988). The location of each site relative to Yasur is shown. Ages of known events are shown. * - Radiocarbon ages from Nairn et al. (1988). The top image is not drawn to scale.

whole suite. In many cases, single tephra beds show a similar range in SiO_2 content (up to 5 wt.%) to the range for the sequence as a whole.

Glass shards from the White Sands sequence are compositionally similar to those from Lake Siwi (Table 2.3) and display similar, sub-horizontal major element trends (Fig. 2.6). Many samples display intra-bed variation amongst glass shards of up to 2-3 wt.%. The average SiO_2 content for this sequence is slightly lower, but within error of the Lake Siwi sequence

(58.55±1.00 wt.%, compared to 58.68±1.11 wt.%). Samples from the top and bottom of the White Sands sequence display similar SiO_2 contents to the Lake Siwi tephras (i.e. 59-60 wt.% SiO_2) (Fig. 2.7b). Between 2 and 2.7m, however, the glass shards cluster at lower SiO_2 contents (58.0 - 58.7 wt.%). Similarly, tephras preserved in this part of the sequence display noticeably higher MgO and CaO contents and lower K_2O contents than those from other parts of the sequence and from the Lake Siwi deposit (Fig. 2.6 a, d and f).

Glass Shard Trace Element Compositions

Similar to the major element contents of the glass shards, most trace element concentrations (Table 2.4) show limited variation with SiO_2 content (Fig. 2.8). Strontium is a notable exception and displays a pronounced negative correlation with SiO_2 within each sequence (Fig. 2.8c). Compatible elements such as Sc and V also show slight decreases with increasing SiO_2, particularly in the Lake Siwi tephras. Samples from White sands can be discriminated from Lake Siwi tephras due to their higher Sr and V and relatively lower La, Rb and Yb concentrations, especially in the lowest SiO_2 samples. The Lake Siwi samples cluster around a mean value when plotted against depth (Fig. 2.7 c, e and g). Samples collected between 2 and 2.7 m from the White Sands sequence display elevated Sc, Va and Sr concentrations and lower abundances of incompatible elements relative to those from the Lake Siwi site. Many samples from both sequences display a wide variation in trace element abundances between individual glass shards. Samples displaying the highest variations show similarly elevated variation in major element compositions.

Phenocryst Major Element Compositions

Plagioclase is the most common phenocryst phase in all samples. Compositional analyses of plagioclase phenocrysts (Table 2.5) were largely restricted to grain rims, since these should have been in equilibrium with the liquid at the time of eruption. All analysed grains are euhedral and unaltered, suggesting they formed in equilibrium with the melt. A few phenocrysts are partially or fully surrounded by a rim of glass. Some crystals display oscillatory zoning, although core to rim transects for a number of the larger crystals show very little compositional variation (2-5 mol% An) (Fig. 2.9b).

Anorthite contents of plagioclase from the Lake Siwi sequence range from An_{47-64}, while the White Sands sequence displays a range of An_{53-76} (Fig 2.9a). No systematic trends are

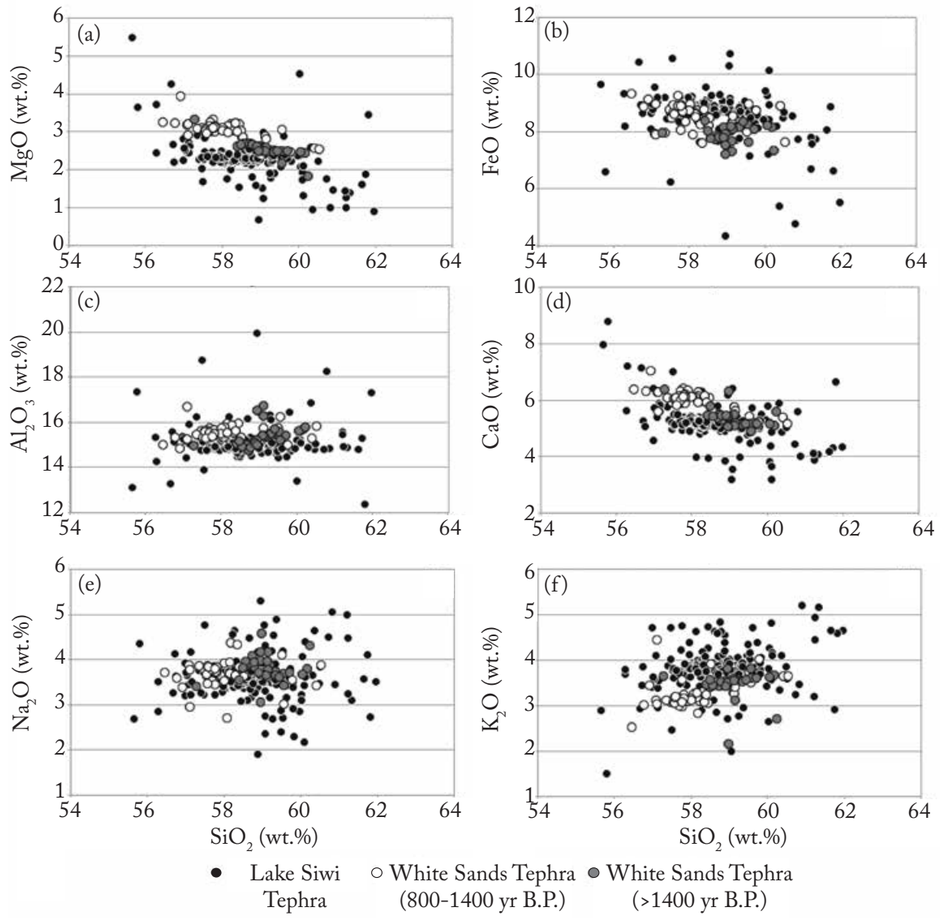

Fig. 2.6 Glass shard variation diagrams showing the abundance of major elements plotted against SiO_2. Samples from White Sands are divided into two populations (those erupted between 800 and 1400 years B.P and those erupted > 1400 years B.P.) based upon differences in MgO, CaO and K_2O. Errors are less than the size of the symbols.

discernable in An content vs. depth for the Lake Siwi sequence (Fig. 2.7i), although mean An contents are higher for plagioclase in some samples towards the base of the sequence. The noticeably higher SiO_2 content in mean glass shard composition at ~ 3.8 m depth is not mirrored by significantly lower anorthite contents in plagioclase at the same depth.

Plagioclase compositions in the White Sands deposit are similar to those from the Lake Siwi locality, except that the former show higher anorthite contents (up to An_{75}) between 2-2.7 m (Fig. 2.7j). This corresponds to the zone of less evolved glass shard compositions at White Sands.

Clinopyroxene is rare and is often fragmented in samples from both sites (Table 2.5).

Table 2.2. Whole rock major element compositions for historic and prehistoric lava flows and lava bombs

Sample	Eruption Date	Lat.	Long.	Sample Type	SiO_2	TiO_2	Al_2O_3	Fe_2O_3*	MnO	MgO	CaO	Na_2O	K_2O	P_2O_5	Total
Basal Lava Footprint	Prehistoric	19° 30' 56" S	169° 26' 43" E	Lava Flow	56.55	0.87	16.36	8.85	0.16	2.93	6.48	3.92	3.09	0.46	99.67
Mud Bomb	~1790 A.D.	19° 31' 6" S	169° 26' 29" E	Lava Bomb	56.58	0.81	17.29	8.45	0.16	2.62	6.70	3.91	2.98	0.45	99.97
1920 Lava Crater	1920 A.D.	19° 32' 05" S	169° 26' 49" E	Lava Flow	55.38	0.81	16.78	9.32	0.17	3.40	7.45	3.58	2.70	0.42	100.00
1920 Lava Road	1920 A.D.	19° 32' 39" S	169° 26' 07" E	Lava Flow	55.19	0.75	17.76	8.58	0.16	3.14	7.59	3.75	2.51	0.38	99.82
Crater Rim Bomb	2009 A.D.	19° 31' 56" S	169° 26' 55" E	Lava Bomb	55.67	0.68	18.98	7.66	0.13	2.47	7.57	3.81	2.52	0.40	99.89

*All Fe expressed as Fe2O3

Table 2.3. Average glass shard major element compositions for Lake Siwi and White Sands tephras

Location	Depth (m)	*n*	SiO_2	± 1σ	TiO_2	± 1σ	Al_2O_3	± 1σ	FeO*	± 1σ	MnO	± 1σ	MgO	± 1σ	CaO	± 1σ	Na_2O	± 1σ	K_2O	± 1σ	Cr_2O_3	± 1σ
Lake Siwi	0.1	4	59.59	0.59	1.05	0.03	15.38	0.30	9.25	0.86	0.21	0.03	2.28	0.39	4.75	1.01	3.98	0.63	3.50	0.97	n.d.	
	0.6	6	59.00	1.33	1.07	0.04	15.72	0.45	9.14	0.34	0.21	0.04	2.58	0.23	5.40	0.25	3.71	0.65	4.05	0.55	0.01	0.01
	0.75	5	59.95	0.74	1.06	0.02	15.09	0.40	8.71	0.37	0.22	0.01	2.37	0.35	4.88	0.57	3.59	0.38	4.13	0.31	n.d.	
	3.3	5	59.26	0.44	1.06	0.04	15.21	0.11	9.00	0.30	0.20	0.03	2.46	0.02	5.27	0.17	3.54	0.05	3.97	0.09	n.d.	
	3.7	3	58.55	0.64	0.98	0.04	15.25	0.46	8.59	1.03	0.19	0.05	2.67	0.34	6.15	0.57	4.08	0.60	3.53	0.63	n.d.	
	3.8	7	60.57	1.45	0.98	0.14	15.94	1.61	7.61	1.27	0.18	0.06	1.90	0.60	4.85	1.17	3.75	0.56	4.19	0.96	0.01	0.02
	3.9	6	60.64	1.24	0.84	0.17	16.40	1.37	7.05	1.80	0.18	0.04	1.56	0.58	4.81	0.63	4.63	0.30	3.89	0.45	0.01	0.01
	3.95	5	59.64	1.28	0.90	0.25	16.36	2.54	7.59	2.19	0.21	0.06	1.91	0.84	5.15	0.91	4.10	0.86	4.12	1.03	0.01	0.01
	4.05	4	58.85	1.62	1.06	0.03	14.47	0.95	9.17	1.16	0.22	0.02	2.95	1.28	5.80	1.18	3.99	0.85	3.46	0.84	n.d.	
	4.15	14	58.98	1.24	1.06	0.06	15.11	0.70	8.95	0.57	0.21	0.03	2.87	0.83	5.60	0.78	3.45	0.38	3.76	0.50	0.01	0.01
	4.7	5	58.94	0.18	1.12	0.03	15.44	0.07	9.01	0.17	0.20	0.02	2.48	0.07	5.33	0.14	3.69	0.04	3.77	0.15	0.02	0.01
	4.75	5	59.49	1.61	1.04	0.07	15.53	0.16	8.53	0.97	0.18	0.03	2.38	0.44	5.20	0.62	3.96	0.63	3.68	0.27	0.01	0.01
	4.8	5	59.42	0.22	1.10	0.03	15.30	0.05	8.80	0.11	0.20	0.01	2.47	0.06	5.25	0.13	3.52	0.20	3.92	0.17	0.01	0.01
	4.85	8	59.17	0.22	1.07	0.04	15.33	0.13	8.99	0.15	0.21	0.03	2.48	0.07	5.20	0.16	3.68	0.15	3.85	0.14	0.01	0.02
	4.9	5	59.45	0.16	1.08	0.02	15.33	0.07	8.78	0.09	0.20	0.02	2.44	0.03	5.20	0.13	3.66	0.15	3.84	0.08	n.d.	
	5.2	8	59.19	0.62	1.00	0.03	15.34	0.10	8.87	0.21	0.22	0.03	2.51	0.11	5.42	0.25	3.65	0.73	3.79	0.39	n.d.	
	6.2	4	59.54	0.46	1.10	0.02	15.38	0.15	8.68	0.34	0.20	0.02	2.30	0.21	5.16	0.14	3.48	0.14	4.14	0.39	0.01	0.01
	6.75	9	59.19	0.81	1.01	0.07	15.15	0.29	8.60	0.45	0.24	0.01	2.64	0.68	5.41	1.07	3.47	0.30	4.27	0.45	0.01	0.01
	6.8	6	59.37	0.76	1.05	0.02	15.40	0.08	8.79	0.40	0.19	0.01	2.32	0.41	5.03	0.89	3.88	0.29	3.94	0.15	0.01	0.01
	6.9	5	59.18	1.12	1.06	0.08	15.10	0.61	8.94	1.17	0.23	0.08	2.52	0.32	5.05	0.36	3.62	0.20	4.27	0.41	0.01	0.01
	6.95	6	59.28	0.40	1.08	0.03	15.22	0.10	8.96	0.26	0.19	0.02	2.51	0.09	5.30	0.13	3.59	0.10	3.85	0.11	0.01	0.00
	7	7	59.38	0.36	1.09	0.02	15.22	0.07	8.86	0.32	0.19	0.03	2.53	0.09	5.27	0.16	3.51	0.24	3.93	0.52	n.d.	
	8.1	6	60.27	0.91	0.97	0.17	14.50	1.20	8.90	1.55	0.19	0.02	2.45	0.77	5.19	1.05	3.45	0.63	4.07	0.54	0.01	0.01
	8.45	6	59.63	0.23	1.10	0.03	15.19	0.06	8.88	0.10	0.19	0.01	2.47	0.05	5.18	0.07	3.52	0.14	3.83	0.05	0.01	0.01
	9.5	7	59.65	0.27	1.02	0.02	15.18	0.06	8.64	0.14	0.19	0.03	2.42	0.05	5.29	0.14	3.61	0.27	3.98	0.09	0.02	0.02
	10.25	5	59.27	0.39	1.02	0.03	15.27	0.08	8.89	0.09	0.22	0.02	2.51	0.05	5.01	0.56	3.91	0.39	3.90	0.19	0.01	0.01
	10.65	3	59.64	0.29	1.08	0.06	15.08	0.03	9.13	0.58	0.24	0.01	2.22	0.42	4.80	0.65	3.46	0.28	4.32	0.46	0.01	0.02
	12.2	5	59.23	0.06	1.02	0.05	15.16	0.04	8.76	0.03	0.20	0.03	2.53	0.03	5.45	0.17	3.73	0.13	3.92	0.04	0.02	0.03
	12.3	5	59.27	0.18	1.04	0.03	15.14	0.07	8.81	0.15	0.23	0.02	2.50	0.04	5.24	0.05	3.70	0.19	4.06	0.33	n.d.	

Table 2.3 (continued). Average glass shard major element compositions for Lake Siwi and White Sands tephras

Location	Depth (m)	*n*	SiO_2	± 1σ	TiO_2	± 1σ	Al_2O_3	± 1σ	FeO*	± 1σ	MnO	± 1σ	MgO	± 1σ	CaO	± 1σ	Na_2O	± 1σ	K_2O	± 1σ	Cr_2O_3	± 1σ
	12.6	5	59.99	0.29	1.07	0.02	15.04	0.16	8.82	0.32	0.21	0.01	2.53	0.36	5.33	0.64	3.20	0.55	3.80	0.31	n.d.	
	12.8	10	59.64	1.29	1.05	0.13	15.32	0.80	8.58	0.70	0.19	0.03	2.56	0.47	5.45	1.24	3.66	0.50	3.53	0.79	0.01	0.01
	13.4	5	59.39	0.62	1.01	0.05	15.32	0.25	8.78	0.10	0.21	0.03	2.53	0.30	5.30	0.18	3.89	0.33	3.55	0.44	0.01	0.01
	14.7	10	60.12	0.91	1.12	0.08	14.96	0.60	8.94	0.58	0.21	0.03	2.53	0.82	4.99	0.66	3.43	0.60	3.67	0.51	0.01	0.01
White Sands	1	11	59.45	0.64	1.03	0.03	15.76	0.62	8.23	0.26	0.21	0.02	2.64	0.18	5.22	0.26	3.67	0.32	3.77	0.12	0.01	0.01
	2.1	6	58.28	1.17	1.01	0.06	15.27	0.36	8.97	0.31	0.21	0.01	3.27	0.55	6.09	0.71	3.58	0.18	3.28	0.51	0.02	0.00
	2.3	8	58.25	0.48	0.95	0.03	15.77	0.23	8.69	0.30	0.19	0.02	3.28	0.08	5.98	0.37	3.68	0.37	3.17	0.22	0.01	0.01
	2.5	6	58.03	0.35	0.95	0.02	15.85	0.47	8.41	0.44	0.19	0.01	3.34	0.07	6.28	0.16	3.81	0.12	3.12	0.05	0.01	0.01
	2.55	6	58.57	0.41	0.98	0.04	15.65	0.23	8.30	0.51	0.19	0.03	3.20	0.12	6.00	0.28	3.50	0.57	3.60	0.55	0.01	0.01
	2.6	8	58.22	0.40	0.97	0.01	15.67	0.12	8.75	0.22	0.19	0.02	3.21	0.09	6.08	0.15	3.72	0.16	3.18	0.06	0.01	0.01
	2.7	10	58.68	0.72	0.97	0.03	15.56	0.13	8.53	0.44	0.18	0.02	3.05	0.24	5.79	0.32	3.89	0.09	3.34	0.21	0.01	0.00
	2.95	11	59.78	0.14	0.99	0.01	15.58	0.10	8.23	0.07	0.18	0.01	2.66	0.04	5.18	0.05	3.76	0.11	3.61	0.03	0.02	0.02
	3.6	9	59.59	0.35	0.98	0.01	15.53	0.64	7.89	0.28	0.18	0.02	2.83	0.05	5.59	0.32	4.06	0.27	3.33	0.45	0.01	0.01
	3.7	8	59.83	0.83	1.00	0.03	15.58	0.40	7.77	0.34	0.19	0.01	2.71	0.43	5.54	0.48	3.79	0.42	3.56	0.36	0.02	0.01

* All iron expressed as FeO

n.d. - Not detected

Table 2.4. Selected trace element concentrations for a sub-set of Lake Siwi and White Sands tephras

Sample	Depth (m)	*n*	Sc	± 1σ	V	± 1σ	Sr	± 1σ	Rb	± 1σ	La	± 1σ	Yb	± 1σ
Lake Siwi	3.8	4	16.84	4.18	204.49	63.54	386.62	71.26	51.32	11.72	14.98	4.14	2.93	0.91
	4.15	5	20.60	2.19	284.07	34.60	426.97	43.06	63.92	11.26	18.38	2.92	3.42	0.50
	4.85	6	19.49	1.16	261.11	35.07	418.06	3.68	58.69	9.44	17.11	2.67	3.21	0.54
	7	6	20.20	0.21	282.37	5.42	421.28	7.73	63.66	1.15	18.49	0.31	3.59	0.12
	8.45	5	19.46	0.26	275.75	4.84	412.29	12.34	63.43	1.69	17.88	0.44	3.41	0.12
	12.8	6	19.42	1.95	272.69	25.31	402.25	20.39	57.70	8.26	17.43	1.49	3.34	0.24
White Sands	2.1	6	21.06	0.63	332.72	18.11	557.78	72.96	50.89	4.46	16.21	2.56	2.93	0.41
	2.6	6	21.61	0.97	332.94	8.39	564.50	9.08	52.57	3.09	15.17	0.56	2.86	0.27
	3.6	3	19.76	0.61	309.44	6.31	521.69	8.36	53.55	0.58	15.71	0.30	2.94	0.18
	3.7	7	18.92	1.08	300.55	18.52	519.80	22.00	57.38	2.56	17.44	1.30	3.05	0.40
BCR-2		3	33.11	0.28	428.81	2.71	342.01	0.24	50.81	0.55	24.38	0.25	3.37	0.07

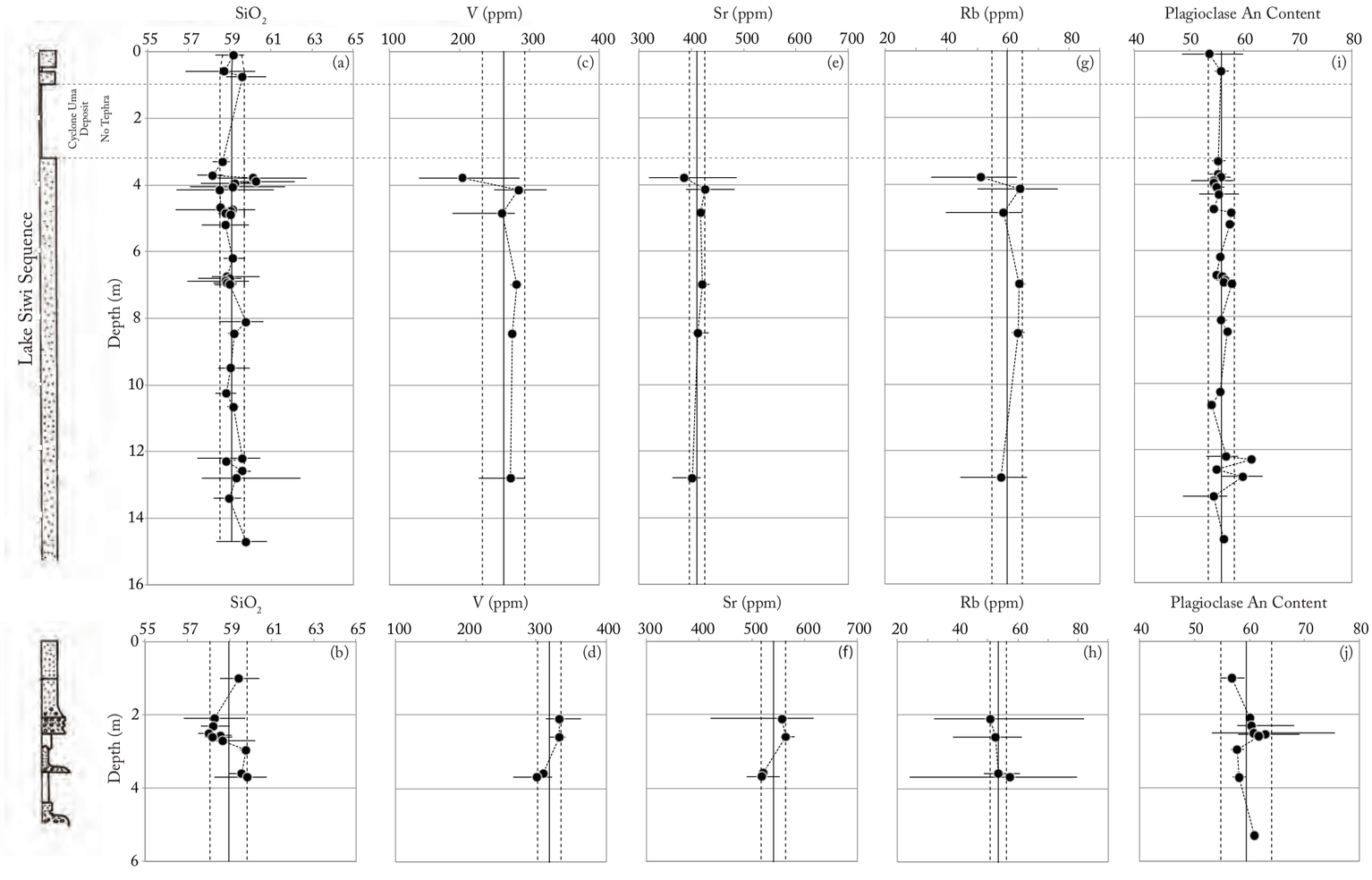

Fig. 2.7 Variation in SiO_2 (a-b), selected trace elements (c-h) and plagioclase An content (i-j) for the Lake Siwi and White Sands sequences. Simplified stratigraphic logs for each sequence are shown to the left, for comparison. Points on each panel represent the mean of an individual sample (single tephra bed), with error bars signifying the range of the sample. The mean and standard deviation for each sequence as whole is also shown.

Table 2.5. Represntative mineral major element analyses and estimated temperatures and pressures of crystallisation

	Location	Depth (m)		SiO_2	TiO_2	Al_2O_3	FeO*	MnO	MgO	CaO	Na_2O	K_2O	Total	An (Mol %)	Fs (Mol %)	Fo (Mol %)	T (°C)[a]	P (MPa)[a]	K_d[b]
Plag.	Lake Siwi	0.6	Rim	55.56	0.05	27.58	0.92	n.d.	0.13	11.24	4.74	0.64	100.86	55	-	-	1076	-	0.19
		3.8	Rim	54.24	0.04	27.77	0.89	n.d.	0.13	11.72	4.57	0.61	99.97	57	-	-	1072	-	0.16
		4.05	Rim	52.83	0.05	28.04	0.88	n.d.	0.12	11.72	4.86	0.60	99.13	55	-	-	1073	-	0.16
		4.15	Rim	54.80	0.04	27.27	0.89	0.03	0.11	11.43	4.66	0.60	99.82	56	-	-	1079	-	0.20
		4.15	Core - same grain	54.76	0.02	27.04	0.92	0.03	0.11	11.30	4.74	0.63	99.56	55	-	-	1078	-	0.21
		6.2	Rim	52.84	0.05	28.34	1.00	0.01	0.13	11.59	4.68	0.60	99.28	56	-	-	1072	-	0.18
		8.1	Rim	53.97	0.05	27.14	0.93	0.01	0.12	11.61	4.62	0.59	99.08	56	-	-	1066	-	0.17
		12.8	Rim	53.03	0.06	27.74	0.83	n.d.	0.12	12.33	4.21	0.52	98.87	60	-	-	1085	-	0.15
		12.8	Core - same grain	52.20	0.03	28.30	0.91	0.02	0.11	13.03	3.83	0.43	98.85	64	-	-	1088	-	0.13
		14.7	Rim	54.05	0.04	27.33	0.89	n.d.	0.13	11.62	4.54	0.58	99.22	57	-	-	1066	-	0.17

Table 2.5 (continued). Represntative mineral major element analyses and estimated temperatures and pressures of crystallisation

	Location	Depth (m)		SiO_2	TiO_2	Al_2O_3	FeO*	MnO	MgO	CaO	Na_2O	K_2O	Total	An (Mol %)	Fs (Mol %)	Fo (Mol %)	T (°C)[a]	P (MPa)[a]	K_d[b]
	White Sands	1	Rim	53.72	0.04	27.70	0.93	n.d.	0.11	11.82	4.47	0.52	99.41	58	-	-	1081	-	0.17
		2.1	Rim	53.12	0.04	28.36	1.14	n.d.	0.14	12.51	4.26	0.44	100.02	60	-	-	1094	-	0.18
		2.3	Rim	54.28	0.05	28.59	0.95	0.03	0.12	11.85	4.51	0.45	100.85	58	-	-	1095	-	0.20
		2.55	Rim	53.49	0.06	27.66	0.97	0.01	0.13	11.94	4.49	0.47	99.24	58	-	-	1090	-	0.20
		2.95	Rim	54.51	0.05	28.25	1.04	0.02	0.11	11.67	4.64	0.47	100.77	57	-	-	1078	-	0.17
		3.7	Rim	52.72	0.06	27.79	0.90	n.d.	0.13	12.16	4.31	0.43	98.52	59	-	-	1086	-	0.16
	Lake																		
Cpx.	Siwi	0.6	Rim	51.52	0.66	2.40	11.38	0.51	14.30	19.04	0.32	0.01	100.14	-	19	-	1049	370	0.26
		8.1	Rim	52.31	0.43	2.73	8.93	0.31	15.27	18.72	0.49	0.32	99.59	-	15	-	1070	670	0.27
	White Sands	2.1	Core	50.10	0.50	2.70	7.64	0.25	15.25	21.38	0.27	0.02	98.24	-	13	-	1048	240	0.26
		2.55	Core	51.81	0.46	2.22	8.36	0.27	16.03	20.02	0.38	0.02	99.59	-	14	-	1077	460	0.27
		2.55	Core	51.54	0.51	2.51	8.50	0.28	15.71	20.04	0.37	0.01	99.47	-	14	-	1079	490	0.27
		3.6	Rim	51.28	0.52	2.17	8.83	0.33	15.91	19.63	0.34	0.02	99.03	-	15	-	1050	260	0.26
	Basal Lava	-	Rim	51.55	0.48	2.23	9.05	0.35	15.44	20.6	0.36	0.01	100.07	-	15	-	1030	60	0.25
		-	Rim	50.80	0.55	3.13	9.11	0.30	15.34	20.49	0.36	n.d.	100.12	-	15	-	1052	270	0.25
	Crater Bomb	-	Rim	51.11	0.46	2.32	9.96	0.34	15.47	19.48	0.42	0.04	99.65	-	16	-	1038	40	0.24
		-	Rim	50.91	0.49	2.34	10.31	0.39	15.37	19.23	0.38	0.03	99.49	-	17	-	1037	20	0.24
		-	Rim	50.46	0.46	2.95	9.73	0.32	14.73	20.18	0.35	0.02	99.34	-	16	-	1052	200	0.25
	Lake																		
Ol.	Siwi	0.1		36.81	n.d.	0.02	28.84	0.78	33.53	0.25	0.02	n.d.	100.35	-	-	67	-	-	-
		3.9		36.50	0.06	0.02	29.64	0.73	32.84	0.28	n.d.	0.01	100.19	-	-	66	-	-	-
		6.2		36.12	0.07	0.06	28.80	0.63	32.93	0.28	n.d.	0.01	99.09	-	-	67	-	-	-
		6.95		36.33	n.d.	0.05	28.41	0.67	33.60	0.29	0.01	0.02	99.49	-	-	68	-	-	-
		10.65		36.61	0.01	0.04	28.98	0.78	33.35	0.27	0.03	n.d.	100.19	-	-	67	-	-	-
		12.3		36.59	0.03	0.03	28.69	0.73	33.29	0.27	0.02	n.d.	99.84	-	-	67	-	-	-
	White Sands	3.7		38.59	0.02	n.d.	25.10	0.59	36.19	n.d.	n.d.	n.d.	100.77	-	-	72	-	-	-

*All iron expressed as FeO

[a] Temperature and pressure calculated using equations from Putirka (2008)

[b] Equilibrium values for plagioclase are K_d = 0.1 +/- 0.11 (Putirka 2008)

[b] Equilibrium values for clinopyroxene are K_d = 0.28 +/- 0.08 (Putirka 2008)

n.d. - not detected

Compositions vary little ($Wo_{39-44}En_{40-45}Fs_{13-22}$) (Fig. 2.9c) and lie within a tight cluster in the augite field, as defined by Moromoto (1989). Rare olivine is present as euhedral phenocrysts in several samples from the Lake Siwi sequence and displays a small compositional range (Fo_{53-55}, n = 16) (Fig. 2.9d). Titanomagnetites are ubiquitous and show limited compositional variation (Fig. 2.9e). Those from Lake Siwi show higher ratios of Fe^{2+}/Total Fe than those from White Sands (0.43 compared with 0.39). Occasional grains from both sequences show higher proportions of Fe^{2+} and greater abundances of Ti. Titanomagnetite grains from both sequences appeared homogenous in BSE images (Fig. 2.9f) and displayed no evidence of Ti exsolution lamellae.

Thermobarometry Calculations

The pressure and temperature at which plagioclase and clinopyroxene phenocrysts crystallised from Yasur's magmas was estimated from mineral-liquid equilibrium pairs using calculations from Putirka (2008). Such thermobarometric calculations are favoured over those relaying solely on mineral compositions (i.e. Nimis 1995) as they minimise the possibility of erroneous results due to mineral zoning or xenocrystic minerals (Keiding and Sigmarsson 2012).

The relative abundance of plagioclase in almost all samples makes it a useful tracer of variation in crystallisation temperature through the tephra sequences. Crystallisation temperatures were estimated using equation 24a of Putirka (2008) which is calibrated for a wide compositional range and provides precise temperature data, with a standard error of estimate (SEE) of ±30°C. The average glass composition for each sample was used as the liquid component. This was found to be in equilibrium with all but one of the plagioclase grains, according to the equilibrium test proposed by Putirka (2008). As the H_2O content of the glass shards was not measured but is necessary for thermometric calculations, an estimated H_2O content of 1 wt.% was used, based upon olivine-hosted melt inclusion data from Métrich et al. (2011). This is amongst the lower end of H_2O contents recorded for volcanic arc magmas (Wallace 2004). Variations of 1 wt. % H_2O result in systematic changes of 31-33°C, with lower melt H_2O driving estimates to higher temperatures.

Temperature estimates for the Lake Siwi tephras range from 1046°C to 1068°C (Table 2.5), with an average of 1056°C. All values fall within the range defined by the mean ± SEE. Plagioclase from the White Sands tephra sequence indicates an overlapping, but slightly

higher temperature range (1059°C to 1092°C) compared to the Lake Siwi sequence. These temperature estimates are lower than, but within error of, optical thermometry estimates using olivine- and plagioclase-hosted melt inclusions, which suggest magma temperatures of ~1107 ± 15°C (Métrich et al. 2011).

Only two clinopyroxene grains from the Lake Siwi tephras are in equilibrium with their respective glass shards according to the equilibrium test proposed by Putirka (2008). Using the Putirka (2008) clinopyroxene-liquid calculations, equations 30 and 33 (SEE of ± 30°C and ± 150 MPa for temperature and pressure respectively) calculated temperatures of 1032°C and 1052°C and pressures of 220 MPa and 500 MPa are obtained. For the White Sands sequence, calculations yield temperatures of 1018 to 1061°C, with pressures ranging from 80 to 340 MPa. Clinopyroxene grains from the lava flow at the base of the Lake Siwi tephra sequence and from a recently erupted lava bomb extend the range of pressures to shallower depths (up to 20 MPa) (Table 2.5).

DISCUSSION

Episodes of Eruptive Activity

Clarifying the record of volcanic activity at Yasur has important implications for understanding the magmatic plumbing system and for future hazard planning. Using the tephra stratigraphy presented here and correlated tephra sequences from Nairn et al. (1988) (Fig. 2.5), three different episodes of eruptive activity at Yasur can be identified over the last 1.5-2 kyr. The current episode of persistent activity appears to have been preceded by higher-magnitude, lower-frequency eruptions before which a period of irregular eruptions of varying intensity and frequency are recorded.

Persistently Active Eruptive Episode (~1270 A.D. to Present)

The most recent eruptive episode is recorded by deposits of medium to coarse ash which form the uppermost tephra deposits in all four tephra sequences. In the more distal sections this corresponds to a 1-2 m thick, friable deposit, which is either massive or shows weak stratification. This thickens towards the volcano and comprises the entire >15 m section at Lake Siwi. This sequence is not only thicker due to its proximity to the vent, but also as a result of the higher degree of tephra preservation afforded by the lake. Furthermore, it is closer to the main axis of tephra deposition. Individual beds are readily discernable in the Lake Siwi sequence,

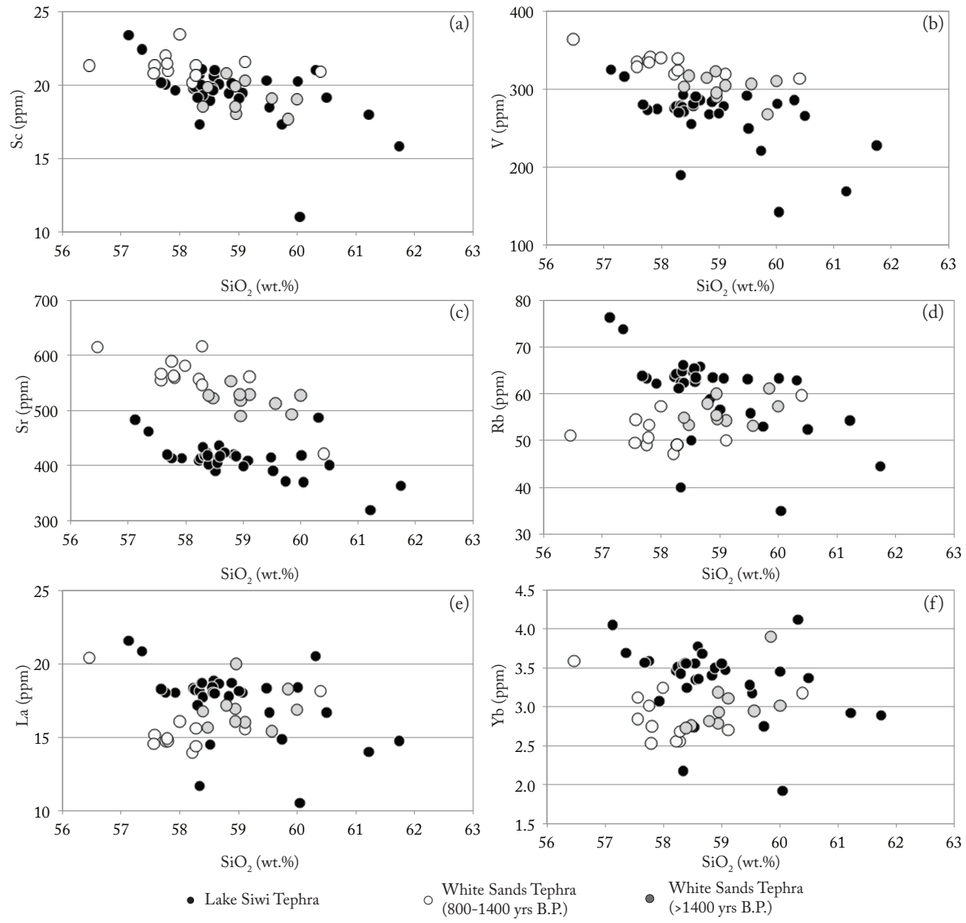

Fig. 2.8 Glass shard variation diagrams, showing selected trace element abundances versus SiO_2. Samples are divided into the same categories as Fig. 6. Errors are less than the size of the symbols.

highlighting small-scale perturbations to the eruptive regime through this period. The small but regular fluctuations in grain size are consistent with the cyclical pattern in activity recognised over the past two decades of monitoring (GVN Bulletin 1999). Their presence throughout the sequence, suggests this regime of activity has persisted since at least ~1690 A.D. Nevertheless, the relative consistency in bed thickness and grain size throughout the ~1.2 km exposure of this sequence, as well as in deep sequences cut through the dispersal axis alongside the main road (Fig. 2.1), suggests the volume and magnitude of individual eruptions has remained relatively constant over the period represented by this sequence. This supports the assumption of persistent activity suggested by the patchy historical record.

The lava bomb at the base of the Lake Siwi sequence offers the only evidence for periods of highly explosive Vulcanian activity throughout the period represented by deposition. Given

the simple morphology of the Yasur cone, this bomb must have originated from the main crater. While no other bombs were found at this distance from the crater, high intensity activity, such as that of 1999, involves bombs falling only ~400 m closer to the vent (GNV Bulletin 1999). The exit velocity and launch angle required to transport this bomb was estimated using the model of Mastin (2001). Assuming launch angles similar to those observed at Yasur in 2011 (~ 70°) an exit velocity of ~150 ms^{-1} would be required. This value is ~40% higher than the exit velocities estimated for lava bombs erupted in 2011, however it is within the range of velocities recorded by Taddeucci et al. (2012) for similar activity at Stromboli (maximum velocities of 172-405 ms^{-1}). Shallower launch angles would require slower exit velocities and could explain the location of this bomb without invoking more powerful blasts. Strong tailwinds (Mastin 2001) and collision with other bombs (Vanderkluysen et al. 2012) may have also contributed to the increased distance it travelled. Despite this bomb, there is no other evidence of more powerful, explosive, tephra-producing eruptions during this period.

Two <10 cm thick mud units at 12.5 m and 12.8 m depth in the Lake Siwi sequence (Upper and Lower Cracked Clay: Fig. 2.2) display polygonal cracks on their upper surfaces, recording lake-drying events related to droughts. Palaeoclimatic records indicate that inter-annual climate variability (e.g. El Niño/Southern Oscillation) was more marked and periods of reduced precipitation more common in the South Pacific during the period 1300 – 1800 A.D. (Hendy et al. 2002; Nunn 2007; Gorman et al. 2012). Such conditions may have increased the incidence of lake-drying events during this period. Extrapolating the tephra accumulation rate calculated above to these cracked mud layers suggests that they were deposited ~1775 A.D. Historical and palaeoclimatic records report a particularly serious El Niño in 1788-95, during which much of the Asia-Pacific region experienced severe drought, including nearby New Caledonia (Grove 2007). The possibility that the cracked clay layers relate to potential drying of Lake Siwi during the 1790's El Niño supports the calculated accumulation rate and reinforces the constancy in output of Yasur throughout the past 200 years. This is a key observation that confirms Yasur is a steady-state volcano according to the definition of Wadge (1982).

Using the accumulation rate, a time-averaged output rate for Yasur through this period can be estimated at ~410-480 $m^3\ d^{-1}$. This is based on a minimum estimate of the area of cumulative tephra deposition during typical activity at Yasur, which is 3.3-3.9 km^2 (Fig. 2.1). This area, as depicted on Fig. 2.1, corresponds to the extent of recent tephras seen in the denuded part of the landscape. Sections exposed along the main road that cuts on an angle through the main fall

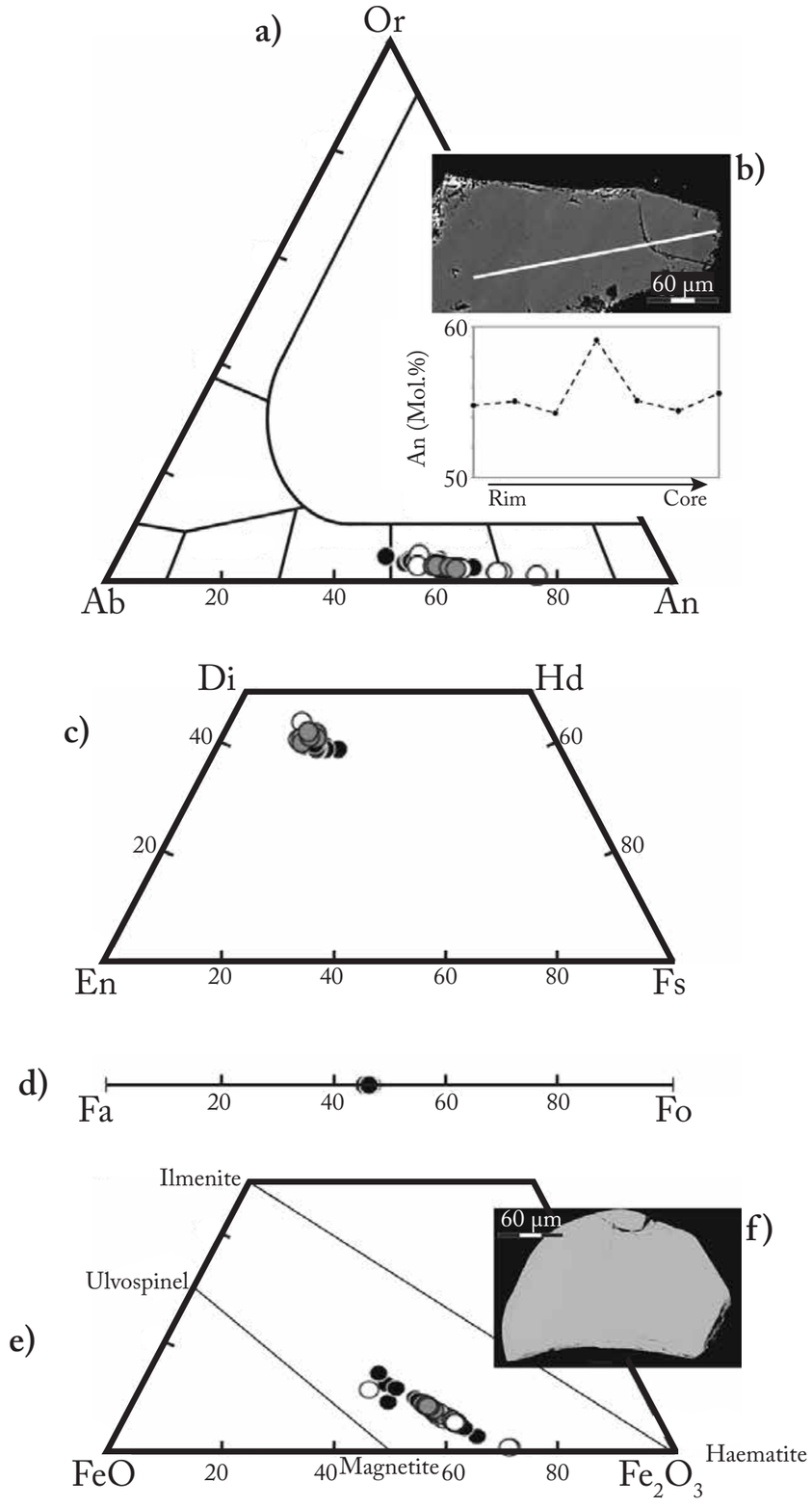

lobe and the stream banks lead to an estimate of c. 0.04-0.05 km^3 deposited during the period represented by this sequence. This assumes the total zone of tephra deposition during typical activity at Yasur, analogous to the area of the ash plain, is ~3.3 km^2 (Fig. 2.1). While tephra deposition is unlikely to be uniform in thickness, the accumulation rate is valid for the centre of this area, and is thus likely to represent an average for the zone as a whole. Assuming tephra densities of ~1500 kg m^{-3} (Métrich et al. 2011) the output rate provides an emission rate of ~5.7 x 10^5 kg d^{-1}, comparable to estimates from filter pack samples by Métrich et al. (2011). While these values should be seen as a minimum, they are significantly lower than calculated output rates for other steady-state volcanic systems such as Arenal, which are one to two orders of magnitude greater (Wadge 1981).

Correlation with the radiocarbon dates from Lownasunen suggest that this episode of persistent, steady-state activity began between 1160-1380 A.D. Similar protracted and persistent eruption has been witnessed at Stromboli, which has seen continued eruptions over the past 1400–1800 years (Rosi et al. 2000), however is generally rare amongst volcanoes worldwide.

Higher Magnitude, Lower Frequency Eruptive Episode (~700 – 1270 A.D.)

Beneath tephras of the current eruptive episode, a series of decimetre thick, coarse ash-lapilli beds are evident in the White Sands sequence and can also be discerned from the stratigraphy of Nairn et al (1988). Examination of a single tephra sequence limits observational bias, assuming no long-term changes in wind patterns. Examination of the late Holocene White Sands sequence thus reliably highlights changes in the magnitude and frequency of eruptions. The coarser grain size seen between 1.5 and 2.7 m, relative to the recent ash deposits (Mdϕ <1, compared with Mdϕ >1 in overlying tephra), suggests that these eruptions were more powerful than those of today. Inability to correlate and map individual beds precludes production of isopach and isopleth maps and thus normal empirical evaluations of eruption column height

Fig. 2.9 a) Ternary diagram showing plagioclase compositions. (b) BSE image of a typical plagioclase crystal, with no apparent zoning (crystal from sample 3.13). Anorthite content for a core-rim traverse of this crystal is shown beneath. (c) Clinopyroxene compositions from both tephra sequences. (d) Olivine compositions from both tephra sequences. (e) Titanomagnetite compositions for both sequences. (f) BSE image of typical titanomagnetite grain, showing homogenous texture. Symbols for all panels are same as Figure 2.6. Errors are less than the size of the symbols.

and VEI are not possible. Nevertheless, some indication of these parameters can be estimated by comparing the deposits at Yasur with similar deposits at other volcanoes, for which these features are known. The White Sands sequence contains at least four ~10 cm thick, lapilli-fall deposits. Deposits of a similar thickness and grain size have been found at a similar distance from the vent along the main ash dispersal axis for the 1730 A.D. eruption of Vesuvius (Arrighi et al. 2001). Arrighi et al. (2001) estimated a bulk erupted volume of 1.18×10^6 m^3 for this Vesuvius Eruption, which lasted 33 days. Assuming tephra densities similar to those seen at Yasur (Métrich et al. 2011), this equates to ~6×10^7 kg d^{-1}. While these values cannot be directly applied to Yasur, they indicate that eruptions during this episode may have had output rates at least one to two orders of magnitude greater than those calculated for the current episode of persistent activity. . To compare, the greatest plume height in the historical record for Yasur is ~3 km, recorded during heightened activity in 1977 (Eissen et al. 1991). During typical daily activity recorded over the recent decades at Yasur, the eruptive plume rarely reaches 500m above the crater. Thus most eruptions during the recent steady-state eruptive episode are VEI 0-1.

Each lapilli-fall bed in the White Sands sequence is separated from the bed above by a weathered upper contact, often consisting of finer-grained tephras. This suggests periods of relative quiescence between the higher magnitude events, with the interval between eruptions sufficient for weathering to occur. A gradual variation in grain size between these deposits and those from succeeding steady-state activity suggests a steady transition rather than a sudden shift between these two styles of activity.

Again, correlation with the tephra sequences of Nairn et al. (1988) provides some temporal framework for this episode of activity. Radiocarbon dates from Lownasunen suggest that it lasted 500-600 years, beginning sometime between 540 and 875 A.D. (Fig. 2.5). At White Sands, five lapilli-fall beds can be discerned during this time, suggesting a statistical recurrence interval for higher magnitude eruptions of ~120 years. Using the estimated output of the higher magnitude eruptions and their recurrence interval, a time averaged output rate of ~4.7×10^4 kg d^{-1} can be estimated for this eruptive episode, an order of magnitude smaller than the output rate for the steady-state episode that followed.

Variable eruptive episode (Before 700 A.D.)

The earliest eruptive episode, recorded at White Sands, displays much greater variability

in terms of eruption style and recurrence rate than succeeding eruptive episodes. Coarse-grained lapilli-fall deposits are interspersed with thick beds of very fine ash. Palaeosols and weathered contacts imply breaks in eruptive activity and at least one unconformity is visible.

While this episode ceased between 540 and 875 A.D., its duration remains unknown. The transition from this period to the episode of higher magnitude eruptions following appears to have been sudden and was marked by an abrupt boundary in the White Sands sequence, with a shift to increased grain size (Fig. 2.4). Radiocarbon dates from White Sands suggest that this transition was preceded by >200 years of lower magnitude volcanic activity, during which a thick bed of weathered fine ash was deposited. This may represent a shift in vent location, as speculated by Nairn et al. (1988).

Compositional variation: Insights into magmatic processes

Examination of the compositional variation in glass shards and mineral grains both within and amongst each eruptive episode is crucial to understanding the magmatic processes controlling the styles of eruption seen in each episode. Furthermore, it may elucidate what processes changed to drive the shift between eruptive episodes.

Persistently Active Eruptive Episode

According to O'Hara (1977) steady-state volcanic activity, which appears to have occurred at Yasur for the past 630-850 years, should be accompanied by eruption of magmas with a uniform chemical composition. Steady-state conditions require rates of magma input and output (through eruption and intrusion) from the magma reservoir be balanced. If the residence time remains constant, the thermal conditions of the magma chamber should be invariant. Assuming the composition of the incoming magma remains constant and the amount of assimilation and mixing is stable, it follows that the magma composition will be buffered over extended periods of time. This implies that magma input and output volumes must vary in concert for the chamber to change in size without disturbing equilibrium. No systematic investigations have yet determined what degree of compositional variability may accompany a buffered magma chamber.

Previously published whole-rock data from Yasur (Nairn et al. 1988; Turner et al. 1999; Métrich et al. 2011; Kremers et al. 2012) suggests the composition of magma erupted since 1920 has not changed (e.g. SiO_2 ranges from 54.5 to 57.44 wt.%, but clusters between 55.5-56.5

wt.%). Whole-rock data for historical and prehistorical lavas presented here suggest that the period over which compositionally homogenous lavas have been erupted is significantly longer, as previously suggested by Métrich et al. (2011).

The Lake Siwi sequence offers an unprecedented opportunity to determine the geochemical variation in a high resolution tephra record to understand equilibrium processes in magmas erupted from a low-rate, steady-state magma system. There is a small variation in individual glass shard compositions, which is of a similar magnitude to the entire variation observed throughout the Lake Siwi sequence. A roughly linear, non-varying trend with small fluctuations about an average value is apparent in both major and trace element compositions, when plotted against depth (Fig. 2.7). This suggests that the magma composition has remained relatively constant since ~1740 A.D. Estimated temperatures of plagioclase crystallisation suggest that Yasur's magma chamber has also remained at a roughly constant temperature throughout this time period.

Comparison with other steady-state volcanoes enables better understanding of the magnitude of such fluctuations in steady-state systems. Stromboli is the most obvious analogue for Yasur, despite its less evolved magma compositions, as it displays similar styles and persistence of eruption (Rosi et al. 2000). A limited data set of highly porphyritic (HP) glass shard compositions erupted from Stromboli since 1930 (Francalanci et al. 2004; Landi et al. 2009) displays similar uniformity to that seen at Yasur. Standard deviation of major element oxides, as a measure of variation through the sequence, is comparable to, but marginally lower than that of the Lake Siwi tephras (0.95 versus. 1.18 for Lake Siwi tephra). Matrix glass analyses from eruptions covering a 32 year period at Erebus, another long-lived, persistently active volcano, display a similarly limited variation in major and trace element concentrations (Kelley et al. 2008). Whole-rock data for both Stromboli (Rosi et al. 2000; Francalanci et al. 2004; Métrich et al. 2010) and Erebus (Kelley et al. 2008), as well as Piton de la Fournaise (Albarede and Tamagnan 1988; Albarede et al. 1997) suggest little variation amongst major element compositions from steady-state magma chambers.

The consistency in composition between lava flows and lava bombs erupted during this period suggests both eruptive styles are controlled by the same magmatic processes. Effusive eruptions, while rare, are most likely a result of higher magma volumes in the conduit, leading to conduit overflow.

Previous investigations of other steady-state volcanoes, such as Stromboli and Arenal

have identified geochemical and textural complexity amongst phenocrysts, despite the homogeneity of whole-rock compositions (Streck et al. 2002, Landi et al. 2004). Minerals from both volcanoes display complex compositional zoning that was attributed to continued crystallisation through successive recharge events in which less evolved magma is supplied and mixed with resident magma. The minerals from Yasur show very narrow compositional ranges (Fig. 2.9), with little variation in composition through the time period recorded in the Lake Siwi sequence (Fig. 2.7i). Furthermore, while occasional crystals display normal zoning patterns these are limited and are less complex than similar crystals from Stromboli (Landi et al. 2004) or Arenal (Streck et al. 2002). Similarly, cross-grain compositional variation is limited (Fig. 2.9b). These factors suggest that the phenocrysts preserved in volcanic rocks from Yasur grew in a stable environment that witnessed limited chemical variation. This points to a very large magma reservoir at Yasur, which has a large buffering capacity. This differs from previous models of steady-state activity, which require a degree of recharge and mixing (O'Hara 1977). Nevertheless, both eruptive dynamics and constant whole-rock and glass shard compositions seen at Yasur still favour the occurrence of steady-state conditions. These seemingly incongruous lines of evidence can be reconciled if mixing and crystallisation are segregated in time or space. Either recharge and mixing are occurring at rates slower than those of crystal growth or they are occurring at greater depth, prior to crystallisation. The latter is consistent with the shallow pressures of crystallisation proposed for a number of clinopyroxene phenocrysts. The low water content of melt inclusions (< 1.3 wt.%) analysed by Métrich et al. (2011), similarly suggest shallow crystallisation, as the solubility of water in magma decreases with lower pressure (Burnham 1975). This suggests crystallisation may be driven by degassing in a magma that has undergone prior recharge and mixing, implying the proportion of the total magmatic system that is in steady-state is significantly greater than at other persistently active volcanoes and is not confined to a shallow reservoir and conduit.

Kelley et al. (2008) propose a similar mechanism to explain the relatively homogenous mineralogy seen at Erebus. They recognise this limits the role of magma replenishment as a direct trigger for eruptions and instead invoke volatile flux as the primary driver of eruptive activity, with higher fluxes producing more vigorous eruptions and visa versa. Gas flux and melt inclusion data for Yasur suggest a similar link between very late stage degassing in the upper conduit and dynamics of Strombolian activity (Oppenheimer at al. 2006; Métrich et al. 2011).

Such fluctuations in volatile flux and their concomitant changes in eruption intensity

help to explain perturbations in glass shard and phenocryst chemistry through the Lake Siwi sequence. Noticeable excursions towards more evolved compositions (SiO_2 > 60 wt.%), such as those at depths of 0.75 and 3.8 m in the Lake Siwi sequence (Fig. 2.7a) can be correlated with both higher microlite content (Fig. 2.3f) and finer grain size (Fig 2.2) (Md > 2.25ϕ). The latter suggests these tephras were associated with less intense eruptions, which would have evacuated less magma from the upper conduit. This would increase residence times in the upper conduit, possibly by days or weeks, allowing high degrees of late stage crystallisation, which would increase microlite contents and force the residual liquid to more evolved compositions. Platz et al. (2007) recognise sub-visible microlites as a major contaminant in in situ analysis of andesitic glasses. Samples erupted during these excursions display the highest intra-sample major and trace element variability of any tephras seen at Yasur. One sigma variation in trace element analyses is over an order of magnitude greater for these samples than for the BCR-2 reference glass (Table 2.4), showing this variation is not the result of analytical errors. Combined with the trend to lower Sr concentrations, with no concomitant changes in plagioclase phenocryst rim An content in these samples, it would appear that crystallisation of plagioclase microlites was higher at the time of this excursion to more evolved compositions. In contrast, less evolved samples, such as that seen at 3.7 m depth in the Lake Siwi sequence, usually display limited intra-sample variability and are often associated with coarser grain size (Fig. 2.2), suggesting more intense eruptions and shorter upper conduit residence times. Using the historical accumulation rate calculation, the less evolved sample seen at 3.7 m depth is likely to have been erupted around 1975, at a time when particularly intense eruptions were recorded (Eissen et al. 1991). This is consistent with whole-rock data presented by Turner et al. (1999) for a bomb erupted at this time, which is amongst the least evolved composition in the literature (SiO_2 = 54.9 wt.% and MgO = 3.39 wt.%). These observations suggest that small perturbations in magma chemistry can be explained by variations in upper conduit residence times, which allow more or less late stage microlite crystallisation. These, in turn are linked with cycles of activity recognised at Yasur.

Overall, the geochemical variations witnessed in tephras from the Lake Siwi sequence support the observations of O'Hara (1977) and Pyle (1992), suggesting that Yasur's magma chamber has been chemically buffered throughout the past 630-850 years. Small fluctuations in magma composition through that time result from minor changes in volatile flux and upper conduit residence times. That mixing and recharge events are not recorded by mineral textures

suggests that steady-state conditions are not limited to Yasur's conduit or magma reservoir, but may extend to depths greater than those at which the erupted phenocrysts are crystallising.

Higher Magnitude, Lower Frequency Eruptive Episode

Prior to this ongoing steady-state activity, the volcano operated in a different fashion, with lower-frequency, higher-magnitude eruptions accompanied by discharge of less evolved magmas, with lower SiO_2 and higher CaO and MgO contents (Fig. 2.6). Similarly, magmas erupted at this time are enriched in compatible trace elements, such as Sc and V, as well as Sr, while they display depleted incompatible element abundances, relative to the succeeding steady-state magmas (Fig. 2.8). Plagioclase compositions during this episode are also consistently more calcic (Fig. 2.7j), while plagioclase-liquid thermometry suggests higher temperatures for crystallisation (> 1080°C) during this period (Table 2.5).

The contrast in deposit characteristics and chemistry between this higher magnitude episode and the steady-state episode following it, can be explained by differing regimes of degassing. The less evolved compositions and discrete eruptive events suggest periodic plugging of the magma pathway during the higher magnitude episode. The higher residual Sr in these magmas suggests significantly less fractionation of plagioclase occurred relative to current activity. This can be explained by a system in which the final stage of degassing-related crystallisation in the open conduit is not occurring. This suggests that the shift between these two eruptive episodes was marked by a transition from a periodically closed (plugged) to fully open conduit. A major episode of faulting, associated with uplift, such as that recorded by Chen et al. (1995), may have opened a new pathway for the magma and facilitated more regular degassing and eruption. Equally, the stratigraphy at White Sands (Fig. 2.4) raises the possibility that the final high-magnitude eruption permanently opened the conduit. The thickness and coarse grain-size of the uppermost lapilli-fall bed at White Sands suggest that it may represent the highest magnitude eruption through this period. At White Sands, the deposit from this eruption grades into the tephra from subsequent persistent activity. This is not recorded in the stratigraphy of Nairn et al. (1988), however.

The lack of titanium exsolution lamellae in titanomagnetites (c.f., Turner et al. 2008) examined from both tephra sequences suggests magma ascent remained rapid during this time. This is corroborated by homogenous melt inclusions from highly explosive eruptions which show little or no interaction with their host minerals and negligible diffusion of H_2O (Métrich

et al. 2011). This suggests that the more violent eruptions tap a magma reservoir at a depth of ~2-4 km, extracting a more volatile-rich, gas-rich magma. Clinopyroxene-liquid barometry calculations presented here, while limited in number, raise the possibility of an even deeper reservoir.

The finer grained beds formed during this period display marginally more evolved compositions, raising the possibility that major eruptions may have been associated with the injection of more primitive material into the magma chamber, while intervening periods of lower magnitude activity facilitated further evolution of magma. Equally these fluctuations may result from differing regimes of degassing or heat loss between high and low magnitude eruptions.

Variable eruptive episode

Tephra from the earliest eruptive episode, preserved at the base of the White Sands sequence, display glass shard compositions similar to those seen in the Lake Siwi section (Fig. 2.6). Sample collection form this part of the sequence was limited and was biased towards the coarser-grained beds, which limits a full appreciation of the chemical variability. Glass shards from the lower-most sample, at the base of the sequence, are highly microlitic and also contain a greater abundance of phenocrysts (Fig. 2.3e). The higher microlite content may be linked with stagnation just prior to eruption, possibly in a lava lake or in the shallow conduit. Mineral compositions from this sample are similar to those from the remainder of this eruptive episode, however, suggesting that the processes controlling phenocryst crystallisation were the same between the samples. Clinopyroxene mineral-liquid pressure estimates suggest shallower crystallisation (< 1.5 kbar) during this eruptive episode.

Reconciling the tephra record with caldera formation and caldera resurgence

For a full interpretation of the tephra deposits discussed here, they must be viewed in context with the Yenkahe Caldera and Yenkahe Resurgent Dome. At first sight, Yasur's current steady-state activity seems incongruous with the rapid rates of uplift identified for the area by Chen et al. (1995) which have been attributed to magma replenishment. Francis et al. (1993) identified endogenous growth through dykes, sills and cumulate complexes to be a common part of steady-state volcanism at centres such as Kilauea and Stromboli based on otherwise irreconcilable gas outputs and eruption volumes. Similarly, Yasur's high gas flux, relative to

its output rate, suggests the emplacement of up to 25 km^3 of un-erupted magma (Métrich et al. 2011). This implies that a large reservoir of magma is available to maintain shallow storage areas with equilibrium compositions, driving steady-state activity.

Steady-state activity and dome resurgence are readily explained in the context of the broader Yenkahe caldera structure. Cole et al (2005) showed that faults created during caldera collapse are often reactivated and exploited in the opposite direction to accommodate caldera resurgence. This is likely the case for the Yenkahe Dome, which is bound and cut by a series of faults (Peltier et al. 2012; Merle et al. 2013). Yasur's location, at the margin of the Yenkahe Horst, suggests that magma also exploits associated faults. These features combine to produce a mechanism for continued magma output.

The eruptive products from Yasur suggest that steady-state activity is fed by magma that has already undergone significant differentiation. These compositions are similar to the composition of the Siwi Ignimbrite (55.2-60.2 wt.% SiO_2) and conform to the same liquid line of descent (Métrich et al. 2011). This suggests a shared magma source for both Yasur and the caldera-forming Siwi eruption. While the differing types of eruptions may signify varying magma replenishment rates, it remains possible that little has changed beyond differing mechanisms of magma rise. The caldera-forming Siwi eruption may represent the initial injection of magma: the violence of the eruption explained by the rapid rise of magma from depth. Faults associated with formation of the Yenkahe Caldera may now enable greater release of gas and magma, both through eruption and intrusion associated with dome resurgence. Current eruptive activity at Yasur is driven by degassing and thus reflects an active pathway for gas and magma from depth to the surface. In this way, steady-state activity at Yasur can be related to the slow 'leaking' of magma from the magma reservoir and differential gas transfer.

Assuming the uplift rates estimated by Chen et al. (1995) have remained constant, resurgence of the Yenkahe Dome may have started as recently as ~2,000 years ago. The stratigraphic evidence presented here suggests that volcanic activity has persisted throughout that time, with a transition from eruptions with highly variable recurrence intervals to predictable, steady-state activity. Nairn et al. (1988) estimated the Siwi Ignimbrite may be a few tens of thousands of years old, based upon erosion patterns. This leaves a significant time gap between caldera formation and the activity described here. Rapid dome uplift and stabilisation of recent volcanic activity may signify renewed magma recharge to the Siwi area after a hiatus in activity following the cataclysmic Siwi eruption. Equally, volcanism may have continued through much

of the post-caldera episode, however the recent history is more readily revealed in the surface geology. Examination of older deposits preserved downstream from Lake Siwi may provide greater insight on the early history of post caldera activity.

CONCLUSION

The tephra records from the Siwi Region of Tanna highlight the remarkable constancy in the composition of magmas erupted through the past >1500 years of post-caldera volcanism and help to elucidate the eruptive history through this period. They indicate that the current episode of relatively low-magnitude, persistent activity has continued for 630-850 years. Activity throughout this period has been characteristic of steady-state behaviour, with a constant output volume accompanied by eruption of magmas with invariant crystallisation temperatures and uniform major and trace element element compositions. This supports previous assertions that suggest steady-state magma chambers should be chemically buffered over extended periods of time. Data from Yasur and other steady-state volcanoes extend this statement to suggest that the magmas should be buffered around a mean composition, with small perturbations, expected in any natural system, reflecting fluctuations in buffering parameters. In the case of Yasur, degassing rate controls the intensity of eruptions, which in turn effects the magma's residence time in the upper conduit, probably by days or weeks. Longer residence times allow further late-stage crystallisation, particularly of microlites, driving the residual liquid to more evolved compositions. The unique compositional and textural homogeneity of Yasur's phenocrysts suggests different processes of mixing and recharge compared with volcanoes such as Stromboli. This raises the possibility that at Yasur mixing occurs at some depth, prior to crystallisation of the main phenocryst phases, suggesting that both shallow and deep magma reservoirs may be chemically buffered.

Prior to the current episode of activity, there was greater variability in the nature of eruptions and the composition of erupted products. An episode of higher magnitude, lower frequency eruptions during this period is linked to the eruption of less evolved magma. This may represent the periodic release of less-differentiated, un-degassed magma following discrete recharge events, however it is more likely to have resulted from periodic plugging of the conduit, trapping volatiles until they were released explosively. The transition to the current episode of activity at Yasur may be associated with the opening of a more accessible path through which magma can reach the surface, either through faulting or as a result of a violent eruption. This eventually produced an open conduit that facilitates steady-state activity. This ease of degassing and eruption, which can be envisaged as a leak in the magma reservoir, combined with the high magma replenishment rate assumed to be driving resurgence of the Yenkahe Dome offers some indication of what factors may be permitting Yasur to sustain eruptions over such timescales.

3. Dynamics and pre-eruptive conditions of catastrophic, ignimbrite-producing eruptions from the Yenkahe Caldera, Vanuatu

Chris W. Firth[1*], Shane J. Cronin[2], Simon P. Turner[1], Heather K. Handley[1], Clement Gaildry[1] and Ian Smith[2]

[1] Department of Earth and Planetary Sciences, Macquarie University, Sydney, NSW 2109, Australia

[2] School of Environment, University of Auckland, Auckland, New Zealand

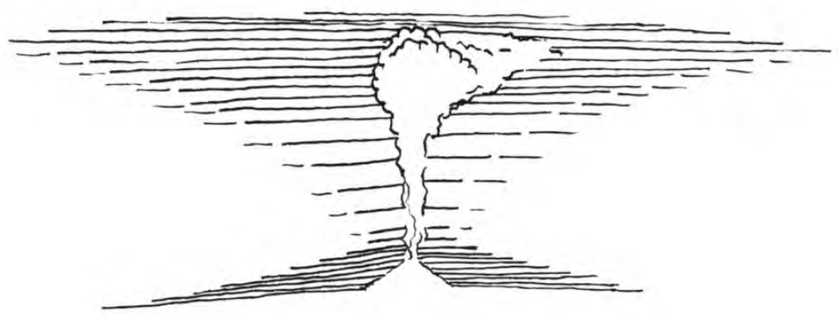

Manuscript submitted to
Journal of Volcanology and Geothermal Research

Submitted: 13th May 2015

Accepted: 7th October 2015

Published: 15th December 2015

A combined stratigraphic and geochemical examination of ~43 kyr of volcanic activity is presented for the Yenkahe Caldera, a mafic-intermediate volcanic system on the island of Tanna, in the Vanuatu Arc. Through this period two catastrophic ignimbrite-producing eruptions have occurred: the Siwi eruption and the older, Old Tanna Ignimbrite eruption. The latter was previously linked with a different edifice to the north-east, however re-examination has shown it was derived from the Yenkahe Caldera. Radiocarbon dating of this ignimbrite gives an age of ~43 kyr B.P. Both eruptions produced voluminous ignimbrite sheets, however differences in deposit sequences show that the eruptions followed distinct courses. Deposits from the more recent Siwi eruption display greater evidence for phreatomagmatic phases during eruption onset. Both ignimbrites are distributed asymmetrically about the caldera, indicating partial collapse in each case. The early stages of the Siwi eruption produced directed pyroclastic surges and spatter fountains. Between these two major eruptions, volcanic activity was maintained through the formation of small, discrete volcanic cones, such as Yasur, which is active today. Whole rock major and trace element data show that intra-caldera activity between cataclysmic eruptions produced magmas of uniform basaltic-trachy-andesitic composition (SiO_2~56 wt.%). Minerals within these lavas appear to be in equilibrium with their host. The Siwi eruption produced the most evolved, trachy-andesitic magma (SiO_2 >58 wt.%), while the Old Tanna eruption is associated with less evolved, basaltic-andesite magma (SiO_2 ~53 wt.%). Juvenile clasts from both ignimbrites display diverse mineral chemistry and mineral disequilibrium textures. From these variations in geochemistry and petrology we suggest that a crystal mush or resident magma remained following low-magnitude, intra-caldera activity. MELTS modelling suggest this was stored at shallow depths, equivalent to pressures <1 kbar. Injection and mingling/mixing with primitive magma rejuvenated this mush component to trigger the ignimbrite eruptions.

INTRODUCTION

Catastrophic, ignimbrite-producing, caldera-forming eruptions are amongst the most violent and damaging forms of volcanic unrest. In small island nations they have the potential for causing severe social disturbance and have even been known to completely destroy civilisations. Well-known examples of such cataclysmic eruptions include the 1620 B.C. eruption of Santorini (e.g. McCoy and Heiken 2000a; Bruins et al. 2008) and the 1815 A.D. Tambora eruption (Oppenheimer 2003). Regional and global effects of such eruptions are also propagated through knock-on phenomena such as tsunamis (Waythomas and Neal 1998; Carey et al. 2000) and climatic perturbations (McCormick et al. 1995; Self et al. 2004). Given the long repose times between such large-magnitude eruptions (10^3-10^5 kyr) they can be overlooked in hazard assessments. Detailed examination of the geology and accurate dating of these deposits is necessary to understand their significance within the wider magmatic system.

Evidence for caldera-forming eruptions has been identified at a number of volcanoes

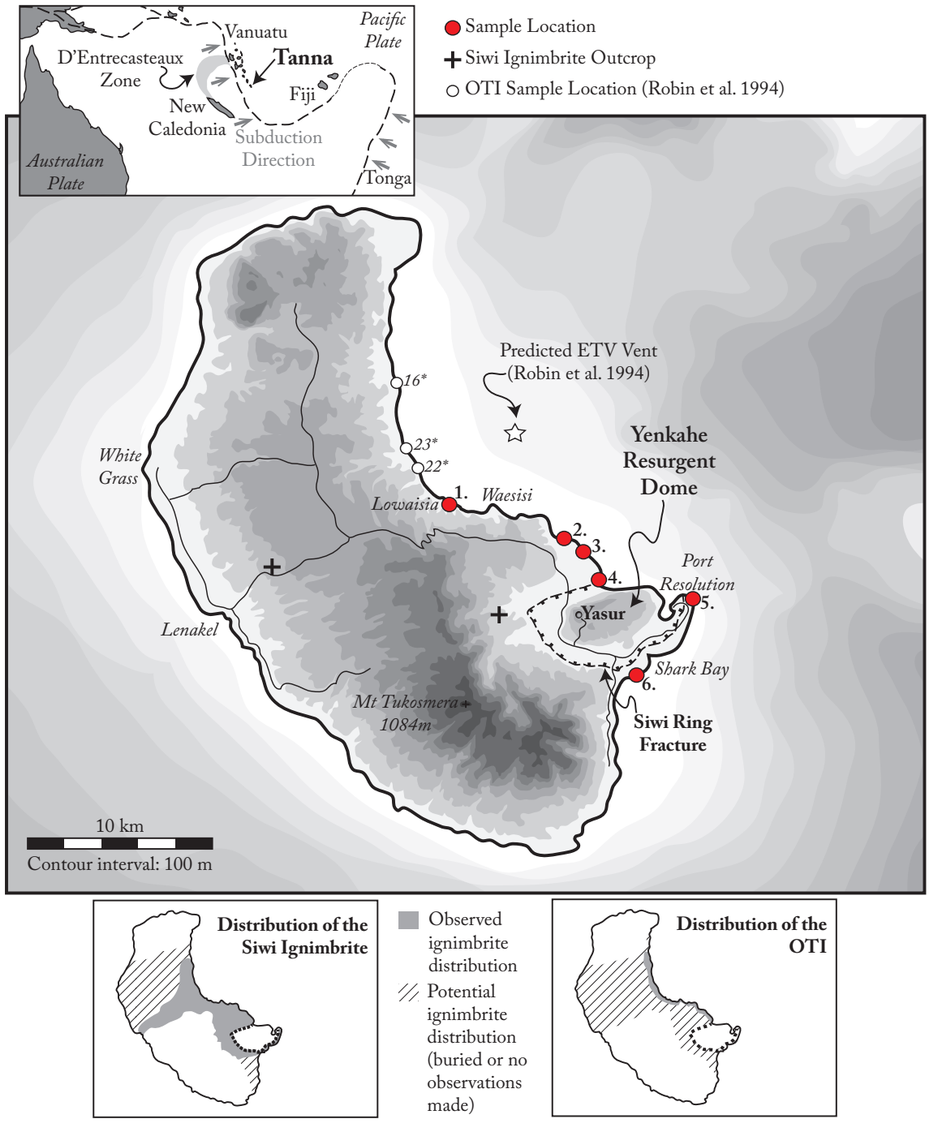

Fig. 3.1 Map of Tanna, showing the location of the Yenkahe Caldera relative to stratigraphic sections discussed here. Stratigraphic sections examined by Robin et al. (1994) are also shown for comparison. The location and tectonic regime of Tanna are shown in the upper inset, while the lower insets show the observed and inferred outcrop distribution of both the Siwi Ignimbrite and OTI.

in the Vanuatu Arc (e.g. Robin et al. 1993; 1995; Monzier et al. 1994; Allen 2005; Gao et al. 2006; Witter and Self 2007). Of these, the Yenkahe Caldera, on the island of Tanna, displays the strongest evidence for violent formation during a paroxysmal eruption, with voluminous ignimbrite deposits preserved around its margin (Nairn et al. 1988; Robin et al. 1994; Allen 2005). Deposits of two ignimbrites have been identified on Tanna: the Siwi Ignimbrite, which

is known to have originated from the Yenkahe Caldera, and the Old Tanna Ignimbrite, which is proposed to have been erupted from a vent off the east coast of Tanna (Robin et al. 1994). Here the stratigraphy of these deposits is re-examined and revised following observations from additional locations. Radiometric ages for formation of the Yenkahe Caldera are also provided for the first time. This is combined with mineralogical, petrological and geochemical examination of pre-, syn- and post-ignimbrite volcanic rocks to understand the processes leading to cataclysmic, caldera-forming eruptions and their context within the wider history of the volcano. This is crucial for a full hazard assessment of the volcanic system.

Geological Setting

Tanna is a large, volcanic island at the southern end of the Vanuatu island arc, in the south-west Pacific Ocean (Fig. 3.1). The island has been volcanically active for the last 2.5 Myr, with three main phases of volcanism: the oldest, Pliocene-Pleistocene Green Hills Formation in the north; the mid-late Pleistocene Tukasmera Volcanics in the south-west and the late Pleistocene-Holocene Yenkahe Group in the south-east. The latter includes deposits from both the Siwi Ignimbrite and subsequent activity at Yasur, which continues today (Carney and MacFarlane 1979).

The Siwi Ignimbrite is genetically linked with the Yenkahe Caldera in the island's south-east (Nairn et al. 1988). This caldera is ~24 km^2 in area and is surrounded by the Siwi Ring Fault (Allen 2005). The caldera is oval-shaped, elongated in an east-west orientation and opens to the sea in the east (Fig. 3.1). Marginal scarps are well defined in the north-east of the caldera, but infilling by post-caldera volcanics, uplift and erosion have masked the caldera margin in other areas. Allen (2005) described the Siwi Ignimbrite as a pumice-rich pyroclastic flow deposit with lenses of variably-welded, lithic-rich spatter agglomerate. Textural and lithofacies characteristics allow the eruption to be divided into a number of phases of varying explosivity, including initial base surges, catastrophic collapse of the chamber roof associated with lava fountaining and final collapse of a Plinian eruption column, producing the voluminous upper ignimbrite unit. This unit is underlain by a volcanic breccia and a plagioclase-phyric lava (Fig. 3.2) and overlain by post-ignimbrite tephra (Allen 2005). Deposits of an older ignimbrite unit, known as the Old Tanna Ignimbrite (OTI), were identified along the eastern coast of the island by Robin et al. (1994) (Fig. 3.1). They consist of ash flow deposits and bedded tuffs, overlain by scoria-flows deposits containing an range of juvenile and accidental clasts. This ignimbrite

was ascribed to a caldera-forming eruption located off the north-east coast of the island, at a, now-obliterated, feature known as the Eastern Tanna Volcano (Robin et al. 1994).

Post-caldera activity has included both volcanism (Nairn et al. 1988; Métrich et al. 2011; Firth et al. 2014) and uplift (Chen et al. 1995; Merle et al. 2013). Current volcanic activity is centred on Yasur (Fig. 3.1), a persistently active scoria cone that has maintained continual Strombolian eruptions for 600-800 years. These erupt geochemically homogenous, basaltic trachy-andesitic magma at a rate of ~410-480 m^3 d^{-1}. Earlier phases of activity involved intermittent higher magnitude eruptions, which emitted tephra and lava of geochemically similar compositions to the current activity (Firth et al. 2014). This regime of post-caldera volcanism has been accompanied by rapid uplift of the 5 x 3 km, fault-bound Yenkahe Dome (Fig. 3.1), at the centre of the caldera (Merle et al. 2013). A time-averaged uplift rate of 156 mm yr^{-1} for this dome places it amongst the most rapidly deforming calderas worldwide (Chen et al. 1995) and is over two orders of magnitude greater than the rate of regional uplift calculated for the remainder of the island (Neef et al. 2003). Such uplift has been attributed to replenishment of an underlying magma reservoir (Chen et al. 1995; Métrich et al. 2011; Merle et al. 2013), with Métrich et al. (2011) estimating as much as 25 km^3 of magma may have been intruded beneath Yasur over the last 1 kyr, based upon current gas fluxes.

STRATIGRAPHY

A late Pleistocene to Holocene record of volcanic activity at the Yenkahe Caldera is exhibited in coastal exposures adjacent to the caldera along the eastern and south-eastern coasts of Tanna (Fig. 3.1).

Re-examination of this stratigraphy has benefited from greater access to field sites, particularly in distal areas (including those unavailable to Allen (2005) due to local owner objections), combined with coastal erosion better exposing some proximal sites. This has allowed the distal sites of Robin et al. (1994) that record the OTI to be correlated with more proximal sites dominated by the Siwi Ignimbrite (Robin et al. 1994; Allen 2005).

Pre-caldera deposits

Deposits of pre-caldera volcanics are preserved within a few exposed palaeo-ridges that are surrounded by valley-filling ignimbrites along the coastal cliffs of eastern Tanna, >3 km from the caldera margin. They include lavas, tephras and intercalated palaeosols, as well as shallow

intrusive features, such as dykes. In some cases intense faulting is observed. The majority of these deposits are discontinuous and display a range of sedimentary facies that hinders simple correlation, however, they contain significant information about the early volcanic system.

A large outcrop of pre-caldera volcanics is exposed to the west of Waesisi (Fig. 3.1), forming a prominent headland. Here the deposits consist of stacked, veneer-like lava flows and thick successions of tephra fall. This deposit is extensively faulted and is cut by at least one dyke. It is abutted to the north and south by deposits of the Old Tanna Ignimbrite, which form an angular unconformity.

In proximal areas, the pre-caldera volcanics are commonly represented by a vesicular, plagioclase-phyric lava flow, which underlies many of the ignimbrite deposits. This is the uppermost unit of the pre-caldera deposits and outcrops in coastal exposures near Sulphur Bay and Friendly Bungalows (Unit 1, Figs. 3.2 and 3.3). A similar flow is also found at the base of coastal exposures near Port Resolution (Fig. 3.4).

Old Tanna Ignimbrite

The OTI was previously described from three sites on the east coast of Tanna (Sites 16*, 22* and 23*, Fig. 3.1) by Robin et al. (1994). It was re-examined between Waesisi and Lowaisia (Site 1), where its stratigraphy appeared most complete (Fig. 3.5). Here three distinct sub-units can be discerned: basal lapilli fall and surge beds, a dark, lithic-rich, pumiceous pyroclastic flow unit and an overlying pumiceous pyroclastic flow unit with locally-present breccia enclaves. The middle, lithic-rich, unit was also recognised at proximal sites including White Sands and Sulphur Bay, where it had previously been identified as a volcanic breccia (Allen 2005).

The basal tephra fall and surge beds reach a thickness of >2 m at Lowaisia (Fig. 3.5). Beds are sub-horizontal and mantle the underlying topography. At least ten individual beds can be discerned, based upon variations in grain size, with alternating ash and pumice lapilli beds. Beds at the top of the sequence are commonly coarser-grained than those at the base, dominated by lapilli rather than ash. The upper margin of this sub-unit is sharp, but non-erosive, defined by a change in grainsize from coarse lapilli to cobble- and boulder-sized blocks. The uppermost lapilli beds are also commonly reddish-brown in colour, compared with grey and yellow colours below.

A clast-supported, lithic-rich, pumiceous, pyroclastic flow deposit overlies the basal units at Lowaisia. This is also found at proximal sites, such as Sulphur Bay and White Sands. It is

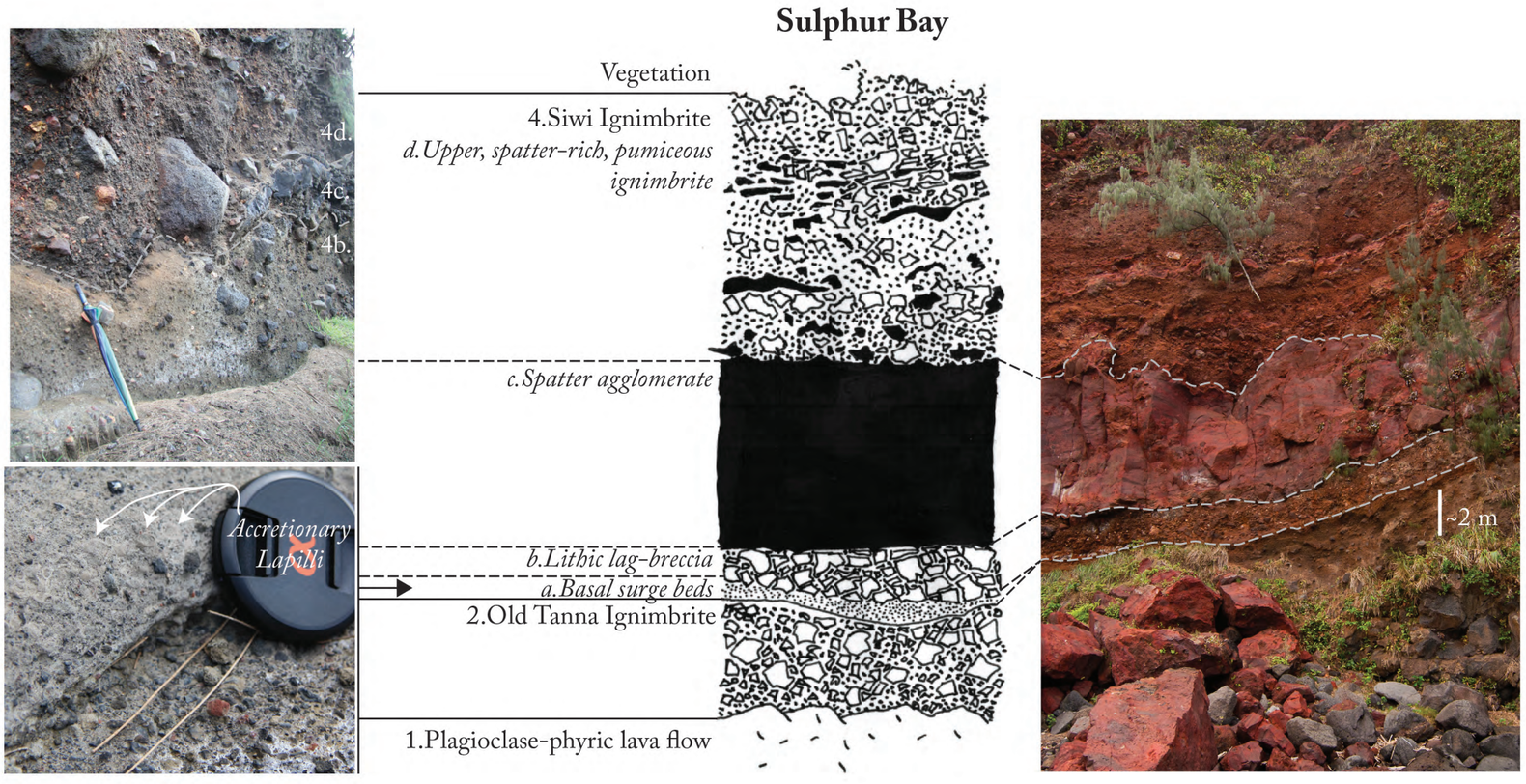

Fig. 3.2 Stratigraphy of the OTI and Siwi Ignimbrite at Sulphur Bay. This corresponds with Site 4 on Fig. 3.1. Note the difference in appearance of this unit between proximal deposits (right photo) and medial deposits (upper left photo). A close-up image of the basal surge beds showing accretionary lapilli is shown in the lower left.

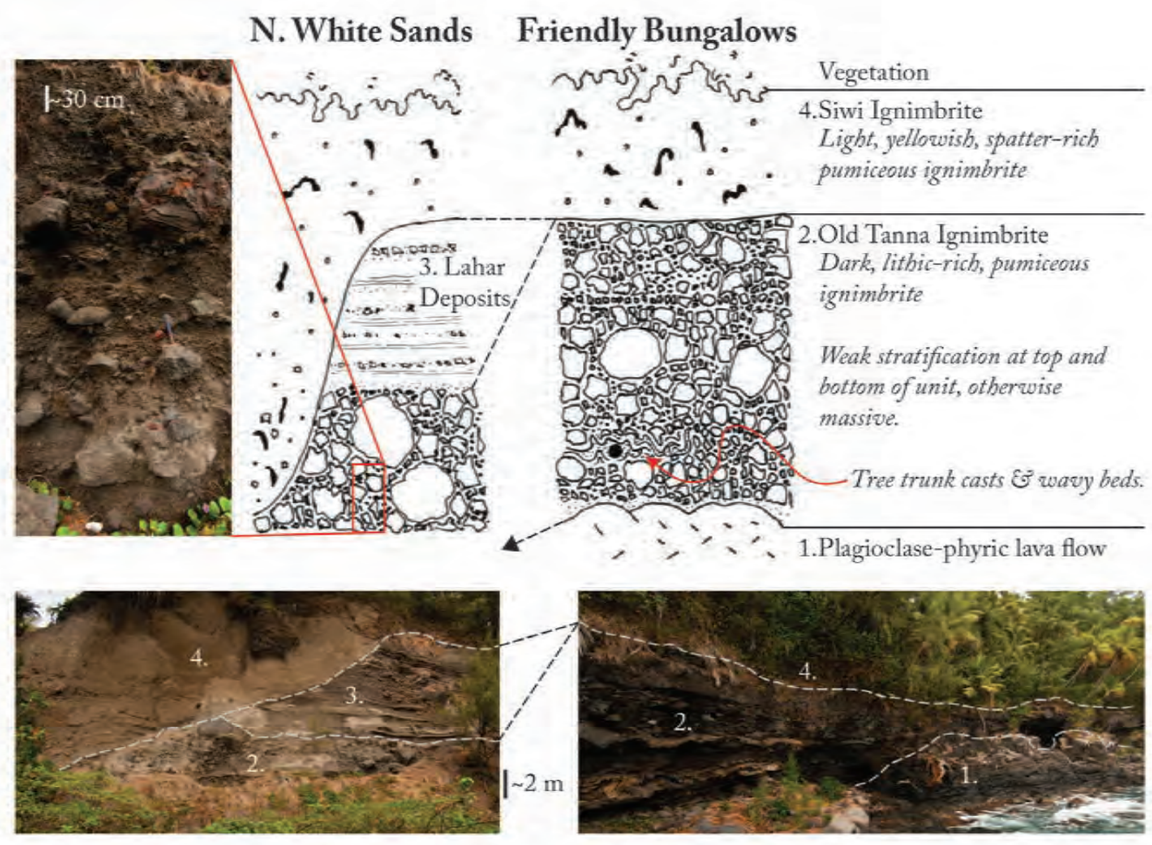

Fig. 3.3 Stratigraphy of the OTI and Siwi Ignimbrite at White Sands (Site 3; Fig. 3.1) and Friendly Bungalows (Site 2; Fig. 3.1). Note the erosional unconformity between the two ignimbrites in the lower left photo. Units are numbered the same as in Fig. 3.2.

rich in lithic fragments, which generally range in size from fine to coarse blocks, many reaching diameters in excess of 5 m. Little lateral variation in grain size is apparent in proximal deposits between Sulphur Bay and Friendly Bungalows. Lithic clasts are heterolithologic and are sub-rounded to sub-angular, with many being cracked and fragmented. The matrix of this deposit is primarily composed of juvenile pumice and small glassy bombs. In more distal sections, around Lowaisia, this unit has a significantly higher concentration of glassy, juvenile material. Here zones of partial welding are present, however the majority of the ignimbrite is unwelded.

This unit is commonly present as a massive, 10 m-thick deposit, with only weak planar bedding discerned at certain location, such as Sulphur Bay. Here, while large blocks (>256 mm diameter) are still common, the grainsize is generally smaller, and horizontal beds of coarse lapilli and fine blocks (<128 mm) are evident. Between White Sands and Friendly Bungalows the unit maintains a roughly constant thickness (Fig. 3.3). However, between Waesisi and Lowaisia its thickness varies considerably in relation to the underlying topography, occasionally pinching out completely over palaeo-ridges. In such cases, deposits reach their maximum thickness on the north-western side of palaeo-valleys (Fig. 3.5).

Between Waesisi and Lowaisia this unit is overlain by a second, pumiceous pyroclastic flow unit. This unit varies in thickness, reaching depths of up to 10 m where it fills palaeo-valleys. Significant lateral variations in grainsize are apparent. The majority of the unit is a massive, pumiceous, fine block-and-lapilli deposit, however enclaves of coarse boulder-breccia are also present. The latter correlate with the thickest deposits of the underlying unit, on the north-western side of palaeo-valleys. This unit is absent from deposits around Sulphur Bay and White Sands. The top of the underlying unit shows strong evidence for re-working at White Sands (Fig. 3.3), where a series of finer-grained, poorly-sorted, horizontally-bedded lahar deposits can be observed. These potentially removed and re-worked some of the upper-most pyroclastic flow unit.

At Lowaisia the ignimbrite abuts an outcrop of pre-caldera volcanics to the south-east and overlies a well-developed palaeosol (Fig. 3.5). The lowermost units mantle the topography and contain abundant fragments of carbonised wood. To the south, near Friendly Bungalows, tree-trunk casts are present (Fig. 3.3), however, no remains of vegetation are preserved. At the same location, cross-bedded surge deposits are seen along with underlying sediment deformation features, representing interaction of the pyroclastic surge with a wet substrate. In these areas the ignimbrite commonly overlies a plagioclase-phyric lava.

The upper contact of the ignimbrite is sharp at all locations, and is commonly horizontal. In some places, such as White Sands, the ignimbrite has been heavily eroded, with the Siwi Ignimbrite present as valley-fill. Otherwise a strongly developed palaeosol directly overlies the OTI and in some cases, a stack of tephras and soils above.

Deposits between the ignimbrite-forming eruptions

North of the caldera margin, deposits of material representing the interval between the two ignimbrite eruptions are scarce. At proximal sites the upper margin of the OTI is erosional, suggesting younger, overlying material has been removed. Such material is present at more distal locations (e.g. Lowaisia), where it consists of a stack of tephras and soil horizons. Detailed examination was not possible, as these deposits were at the top of the cliff and could not be readily accessed.

South of the Yenhake Caldera, a succession of pre-Siwi Ignimbrite pyroclastic deposits occur in the area of Shark Bay (Fig. 3.4). These units directly underlie the Siwi Ignimbrite, however, their relationship with the OTI cannot be confirmed as it is not found in this area. The lowermost unit is a >6 m thick, highly oxidised spatter deposit (Fig. 3.4), consisting of spatter and lithic blocks. This unit is clast supported, with clasts from <5 cm to >1m. Many of the larger lithic clasts are sub-rounded. The unit is predominantly welded, with spatter-rich lenses displaying the highest degree of welding. In some zones, a eutaxitic texture is apparent. Much of this deposit is oxidised, evidenced by its red colour (Fig. 3.4). The spatter deposit is separated from the Siwi Ignimbrite by a 6-10 m thick succession of weathered pumiceous tephra units, each a few tens of cm-thick with intercalated palaeosol horizons.

Siwi Ignimbrite

The stratigraphy of the Siwi Ignimbrite has been described previously (e.g. Robin et al. 1994; Allen 2005). The earlier findings are summarised here, alongside a number of additional points. The Siwi Ignimbrite consists of four units: basal lapilli fall and surge beds; a lower, lithic-rich, pumiceous ignimbrite; a variably-welded spatter agglomerate; and an upper, spatter-rich, pumiceous ignimbrite. The total sequence can reach thicknesses in excess of 30 m in proximal deposits. In distal deposits, and deposits to the south of the caldera, only the upper, spatter-rich, pumiceous ignimbrite is present. Similarly, deposits to the south of the caldera are typically poorer in glassy spatter clasts than those to the north.

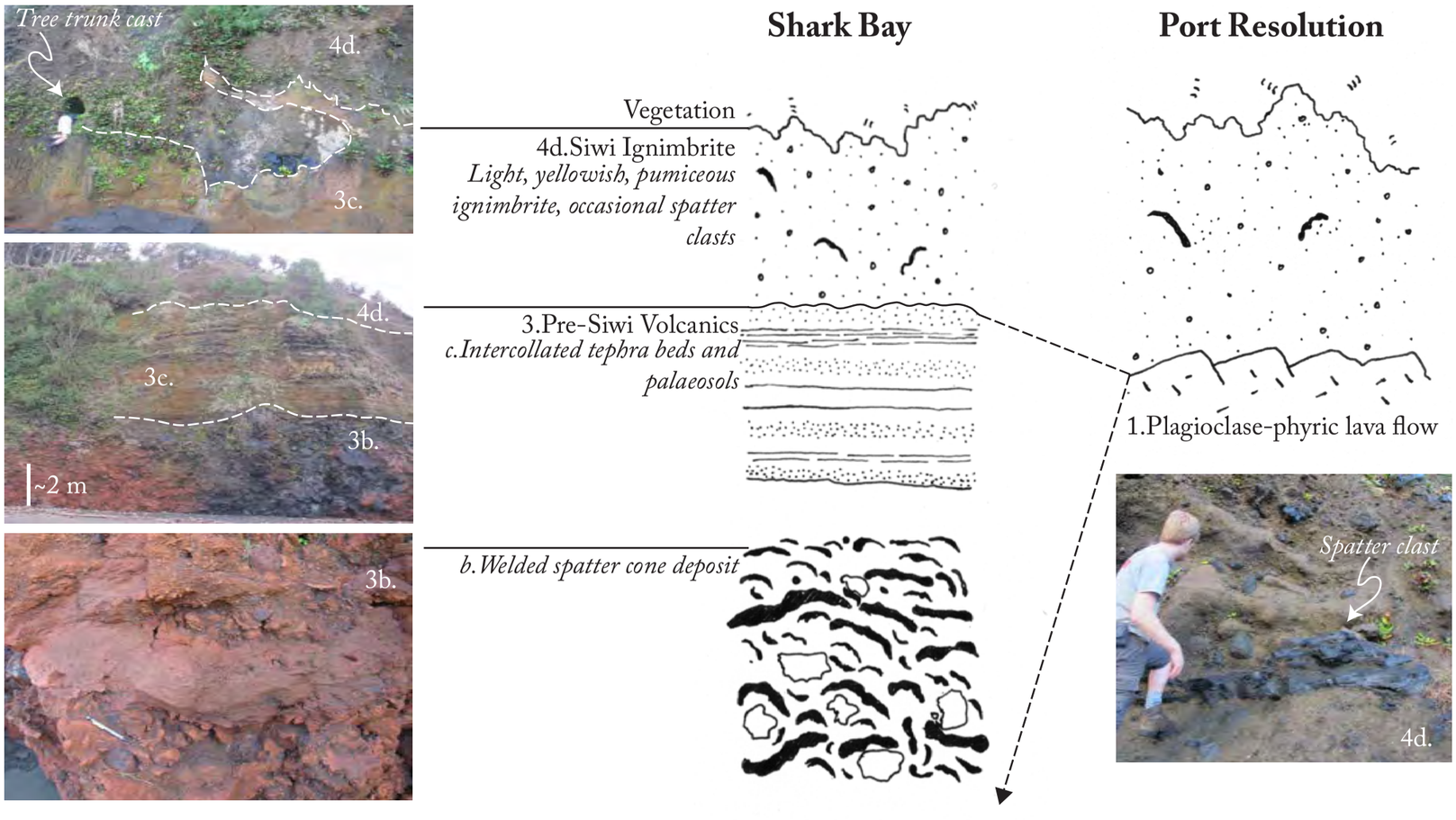

Fig. 3.4 Stratigraphy of the Siwi Ignimbrite and underlying volcanics at Port Resolution (Site 5; Fig. 3.1) and Shark Bay (Site 6; Fig. 3.1).

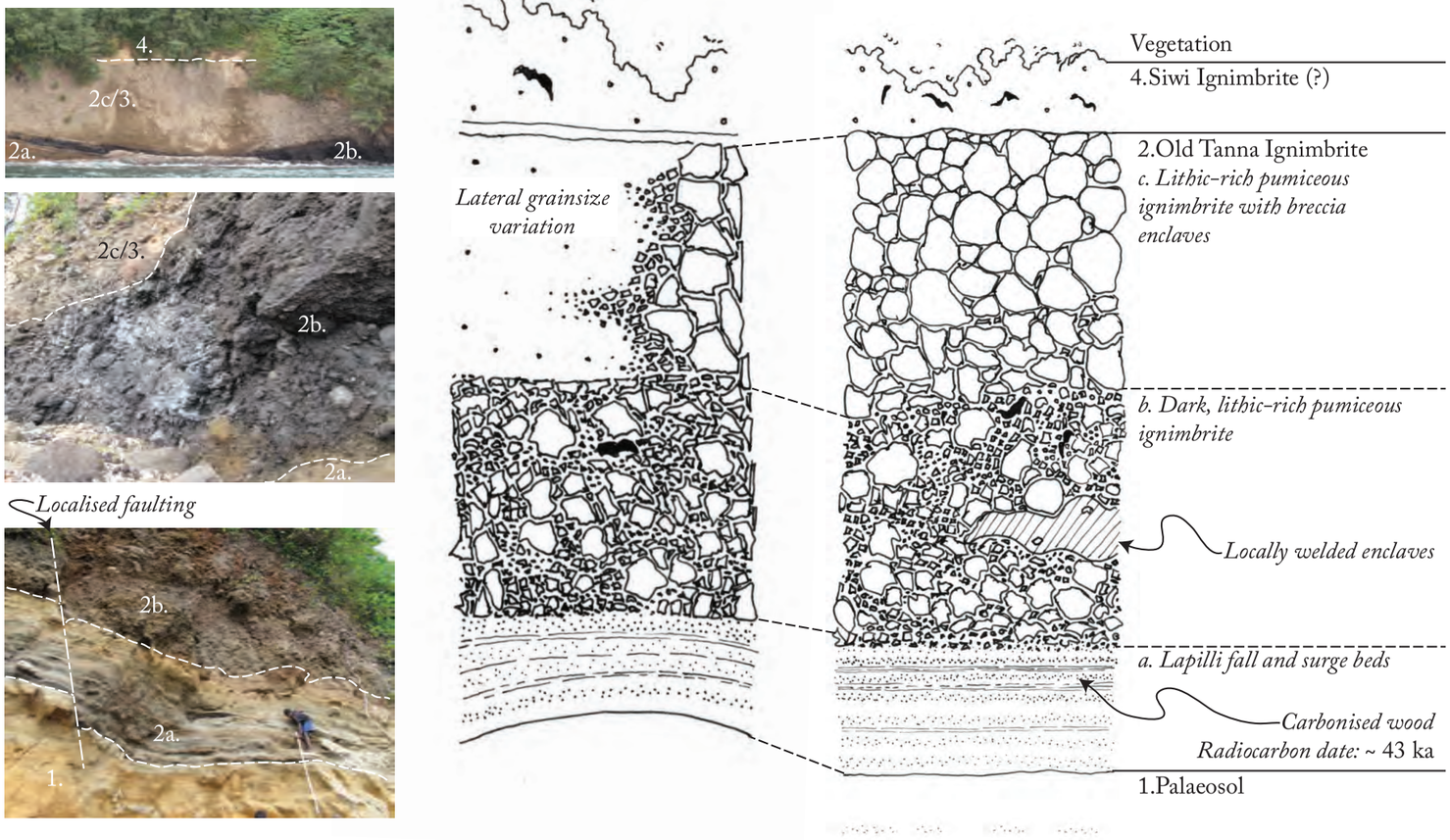

Fig. 3.5 Stratigraphy of the OTI at Lowasia (Site 1; Fig. 3.1).

The lowermost sub-unit of the Siwi Ignimbrite contains a series of thin lapilli fall and surge beds. These consist primarily of pumice lapilli and lithic clasts in an indurated, ash matrix. In a number of instances, accretionary lapilli are also evident (Fig. 3.2). Individual beds are usually only 1-2 cm thick and the entire succession totals less than 1 m in thickness in most outcrops. Cross-bedding is evident in a number of locations. The upper contact of these beds is often erosional. In the proximal deposits, near Sulphur Bay, they are overlain by a 1-2 m thick, coarse, lithic breccia. This grades laterally into an un-welded, pumiceous ignimbrite in more distal deposits.

In the Sulphur Bay/White Sands area, the most striking feature of the Siwi Ignimbrite is a 2-5 m thick, variably welded spatter agglomerate, which separates the upper and lower pumiceous ignimbrites (Fig. 3.2). This ranges in texture from a spatter-dominated layer to a fully welded, compacted, eutaxitic agglomerate. The degree of welding and stratigraphic position of intense welding varies throughout the exposures, thus welding cannot be used as a stratigraphic marker. In the Sulphur Bay area the spatter-agglomerate is a striking red colour, due to syn-depositional oxidation and cooling, or as a result of post-depositional hydrothermal alteration. The latter is likely given the presence of hot-springs at the base of the deposits. With distance from the caldera margin it becomes black. In places along the coast between Sulphur Bay and White Sands this unit pinches out and disappears, but then re-appears further along the coast in locations where the deposit is thicker.

The upper-most unit of the Siwi Ignimbrite is a >10 m-thick, spatter-rich, pumiceous ignimbrite. In proximal to medial deposits, spatter is present as decimetre- to metre-sized fluidal and vitric clasts. In places, these are welded to produce thin eutaxitic lenses within a pumiceous matrix. Decimetre- to metre-sized lithic blocks are also common within this unit. Spatter and lithic clasts become smaller and less common in distal deposits, which are typically distinguished by a mustard-coloured, pumiceous matrix with occasional black spatter clasts. Distal deposits are typically massive to poorly stratified, yet commonly 5 – 10 m-thick. Such deposits are a common sight in eroded gullies and road cuttings across much of south-east Tanna and have been identified as far away as Lenakel on the west coast (Fig. 3.1).

Like the OTI, tree-trunk casts are observed within the Siwi Ignimbrite. They are particularly obvious south of the caldera, near Shark Bay, where the ignimbrite shares a wavy and irregular contact with underlying soil resulting from up-rooting of trees as the pyroclastic flow moved past. To the north, at Waesisi, the Siwi Ignimbrite is deposited onto a thick palaeosol.

Post-Siwi Deposits

The stratigraphy of post-Siwi Ignimbrite activity is best displayed along the Siwi River, by the northern margin of the Yenkahe Caldera (Fig. 3.1). The most recent of these deposits are derived from the currently active cone, Yasur, and represent activity over the past ~2 kyr (Firth et al. 2014). These deposits are stratigraphically separated from the Siwi Ignimbrite by at least two thick lava flows and intercalated tuffs.

Both lavas are vesicular, plagioclase-phyric, pahoehoe flows, similar to the prehistoric plagioclase-phyric basaltic andesite that impounded Lake Siwi (Firth et al. 2014). The two flows are separated by a 1-2 m-thick succession of lapilli fall beds that potentially represent formation of a tuff ring. A second, better-exposed, tuff-ring succession overlies the upper lava flow, separating it from the more recent deposits of Yasur. Moving from west to east, beds of lapilli tuff initially dip steeply to the west, then the south, then to the east over a space of ~600 m, describing the sides of an eroded tuff cone. This deposit consists primarily of pumiceous lapilli, with lithic clasts also present. Bomb sags are seen in a number of beds.

In more distal locations, post-ignimbrite deposits consist primarily of tephra fall beds. Identification of the contact between these and the underlying Siwi Ignimbrite is obscured by vegetation and lack of exposure.

Age Estimates

Three charcoal samples were collected from the basal surge and fall beds of the OTI at Lowaisia. All samples were radiocarbon dated at the University of Waikato: one by beta counting, while the remainder were analysed by accelerator mass spectrometry due to their limited sample size. All samples returned roughly concordant ages (Table 3.1) that suggest emplacement of the OTI ~ 43-48 ka B.P.

No datable material has yet been identified within the younger Siwi Ignimbrite. While tree-trunk casts were identified, remains of the trees have disappeared. Some constraints on the age of this unit can be inferred from uranium-series systematics, with a lack of Ra-Th disequilibrium in juvenile material suggesting a minimum age of 8 ka (Firth et al. in review). Erosive contacts between the ignimbrite units suggest that the Siwi Ignimbrite is considerably younger than the OTI. More precise age constraints cannot be obtained from the stratigraphy.

SAMPLING AND ANALYTICAL METHODS

Fifty-two volcanic rock samples were collected from south-east Tanna for geochemical analysis. Of these, 27 represent pre-caldera volcanics rocks: 15 pre-caldera lava flows and 12 lithic blocks collected from the OTI and Siwi Ignimbrite. The latter offer a comparable suite of pre-caldera eruptives scoured from the volcanic edifice and shallow plumbing system during the OTI and Siwi eruptions. In addition, three samples of juvenile material were collected from the OTI and a further 20 juvenile clasts from the Siwi Ignimbrite. These clasts include pumice and glassy spatter, as well as two samples of welded, eutaxitic spatter agglomerate from the Siwi Ignimbrite.

Electron microprobe (EMP) analyses of mineral and glass chemistry were undertaken at the Geochemical Analysis Unit (GAU) at Macquarie University, Australia. Attention was focused upon the ignimbrite units, however, a number of pre-caldera samples were also analysed. Polished thin sections were analysed on a Cameca SX 100 EMP using a focused 1 µm diameter electron beam, with an energy of 15 kV and a beam current of 20 nA. A wider, defocused, 10 µm beam was used for glass analyses, to minimise Na loss. Accuracy and precision were estimated from replicate analyses of appropriate mineral standards: $CaSiO_3$ for Si, TiO_2 for Ti, kyanite for Al, VG-A99 for Fe, MgO for Mg, wollastonite for Ca, jadeite for Na and orthoclase for K.

Whole rock major element contents and trace element concentrations were determined for all samples. Samples were crushed and then milled in an agate mill before being fused into glass discs with a lithium borate Spectrachem 12-22 flux. Major elements were analysed on the glass disks by X-ray fluorescence, using a Siemens SRS3000 X-ray spectrometer at the University of Auckland, New Zealand. Trace elements were analysed on the same glass discs by laser ablation inductively coupled mass spectrometry (LA-ICP-MS). Analyses were carried out at the Australian National University using an Excimer LPX 120 laser and Agilent 7500 ICP-MS following the method of Eggins et al. (1998). Data reduction relied upon analyses of NIST 612 glass, which bracketed every 15 sample analyses, and Si, analysed by XRF, as internal and external standards respectively. Replicate analyses of USGS standards BCR-2 and AGV-2 suggest accuracy of < 1% for major elements (Except Fe_2O_3: ~3.5%) and < 5% for reported trace elements (Table 3.2).

Sr, Nd and Hf isotopes were analysed for a sub-set of 14 samples, focused primarily on juvenile clasts from the Siwi Ignimbrite. Powdered samples were dissolved in an HF-HNO_3 mix in heated Teflon beakers in the clean laboratory of the GAU. Sr and the REE were separated

Table 3.1. Radiocarbon dates for the Old Tanna Ignimbrite

Sample	Method	Age (yrs B.P.)	Error (years)
C1	AMS	>48,000	
C2	AMS	49,530	4495
C4	Beta Counting	43,257	858

by passing the solution through a cationic column, followed by removal of Sm and Nd on an HDEHP column. The methods described by Blichert-Toft et al. (1997) were employed to isolate Hf. Sr and Nd isotopes were analysed in static mode on a ThermoFinnigan Triton thermal ionisation mass spectrometer (TIMS) at the GAU, using single and double Re filaments respectively. Mass fractionation was corrected for by normalizing Sr to $^{86}Sr/^{88}Sr = 0.1194$ and Nd to $^{146}Nd/^{144}Nd = 0.7219$. Analyses of BHVO-2 returned values of 0.703451 and 0.512980 for $^{87}Sr/^{86}Sr$ and $^{143}Nd/^{144}Nd$ respectively. Hf isotopes were analysed in static mode on a Nu Instruments multi-collector, inductively coupled plasma mass spectrometer at the GAU using methods described by Griffin et al. (2000). Data was normalised to a $^{179}Hf/^{177}Hf$ ratio of 0.7325. Analysis of BHVO-2 returned a value of 0.2831189 ($\pm 7.41 \times 10^{-6}$), while JMC475 returned a value of 0.2821644 ($\pm 3.71 \times 10^{-6}$).

WHOLE ROCK, GLASS AND MINERAL GEOCHEMISTRY

Whole Rock Major and Trace Element Geochemistry

Samples from both ignimbrites, alongside pre- and post-caldera volcanic rocks produce strong linear arrays when major and trace elements are plotted against SiO_2 (Fig. 3.6). Both ignimbrite units are restricted in major and trace element composition, while pre-caldera volcanic rocks vary more widely. Juvenile material from the OTI classifies as basaltic trachy-andesite (52.9-53.3 wt.% SiO_2) and displays high MgO, Al_2O_3 and CaO and low K_2O when compared with rocks from the wider volcanic system (Table 3.2; Fig. 3.6). In contrast, juvenile material from the Siwi Ignimbrite represents the most evolved compositions analysed, with SiO_2 contents >58 wt.% and MgO contents <2.5 wt.% (Table 3.2; Fig. 3.6). These samples classify as trachy-andesites. Depletion of CaO, V and Sr, and enrichment of K_2O, Rb and La with increasing SiO_2 can be discerned within the suite of Siwi eruptives, despite the limited range in SiO_2 content (Fig. 3.6). Pre-caldera volcanic rocks complete the arrays seen in Fig. 3.6, ranging in composition from basaltic through basaltic trachy-andesite to trachy-andesitic

Table 3.2 Whole rock major and trace element and isotope compositions of volcanic rocks from the Yenkahe Caldera

	Pre-caldera volcanics							OTI
Sample	TUK-1	TUK-2	TUK-3	WAEC	WAEL	WAEW	TB1	WSG-14
Location	Tukasmera	Tukasmera	Tukasmera	Waesisi	Waesisi	Waesisi	P. Resolution	White Sands
Rock type	Lava	Lava	Lava	Lava	Lava	Lava	Lava	Juvenile
SiO_2	47.41	54.85	47.02	46.32	47.53	54.36	56.25	52.94
TiO_2	0.70	0.69	0.78	0.85	0.83	0.81	0.79	0.81
Al_2O_3	13.51	17.60	14.26	17.98	16.62	16.40	17.31	16.46
Fe_2O_3	13.01	8.85	11.85	14.53	13.71	10.50	8.86	10.52
MnO	0.21	0.15	0.19	0.22	0.22	0.19	0.17	0.19
MgO	9.45	2.97	10.19	6.42	6.26	3.54	2.77	4.07
CaO	13.31	7.86	13.51	10.85	11.10	7.75	7.01	8.36
Na_2O	1.56	3.41	1.54	1.98	2.33	3.69	3.87	3.67
K_2O	0.64	2.33	0.43	0.48	0.93	2.13	2.78	1.87
P_2O_5	0.11	0.35	0.09	0.15	0.16	0.35	0.44	0.29
Total	99.89	99.06	99.85	99.78	99.68	99.71	100.25	99.18
Sc	55.07	19.67	53.00	47.63	40.44	24.49	20.37	-
Ti	4430.94	4382.11	4903.14	5298.66	5198.72	5148.33	5870	-
V	392.40	216.58	367.71	435.53	396.41	310.67	235.24	-
Cr	328.21	39.27	377.46	66.56	55.03	10.97	21.85	-
Co	47.63	19.72	46.45	43.21	39.22	24.27	20	-
Ni	74.47	19.83	79.06	34.29	25.22	7.26	16	-
Zn	63.82	72.47	56.76	81.69	80.09	80.91	98.91	-
Ga	12.83	16.78	12.95	18.15	16.88	16.59	17.33	-
Rb	7.08	27.76	4.69	3.20	10.11	26.55	35.55	-
Sr	390.98	565.74	314.13	663.30	862.75	632.32	642.59	-
Y	10.12	21.92	10.07	21.23	16.07	19.30	23.12	-
Zr	19.71	83.54	17.35	36.92	40.36	72.21	98.48	-
Nb	0.26	1.10	0.25	0.45	0.51	1.01	1.41	-
Cs	0.09	0.89	0.09	0.10	0.27	0.82	1.13	-
Ba	149.12	505.63	94.51	178.12	193.01	437.25	568.47	-
La	3.07	11.19	2.08	7.25	7.57	10.07	13.81	-
Ce	7.15	23.29	5.19	13.51	16.34	22.41	30.33	-
Pr	1.06	3.51	0.81	2.56	2.46	3.06	4.28	-
Nd	5.74	16.70	4.38	13.41	12.74	15.32	19.60	-
Sm	1.58	4.35	1.43	3.78	3.36	3.70	4.75	-
Eu	0.57	1.17	0.57	1.23	1.04	1.15	1.38	-
Gd	1.78	3.99	1.71	4.01	3.36	3.54	4.68	-
Tb	0.30	0.62	0.31	0.58	0.51	0.54	0.67	-

Table 3.2 Whole rock major and trace element and isotope compositions of volcanic rocks from the Yenkahe Caldera

WSP-14	SB-14	BR1	BR4	BR5	BR6	BR8	BR7	BR3
White Sands	Sulphur Bay	White Sands	F. Bungalows	F. Bungalows	F. Bungalows	F. Bungalows	F. Bungalows	F. Bungalows
Juvenile	Juvenile	Lithic	Lithic	Lithic	Lithic	Lithic	Lithic	Lithic
53.09	53.36	54.03	56.66	57.64	53.02	56.56	57.68	56.06
0.81	0.82	0.87	0.89	0.89	0.75	0.92	0.97	0.90
16.59	16.6	16.55	16.05	16.15	14.35	15.86	15.36	15.90
10.45	10.5	10.72	9.53	8.95	10.09	9.73	9.27	10.18
0.19	0.19	0.20	0.17	0.18	0.18	0.19	0.18	0.20
3.99	3.98	3.58	3.12	2.37	7.77	2.91	2.70	3.05
8.26	8.14	8.10	6.46	5.70	8.63	6.25	5.61	6.56
3.64	3.61	3.61	3.83	3.94	2.99	3.79	3.87	4.08
1.86	1.91	1.89	2.94	3.43	2.02	3.15	3.54	2.39
0.30	0.31	0.33	0.46	0.56	0.32	0.51	0.57	0.41
99.18	99.42	99.88	100.13	99.81	100.11	99.88	99.74	99.71
-	-	26.06	22.47	18.77	30.61	20.85	20.57	23.04
-	-	6052	6302	6349	5255	6381	6791	6371
-	-	326.24	320.18	227.99	291.02	263.73	287.44	305.24
-	-	6.26	10.91	9.25	360.34	17.89	9.90	5.37
-	-	26	22	18	36	21	19	23
-	-	12	13	10	109	17	12	5
-	-	106.12	93.08	98.62	80.53	101.82	98.72	103.40
-	-	16.96	16.87	17.39	15.26	17.24	17.37	17.47
-	-	21.35	38.28	44.14	24.03	39.44	45.21	27.87
-	-	599.36	548.09	505.30	507.47	521.32	451.90	611.94
-	-	20.02	22.81	27.17	17.95	24.98	26.55	22.73
-	-	63.81	97.51	119.03	67.76	107.77	119.21	77.95
-	-	0.95	1.44	1.80	0.95	1.60	1.76	1.16
-	-	0.63	0.95	1.39	0.73	1.18	1.45	0.82
-	-	425.45	573.69	653.64	405.22	593.49	648.87	518.03
-	-	9.38	13.80	16.60	9.49	15.30	16.54	11.52
-	-	21.69	30.74	37.42	21.47	34.07	36.87	25.90
-	-	3.11	4.21	5.15	3.02	4.75	5.06	3.72
-	-	14.54	19.62	23.24	13.92	21.68	22.98	17.34
-	-	3.72	4.67	5.40	3.55	5.15	5.58	4.41
-	-	1.22	1.38	1.48	1.08	1.39	1.47	1.32
-	-	3.90	4.50	5.40	3.64	4.95	5.27	4.58
-	-	0.55	0.66	0.79	0.51	0.76	0.77	0.63

Table 3.2 (cont) Whole rock major and trace element and isotope compositions of volcanic rocks from the Yenkahe Caldera

	Pre-caldera volcanics							OTI
Sample	TUK-1	TUK-2	TUK-3	WAEC	WAEL	WAEW	TB1	WSG-14
Dy	1.85	3.99	1.99	3.70	3.13	3.48	4.39	-
Ho	0.38	0.83	0.42	0.74	0.62	0.74	0.92	-
Er	1.17	2.31	1.20	2.20	1.75	2.15	2.75	-
Tm	0.18	0.34	0.16	0.29	0.25	0.34	0.41	-
Yb	1.09	2.39	1.08	2.00	1.68	2.19	2.68	-
Lu	0.16	0.34	0.17	0.29	0.24	0.32	0.40	-
Hf	0.57	2.42	0.58	1.23	1.29	2.00	2.98	-
Ta	0.01	0.06	0.01	0.03	0.03	0.06	0.08	-
Pb	2.80	10.85	1.76	3.30	4.33	8.50	14.81	-
Th	0.39	1.68	0.24	0.58	0.72	1.47	2.29	-
U	0.22	0.91	0.13	0.13	0.32	0.80	1.19	-
$^{87}Sr/^{86}Sr$	-	-	-	-	-	-	0.703586	-
$^{143}Nd/^{144}Nd$	-	-	-	-	-	-	0.513017	-
$^{176}Hf/^{177}Hf$	-	-	-	-	-	-	0.283161	-

compositions (Table 3.2, Fig. 3.6). At their more-primitive end, the pre-caldera volcanic rocks are compositionally similar to prehistoric Tanna basalts analysed by Dupuy et al. (1982) and Peate et al. (1997) (Fig. 3.6). The pre-caldera basalts display a greater diversity in elemental abundances at a given SiO_2 content than their more evolved counterparts. This is most noticeable for elements such as aluminium (Fig 3.8c), which displays up to 5 wt.% variation at a constant silica content. Similarly, variations amongst these samples of up to 600 ppm can be discerned for Sr (Fig. 3.6g). More evolved pre-caldera volcanic rocks, with >53 wt.% SiO_2, form strong linear arrays on major and trace element variation diagrams (Fig. 3.6). Lithic clasts found within both ignimbrite units predominantly fall within this group of rocks. These clasts are of similar or more evolved compositions than juvenile components of the OTI and are less evolved than juvenile material from the Siwi Ignimbrite. Such compositions are broadly similar to current post-caldera volcanism (e.g. Métrich et al. 2011; Firth et al. 2014).

Whole Rock Isotope Geochemistry

Spatter and pumice clasts from the Siwi Ignimbrite share consistent Sr, Nd and Hf isotopic ratios (Table 3.2). $^{87}Sr/^{86}Sr$ ranges from 0.703520 to 0.703595, while $^{143}Nd/^{144}Nd$ varies between 0.513017 and 0.513953 (Fig. 3.7a). $^{176}Hf/^{177}Hf$ ranges from 0.283141 to 0.283184 (Fig. 3.7c and

Table 3.2 (cont) Whole rock major and trace element and isotope compositions of volcanic rocks from the Yenkahe Caldera

WSP-14	SB-14	BR1	BR4	BR5	BR6	BR8	BR7	BR3
-	-	3.77	4.25	5.02	3.40	4.71	4.92	4.22
-	-	0.77	0.85	1.06	0.71	0.98	1.02	0.88
-	-	2.29	2.72	3.17	2.05	2.91	3.08	2.76
-	-	0.34	0.39	0.46	0.31	0.45	0.45	0.39
-	-	2.21	2.49	3.07	2.01	2.87	3.03	2.56
-	-	0.33	0.38	0.47	0.30	0.43	0.46	0.38
-	-	1.90	2.89	3.53	2.01	3.17	3.45	2.43
-	-	0.06	0.10	0.11	0.06	0.09	0.10	0.07
-	-	12.17	14.59	16.05	9.64	14.49	16.41	12.28
-	-	1.37	2.23	2.74	1.44	2.44	2.70	1.75
-	-	0.75	1.23	1.50	0.80	1.38	1.53	0.94
-	-	-	-	-	-	-	-	-
-	-	-	-	-	-	-	-	-
-	-	-	-	-	-	-	-	-

d), with a single outlier having a ratio of 0.283247. This sample also has the most radiogenic Nd isotope composition (Fig. 3.7c). When plotted against SiO_2, $^{87}Sr/^{86}Sr$ and $^{143}Nd/^{144}Nd$ cluster, with limited variation in SiO_2 (Fig. 3.7e and f). $^{143}Nd/^{144}Nd$ is more scattered, producing a weakly-linear, vertical array. The basal lava (Sample TB1) that directly underlies the OTI has comparable $^{87}Sr/^{86}Sr$ (0.703586), $^{143}Nd/^{144}Nd$ (0.513017) and $^{176}Hf/^{177}Hf$ (0.283161) isotope ratios to the juvenile material from the Siwi Ignimbrite (Fig. 3.7). Siwi Ignimbrite and pre-caldera volcanic rocks display comparable Sr and Hf isotopes, and slightly higher Nd isotopes, to those previously analysed for the Vanuatu Arc (Peate et al. 1997; Pearce et al. 2007). The Nd isotopes are comparable with recently erupted volcanic bombs from Yasur, however (Handley et al. in prep).

Enclave Petrology and Glass Geochemistry

Juvenile clasts from the OTI preserve sub-rounded to sub-angular enclaves and veins of brown glass and phenocrysts, in contrast with the black glass of the host pumice (Fig. 3.8a). Veins and enclaves can also be discerned by their lower vesicle abundance. The enclaves reach diameters up to 10 mm, while veins are commonly 2-3 mm wide, but extend for lengths of >10 cm. Glass within these enclaves is trachy-andesitic in composition (~58-59 wt.% SiO_2;

Table 3.2 (cont) Whole rock major and trace element and isotope compositions of volcanic rocks from the Yenkahe Caldera

	Siwi Ignimbrite							
Sample	WS6	WS7	WS5	FB3	TB5	PR1	WS2	WS3
Location	White Sands	White Sands	White Sands	F. Bungalows	P. Resolution	P. Resolution	White Sands	White Sands
Rock type	Spatter agglomerate		Juvenile	Juvenile	Juvenile	Juvenile	Juvenile	Juvenile
SiO_2	59.72	59.22	59.65	59.55	59.15	59.97	59.78	58.34
TiO_2	0.91	0.92	0.91	0.93	0.90	0.90	0.91	0.85
Al_2O_3	15.35	15.23	15.35	15.37	15.44	15.32	15.43	16.04
Fe_2O_3	8.58	8.61	8.63	8.77	8.81	8.45	8.56	8.50
MnO	0.19	0.19	0.19	0.19	0.19	0.19	0.19	0.17
MgO	2.03	2.06	2.09	2.07	2.26	1.96	2.03	2.46
CaO	4.50	4.54	4.55	4.62	4.91	4.37	4.52	5.56
Na_2O	4.22	4.33	4.24	4.18	4.20	4.27	4.22	4.06
K_2O	3.94	3.90	3.92	3.81	3.71	4.00	3.93	3.52
P_2O_5	0.64	0.64	0.65	0.65	0.61	0.65	0.64	0.56
Total	100.09	99.64	100.17	100.15	100.18	100.08	100.20	100.07
Sc	16.66	16.95	16.91	17.32	18.47	17.04	17.15	17.94
Ti	6327	6394	6465	6558	6563	6520	6462	5994
V	178.88	181.82	183.66	191.99	197.94	171.31	179.16	197.56
Cr	7.16	5.93	9.54	8.61	7.10	7.96	8.48	23.21
Co	15	15	15	16	17	15	15	17
Ni	6	6	8	7	8	7	9	13
Zn	115.49	113.90	111.58	110.23	108.13	106.58	108.71	100.17
Ga	17.07	16.75	16.84	17.13	16.81	17.46	16.85	16.94
Rb	52.19	50.52	52.97	50.17	49.19	54.51	53.08	47.03
Sr	427.77	433.02	433.35	440.93	469.88	431.92	438.31	490.71
Y	28.97	29.35	29.40	29.70	29.29	30.46	29.94	25.78
Zr	130.24	131.56	131.58	131.35	129.51	137.91	133.06	114.42
Nb	1.95	1.95	1.98	2.02	1.94	2.07	2.00	1.74
Cs	1.63	1.50	1.63	1.52	1.55	1.71	1.66	1.48
Ba	705.00	712.15	705.28	700.40	687.08	725.91	705.50	647.26
La	18.39	18.19	18.24	18.38	18.60	19.09	18.45	16.07
Ce	41.38	41.24	43.34	41.49	39.90	42.66	41.54	36.74
Pr	5.64	5.65	5.62	5.74	5.45	5.90	5.74	5.04
Nd	25.25	25.37	25.68	25.98	25.14	26.73	26.14	22.48
Sm	6.01	6.01	5.98	6.17	6.04	6.24	6.07	5.35
Eu	1.58	1.57	1.59	1.60	1.61	1.64	1.60	1.47
Gd	5.69	5.66	5.68	6.04	5.97	6.29	5.93	5.10
Tb	0.85	0.86	0.84	0.85	0.85	0.88	0.82	0.75

Table 3.2 (cont) Whole rock major and trace element and isotope compositions of volcanic rocks from the Yenkahe Caldera

TB7	WAE3	WS-6	WSG-1	WSG2	WSG-15	WSG-28	WSP-2	WSP-3
P. Resolution	Waesisi	Waesisi	White Sands	White Sands	White Sands	White Sands	White Sands	White Sands
Juvenile	Juvenile	Juvenile	Juvenile	Juvenile	Juvenile	Juvenile	Juvenile	Juvenile
59.82	59.52	59.39	59.45	59.03	59.35	58.96	59.00	59.34
0.90	0.91	0.90	0.91	0.91	0.92	0.91	0.93	0.91
15.35	15.36	15.17	15.19	15.27	15.20	15.21	15.24	15.16
8.55	8.66	8.93	8.94	9.13	9.04	9.14	9.22	9.02
0.19	0.19	0.19	0.19	0.19	0.19	0.19	0.19	0.19
2.04	2.04	1.96	1.93	2.08	1.98	2.05	2.03	1.96
4.52	4.57	4.53	4.53	4.73	4.56	4.72	4.62	4.52
4.24	4.21	4.17	4.20	4.09	4.20	4.13	4.17	4.19
3.93	3.90	3.95	3.96	3.81	3.94	3.84	3.87	4.00
0.64	0.64	0.64	0.64	0.63	0.64	0.64	0.63	0.64
100.17	99.99	99.84	99.93	99.89	100.02	99.79	99.90	99.92
17.26	17.27	16.58	16.40	16.92	17.01	17.41	17.61	16.98
6521	6487	5600.57	5554.64	5667.62	5779.17	5890.16	5947.08	5783.60
177.18	184.26	173.30	172.43	190.84	186.12	198.36	203.84	191.71
7.94	6.48	6.38	6.53	7.24	6.52	7.69	6.46	10.81
15	15	14.51	14.17	15.26	14.99	15.32	15.77	15.04
6	6	2.66	3.46	1.93	1.92	4.32	3.60	2.90
107.88	109.61	93.26	92.56	96.10	98.60	97.16	101.99	99.15
17.15	16.82	15.19	15.79	15.87	16.27	16.29	16.95	16.40
53.02	51.89	51.41	52.47	52.28	52.80	53.67	54.79	56.80
432.71	448.75	426.60	424.44	443.60	435.48	454.75	458.15	443.13
30.14	30.38	29.83	29.37	29.30	30.05	30.56	30.91	30.85
135.62	135.15	136.89	135.81	134.03	137.85	137.00	140.38	143.01
2.01	1.99	2.04	1.98	1.92	1.98	1.99	1.99	2.08
1.64	1.64	1.57	1.70	1.60	1.76	1.71	1.70	1.75
714.18	708.90	685.09	681.31	677.75	703.41	703.72	711.14	725.21
18.64	18.61	17.69	17.63	17.49	18.03	18.35	18.29	18.46
41.69	41.47	39.13	39.31	38.98	40.52	40.11	40.93	41.86
5.70	5.74	5.45	5.34	5.32	5.55	5.60	5.61	5.56
25.97	26.13	24.81	25.65	25.55	26.21	26.48	26.35	26.69
6.25	6.10	6.37	5.90	5.96	6.10	6.26	6.15	6.26
1.68	1.66	1.51	1.50	1.52	1.56	1.52	1.60	1.51
6.04	5.89	5.54	5.50	5.40	5.84	5.66	5.56	5.85
0.87	0.85	0.82	0.83	0.82	0.83	0.85	0.85	0.89

Table 3.2 (cont) Whole rock major and trace element and isotope compositions of volcanic rocks from the Yenkahe Caldera

	Siwi Ignimbrite							
Sample	WS6	WS7	WS5	FB3	TB5	PR1	WS2	WS3
Dy	5.37	5.37	5.36	5.50	5.43	5.67	5.43	4.67
Ho	1.12	1.08	1.12	1.08	1.14	1.15	1.15	0.99
Er	3.34	3.36	3.40	3.43	3.35	3.54	3.43	2.96
Tm	0.48	0.51	0.50	0.51	0.50	0.52	0.50	0.43
Yb	3.31	3.33	3.30	3.39	3.32	3.39	3.42	3.01
Lu	0.49	0.50	0.50	0.50	0.49	0.52	0.50	0.44
Hf	3.72	3.78	3.77	3.73	3.79	3.94	3.83	3.28
Ta	0.13	0.12	0.12	0.12	0.13	0.13	0.12	0.11
Pb	17.99	16.16	17.84	17.63	17.56	18.09	17.66	15.84
Th	3.00	3.00	3.03	3.03	2.99	3.17	3.09	2.70
U	1.66	1.69	1.70	1.69	1.61	1.77	1.70	1.47
$^{87}Sr/^{86}Sr$	0.703574	0.703570	0.703946	0.703548	0.703520	0.703555	0.703595	0.703574
$^{143}Nd/^{144}Nd$	0.513049	0.513027	0.513029	0.513053	0.513041	0.513041	0.513041	0.513036
$^{176}Hf/^{177}Hf$	0.283153	0.283149	0.283171	0.283247	0.283154	0.283176	0.283184	0.283171

Table 3.3). The compositions of the surrounding, host glass could not be ascertained as bubble-walls were not sufficiently thick for EMP analysis, or else were contaminated by microlites. Nevertheless, enclave glass compositions are significantly more evolved than the whole rock composition.

Mineral Geochemistry

Plagioclase is ubiquitous in all volcanic rocks analysed in this study. In pre-caldera lavas plagioclase is commonly present as euhedral phenocrysts which reach lengths of up to 4 mm. In the case of the basal lava, these crystals share a relatively uniform composition with little variation between core and rim (An_{52-57} n=5; Table 3.4). Mineral chemistry varies widely between the samples, however. One sample contains plagioclase phenocrysts with rim compositions ranging from An_{53-61}, while in another sample, plagioclase rim compositions predominantly fall between An_{76-82}. Microlitic plagioclase is also present in all pre-caldera lavas, with microlites predominantly present as laths, varying in size from <20 to >100 μm.

Both ignimbrites display a greater diversity in plagioclase composition, accompanied by an abundance of plagioclase grains displaying disequilibrium features, such as sieve-textures and resorbed edges. Three populations of plagioclase are found within the OTI, classified

Table 3.2 (cont) Whole rock major and trace element and isotope compositions of volcanic rocks from the Yenkahe Caldera

TB7	WAE3	WS-6	WSG-1	WSG2	WSG-15	WSG-28	WSP-2	WSP-3
5.63	5.71	5.20	5.46	5.29	5.53	5.53	5.44	5.66
1.15	1.15	1.08	1.14	1.11	1.13	1.14	1.15	1.17
3.53	3.44	3.25	3.32	3.26	3.18	3.44	3.30	3.34
0.51	0.51	0.49	0.51	0.48	0.49	0.48	0.50	0.50
3.37	3.41	3.37	3.27	3.34	3.36	3.46	3.52	3.33
0.52	0.51	0.49	0.51	0.49	0.50	0.50	0.51	0.49
3.92	3.96	3.82	3.69	3.61	3.84	3.91	3.83	3.80
0.13	0.12	0.11	0.11	0.12	0.11	0.12	0.11	0.12
18.00	17.81	15.19	15.79	15.43	16.43	16.26	16.23	17.17
3.13	3.14	2.99	2.96	2.98	3.08	2.95	3.11	3.11
1.73	1.67	1.60	1.63	1.59	1.64	1.62	1.68	1.67
0.703560	0.703540	-	-	-	-	-	-	-
0.513034	0.513037	-	-	-	-	-	-	-
0.283175	0.283169	-	-	-	-	-	-	-

by mineral chemistry and texture. The most calcic compositions (An_{86-87}; Table 3.4) belong to skeletal phenocrysts (Fig. 3.8b), which have been heavily resorbed (Fig. 3.9a). Euhedral phenocrysts with An_{66-72} display sieve textures, in which small patches of glass fill holes within the crystal. Lastly, small (<200 μm) euhedral to subhedral crystals and microlites form a third population, with compositions of An_{53-68} (Table 3.4; Fig 3.9a). Similarly, two populations can be identified amongst plagioclase crystals in juvenile material from the Siwi Ignimbrite. Larger phenocrysts (0.5-1 mm), which have $An_{>50}$, typically display sieve textures (Fig. 3.8d) and resorbed edges, while smaller phenocrysts ($An_{<50}$) are commonly more euhedral. Skeletal grains, such as those identified within the OTI, were not seen in the Siwi Ignimbrite, while microlites are significantly less abundant (<1%). Optical zonation and compositional variation between cores and rims of plagioclase crystals could not be discerned in either ignimbrite. Within the Siwi Ignimbrite, phenocrysts are commonly larger than in the OTI and are often accumulated in clusters or glomerocrysts (Fig. 3.8c). The latter record two episodes of crystal growth, with euhedral grains partly surrounded by second stage plagioclase crystals.

Additional plagioclase phenocrysts are found within trachy-andesitic enclaves in samples from the OTI. These are rarely euhedral, with many grains fragmented, and some displaying resorbed edges. They have less calcic compositions than plagioclase in the reminder of the

Table 3.2 (cont) Whole rock major and trace element and isotope compositions of volcanic rocks from the Yenkahe Caldera

	Siwi Ignimbrite							
Sample	WSP-4	WSP-15	WSP-26	TB3	PR3	TB4	PR2	FB2
Location	White Sands	White Sands	White Sands	P. Resolution	P. Resolution	P. Resolution	P. Resolution	F. Bungalows
Rock type	Juvenile	Juvenile	Juvenile	Lithic	Lithic	Lithic	Lithic	Lithic
SiO_2	58.71	59.00	58.94	56.42	55.40	57.06	57.98	56.40
TiO_2	0.96	0.92	0.92	0.86	0.87	0.93	0.90	0.87
Al_2O_3	15.17	15.25	15.20	16.26	16.13	15.64	15.87	16.09
Fe_2O_3	9.43	9.20	9.14	9.72	10.23	9.47	9.01	9.69
MnO	0.19	0.19	0.19	0.18	0.19	0.18	0.18	0.18
MgO	2.10	2.05	2.06	3.16	3.36	2.57	2.34	3.14
CaO	4.77	4.65	4.71	6.69	7.04	5.73	5.51	6.54
Na_2O	4.12	4.08	4.12	3.86	3.87	3.78	3.91	3.89
K_2O	3.81	3.83	3.88	2.74	2.24	3.39	3.52	2.79
P_2O_5	0.64	0.64	0.64	0.45	0.38	0.53	0.56	0.45
Total	99.90	99.82	99.80	100.34	99.71	99.28	99.78	100.04
Sc	17.91	17.15	17.04	22.45	23.82	20.30	18.99	21.71
Ti	6246.27	5873.62	5844.88	6294	6129	6722	6486	6176
V	218.65	199.44	195.95	281.21	309.57	253.92	230.24	283.75
Cr	6.57	6.98	7.37	11.44	8.86	9.86	13.82	10.12
Co	17.10	15.56	15.29	22	24	20	18	22
Ni	3.27	12.66	3.91	12	11	12	15	13
Zn	104.46	98.43	99.96	103.13	99.47	105.91	101.82	98.07
Ga	16.96	16.75	16.36	17.39	17.52	17.32	17.16	17.48
Rb	54.08	52.85	53.97	34.45	35.18	45.09	46.21	35.63
Sr	462.85	450.41	446.45	589.81	614.93	502.59	490.33	566.93
Y	30.31	30.45	28.65	23.09	21.61	28.10	27.52	23.20
Zr	136.91	139.38	131.44	94.33	77.24	119.22	121.81	92.94
Nb	2.03	2.03	1.93	1.35	1.11	1.75	1.80	1.37
Cs	1.70	1.72	1.68	1.09	1.11	1.36	1.46	1.11
Ba	715.90	697.72	687.51	552.77	500.40	654.28	658.98	552.07
La	18.06	18.11	17.64	13.24	11.20	17.04	16.72	13.79
Ce	41.31	40.95	39.73	29.72	25.29	36.88	37.69	29.77
Pr	5.57	5.55	5.43	4.09	3.56	5.15	5.16	4.17
Nd	26.19	26.23	25.59	19.33	16.47	23.58	23.47	19.38
Sm	6.42	6.11	6.02	4.86	4.22	5.63	5.71	4.68
Eu	1.58	1.57	1.57	1.35	1.30	1.52	1.48	1.30
Gd	5.61	5.53	5.37	4.89	4.11	5.62	5.53	4.57
Tb	0.86	0.85	0.84	0.67	0.63	0.80	0.78	0.67

Table 3.2 (cont) Whole rock major and trace element and isotope compositions of volcanic rocks from the Yenkahe Caldera

	Standards				
WSG-16	BCR-2*	AGV-2#	BHVO-2	JMC 475	SRM
White Sands					
Lithic	Standard	Standard	Standard	Standard	Standard
53.13	53.75	59.78	-	-	-
0.82	2.27	1.05	-	-	-
16.38	13.38	17.00	-	-	-
11.05	14.29	6.92	-	-	-
0.19	0.20	0.10	-	-	-
3.99	3.55	1.78	-	-	-
8.18	7.05	5.20	-	-	-
3.57	3.13	4.26	-	-	-
1.97	1.79	2.95	-	-	-
0.31	0.35	0.48	-	-	-
99.59					
24.63	33.81	15.05	-	-	-
5054.60	14189.86	6703.24	-	-	-
362.88	422.83	128.18	-	-	-
7.07	23.48	23.44	-	-	-
26.06	37.39	16.07	-	-	-
14.08	20.09	25.31	-	-	-
78.95	132.36	94.96	-	-	-
16.35	22.22	20.94	-	-	-
23.64	45.25	63.87	-	-	-
657.98	350.68	681.13	-	-	-
18.24	36.77	20.53	-	-	-
65.21	198.30	250.38	-	-	-
0.89	12.66	14.70	-	-	-
0.76	1.07	1.12	-	-	-
424.82	700.82	1181.86	-	-	-
8.97	25.77	39.44	-	-	-
19.97	55.20	73.30	-	-	-
2.83	6.96	8.44	-	-	-
13.78	30.34	32.70	-	-	-
3.27	6.94	5.88	-	-	-
1.09	2.04	1.64	-	-	-
3.51	7.11	4.97	-	-	-
0.52	1.10	0.67	-	-	-

Table 3.2 (cont) Whole rock major and trace element and isotope compositions of volcanic rocks from the Yenkahe Caldera

	Siwi Ignimbrite							
Sample	WSP-4	WSP-15	WSP-26	TB3	PR3	TB4	PR2	FB2
Dy	5.58	5.55	5.33	4.40	4.06	5.04	5.02	4.38
Ho	1.12	1.07	1.08	0.91	0.84	1.07	1.07	0.88
Er	3.33	3.29	3.15	2.72	2.43	3.23	3.19	2.69
Tm	0.48	0.50	0.46	0.42	0.37	0.49	0.48	0.38
Yb	3.43	3.29	3.16	2.68	2.43	3.13	3.09	2.62
Lu	0.50	0.51	0.49	0.40	0.37	0.46	0.45	0.38
Hf	3.88	3.90	3.76	2.78	2.30	3.44	3.53	2.77
Ta	0.12	0.12	0.12	0.09	0.07	0.11	0.11	0.08
Pb	16.52	16.09	16.24	8.56	12.07	24.44	16.32	13.12
Th	3.04	3.00	2.95	2.18	1.69	2.75	2.78	2.12
U	1.71	1.61	1.70	1.14	0.95	1.49	1.51	1.17
$^{87}Sr/^{86}Sr$	-	-	-	0.703711	-	0.704743	-	0.703560
$^{143}Nd/^{144}Nd$	-	-	-	0.513038	-	0.513047	-	0.513031
$^{176}Hf/^{177}Hf$	-	-	-	0.283147	-	0.283156	-	0.283141

samples, with phenocrysts exhibiting An_{54-60} and microlites displaying An_{51-54} (Table 3.4).

Clinopyroxene is less common as a phenocryst phase, however remains present in almost all samples. Compositionally it shows only small variations between pre-caldera lavas (Wo_{39-42} Fs_{43-45} En_{14-17}) and juvenile material from the OTI (Wo_{34-37} Fs_{19-20} En_{44-46}) and Siwi Ignimbrite (Wo_{38-42} Fs_{39-44} En_{14-23}) (Table 3.4; Fig. 3.9b). Within the OTI, clinopyroxene compositions do not vary widely between enclaves and the remainder of the sample.

Olivine is rare amongst all samples, with the exception of some of the most primitive pre-caldera lavas, where it is a major phenocryst phase and is present as large (>2 mm), euhedral grains. The composition of these grains was not ascertained. Olivine phenocrysts within the basal lava record compositions of Fo_{80}. Olive was not identified within juvenile material from the OTI. Rare olivine phenocrysts in the Siwi Ignimbrite record compositions of Fo_{66-69} (Table 3.4; Fig. 3.9c).

DISCUSSION

Stratigraphy and significance of the OTI

The OTI was originally described at three locations on the north-eastern coast of Tanna (Fig. 3.1), however these were not correlated with sites closer to the Yenkahe Caldera (Robin

Table 3.2 (cont) Whole rock major and trace element and isotope compositions of volcanic rocks from the Yenkahe Caldera

	Standards				
WSG-16	BCR-2*	AGV-2#	BHVO-2	JMC 475	SRM
3.16	6.82	3.76	-	-	-
0.66	1.35	0.70	-	-	-
2.13	3.92	1.97	-	-	-
0.30	0.54	0.27	-	-	-
1.99	3.56	1.75	-	-	-
0.28	0.54	0.27	-	-	-
1.86	5.29	5.63	-	-	-
0.05	0.81	0.91	-	-	-
8.28	13.36	15.05	-	-	-
1.38	6.25	6.58	-	-	-
0.75	1.73	1.96	-	-	-
-	-	-	0.703451	-	0.710214
-	-	-	0.512980	0.511118	-
-	-	-	0.283119	0.282164	-

*Average of 9 analyses

Average of 7 analyses

et al. 1994). Outcrops of pre-ignimbrite rocks, such as those at Waesisi, suggest the topography prior to the OTI eruption consisted of a series of valleys and ridges radiating out from a large volcanic edifice. Successive ignimbrite eruptions have both destroyed the volcanic edifice and filled the valleys. This can be seen at Lowaisia where basal surge and fall units mantle an undulating palaeosol, and also where these and overlying units abut the remnant pre-ignimbrite edifice at Waesisi. This topography makes accurate correlation difficult as current exposures run largely perpendicular to the original ridge-valley network. As such, the occurrence and thickness of certain units varies widely between exposures. The stratigraphy presented by Robin et al. (1994) is correlated with that given here in Fig. 3.10. This shows that deposits of the OTI extend all the way to the margin of the Yenkahe Caldera, where they were previously identified as a volcanic breccia by Allen (2005). The full stratigraphy of the OTI is best preserved at Lowaisia.

Robin et al. (1994) suggested the OTI was derived from the Eastern Tanna Volcano (Fig. 3.1), however re-examination of the deposit stratigraphy suggests that it is instead derived from the Yenkahe Caldera. The occurrence of the Eastern Tanna Volcano was largely inferred

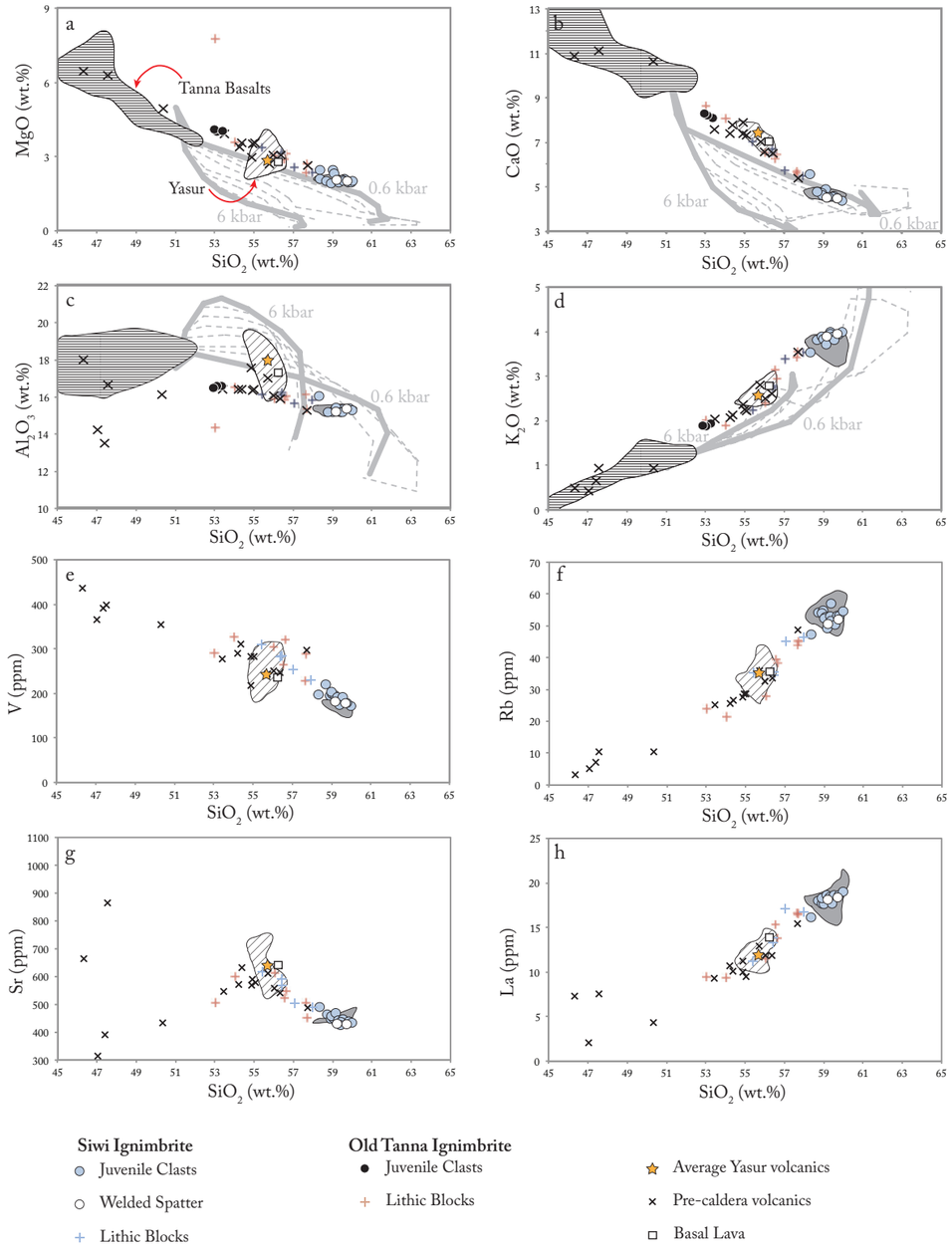

Fig. 3.6 Variation diagrams, showing the abundance of selected major and trace elements against SiO_2. Fields showing previous literature analyses for Tanna basalts (Dupuy et al. 1982; Peate et al. 1997), juvenile material from the Siwi Ignimbrite (Robin et al. 1994; Allen 2005; Métrich et al. 2011) and recently erupted bombs from Yasur (Nairn et al. 1988; Turner et al. 1999; Métrich et al. 2011; Firth et al 2014) are marked, with the average of the final group displayed by a star. Predictions from a suite of MELTS models run at different pressures are shown as grey lines in panels a-d. Solid lines represent end pressures of 0.6 and 6 kbar, while dashed lines represent intermediate pressures of 0.8, 1, 2, 3, 4 and 5 kbar.

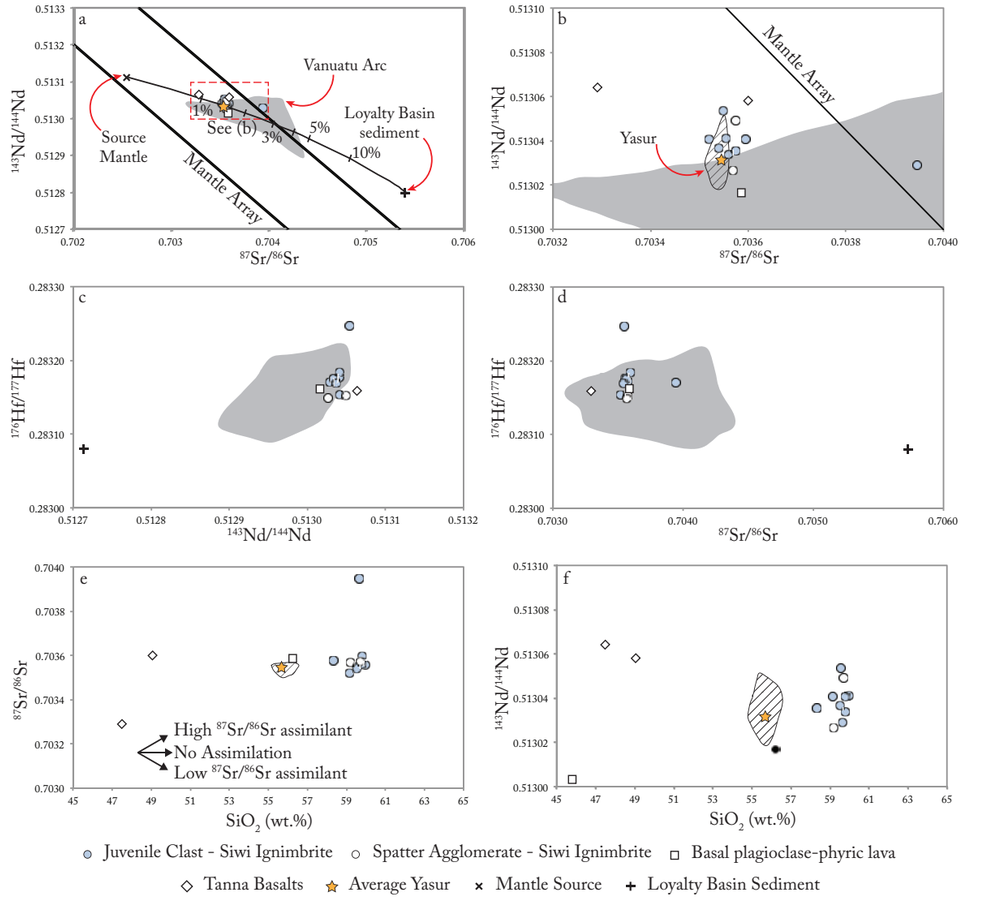

Fig. 3.7 (a) Sr and Nd isotopes for the Siwi Ignimbrite and basal, plagioclase-phyric lava. The source mantle (Pacific-MORB) and loyalty basin sediments are shown for reference (Peate et al. 1997), while a grey field denotes isotope values for the arc as a whole (Peate et al. 1997). (b) Close-up of Panel (a) to detail Sr and Nd isotopes for the Yenkahe Caldera. A field showing isotopic ratios for Yasur (Handley et al. in prep) is given, while basalts from Tanna are also shown (Peate et al. 1997). Hf isotope ratios are plotted against $^{143}Nd/^{144}Nd$ (c) and $^{87}Sr/^{86}Sr$ (d), with the field for Vanautu arc lavas (Peate et al. 1997; Pearce et al. 2007) shown for comparison. $^{87}Sr/^{86}Sr$ and $^{143}Nd/^{144}Nd$ are plotted against SiO_2 in panels (e) and (f) to investigate the possibility of crustal assimilation. Vectors showing explaining potential trends are displayed in panel (e).

Table 3.3 Composition of glass veins and inclusions within the Old Tanna Ignimbrite samples

	SiO_2	TiO_2	Al_2O_3	FeO	MnO	MgO	CaO	Na_2O	K_2O	Total
Vein	58.72	1.05	14.34	8.85	0.24	2.28	5.00	3.87	3.94	98.29
Inclusion	58.10	1.09	14.37	9.23	0.22	2.56	5.37	4.02	3.83	98.79
Inclusion	59.49	1.06	14.36	8.87	0.23	2.28	5.00	4.17	3.85	99.31
Inclusion	58.81	1.08	14.26	8.63	0.21	2.32	4.97	4.02	4.06	98.36

from bathymetric data (Robin et al. 1994), however this offers no conclusive evidence for the presence of an edifice to the east of Tanna. Robin et al. (1994) suggest the pre-ignimbrite volcanics at Waesisi form the south-west flank of this edifice, however observed dips within this deposit are inconsistent with this, instead suggesting it is linked to an edifice associated with the Yenkahe Caldera. Furthermore, deposits features, such as the thickening of surge and flow units to the north-west side of palaeo-valleys suggest an origin to the south-east, in the direction of the Yenkahe Caldera. Coarsening of the overlying breccia in the same locations also attests to slowing of a north-west directed flow as a result of pre-ignimbrite topography. The first of the major flow units from the OTI, which outcrops most extensively, shows significant variations in lithic content with distance for the Yenkahe Caldera margin. Proximal sites display high lithic content (>50% volume), with individual clasts reaching diameters of >5 m, while Robin et al. (1994) note accidental clasts account for <2% of this unit at Site 22. These features are consistent with a lag breccia (c.f. Wright and Walker 1977; Walker 1985; Branney and Kokelaar 2002) originating from the Yenkahe Caldera.

The lack of basal fall and surge units in proximal deposits at Sulphur Bay and White Sands potentially reflect the influence of pre-ignimbrite topography. Opening surges are likely to have been directed and, as such, their deposits are highly topographically confined. Fall units should have been emplaced more radially, however. Sites recording fall deposits, such as Lowaisia, are clustered along the same ash dispersal axis followed by current eruptive activity from Yasur, raising the possibility that fall deposits at other locations were thinner. Alternatively, sediment deformation features at White Sands are consistent with emplacement of the overlying pyroclastic flow unit atop a wet substrate, however tree-trunk casts suggest the ignimbrite was not emplaced in a submarine environment. Combined, these features suggest potential emplacement in a littoral zone. This may explain the absence of basal fall units, which could have been mobilised and removed by water prior to emplacement of the overlying ignimbrite. To the north, tephra fall and surge beds overlie a sharp, and at times erosive, contact onto a terrestrial soil sequence at Lowaisia. This attests to sub-aerial emplacement of the OTI in this region. The presence of charcolised tree fragments within the basal surge deposits further support this. In contrast, Robin et al. (1994) proposed submarine emplacement, on the basis of palagonite matrix within the lower fall and surge beds at Site 16. Palagonite was identified within the lower horizons from the soil stack underlying the OTI at Lowaisia, raising the possibility that Robin et al. (1994) included the older soil/tephra sequence below the OTI as part of the eruptive

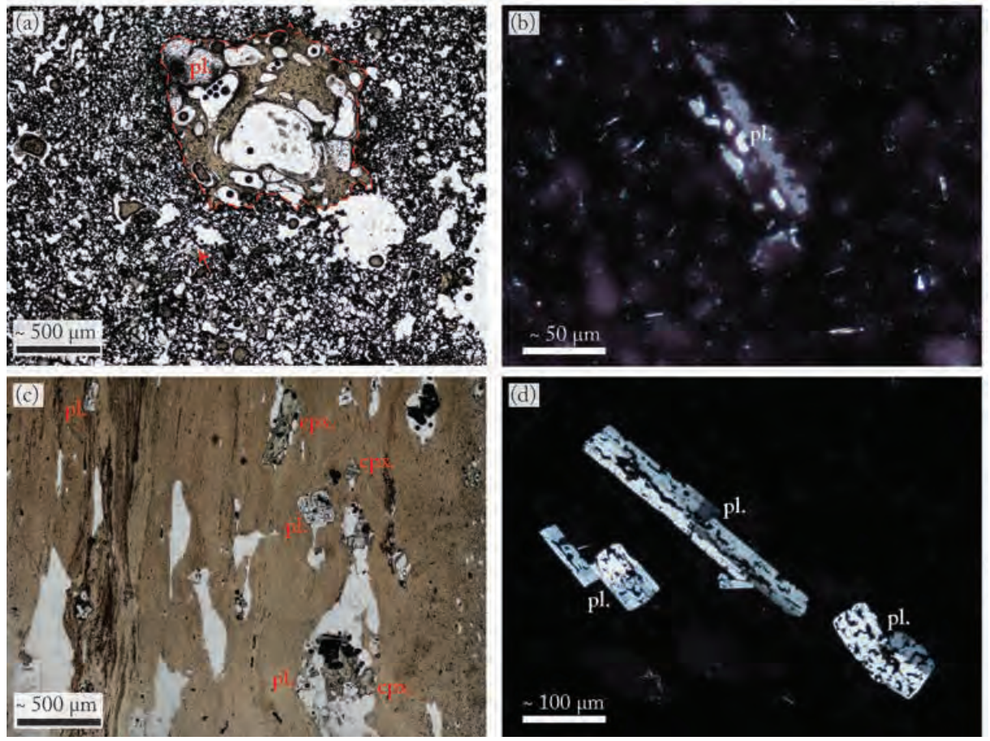

Fig. 3.8 (a) Photomicrograph showing basaltic-trachy-andesitic enclave (outlined by dotted line) within pumice from the OTI. Note the difference in size between phenocrysts and vesicles within the enclave and surrounding pumice. The arrow points out a small plagioclase phenocryst. (b) Photomicrograph under cross-polarised light showing skeletal plagioclase phenocryst within the OTI. (c) Plane-polarised light photomicrograph showing the eutaxitic texture of spatter agglomerate from the Siwi Ignimbrite. Plagioclase and clinopyroxene phenocrysts are identified. Note the glomerocrysts in the lower right corner of the image. (d) Sieve-textured plagioclase phenocrysts within the Siwi Ignimbrite shown in cross-polarised light.

sequence. Descriptions given by Robin et al. (1994) for their Site 23, also raise the possibility that they included distal deposits of the Siwi Ignimbrite as part of the eruption sequence for the OTI. They describe a pumice-rich flow unit containing abundant elongate and ribboned, dense vitric clasts, which is interpreted as the final stage of the OTI eruption. Geochemical analyses of clasts from this unit are comparable with clasts from the Siwi Ignimbrite (57-58.6 wt.% SiO_2).

Radiocarbon dates of the charcoal collected from the basal surge units at Lowaisia provide an age of ~43 kyr for the OTI eruption. This age is significantly younger than the late Pliocene to Pleistocene age suggested by Robin et al. (1994) and suggests that the Yenkahe magmatic system has been active for at least 45 kyr.

Table 3.4 Representative mineral major element analyses.

		Sample	Grain type		SiO_2 (wt.%)	TiO_2 (wt.%)	Al_2O_3 (wt.%)	FeO (wt.%)	MnO (wt.%)	MgO (wt.%)	CaO (wt.%)	Na_2O (wt.%)	K_2O (wt.%)	Total	An (mol.%)	Fs (mol.%)	Fo (mol.%)
Plag.	Pre-Caldera	TB1	P	Core	52.89	0.04	28.57	0.90	0.00	0.12	12.00	4.48	0.53	99.72	58	-	-
		TB1	P	Rim	53.82	0.04	28.30	0.90	0.02	0.10	11.77	4.61	0.54	99.72	57	-	-
		BR1	P	Rim	46.44	0.03	32.79	1.05	n.d.	0.10	16.89	1.95	0.12	99.36	82	-	-
		BR6	P	Rim	53.66	0.03	28.05	0.91	0.01	0.11	11.67	4.68	0.55	99.67	56	-	-
		BR6	P	Rim	53.42	0.05	27.88	0.99	n.d.	0.14	11.43	4.78	0.57	99.27	55	-	-
	OTI	SB14	Skeletal P	Rim	46.10	n.d.	32.90	0.91	n.d.	0.09	17.87	1.44	0.07	99.38	87	-	-
		WSP14	Skeletal P	Rim	47.36	n.d.	32.88	0.99	n.d.	0.11	17.67	1.44	0.13	100.58	86	-	-
		WSP14	Skeletal P	Core	47.38	n.d.	32.57	0.92	n.d.	0.09	17.69	1.56	0.07	100.28	86	-	-
		SB14	Sieve P	Rim	50.87	0.03	30.11	0.83	n.d.	0.09	14.42	3.16	0.21	99.72	71	-	-
		WSG14	P	Rim	53.39	0.06	27.74	1.14	n.d.	0.26	12.05	4.38	0.48	99.50	59	-	-
		WSG14	P	Rim	52.91	0.04	28.23	1.40	n.d.	0.20	13.16	3.62	0.22	99.78	66	-	-
		WSP14	GM	Rim	55.24	0.07	26.89	1.37	n.d.	0.16	11.15	4.99	0.64	100.51	53	-	-
		SB14	GM	Rim	52.40	0.09	27.53	1.64	n.d.	0.24	12.54	4.15	0.35	98.94	61	-	-
		WSP14	Encl - P	Rim	53.16	0.03	27.67	1.11	n.d.	0.13	12.31	4.12	0.51	99.04	60	-	-
		WSP14	Encl - GM	Rim	55.85	0.05	26.48	1.26	n.d.	0.11	10.44	5.05	0.72	99.96	51	-	-
	Siwi Ignimbrite	WS3	Sieve P	Rim	54.75	0.05	27.41	0.80	n.d.	0.10	10.85	5.17	0.59	99.72	52	-	-
		WS6	Sieve P	Rim	51.18	n.d.	29.01	0.85	n.d.	0.09	13.26	3.85	0.39	98.63	64	-	-
		WS7	Sieve P	Rim	52.51	0.04	27.88	0.90	n.d.	0.11	12.42	4.46	0.34	98.66	59	-	-
		WS3	P	Rim	56.64	0.05	25.39	0.62	n.d.	0.07	8.47	6.18	0.94	98.36	41	-	-
		WS6	P	Rim	55.67	0.03	26.16	0.70	n.d.	0.06	9.73	5.90	0.76	99.01	46	-	-
		WS7	P	Rim	56.94	0.06	25.72	0.58	n.d.	0.08	9.05	6.22	0.93	99.58	42	-	-
		PR1	P	Rim	56.60	0.07	25.20	0.60	n.d.	0.08	8.54	6.12	0.91	98.12	41	-	-
		PR1	P	Rim	56.57	0.04	25.29	0.61	n.d.	0.07	8.90	5.87	0.86	98.21	43	-	-
		PR2	P	Rim	55.25	0.04	26.26	0.64	n.d.	0.07	10.00	5.41	0.66	98.33	49	-	-
Cpx.	Pre-Caldera	BR1	P	Rim	51.54	0.41	1.86	9.98	0.53	15.47	19.45	0.34	n.d.	99.58	-	17	-
		BR6	P	Rim	51.55	0.45	2.36	9.95	0.35	15.83	19.37	0.41	0.01	100.29	-	16	-
		TB1	P	Rim	51.08	0.53	2.24	10.56	0.39	15.25	19.74	0.32	0.02	100.14	-	17	-
	OTI	WSG14	Encl - P	Rim	48.60	0.95	6.37	10.23	0.29	12.74	20.06	0.70	0.09	100.03	-	20	-
		WSG14	Encl - P	Rim	48.94	1.00	5.58	10.18	0.26	13.13	20.40	0.50	0.15	100.14	-	19	-
		WSP14	Encl - P	Rim	52.25	0.61	2.70	11.58	0.42	15.65	18.13	0.29	n.d.	101.63	-	19	-
	Siwi Ignimbrite	WS3	P	Rim	51.26	0.50	1.86	10.65	0.49	15.21	19.81	0.32	n.d.	100.10	-	18	-
		WS3	P	Rim	50.89	0.54	1.78	11.55	0.56	14.74	19.54	0.31	n.d.	99.91	-	19	-
		WS3	P	Rim	50.54	0.54	2.05	10.75	0.51	15.29	19.52	0.42	n.d.	99.62	-	18	-
		WS7	P	Rim	51.11	0.54	1.64	11.70	0.54	14.84	19.45	0.39	n.d.	100.21	-	19	-
		PR1	P	Rim	49.77	0.59	1.62	13.03	0.65	13.65	18.91	0.30	n.d.	98.52	-	22	-
		PR2	P	Rim	50.00	0.62	2.51	11.04	0.47	14.92	19.60	0.36	n.d.	99.52	-	18	-
Olivine	Pre-Caldera	TB1	P	Rim	37.15	0.01	0.03	29.92	0.66	33.59	0.28	0.05	0.01	101.71	-	-	74
		TB1	P	Rim	36.85	n.d.	0.03	29.96	0.70	33.72	0.29	0.03	0.01	101.60	-	-	74
		BR6	P	Rim	38.18	n.d.	0.05	23.17	0.50	38.84	0.25	0.06	n.d.	101.05	-	-	81
	Siwi Ignimbrite	WS3	P	Rim	35.38	n.d.	n.d.	35.83	1.06	27.71	0.27	n.d.	n.d.	100.25	-	-	66
		WS7	P	Rim	35.76	n.d.	n.d.	34.04	0.93	29.91	0.28	n.d.	n.d.	100.92	-	-	69

P - Phenocryst; GM - Groundmass; Encl - Enclave

Stratigraphy and eruption history of the Yenkahe Caldera

Linking the OTI to the Yenkahe Caldera has important implications for the stratigraphy of the magmatic system. At least two voluminous, ignimbrite-producing eruptions have occurred within the last ~43 kyr, collectively forming the composite Yenkahe Caldera.

Outcrops of pre-caldera volcanics at Waesisi indicate a volcanic edifice was present prior to 43 kyr. These include lahar and related volcaniclastic deposits that are similar to the current Tukisumera edifice flanks, located to the SW of the Yenkahe Caldera. Lava flows and tephra fall deposits erupted during periods of lower magnitude activity since the OTI eruption indicate that voluminous, semi-continuous volcanic activity was maintained throughout the bulk of the history of this volcanic centre. Deposits from a number of areas, including the Siwi River and Shark Bay, suggest that rather than being centred on a large volcanic edifice, such intra-caldera activity repeatedly formed smaller volcanic cones. Yasur is the most recent manifestation of this phenomenon. A tuff ring succession dissected by the Siwi River to the east of the ash plain records an earlier phase of explosive, potentially phreatomagmatic, activity adjacent to Yasur. In addition, Nairn et al. (1988) report the presence of a number of Holocene volcanic cones within the Yenkahe Caldera, including Ombus, on the south of the Yenkahe Dome. Similarly, spatter cone deposits at Shark Bay, south of the caldera, suggest earlier episodes of cone building prior to eruption of the Siwi Ignimbrite. The majority of scoria cones and tuff rings built prior to the Siwi eruption were likely located within the caldera, like Yasur, and thus were destroyed during caldera-producing eruptions. Additional, circumstantial evidence for inter-ignimbrite volcanism being centred on small, discrete cones, is provided by the absence of remnants of a post-OTI/pre-Siwi volcanic edifice.

The most recent activity within the Yenkahe Caldera is persistent Strombolian eruptions at Yasur (Firth et al. 2014), accompanied by rapid uplift of a dome at the centre of the caldera (Chen et al. 1995; Merle et al. 2013). These have significantly modified the caldera and potentially hidden or disrupted deposits recording early post-Siwi activity. The caldera may have been flooded following the Siwi eruption, as indicated by Métrich et al. (2011), who report the presence of early post-caldera tuff beds overlying shelly, shallow-marine sand near the caldera margin at Port Resolution. The depositional facies within tuff cone remnants on the Siwi River upstream of Sulphur Bay is very similar to phreatomagmatic tuff cones seen at island margins on comparable Vanuatu islands of Ambrym (Németh and Cronin 2011) and Ambae (Németh and Cronin 2009). This suggests magma-water interaction at or near the coastline.

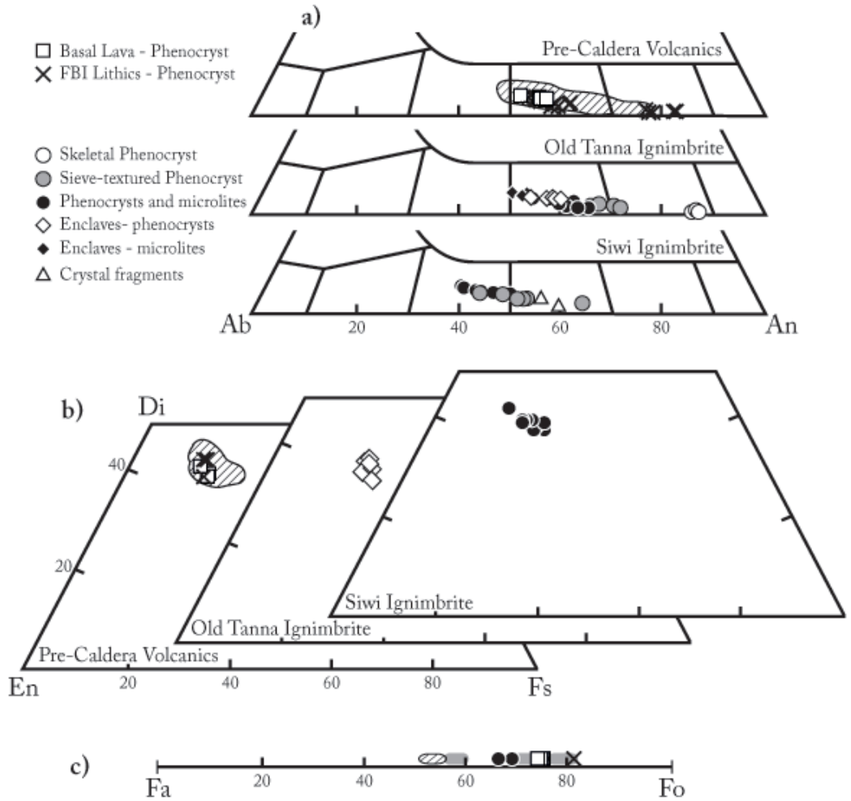

Fig. 3.9 (a) Ternary diagrams showing plagioclase rim compositions. A striped field showing compositions erupted by Yasur (Firth et al. 2014) is superimposed on the Pre-caldera diagram for comparison. (b) Ternary diagrams showing clinopyroxene compositions. (c) Olivine compositions of pre-caldera and Siwi Ignimbrite rocks. The striped field shows compositions from Yasur, while grey fields show olivine compositions recorded by Métrich et al. (2011) for the Siwi Ignimbrite.

Local oral traditions report that Yasur grew from the sea (J. Hammond pers. comm. 2014), raising the possibility that the Yenkahe Caldera may have been a shallow harbour filled by sea water as recently as 2-3 ka. Time averaged uplift rates for the Yenkahe dome (Chen et al. 1995) and tephra records of activity at Yasur (Firth et al. 2014) are consistent with this scenario.

Eruption dynamics of the OTI and Siwi Ignimbrite

While high-magnitude, ignimbrite-producing eruptions are a repeated feature of the Yenkahe magmatic system, differences in deposit characteristics between the ignimbrites suggest such eruptions can differ in a number of ways. Basal lapilli fall and surge beds are a feature of deposits from both the Siwi and OTI eruptions. They record vent opening and the

expulsion of small volumes of magma following initial overpressure of the magma chamber (*c.f.* Druitt and Sparks 1984). Variability in the occurrence of opening surge deposits in the OTI suggests these were directed towards certain sectors, or erupted from isolated sites along a newly developing caldera ring fault system. Where present, these beds reach significantly greater thickness than the basal surge units of the Siwi Ignimbrite. Their association with well-sorted, horizontally-bedded, ash and lapilli air-fall deposits suggests derivation from a large, Plinian eruption column, which generated extensive tephra fall as well as directed, hot, ash-cloud surges. The presence of charcoal fragments within these deposits suggests surges knocked-over and charcoalised vegetation. The number and thickness of the OTI tephra fall and surge beds at Lowaisia attests to a complex eruption sequence, with a number of pulses and variations in eruptive intensity. A final coarsening upwards fall sequence at Lowaisia suggests an increase in eruption intensity before caldera collapse. Unlike the OTI, basal surge deposits of the Siwi Ignimbrite are locally present along the caldera margin, and opening fall units are not identified in more distal deposits. Allen (2005) suggests that basal surges were generated by a series of phreatomagmatic blasts, citing high lithic content and fine ash coatings on clasts as evidence. Accretionary lapilli identified in these deposits north of Sulphur Bay (Fig. 3.2) are consistent with this origin. This suggests that the Siwi eruption opened with energetic phreatomagmatic explosions, but lacked the opening Plinian eruption column recorded for the OTI eruption (Fig. 3.11).

The high microlite abundance in juvenile clasts of the OTI indicates the magma underwent a prolonged period of degassing prior to eruption (e.g., Blundy and Cashman 2001; Cashman and Blundy 2000; Hammer et al. 1999). The degassing is likely associated with the opening Plinian fall phase, consistent with a gradual increase in eruptive intensity. By contrast, juvenile clasts of the Siwi ignimbrite are microlite-free, suggesting negligible degassing of the magma prior to eruption. The onset of the Siwi eruption was thus brief and was strongly influenced by magma-water interaction rather than magmatic volatile expansion and release.

The differences in the onset phases of the two major ignimbrite eruptions may relate to the fact that no caldera existed before the OTI eruption, whereas this ring-fault structure was then partly or fully re-activated during the Siwi eruption (Fig. 3.11). The OTI is distinctive in containing large volumes of pre-ignimbrite volcanic lithics with large zones of lithic lag-breccia including boulders with diameters >5 m (five-times the size of those in the Siwi Ignimbrite) up to 2.5 km from the caldera. This relates to a pre-existing edifice that was likely destroyed

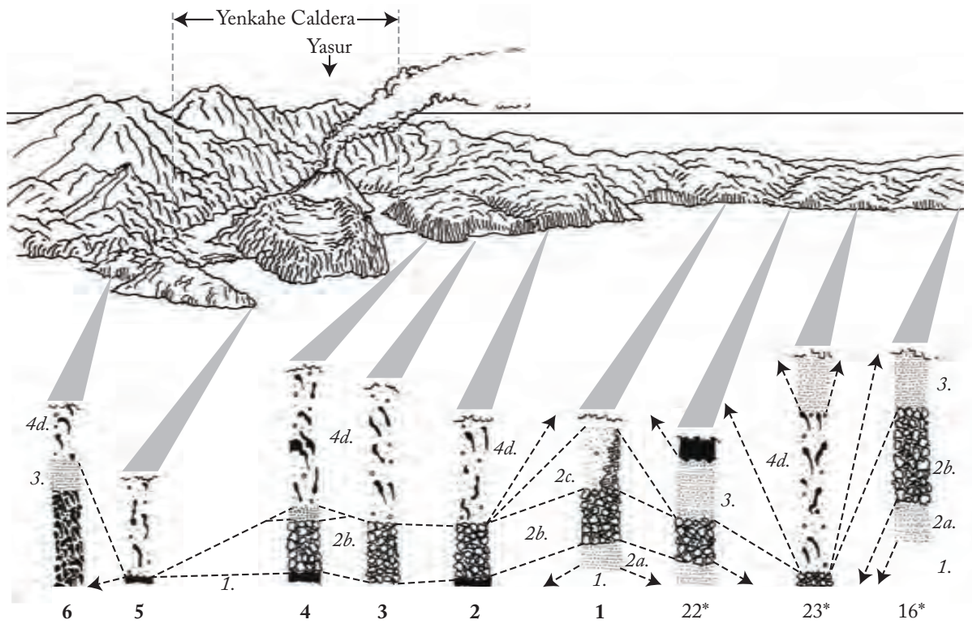

Fig. 3.10 Stratigraphic correlation, linking sites examined in the text with those described by Robin et al. (1994). The location of each stratigraphic column is shown on the upper cartoon (not to scale), while bold numbers below correspond with the sites numbered in Fig. 3.1. Numbers in italics denote stratigraphic units and correlate with Fig. 3.2-3.5: *1.* Pre-OTI deposits; *2.* OTI deposits; *3.* Post-OTI/Pre-Siwi Ignimbrite deposits; *4.* Siwi Ignimbrite deposits.

during the OTI eruption. The later Siwi eruption likely began in the ring-fault system of the existing caldera, as magma rose into deep-seated, water-filled cracks, triggering vigorous phreatomagmatic explosions and rapid unroofing. The common spatter within parts of the Siwi Ignimbrite represents magma forced through pre-existing ring-fault segments in later phases of the eruption.

The main pyroclastic flow units of both ignimbrites, which represent the paroxysmal stages of eruption, differ in structure and componentry, suggesting eruption dynamics also varied in this phase of the eruption. The abundance of lithic clasts in all subunits of the Siwi Ignimbrite indicates that vent erosion continued throughout the eruption, although they reached peak levels at the transition from the spatter agglomerate to upper ignimbrite. In contrast, pyroclastic flow deposits of the OTI are massive, suggesting an origin from a single eruptive phase. The preceding fall units of the OTI are lithic poor, followed by a rapid transition to a massive, lithic-rich ignimbrite. This suggests that caldera collapse occurred more rapidly

during the OTI eruption, following hours or days of variable Plinian eruptions (Fig. 3.11). Similar temporal variations in eruption dynamics are recorded for explosive, caldera-forming eruptions such as Mount Pinatubo in 1991 (Stix and Kobayashi 2008).

While the body of the OTI is predominantly massive, localised stratification occurs in enclaves that lack the largest lithic boulders. The lowermost portion of the ignimbrite is often finer-grained, with an upwards-coarsening transition towards the centre of ignimbrite, where the largest boulders are concentrated. This suggests that caldera collapse peaked in intensity during the middle of the ignimbrite-emplacement phase.

Another striking difference between both ignimbrites, is the abundance of fluidal spatter clasts in the Siwi Ignimbrite. Spatter is more commonly associated with low-magnitude, mafic eruptions (Sumner 1998; Sumner et al. 2005), however, has also been identified in other andesitic ignimbrites (e.g. Caulfield et al. 2011; Mellors and Sparks 1991; Valentine et al. 2000). Its presence indicates the eruption of hot, fluid magma, which was still plastic upon deposition, and has been linked with spatter fountaining (Allen 2005; Caulfield et al. 2011). The presence of dense and poorly vesicular spatter was taken as an indication of phreatomagmatism (Mellors and Sparks 1991), however, this is inconsistent with the particle shapes and weak fragmentation seen in the Siwi Ignimbrite. Instead, it potentially formed where degassed magma at the reservoir margins was squeezed-out through ring faults and/or drawn out as the central gas-rich magma expanded and violently erupted. Allen (2005) suggested that the Siwi spatter agglomerate represents a climactic eruption phase, in which the roof of the magma chamber collapsed. This could also explain the high lithic content in spatter deposits. The Siwi spatter agglomerate is confined to the northern rim of the caldera, which indicates a localised episode of spatter fountaining, rather than wholesale distribution of spatter by pyroclastic flows. Similar deposits have been described at Mt Mazama and attributed to early leaks of magma prior to the climactic Crater lake eruption (J. Stix pers. comm.)

The final stage of the Siwi eruption involved widespread emplacement of a pumiceous ignimbrite that is ubiquitous in geological exposures over much of southern Tanna. Allen (2005) ascribed these deposits to pyroclastic flows produced by a collapsing eruption column. The wide, radial dispersion of this unit around the caldera adds weight to this assertion. Deposits of this unit, >1 m in thickness, are observed in road cuttings on the western side of Tanna, over 18 km from the caldera. To reach this location, the pyroclastic flows surmounted a plateau that runs the length of the island at an elevation of 400-500 m (Fig. 3.1). Tree casts at Shark

Bay are associated with complex inverse soil sequences, caused by up-rooting of trees by the pyroclastic flow (*c.f.,* Froggatt et al. 1981). Similar, pumice-rich flow units are less obvious in the OTI, raising the possibility that pyroclastic flows were generated more by caldera collapse, than collapse of the eruption column (Fig. 3.11).

Both ignimbrites are distributed asymmetrically with respect to the Yenkahe Caldera, with deposits thicker and more complete to the caldera's north (Fig. 3.1). Lower units of the Siwi Ignimbrite are not found in deposits on the south side of the caldera, and spatter clasts are rare in this area. The asymmetrical distribution of the OTI is even more pronounced, with no deposits identified to the south of the caldera. This may be a product of poor preservation, greater burial by subsequent volcanic material or lesser degrees of erosion, however. Palaeotopography may also have influenced ignimbrite distribution. Asymmetrical ignimbrite distribution was noted in the Kaingaroa Ignimbrite in New Zealand (Beresford and Cole 2000), and linked with trap-door style, asymmetrical caldera subsidence during eruption, with initial eruptive activity restricted to one side of the caldera and only the ultimate units distributed more radially, due to symmetrical column-collapse. This scenario best describes thedistribution of the Siwi Ignimbrite, with initial eruptive activity restricted to the vicinity of Sulphur Bay, where common spatter clasts attest to violent spatter fountaining. Brothelande et al. (in press) note a significantly greater offset in the Siwi Ring Fracture along the northern margin of the caldera, interpreted as evidence for trapdoor-style subsidence. Furthermore, the absence of lower units of the Siwi Ignimbrite in deposits along the south-eastern margin of tha caldera, at Port Resolution, is hard to reconcile with erosion or the influence of palaeotopography, instead supporting asymetrical caldera collapse.

Thus, while both ignimbrites are sourced from the same caldera, stratigraphic differences highlight diversity within the style of their eruption. This diversity is partly a function of the dynamics of caldera collapse and influence of water, but may also be a product of magma chemistry.

Geochemistry and petrology of the Yenkahe Magmatic System

Linear whole rock major and trace element arrays (Fig. 3.6) and comparable Sr, Nd and Hf isotopes (Fig. 3.7), suggest volcanic rocks erupted from the Yenkahe system belong to the same magmatic evolution series and have been feed by the same homogenous parental basalt. This is in agreement with previous findings by Métrich et al. (2011). Some compositional diversity

can be seen amongst the pre-caldera basalts, primarily in elements such as Al_2O_3 and Sr (Fig. 3.6). Basalts examined in this study are present as lava flows at two localities: Tukasmera and Waesisi. Samples from Tukasmera can be discriminated by lower Al_2O_3, Sr and La and higher CaO (Table 3.2) than samples with similar SiO_2 from Waesisi. The Waesisi samples are believed to represent an early phase of the Yenkahe volcanic rocks, while the Tukasmera basalts represent late-stages of the mid-late Pleistocene Tukasmera volcanics. Variation between these two basaltic suites is largely limited to compatible elements and, as such, may be attributed to differences in crystallisation rather than parental magma composition.

Juvenile material from both ignimbrites can be discriminated from recent and pre-caldera volcanics by their distinct composition. Magma involved in the Siwi eruption has the most evolved composition recorded amongst the Yenkahe Volcanics, while the juvenile component of the OTI includes noticeably more mafic compositions. Whole rock analyses of juvenile clasts from the Siwi Ignimbrite are consistent with previous analyses by Robin et al (1994), Allen (2005) and Métrich et al. (2011) and suggest magma involved in this eruption was restricted in composition. Samples presented here from the OTI also support a narrow compositional range for this ignimbrite, however this is not in agreement with previous findings by Robin et al. (1994). They argue that the OTI was compositionally heterogeneous, resulting from eruption of a chemically zoned magma chamber. Samples presented here for the OTI fall at the least evolved end of the compositional spectrum identified by Robin et al. (1994). These authors also identified significant heterogeneity in glass composition within samples. This can be reconciled with the enclaves of more evolved glass observed within pumice from the OTI. The compositional diversity identified by Robin et al. (1994) might potentially result from varying proportions enclave glass in juvenile material from the OTI. Nevertheless, it might also be due to the potential inclusion by Robin et al. (1994) of units above and below the OTI as part of this eruptive sequence.

The majority of pre-caldera volcanics, including lithics collected from both ignimbrites, display whole rock chemistry broadly similar to that of volcanic rocks erupted from Yasur over the past ~800 years (Nairn et al. 1988; Turner et al. 1999; Métrich et al. 2011; Firth et al. 2014). In particular, the basal lava, which underlies the OTI, displays almost identical major and trace element abundances to the average composition of recently erupted magma from Yasur (Fig. 3.6). This lava is also petrologically similar to post-Siwi lavas, including two lava flows that originated from Yasur (Firth et al. 2014). All contain plagioclase phenocrysts reaching

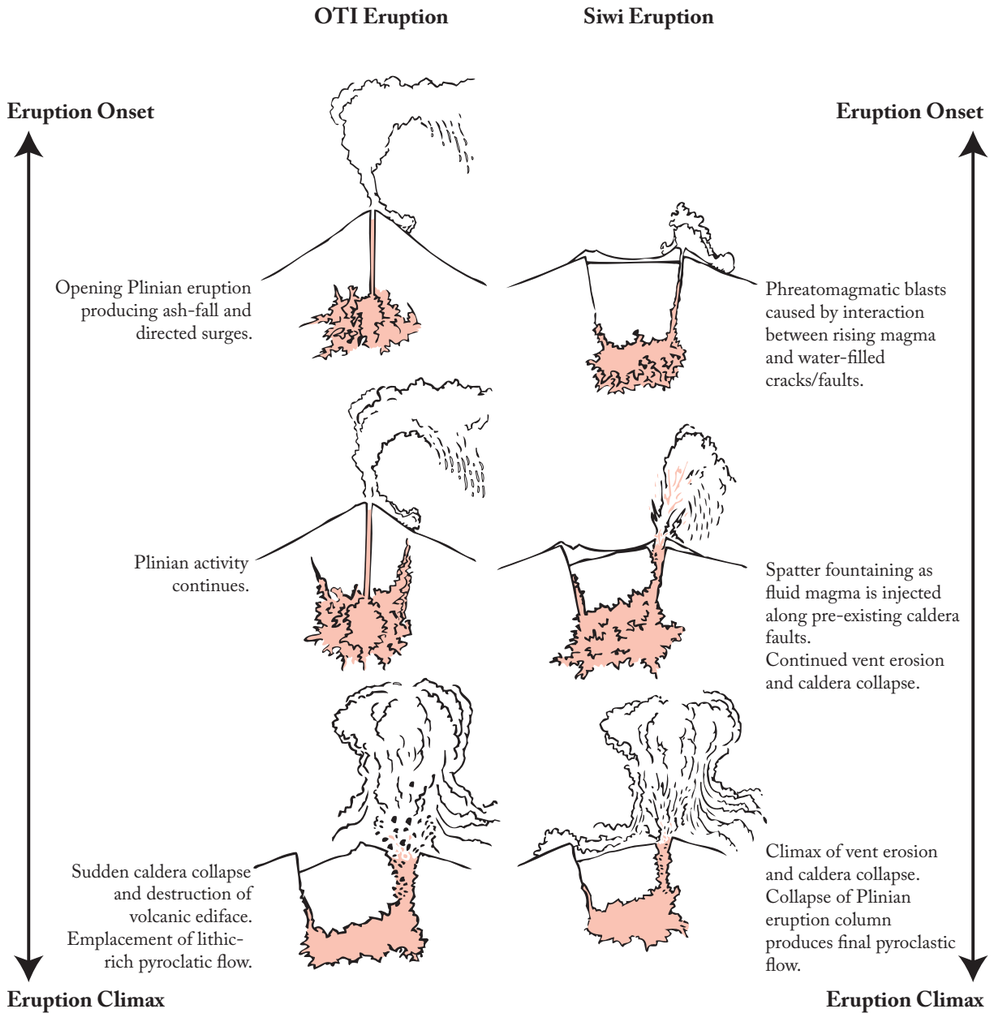

Fig. 3.11 Cartoons comparing the eruption sequence for the OTI and Siwi eruptions.

lengths >3 mm. Phenocryst compositions are comparable between all analysed lava flows. These geochemical and petrological features highlight the fact that periods of relatively low-magnitude eruptive behaviour between major ignimbrite eruptions are fed by compositionally similar magmas that are likely to have undergone comparable processes of differentiation under similar pressure and temperature conditions.

Inflections in major and trace element arrays are apparent at ~52-53 wt.% SiO_2, differentiating pre-caldera basalts from the remainder of samples. These are most obvious for incompatible trace elements such as Rb and La (Fig. 3.6), but can also be discerned in a number of major element diagrams (e.g. K_2O: Fig. 3.6). This inflexion potentially represents the onset

of plagioclase crystallisation, given the increased compatibility shown by CaO and Sr in more evolved rocks and precludes two end-member mixing.

Sr, Nd, and Hf isotope ratios of the Siwi Ignimbrite are comparable with pre-caldera lavas and recent Yasur volcanic rocks (Handley et al. in prep). All can be explained by ~1.5% addition of a subduction component dominated by sediment from the North Loyalty Basin to mantle with a Pacific-MORB composition (Fig. 3.7a). This is consistent with previous findings by Peate et al. (1997). The lack of variation in either Sr or Nd isotopes when plotted against an index of differentiation such SiO_2, suggests that assimilation with an isotopically distinct crustal component did not occur during differentiation of the Yenkahe volcanics.

Potential triggers of the ignimbrite-producing eruptions

The geochemistry and petrology of juvenile clasts from each ignimbrite provide a key to understand the magmatic processes that may have contributed to, or triggered, these catastrophic eruptions. Juvenile material from both ignimbrite-producing eruptions is compositionally distinct, with the OTI erupting basaltic andesites and basaltic trachy-andesites (52-53 wt.% SiO_2), while the Siwi Ignimbrite erupted trachy-andesites (58-60 wt.% SiO_2) (Fig. 3.6). Such compositional diversity between sequential ignimbrite producing eruptions from the same magmatic systems has also been reported from Santorini (Druitt et al. 1999). Nevertheless, the compositions of both ignimbrites are more mafic than those associated with many caldera-forming eruptions, which are most commonly associated with dacitic-rhyolitic magmas (Blake 1984; Wilson 2008). Volatile-melt segregation is more readily achieved in mafic-intermediate magmas, limiting their ability to generate highly explosive eruptions (Vinkler et al. 2012). Comparable magma compositions to that involved in the Siwi Ignimbrite were implicated in a number of other violent, ignimbrite-producing eruptions, including the Upper Scoria eruptions at Santorini (Druitt et al. 1999) and the paroxysmal 1815 eruption of Tambora (Self et al. 1984; Gertisser et al. 2012), while marginally less evolved magmas were involved in caldera-producing eruptions at Tofua (Caulfield et al. 2011) and Villarrica (Lohmar et al. 2012). Truly mafic compositions, similar to that of the OTI, are less commonly associated with ignimbrite production and caldera formation (Cashman and Sparks 2013). Only two Plinian basaltic eruptions have occurred in historical times, those of Tarawera in 1886 A.D. and Etna in 122 B.C. (Houghton et al. 2004), however, neither was associated with caldera formation. Prehistoric, mafic, caldera-forming eruptions have been identified at both Colli Albani (Vinkler et al. 2012)

and Masaya (Bice 1985). Nevertheless, such eruptions are geologically rare.

Robin et al. (1994) proposed a phreatomagmatic trigger for the both the OTI and Siwi Ignimbrite. Both Robin et al. (1994) and Allen (2005) identified a range of depositional features to justify phreatomagmatism for the Siwi Ignimbrite, however these do not unequivocally indicate that water infiltration was the eruption trigger. The revelation that both ignimbrites were erupted sub-aerially further weakens the argument for a phreatomagmatic origin.

Injection, and subsequent mixing of mafic magma into a reservoir of more evolved magma (e.g. Sparks et al. 1977; Pallister et al. 1992; Self 1992; Leonard et al. 2002), or a crystal mush (e.g. Bachmann and Bergantz 2008; Bergisser and Bergantz 2011; Lohmar 2012; Cooper and Kent 2014), is another common trigger of ignimbrite-producing eruptions. Both ignimbrites from the Yenkahe system display significant petrological and mineralogical diversity, relative to pre- and post-caldera volcanics, which may be interpreted as evidence for magma mixing or crystal mush rejuvenation. In particular, the presence in both ignimbrites of high-anorthite plagioclase displaying dis-equilibrium textures is strong evidence for magma mixing, mingling or mush remobilisation. Tsuchiyama (1985) showed experimentally that such textures occur when the dissolving mineral is more calcic than the equilibrium composition and is heated at temperatures greater than the plagioclase liquidus. Thus the texture of these minerals likely records their interaction with a more evolved component at relatively high temperature. Furthermore, it implies these minerals represent antecrysts entrained from the mafic mixing component. Similar textures have been observed at in ignimbrites at Santorini (Stamatelopoulou-Seymour et al. 1990) and Villarrica (Lohmar et al. 2012), and interpreted as evidence for magma mixing/remobilisation as the ignimbrite trigger. Large, euhedral plagioclase phenocrysts of the type seen in both current volcanic bombs from Yasur (An_{55-64}; Firth et al. 2014) and pre- and post-caldera lava flows (An_{52-57}) are absent in juvenile material from both ignimbrites, suggesting processes of plagioclase crystallisation differed markedly between these two distinct styles of eruption. The Siwi Ignimbrite also contains a diversity in olivine compositions, with the most magnesium-rich olivine grains (Fo_{77-80}) hosting a suit of basaltic melt inclusions (~49.5 wt.% SiO_2) (Métrich et al. 2011). This suggests many of the olivine crystals present in the Siwi Ignimbrite represent antecrysts, potentially entrained during magma mixing prior to the Siwi eruption.

In addition to the diversity of mineral compositions seen within both ignimbrites, they contain enclaves and glomerocrysts that are not seen within other volcanic rocks from the

Yenkahe Caldera. A number of xenoliths within magmas from both eruptions are highly angular and likely represent lithic fragments of chamber roof or conduit walls that were entrained within the magma as it ascended prior to eruption. Nevertheless, juvenile clasts from both ignimbrites display petrological evidence for some degree of magma mingling or mush remobilisation. Within pumice grains from the OTI, veins and enclaves of trachy-andesitic glass (Fig. 3.8a) are present. These appear similar to enclaves described by Bacon (1986) and Murphy et al. (2000), with the obvious difference that the material forming the enclaves was a cooler and more evolved magma than the surrounding host. The former is evidenced by the quenched, vesicle-free texture of glass immediately surrounding (<1 mm) the enclaves. Both veins and enclaves display shapes and edge textures that are unlikely to represent entrainment of solid particles, and thus argue for mingling of two liquid components. Minerals within the enclaves are compositionally similar to those in the basal lava, which stratigraphically precedes the OTI, while the enclave glass compositions are reconcilable with the whole rock composition of the basal lava. These features raise the possibility that the enclaves represent a residual magma associated with pre-caldera activity. The less evolved whole rock composition suggests this component was mixed with a more mafic recharge magma, however the presence of the enclaves attests that this mixing was not homogenous. Such a scenario is consistent with the mineral disequilbrium textures seen with these volcanic rocks, as noted previously.

While veins and enclaves are absent from juvenile material in the Siwi Ignimbrite, glomerocrysts and crystal clusters are common, and constitute a majority of the crystal cargo of these rocks. Such crystal textures have previously been interpreted as evidence for interaction with a crystal mush (Hansen and Grönvold 2000; Jerram et al. 2003), raising the possibility that such a scenario occurred to produce the Siwi Ignimbrite.

Despite considerable petrological and mineralogical evidence for either magma-magma or magma-mush interaction triggering both ignimbrite eruptions, the noticeable difference in magma composition involved in each eruption suggests they may result from different processes, or, if both eruptions were produced by the same process, it occurred to differing degrees. The presence of melt globs and veins within pumice of the OTI may suggest poor mixing between end-member compositions. Equally, it could be taken as evidence for mixing or mingling between two liquid components, thus supporting the notion of magma-magma, rather than magma-mush interaction. In contrast the homogeneity of the Siwi Ignimbrite could potentially reflect more complete mixing, while the presence of glomerocrysts supports the

remobilisation of a crystal mush.

Both scenarios require input of a volatile-rich, mafic magma to rejuvenate a body of more evolved, potentially partly-crystallised, magma residing beneath the volcano. Such a scenario can reconcile the two juxtaposed styles of activity within the Yenkahe Caldera, namely long periods of persistent, low-magnitude activity interspersed with rare, paroxysmal eruptions. Métrich et al. (2011) suggest that up to 25 km^3 of magma may have degassed without erupting over the last 1000 years of activity at Yasur. This volume of magma is likely stored beneath the volcano in some form of intrusive body, either as an evolved magma or a crystal mush. Reheating, through addition of fresh, hot, basaltic magma could potentially remobilise a portion of this intruded magma, as has been proposed for a range of volcanoes including Pinatubo (Pallister et al. 1992), Montserrat (Murphy et al. 2000) and Villarrica (Lohmar et al. 2012). Strontium and neodymium isotopes add some weight to this scenario, with juvenile material from the Siwi Ignimbrite producing a scattered array extending between the most recent Tanna basalt of Peate et al. (1997) and the Yasur and pre-caldera volcanics (Fig. 3.7b). The former may represent a recharge magma, while the latter represent either a resident magma or a crystal mush derived from it. Similar, bi-polar, persistent to quasi-persistent, low-magnitude eruptive behaviour is common within a number of other caldera systems, including Masaya (Rymer et al. 1998; Stix 2007), Sakurajima (Aramaki 1984) and Krakatau (Dahren et al. 2012).

Under both mixing scenarios, the end-member compositions are poorly constrained. Basaltic melt inclusions analysed by Métrich et al. (2011) potentially represent the replenishment magma involved with the Siwi Ignimbrite. Given the observation of Métrich et al. (2011) that the magmatic system on Tanna has been fed by parental magma with a relatively constant composition throughout the last ~2 Myr, it is conceivable that the recharge magma involved in the OTI Eruption was of a similar composition. Glass veins and globs in pumice of the OTI potentially represent the other end-member involved in mixing to produce the erupted composition. Simple binary mixing calculations using these compositions reproduce the whole rock composition of the OTI when ~38% trachy-andesite is mixed with ~62% basalt. Mixing calculations for the Siwi Ignimbrite are limited as the composition of the evolved end-member remains unknown. The trachy-andesite end-member implicated in the OTI eruption is less evolved than the composition of the Siwi magma, so cannot represent one of its constituents. Instead, a more-evolved end-member is required. A relatively evolved magma or mush that remained un-erupted and was derived from pre-Siwi magma by crystal fractionation is a viable

contender. Back-calculations from the Siwi Ignimbrite composition suggest <40% basalt was mixed with a trachytic magma, produced by ≥50% fractionation of a magma compositionally similar to that erupted from Yasur. Lithic clasts and pre-caldera volcanics suggest that such compositions are commonly erupted between major ignimbrite-producing events (Fig. 3.6), showing this is not unlikely. The exact composition of the evolved end-member involved with the Siwi magma influences the degree of mixing required, with a more evolved composition requiring greater addition of basalt and vice versa. These calculations show that mixing can viably explain the compositions of both ignimbrites, however, are inconclusive as to the degree of mixing and composition of end-member components. Nevertheless, these variables are responsible for the compositional differences between the two ignimbrites.

Mixing processes are commonly envisaged to prime a magma chamber for eruption by adding volatiles while also superheating the resident magma and inducing convection (Self and Sparks 1978). Melt inclusion studies by Métrich et al. (2011) suggest that the basaltic recharge magma involved in the Siwi eruption was rich in volatiles relative other magmas erupted from the Yenkahe System, having >1 wt.% H_2O, as well as elevated S and CO_2. Putirka (2008) reports a number of formulas by which the temperature of a magmatic glass might be estimated. These suggest a temperature >1100°C for the basaltic magma. Combined, these features speak for addition of a hot, volatile-rich magma. Convective overturn of the recharge and resident magmas, in addition to heating of the resident magma, promotes supersaturation of volatiles within the magma chamber (Sparks et al. 1977). In high viscosity silicic magmas this induces overpressure, causing explosive eruption. Vinkler et al. (2012) invoke bubble nucleation within the magma chamber to explain overpressure within less viscous mafic melts, such as Colli Albani. Under such a scenario, the extent of bubble growth is limited inducing catastrophic overpressure.

Disequilibria between minerals and their host magmas in both ignimbrites hampers the use of mineral barometers (e.g. Putirka 2008) in estimating the depth of magma storage. Nevertheless, MELTS modelling (Ghiorso and Sack 1995) raises the possibility that magma was stored at shallow depths (Fig. 3.6). A suite of models were run at different pressures to investigate the depth of potential differentiation to produce the Siwi Ignimbrite composition (Fig. 3.6). All models have the same starting composition, which is that of a basaltic melt inclusion analysed by Métrich et al. (2011) and interpreted as representative of a parental magma. Models assume initial H_2O = 2.1 wt.% and initial fO_2 was set at QFM (Métrich et

al. 2011). Even assuming the final composition is a product of mixing, the more evolved end-member is still likely derived from a shared parental magma through fractionation. On plots of MgO and CaO versus SiO_2 (Fig. 3.6a and b), the 0.6 kbar curve most closely simulates the Siwi Ignimbrite composition. The 1 kbar curve best explains Al_2O_3 and K_2O contents for the Siwi Ignimbrite (Fig. 3.6c and d). Overall, shallower (>1 kbar) differentiation is most readily reconciled with the composition of the Siwi magma.

Eruption magnitude and implications for hazard management

From a hazard perspective, the identification of two ignimbrites originating from the Yenkahe caldera is of great importance. It shows that the caldera is capable of repeated catastrophic eruptions. While the exact age of the Siwi Ignimbrite remains unknown, a repose period of 10-30 kyr is likely given the stratigraphic relationship of the two ignimbrites and the lack of Ra-disequilibrium observed in the Siwi Ignimbrite (Firth et al. in review). Furthermore, geochemical differences between both ignimbrites show that the magma composition does not seem to control the occurrence of catastrophic eruptions. Deposits of both ignimbrites are widespread across Tanna, maintaining significant thickness away from the caldera margin. This attests to the magnitude of their eruptions. Accurately estimating the exact magnitude of these eruption is difficult, as an unknown proportion of their products were deposited offshore. Allen (2005) estimates a preserved deposit volume of >1 km^3. Identification of deposits of Siwi Ignimbrite mantling the central plateau of Tanna and on its western flanks increases this value. The initial caldera volume offers some indication of the volume of erupted material. With limitations in estimating dome uplift and infilling by post-caldera tephra, the caldera volume was likely between 2.5 and 5 km^3, suggesting eruptions of VEI >5 (Newhall and Self 1982).

The Siwi eruption occurred prior to human settlement of Vanuatu (~2.5 ka). The mid-fifteenth century Kuwae eruption gives some indication of the societal disruptions caused by a similar eruption in the Vanuatu Arc (Monzier et al. 1994). Tanna is home to over a tenth of the population of Vanuatu, and any eruption there today would cause significant disruption to the country as a whole. Given the relative rarity of mafic Plinian eruptions, precursory activity remains poorly understood.

Given the island setting of the Yenkahe Caldera, tsunami generation during paroxysmal eruptions is another key threat to local populations, particularly on neighbouring islands. Tsunamis have the ability to cause significant death and destruction at great distances from the

volcano (Latter 1981) and have been generated during other Plinian, caldera-forming eruptions, at volcanoes including Santorini (McCoy and Heiken 2000b; Bruins et al. 2008), Krakatau (Carey et al. 2000; Self and Rampino 1981) and Aniakchak (Waythomas and Neal 1998). The most common cause for these tsunamis is pyroclastic flows rapidly entering the sea (Carey et al. 2000; Waythomas and Neal 1998). The Yenkahe caldera opens to the sea in the east and any displacement of the caldera floor could potentially generate tsunamis. Such a process has been implicated in tsunami generation during the Minoan eruption at Santorini (McCoy and Heiken 2000b). Lawrie (1898) record the occurrence of a 12 m high tsunami in Port Resolution following an earthquake in 1878 associated with uplift of the Yenkahe Resurgent Dome (Chen et al. 1995), highlighting the threat caused by such a hazard in this location.

CONCLUSIONS

Re-examination of the volcanic stratigraphy of the Yenkahe Caldera, on the island of Tanna, in Vanuatu, has shown that it is a composite feature, formed and modified by at least two catastrophic ignimbrite-producing eruptions within the last 43 kyr. While both eruptions emplaced extensive ignimbrite sheets, facies analysis shows that the eruptions followed different sequences. The older OTI records a long-lasting Plinian eruption sequence, followed by rapid caldera collapse that destroyed a pre-existing composite edifice. In contrast, the more recent Siwi eruption involved varying degrees of magmatic and phreatomagmatic phases. Both ignimbrites were erupted asymmetrically about the caldera, with deposits thickest to its north, indicating trapdoor-like collapse, forming directed pyroclastic surges and spatter fountains.

Between major ignimbrite eruptions a stable magmatic system prevailed, with activity similar to that seen at Yasur through the past 1-2 kyr producing scoria cone, tuff ring and spatter cone deposits. Lavas erupted during these episodes of activity have comparable compositions and all contain euhedral phenocrysts that are in equilibrium with their host magma. In contrast both ignimbrites, which have compositions dissimilar to that of intra-caldera lavas, erupted pyroclastic material that contains minerals displaying a range of disequilibrium textures. These suggest that a crystal mush or resident magma was remobilised by mafic recharge to produce the large volumes of magma required for such eruptions. This crystal mush component accumulated during thousands of years of low-magnitude, intra-caldera volcanism, in which significant volumes of magma degas without eruption. Previous studies (e.g. Métrich et al. 2011) confirm that such processes are occurring at Yasur today, potentially forming a new crystal mush body.

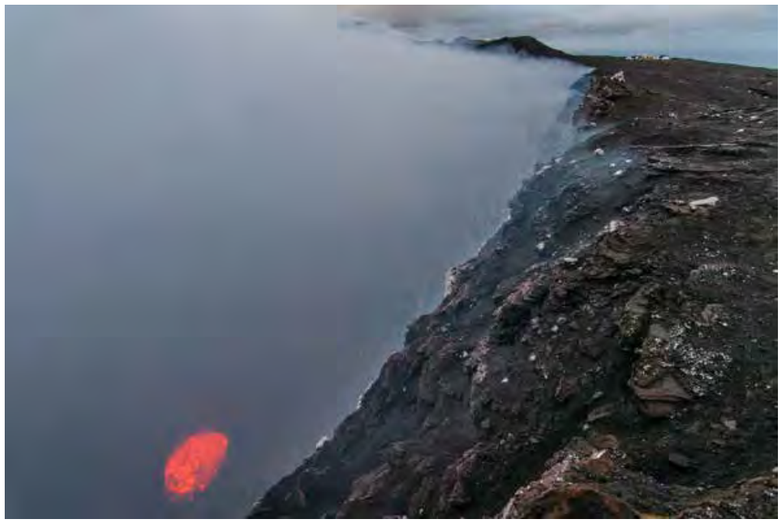

Marum’s lava lake appears through the gas plume

Theme 2:

Ambrym Volcano

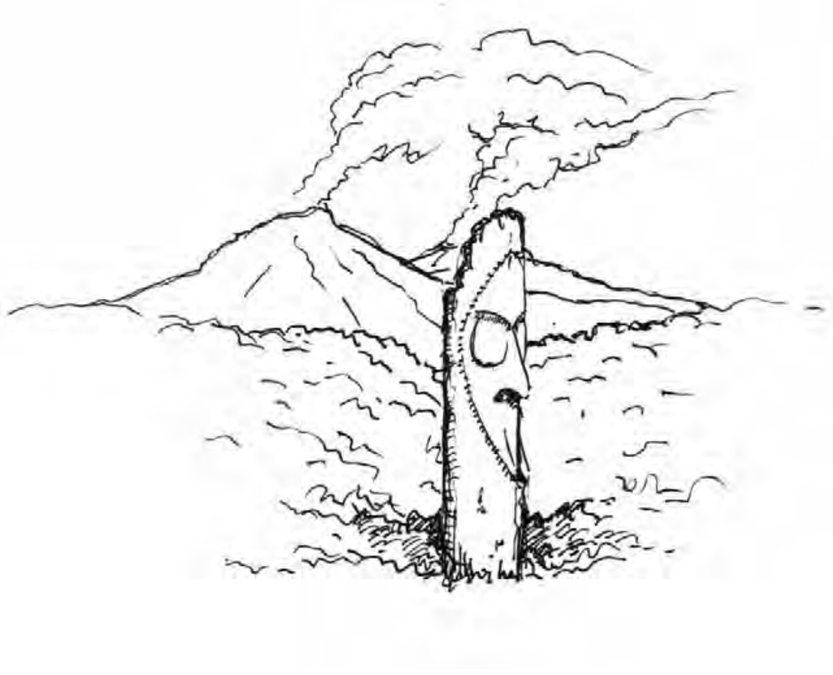

3. Variable conditions of magma storage and differentiation with links to eruption style at Ambrym Volcano, Vanuatu

Chris Firth[1*], Heather Handley[1], Simon Turner[1], Shane Cronin[2], Ian Smith[2]

[1] Department of Earth and Planetary Sciences, Macquarie University, Sydney, NSW 2109, Australia

[2] School of Environment, The University of Auckland, Private Bag 92019, Auckland

Ambrym, a basaltic volcano in the Vanuatu Arc, has displayed variable eruptive behaviour throughout the past century, with major eruptions occurring on both the volcano's flanks and at multiple vents within its caldera. These have been interspersed by periods of relative quiescence marked by extensive passive degassing at active, intra-caldera lava-lakes, which experience occasional Strombolian explosions. Volcanic rocks from all vents and eruptive styles display similar isotope and incompatible trace element compositions, suggesting all are derived from the same primary melt by fractional crystallisation. Major eruptions are commonly responsible for effusion of the least-evolved lavas examined (SiO_2 ~50 wt.%; MgO ~5 wt.%). While all are geochemically similar, petrological differences discriminate between lavas erupted during flank and intra-caldera eruptions. Phyric basalts with homogenous mineral compositions are common to flank eruptions, while crystal-rich basalts with variable mineral compositions, many not in equilibrium with their host liquid, are a feature of intra-caldera lavas. Lava lake samples are slightly more evolved than those from effusive eruptions (SiO_2 ~51-52 wt.%; MgO ~4 wt.%), as a result of additional crystallisation during periods of relative quiescence. The diverse petrology of the intra-caldera lavas can be explained by mixing of replenishment magmas similar to those erupted from the volcano's flanks with residual magma from lava lake activity. Flank eruptions exploit dykes that bypass the shallow reservoir involved with lava lake activity, limiting their interaction with this component.

Manuscript submitted to
Journal of Petrology

Submitted: 25th February 2015

Decision: Provisionally accepted with changes

Re-submitted 1st October 2015

INTRODUCTION

Eruptions at basaltic volcanoes exhibit a variety of styles ranging from quiet effusive eruptions, through Strombolian and Vulcanian blasts to occasional sub-Plinian and rare catastrophic Plinian events (Cashman and Sparks 2013). Furthermore, a single basaltic volcano will commonly exhibit a range of eruptive styles throughout its historical record. Examples include Mt Etna (e.g. Coltelli et al. 1998; Houghton et al. 2004; Branca and Del Carlo 2005; Polacci et al. 2006), Klyuchevskoy (Rose and Ramsey 2009), Llaima (Bouvet de Maisonneueve et al. 2013), Ambrym (Robin et al. 1993) and even Kilauea (Swanson et al. 2012; Sides et al. 2014). The presence of both summit and flank eruptions at a number of these volcanoes adds further complexity (e.g. Corsaro et al. 2007; Michon et al. 2015). Variations in eruptive style are a product of variable rates of magma ascent or volatile release, which are in turn influenced both by magma characteristics (e.g. viscosity, density, volatile and crystal content) and the geometry of the volcanic plumbing system (e.g. Jaupert and Vergniolle 1988; Woods and Koyaguchi 1994; Roggensack et al. 1997; Cashman 2004; Polacci et al. 2005; Edmonds 2008). For a full appreciation of the hazards posed by a volcano it is necessary to understand the relative contributions of these factors in determining the eruption style. This can be readily achieved using a forensic approach, piecing together evidence after the event using geochemical and petrological means (e.g. Blundy and Cashmann 2008). In this way, the influence of sub-surface processes, such as melting, differentiation, storage and ascent can be determined for a

particular eruption. Combining this knowledge with historical records and observations of the actual eruption produces a holistic view of the event, tracking magma from initial melting in the source region, through the crust to the eventual eruption and production of lava flows and pyroclastic deposits on the Earth's surface. Comparison between different events at the same volcano highlights the variety of magmatic processes occurring beneath it, which is crucial for hazard assessment and planning. The layout of the volcano's plumbing system can also be understood in this way, allowing better targeting of geophysical monitoring techniques. Here the products of eight historical eruptions from Ambrym, a basaltic volcano in Vanuatu, are examined and compared to elucidate the magmatic processes occurring at this volcano and their potential influence on eruptive activity.

BACKGROUND

Ambrym island lies at the centre of the Vanuatu volcanic arc. It measures ~30 x 45 km, with the long axis parallel to regional faults, which are oriented at ~N 105° (Fig. 4.1). At the centre of the island lies a roughly circular, 12 km-wide caldera, which may have formed as recently as 2 ka (McCall et al. 1969). The origin of the caldera remains contentious. Robin et al. (1993) linked caldera formation with a Plinian, phreatomagmatic eruption that also produced a giant tuff cone and dacitic ignimbrite. A competing theory proposes the caldera resulted from non-explosive subsidence such as that seen at other sub-aerial, mafic island volcanoes, such as Kilauea (McCall et al. 1969; Cronin and Németh 2005). McCall et al. (1969) suggested any pyroclastic deposits were of insufficient volume to explain the caldera and remarked on the lack of change in eruptive sequences from before and after caldera formation. Future work is needed to clarify the processes responsible for caldera formation on Ambrym.

Current, inter-caldera volcanism is centred around two active cones: Marum and Benbow (Fig. 4.1). Benbow is a simple cone, composed primarily of pyroclastic deposits with minor

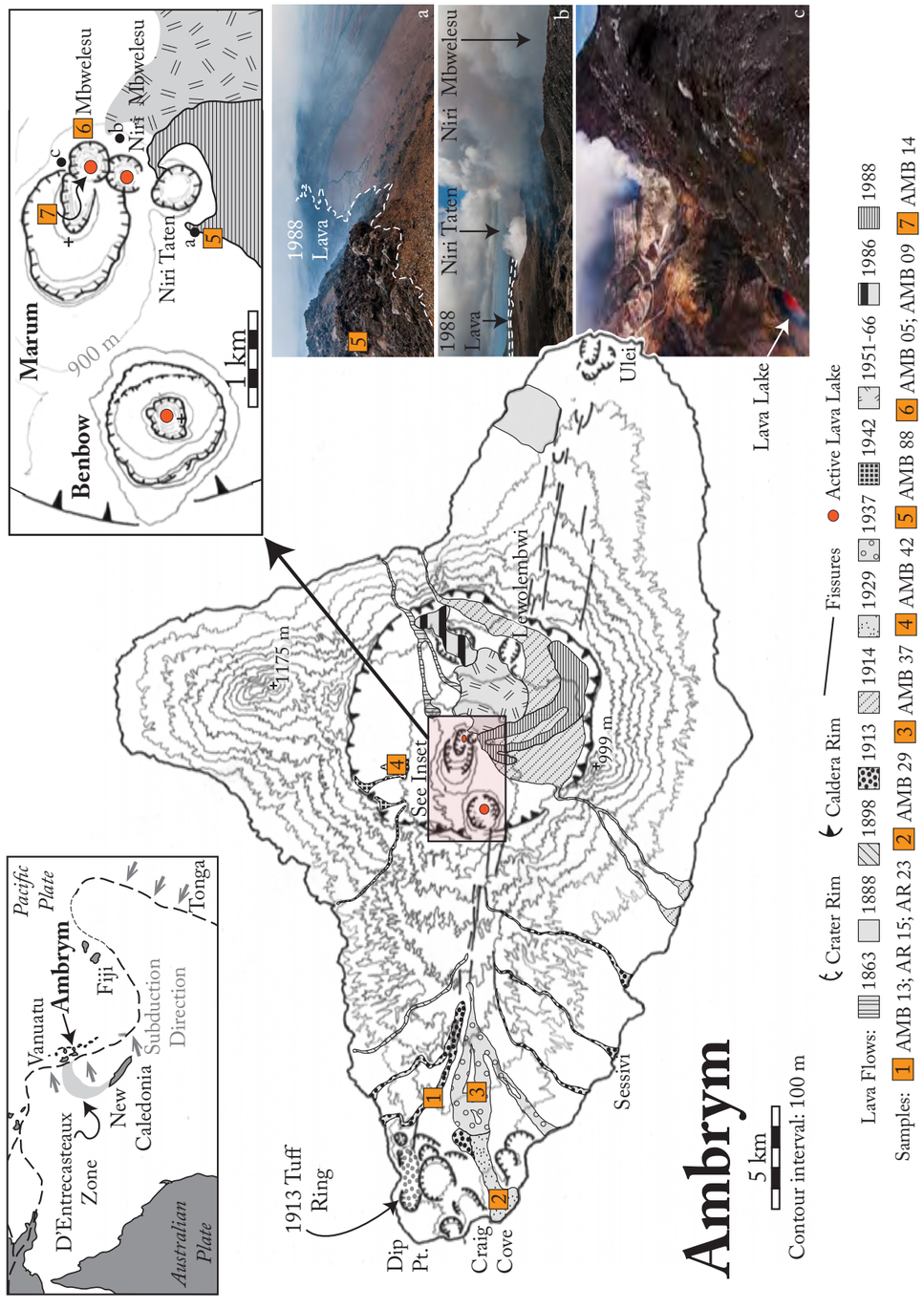

Fig. 4.1 Map of Ambrym volcano, showing location of historical lava flows (after Quantain 1978; Mozier and Charley 1989) and sampling locations. The upper left inset shows the location of Ambrym within the tectonic configuration of the south-west Pacific. Photographs showing (a) the 1988 lava flow (and the gas plume from Marum), (b) the caldera looking west from Marum, and (c) the interior of Marum vent with the lava lake and gas plume, are also present. Scoria samples from the 2005 and 2009 activity were collected ~100 m east of where photo (c) was taken. The locations where these images were taken are shown as black circles on the close-up map of Benbow and Marum (upper right).

lava flows, while Marum is more complex, with thick successions of phreatomagmatic tephra and scoriaceous ash and lapilli divided by sills, dykes, lava sheets and crystallised lava ponds (Fig. 4.1). Marum cone hosts two active vents, Mbwelesu and Niri Mbwelesu, while a third vent, Niri Taten, opened on its outer flanks during the 1988 eruption (Fig. 4.1). All three vents are deep (>200 m), steep-sided and commonly host active lava lakes (Németh and Cronin 2008). Monzier and Charley (1989) suggest that the morphology of Marum's vents changed considerably between 1943-1989, whilst Benbow remained almost unchanged throughout this time. Based on gas flux studies, Allard et al. (2015) suggest both vents are fed by a shared magma reservoir, however variations in CO_2 flux imply distinct processes of magma rise, gas segregation and eruption.

The earliest record of activity on Ambrym came from Captain James Cook in 1774, when he described twin plumes of 'smoke' rising from the volcano (Cook 1777). Violent flank eruptions that effected coastal settlement on the island were recorded throughout the late 19th and early 20th centuries (e.g. 1888, 1894, 1913, 1929 and 1937), however the eruptive record remained discontinuous throughout this period as few observations were made within the caldera (Carniel et al. 2003).

Eruptive products from Ambrym are typically basalts with tholeiitic affinities (Gorton 1977), however Robin et al. (1993) and Picard et al. (1995) present evidence for a bimodal magmatic suite, with a minor dacitic peak. A range of picritic compositions are also recorded by Picard et al. (1995), however these are restricted to the oldest lavas on the island. They propose that these are derived from a deeper melt source than the current volcanics. Both medium and high potassium differentiation trends have been identified in volcanic rocks from Ambrym, and these are explained by differences in the crystallising assemblage (Picard et al. 1995). Post-caldera basalts conform to a single differentiation trend that extends between medium and high potassium, while a limited number of more evolved samples led Picard et al (1995) to identify an additional high potassium differentiation trend. With the exception of a small volume of high-potassium andesite erupted in 1986, historical lavas have been basaltic in composition (Robin et al. 1993; Picard et al. 1995; Németh and Cronin 2011; Allard et al. 2015).

SAMPLE SELECTION

Historical eruptions at Ambrym conform to three distinct styles (Melchior 1988), including fissure-fed eruptions on the volcano's flanks, effusive intra-caldera eruptions and

lava lake activity. To investigate the influence of pre-eruptive magmatic processes on changes in eruption style thirteen samples of historical lava and tephra erupted from Ambrym during the last century were collected for analysis. These represent a variety of eruptions, with five samples from extra-caldera, fissure-fed lava flows (1913, 1929 and 1937 eruptions), two from intra-caldera lava flows (1942 and 1988 eruption) and six from lava lake activity (2005, 2009 and 2014). A brief summary of eruptive activity during which each of the samples analysed in this study was erupted is provided here.

Fissure-fed Flank Eruptions (1913, 1929 and 1937 Samples)

Fissure-fed flank eruptions are the highest magnitude eruptions witnessed at Ambrym. At least four major flank eruptions have occurred during historical times (1896, 1913, 1929 and 1937). All were remarkably similar, with sub-Plinian activity at Benbow cone preceding propagation of lava flows from a 19 km long fissure system on the western flank of the volcano (Purey-Cust 1896; Frater 1917; Gregory 1917; Paton 1937; Eissen et al. 1991). All four eruptions issued from fissures of the same orientation (Fig. 4.1), with lava flows from later eruptions commonly covering those from earlier eruptions (Paton 1937). Phreatomagmatic explosions occurred along the coast and offshore near Craig Cove and Dip Point during the 1913 and 1929 eruptions, as a result of fissures opening through water-saturated coastal soils or off-shore (Eissen et al. 1991; Németh and Cronin 2011). The 1913 eruption produced an elongated tuff ring during explosive phreatomagmatic activity that destroyed the hospital and missionary headquarters, killing 21 people (Gregory 1917; Mastin and Witter 2000; Németh and Cronin 2011). Figure 4.1 shows an abundance of similar tuff rings and craters where the fissure system converges on the western coast of the island, highlighting the importance of this type of activity at Ambrym. As this is also the most populous part of the island, this style of eruption is the most dangerous at Ambrym (Melchior 1988). The 1913 eruption was followed in early 1914 by intra-caldera lava effusion from Marum.

Five samples representing fissure-fed flank eruptions are included in this study. All are from lava flows in the western part of Ambrym Island (Fig. 4.1). Three samples are from the 1913 eruption, while one sample is included from each of the 1929 and 1937 eruptions.

Effusive, Intra-caldera Eruptions (1942 and 1988 Samples)

At least five lava flows were emplaced from intra-caldera eruptions during the twentieth

century (Monzier and Charley 1989), with an additional flow emplaced in February 2015 (B. Ambrose pers. comm.). All flows originated from the vicinity of Marum, with the exception of the 1986 lava, which was erupted from a vent in the east of the caldera (Fig. 4.1). The best documented of these eruptions occurred in 1988-89 (Monzier and Charley 1989). Activity during this eruption was focused on Marum, and included both effusive and explosive activity. Two lava flows escaped from the Niri Mbwelesu crater (Fig. 4.1) through pyroclastic deposits on its southern flanks. The first, erupted in August 1988, saw 10^6 m^3 of lava emitted over a 24 hour period. Monzier and Charley (1989) report that the Niri Mbwelesu crater contained a high-level lava lake that was not present immediately after this event, suggesting that the lake drained to produce the lava flow. The second lava flow (April 1989), which emerged from the same vent was more voluminous, partly covering its predecessor. The Niri Taten vent, on the southern flank of Marum, also opened during this eruption. Nemeth and Cronin (2008) suggest that this was associated with a phreatomagmaic or phreatic explosion.

The distribution of intra-caldera lava flows shown in in Fig. 4.1 suggests other intra-caldera eruptions followed similar patterns, with lava flows breaking out through the flanks of Marum. Occasionally these breached the caldera rim to reach the coast as narrow, topographically-confined lava flows. Samples of the 1942 and 1988 lavas are included in this study.

Lava Lake Activity (2005, 2009 and 2014 samples)

Activity is maintained during periods of relative quiescence, with one or more active lava lakes in both Marum and Benbow (Németh and Cronin 2008). These commonly experience mild, Strombolian eruptions that produce intra-caldera and occasionally extra-caldera ash fall. Passive degassing persists through these periods, at rates equalled in a worldwide context only by Etna (SO_2 flux = 5440 tons day^{-1}: Bani et al. 2012; Allard et al. 2015). This causes chronic health impacts downwind of the volcano (Allibone et al. 2012).

Six samples representing lava lake activity at Marum are included in this study. The 2014 sample is a freshly-erupted bomb collected from a terrace adjacent to the lava lake in Mbwelesu Crater. At the time a second lake was active in Niri Mbwelesu, while a lake was also active in Benbow. Gas flux measurements indicate degassing was at average levels at this time (Chapter 5).

The remainder of the samples are tephras collected from the rim of Marum. Of these, one sample represents activity in 2005, at a time when Ambrym was the highest point-source emitter of SO_2 on the planet. During this time SO_2 fluxes reached 33,000 tons day^{-1}, over five times greater than the average flux for this volcano (Bani et al. 2009; Bani et al. 2012). This episode of extreme degassing was accompanied by localised tephra fallout, which produced a ~50 cm thick lapilli fall bed on the crater rim, from which the sample was collected. Four freshly-erupted tephra samples were collected from the same location in 2009. Three are scoria, while the fourth is a reticulite. Gas fluxes were at average levels during this time (Bani et al. 2012) and a lava lake was present in Mbewlesu.

METHODS

Mineral Chemistry

Mineral chemistry was determined using electron microprobe analysis (EMPA) for six samples, chosen to represent each major eruption. Polished thin sections were analysed on a Cameca SX 100 EMP at the Geochemical Analysis Unit (GAU) at Macquarie University. Analyses were conducted using a focused 1 μm diameter electron beam, with an energy of 15 kV and a beam current of 20 nA. Accuracy and precision were estimated from replicate analyses of appropriate synthetic and natural standards: $CaSiO_3$ for Si, TiO_2 for Ti, kyanite for Al, VG-A99 for Fe, MgO for Mg, wollastonite for Ca, jadeite for Na and orthoclase for K. Glass compositions were determined for a number of samples using the same procedure, however a defocused 10 μm diameter beam was used to minimise Na loss.

Whole Rock Chemistry

Whole-rock major element compositions of all samples were determined by X-Ray Fluorescence Spectrometry (XRF), using the method of Norrish and Chappell (1977). Analyses were obtained using a Spectro XLAB 2000 polarising XRF spectrometer at the GAU. Accuracy and analytical precision were determined to be ~0.5% for major elements, based upon replicate analyses of USGS reference material BHVO-2 (values are presented in Table 4.3 for comparison). Two samples from the 1913 eruption (AR 15 and AR 23) were analysed using the same techniques on a Siemens SRS3000 XRF at Auckland University.

A full suite of trace elements was analysed on eight samples by solution ICP-MS. Samples were digested in an HF-HNO_3-HCl mixture, with H_3BO_4 used to neutralise HF. Once in solution, samples were analysed on an Agilent 7500 ICP-MS at the GAU. BHVO-2 was prepared and analysed as an unknown to assess accuracy (Table 4.3).

Sr and Nd isotopic ratios were analysed for a sub-set of five samples. Following dissolution, Sr and REE were separated by passing the solution through a cationic column, followed by removal of Sm and Nd on an HDEHP column. A ThermFinnigan Triton thermal ionisation mass spectrometer was used to analyse Sr and Nd isotopes at the GAU. Analyses were conducted on static mode, using single and double Re filaments for Sr and Nd respectively. Mass fractionation was corrected for by normalizing Sr to $^{86}Sr/^{88}Sr$ = 0.1194 and Nd to $^{146}Nd/^{144}Nd$ = 0.7219. Analyses of BHVO-2 are shown in Table 4.3.

PETROGRAPHY AND MINERAL CHEMISTRY

All historical lavas examined from Ambrym are vesicular, plagioclase glomeroporphyritic basalts and basaltic andesites. The exception is the 1988 lava, which is largely aphyric, with rare clinopyroxene phenocrysts. In the remainder of the samples, plagioclase is the dominant phenocryst phase, alongside rarer clinopyroxene, olivine and spinel (Table 4.1). Phenocrysts are typically surrounded by a microlitic groundmass, which is similarly dominated in all samples by plagioclase and spinel, with minor clinopyroxene and rare olivine. Groundmass ranges between the samples from glassy with occasional microlites to holocrystalline. All samples are vesicular.,

Fissure-fed Flank Eruptions (1913, 1929 and 1937 Samples)

Lavas erupted in during flank eruptions in 1913, 1929 and 1937 are vesicular, plagioclase- and clinopyroxene-phyric basalts. The phenocryst assemblage in all lavas is dominated by plagioclase (Table 4.1) which is present as euhedral crystals (~0.5 to 1 mm), often accumulated into glomerocrysts (Fig. 4.2a). Plagioclase rim compositions range from An_{77} to An_{85} (Table 4.2; Fig. 4.3). Plagioclase grains commonly lack optical zoning, and chemical variations between core and rim are not observed. Clinopyroxene ($Wo_{36-40}Fs_{14-23}En_{41-46}$; Table 4.2) is also found in all flank lavas (Table 4.1), both as a minor component of glomerocrysts, where it partially surrounds plagioclase crystals, and also as individual phenocrysts. Plagioclase and clinopyroxene compositions do not vary between glomerocrysts and phenocrysts. Olivine (Fo_{75-76}) is a rare phenocryst phase in these lavas (Table 4.1).

All flank lavas have a microlitic groundmass, with the exception of sample AR 15, from the 1913 eruption. Microlites in all samples are dominated by laths of plagioclase. Micron-size cubes of spinel and occasional clinopyroxene grains are also present (Table 4.1). The

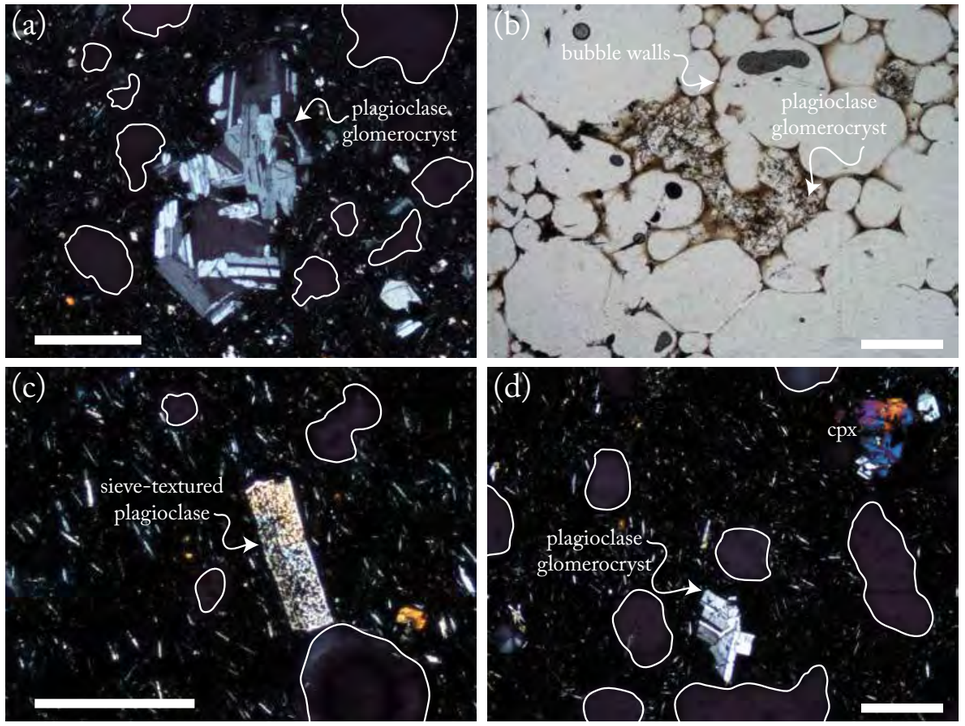

Fig 4.2 a) Plagioclase glomerocryst within the 1929 lava, shown in cross-polarised light. Over 20 individual crystals can be discerned within the glomerocrysts. Vesicles are outlined in white. Note the microlitic groundmass. b) Plagioclase glomerocrysts within scoria erupted in 2009, shown in plane-polarised light. Compare the thin bubble walls and high vesicle abundance with the other three images. c) Sieve-textured plagioclase phenocryst in the 1988 lava in cross-polarised light. Vesicles are outlined in white. d) Plagioclase glomerocrysts and clinopyroxene phenocryst within the 1988 lava. Note the higher microlite abundance and paucity of vesicles in the 1988 lava relative to the 1929 sample in image (a). Vesicles are outlined in white. The white scale bar represents 100 μm in all images.

groundmass in the 1913 lava is predominantly micron-sized, while the 1929 and 1937 lavas have larger microlites (up to100 μm). Vesicles vary in size from ~0.1 mm to >3 mm and are interconnected in some instances.

A number of small xenoliths are present in sample AR 23. These are ~ 1- 2 mm wide and consist of microlitic material, similar to the groundmass of other lavas from Ambrym. The microlites primarily consist of plagioclase and clinopyroxene. These most likely represent fragments of previously crystallised lava that was entrained at shallow depths, shortly before eruption.

Table 4.1. Percentage abundance of phenocrysts, groundmass, glass and vesicles in volcanic rocks from Ambrym

Eruption	Sample No.	Plagioclase Phenocryst	Plagioclase GM	Clinopyroxene Phenocryst	Clinopyroxene GM	Olivine	Spinel	Microlites + Glass	Microlite-free glass	Vesicles
1913	AMB 13	15	-	>1	-	1	>1	50	-	34
	AR 15	9	5	6	-	>1	>1	28	-	53
1929	AMB 37	18	27	2	2	>1	>1	13	-	38
1937	AMB 50	5	37	1	1	>1	>1	12	-	44
1942	AMB 42	8	73	3	3	-	>1	3	-	10
1988	AMB 88	1	69	4	13	>1	>1	8	-	5
2009	AMB 09	5	-	>1	-	-	>1	-	27	68
2014	AMB 14	10	-	>1	-	>1	>1	-	19	71

Table 4.2. Representative mineral major element analyses

	Eruption	Grain	SiO_2	TiO_2	Al_2O_3	FeO*	MnO	MgO	CaO	Na_2O	K_2O	Cr_2O_3	Total	An (Mol %)	Fs (Mol %)	Fo (Mol %)
Plagioclase	1913	P. Rim	49.63	0.02	29.89	1.13	n.d.	0.16	14.28	3.31	0.29	n.d.	98.71	69	-	-
		P. Rim	47.10	0.03	31.99	1.09	n.d.	0.13	16.65	1.90	0.15	n.d.	99.04	82	-	-
		P. Rim	46.49	0.02	32.37	1.10	0.02	0.12	16.81	1.95	0.16	n.d.	99.04	82	-	-
		P. Rim	47.04	0.03	32.33	1.10	0.01	0.14	16.33	2.33	0.15	0.01	99.47	79	-	-
	1929	P. Rim	46.97	0.04	32.04	1.01	n.d.	n.d.	17.10	1.76	0.13	n.d.	99.05	84	-	-
		P. Rim	48.78	n.d.	30.86	1.14	n.d.	0.04	15.67	2.41	0.21	0.09	99.21	77	-	-
		P. Rim	46.79	0.02	32.13	1.13	0.05	0.02	17.17	1.68	0.15	n.d.	99.14	84	-	-
	1937	P. Rim	47.44	0.04	32.32	1.06	0.02	0.10	16.39	2.31	0.16	n.d.	99.84	79	-	-
		P. Rim	47.40	n.d.	32.55	1.10	0.02	0.12	16.76	2.19	0.14	n.d.	100.27	80	-	-
		P. Rim	46.29	0.03	32.60	1.05	0.01	0.13	17.02	1.93	0.12	0.01	99.21	82	-	-
	1942	P. Rim	46.63	n.d.	32.44	0.91	n.d.	0.11	17.45	1.64	0.12	n.d.	99.30	85	-	-
		P. Rim	46.84	0.03	32.50	1.07	n.d.	0.10	17.21	1.82	0.12	n.d.	99.69	83	-	-
		Groundmass	53.24	0.06	27.87	1.45	n.d.	0.20	12.37	4.08	0.54	n.d.	99.81	61	-	-
		Groundmass	51.67	0.07	28.23	1.47	n.d.	0.22	13.08	3.88	0.44	n.d.	99.06	63	-	-
	1988	P. Rim	46.74	n.d.	32.02	0.93	0.01	0.12	16.96	1.75	0.11	0.02	98.66	84	-	-
		P. Rim	50.77	0.09	29.39	1.28	0.02	0.15	13.65	3.58	0.77	n.d.	99.70	65	-	-
		P. Core	53.86	0.04	28.38	0.62	0.00	0.05	10.90	5.37	0.52	n.d.	99.73	51	-	-
		Groundmass	55.19	0.12	26.09	1.61	0.01	0.16	10.03	5.01	1.05	0.00	99.26	49	-	-
		Groundmass	51.60	0.08	28.85	1.53	0.01	0.32	13.28	3.81	0.49	n.d.	99.95	64	-	-
	2009	P. Rim	50.07	0.02	29.56	1.16	0.00	0.07	14.49	2.98	0.31	0.00	98.66	72	-	-
		P. Core	51.10	0.04	28.79	1.09	0.00	0.08	13.72	3.32	0.38	0.00	98.53	68	-	-
		P. Rim	49.43	0.05	30.58	1.19	n.d.	0.05	15.53	2.56	0.25	n.d.	99.65	76	-	-
	2014	P.Rim	53.42	0.04	27.73	1.23	n.d.	0.19	12.25	4.09	0.56	n.d.	99.51	60	-	-
		P. Rim	50.62	0.03	29.88	1.19	n.d.	0.13	14.78	3.12	0.30	n.d.	100.05	71	-	-
Cpx.	1913	P. Rim	49.76	0.53	4.10	8.83	0.21	14.78	21.49	0.29	n.d.	0.02	100.01	-	15	-
		P. Rim	49.69	0.48	3.59	8.34	0.24	14.90	21.67	0.31	n.d.	0.03	99.25	-	14	-
		P. Rim	49.81	0.50	4.42	8.49	0.21	14.80	21.74	0.34	0.02	0.10	100.43	-	15	-
	1929	P. Rim	48.29	0.90	5.28	10.38	0.25	13.32	20.84	0.34	0.01	n.d.	99.62	-	19	-
		P. Rim	47.45	1.34	6.66	11.70	0.27	11.83	19.26	0.66	0.08	n.d.	99.26	-	23	-
	1937	P. Rim	49.53	0.55	4.19	8.91	0.21	14.72	21.15	0.37	n.d.	0.03	99.64	-	16	-
		P. Rim	49.02	0.54	3.86	8.45	0.21	14.50	21.35	0.31	0.01	n.d.	98.24	-	15	-
		P. Rim	49.45	0.54	3.94	8.68	0.21	14.65	21.21	0.36	0.01	0.03	99.08	-	15	-
	1942	P. Rim	49.95	0.60	3.90	8.71	0.23	14.35	21.54	0.30	n.d.	n.d.	99.58	-	15	-
		P. Rim	51.23	0.50	3.05	8.59	0.21	15.08	21.45	0.31	n.d.	n.d.	100.42	-	15	-

Table 4.2 (cont). Representative mineral major element analyses

	Eruption	Grain	SiO_2	TiO_2	Al_2O_3	FeO*	MnO	MgO	CaO	Na_2O	K_2O	Cr_2O_3	Total	An (Mol %)	Fs (Mol %)	Fo (Mol %)
		Groundmass	47.82	0.75	4.75	9.89	0.24	13.91	20.72	0.27	0.03	0.04	98.42	-	18	-
	1988	P. Rim	49.02	0.81	3.70	11.71	0.39	14.10	19.58	0.35	0.08	n.d.	99.73	-	20	-
		P. Rim	50.44	0.54	2.33	10.68	0.62	14.06	20.67	0.29	n.d.	0.02	99.65	-	18	-
		P. Rim	49.51	0.95	8.77	12.24	0.44	11.26	16.70	1.18	0.16	n.d.	101.21	-	28	-
		Groundmass	46.50	1.04	6.55	10.62	0.23	12.97	21.15	0.33	n.d.	0.03	99.42	-	20	-
		Groundmass	46.99	0.97	5.62	10.84	0.26	13.65	20.32	0.36	0.01	0.01	99.03	-	20	-
	2009	P. Rim	50.56	0.55	3.84	9.32	0.30	14.60	20.71	0.31	0.01	0.02	100.22	-	16	-
		P. Rim	50.26	0.44	3.39	8.18	0.22	14.88	21.58	0.27	n.d.	0.04	99.26	-	14	-
	2014	P. Rim	50.91	0.58	3.50	9.73	0.34	15.19	19.90	0.31	n.d.	n.d.	100.46	-	17	-
		P. Rim	51.34	0.48	3.76	8.69	0.27	14.74	21.16	0.34	n.d.	n.d.	100.78	-	15	-
Olivine	1913	P. Rim	38.56	0.01	0.04	22.45	0.48	39.29	0.33	n.d.	0.01	0.02	101.17	-	-	76
		P. Rim	38.25	n.d.	0.02	22.23	0.44	39.48	0.26	0.04	n.d.	n.d.	100.71	-	-	76
	1929	P. Rim	38.59	0.01	0.03	22.14	0.43	38.51	0.30	n.d.	0.01	n.d.	100.03	-	-	76
		P. Rim	37.42	0.05	0.12	27.00	0.56	34.44	0.37	0.05	0.04	n.d.	100.05	-	-	69
	1937	P. Rim	38.24	n.d.	0.04	22.13	0.42	39.41	0.29	0.01	0.01	0.02	100.55	-	-	76
	1988	P. Rim	35.95	0.02	0.00	33.00	1.02	29.96	0.21	0.01	n.d.	n.d.	100.18	-	-	62
		P. Rim	37.93	0.02	0.03	23.49	0.51	37.19	0.29	0.02	0.01	0.01	99.49	-	-	74
	2014	P. Rim	36.96	n.d.	n.d.	22.65	0.51	38.77	0.33	n.d.	n.d.	n.d.	99.22	-	-	75
		P. Rim	37.08	n.d.	n.d.	22.28	0.55	39.04	0.33	n.d.	n.d.	n.d.	99.28	-	-	76

n.d. - not detected

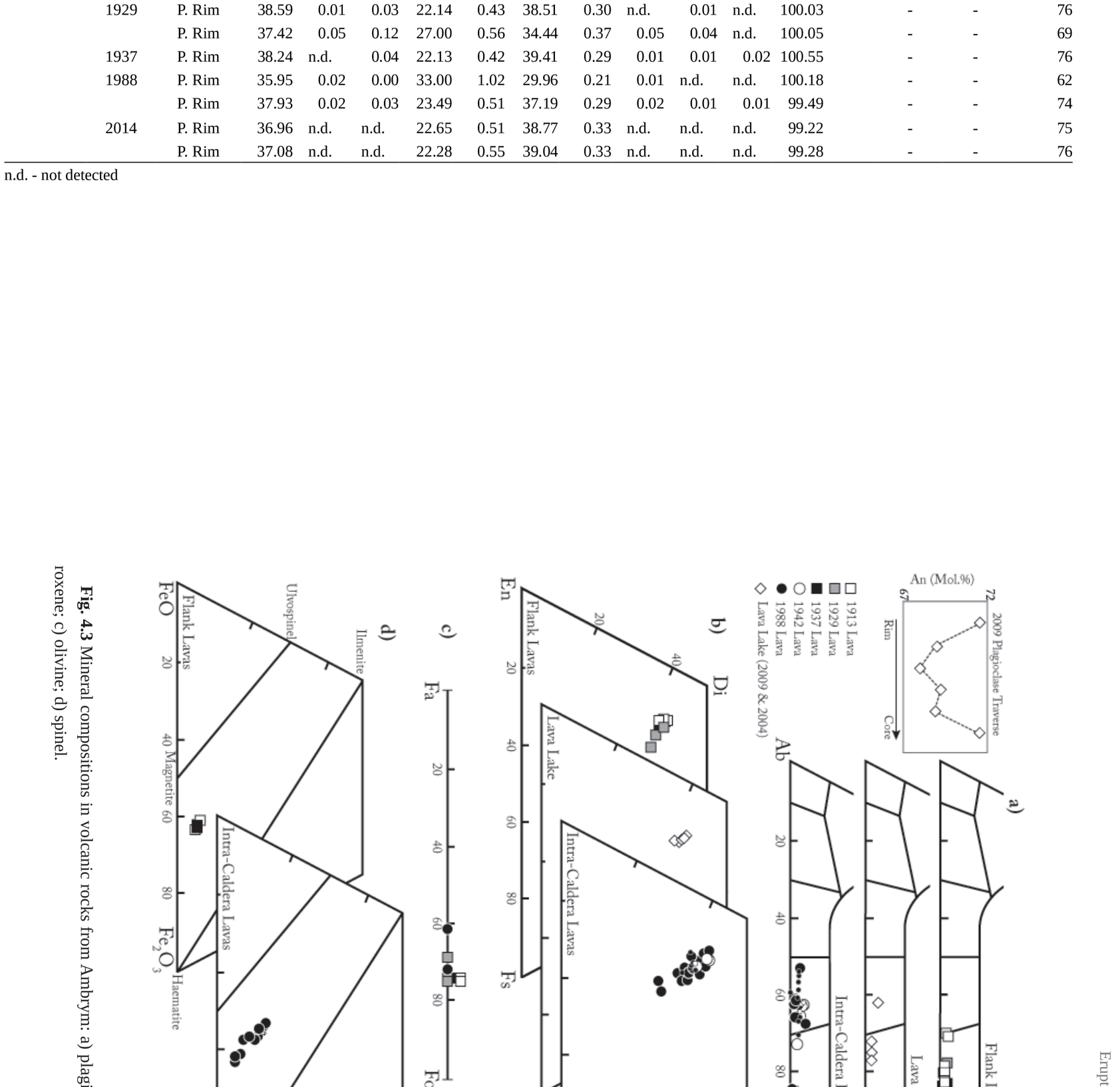

Fig. 4.3 Mineral compositions in volcanic rocks from Ambrym: a) plagioclase; b) clinopyroxene; c) olivine; d) spinel.

Effusive, Intra-caldera Eruptions (1942 and 1988 Samples)

The 1942 and 1988 lavas differ considerably from the remainder of samples analysed in this study, both in terms of petrography and mineral chemistry. While still vesicular, the vesicles are smaller and less abundant than in the other samples (Table 4.1). Phenocrysts too, are less abundant, and are less often accumulated into glomerocrysts. Both lavas are dominated by a holocrystalline groundmass, composed primarily of small, lath-like crystals of plagioclase and more minor clinopyroxene and micron-scale spinel grains (Table 4.1). Groundmass crystals are commonly larger than in other samples (50-500 µm) and account for a significantly greater proportion of the sample (Table 4.1).

In contrast with the other samples, clinopyroxene is the dominant phenocryst phase in the 1988 lava. Clinopyroxene compositions ($Wo_{33-40}Fs_{14-24}En_{41-46}$) are comparable with other samples, however display greater variation (Fig. 4.3). A number of the larger phenocrysts display concentrically-zoned overgrowth rims surrounding an un-zoned core. Where core and rim analyses were made, the cores consistently displayed higher Mg# (Table 4.2). Clinopyroxene is commonly observed to display an ophitic texture, partly surrounding plagioclase grains. Plagioclase is much less common as a phenocryst phase in both the 1942 and 1988 lavas compared with many of the other samples (Table 4.1). Plagioclase rim compositions vary widely (An_{48-85}; Table 4.2). Compositions similar to those seen in the flank lavas (An >75 mol.%) are rare and are restricted to the largest phenocrysts, which commonly display sieve textures, with large, rounded holes throughout the grain (Fig. 4.2c). Overgrowth rims are also found on some of these grains. These features are most apparent in grains in the 1988 lava, but can also be observed in the 1942 lava. The majority of plagioclase in both lavas consists of groundmass crystals <500 µm in length. These grains, which take the form of both small euhedral crystals and elongate laths, are noticeably less calcic (An <65 mol.%) than larger phenocrysts. In the 1942 lava the composition of groundmass plagioclase is restricted (An_{60-63}), however a wider range in composition is seen in the 1988 lava (An_{48-65}; Table 4.1). A number of the larger groundmass crystals display reverse zoning, with cores of An_{51} and rims of An_{65}. A single olivine phenocryst was identified in the 1988 lava. It has a noticeably less magnesian composition (Fo_{62}) than olivine in all other samples. The composition of spinel is also more diverse in this sample, with some grains displaying lower Fe^{3+} and higher Ti (Fig. 4.3d).

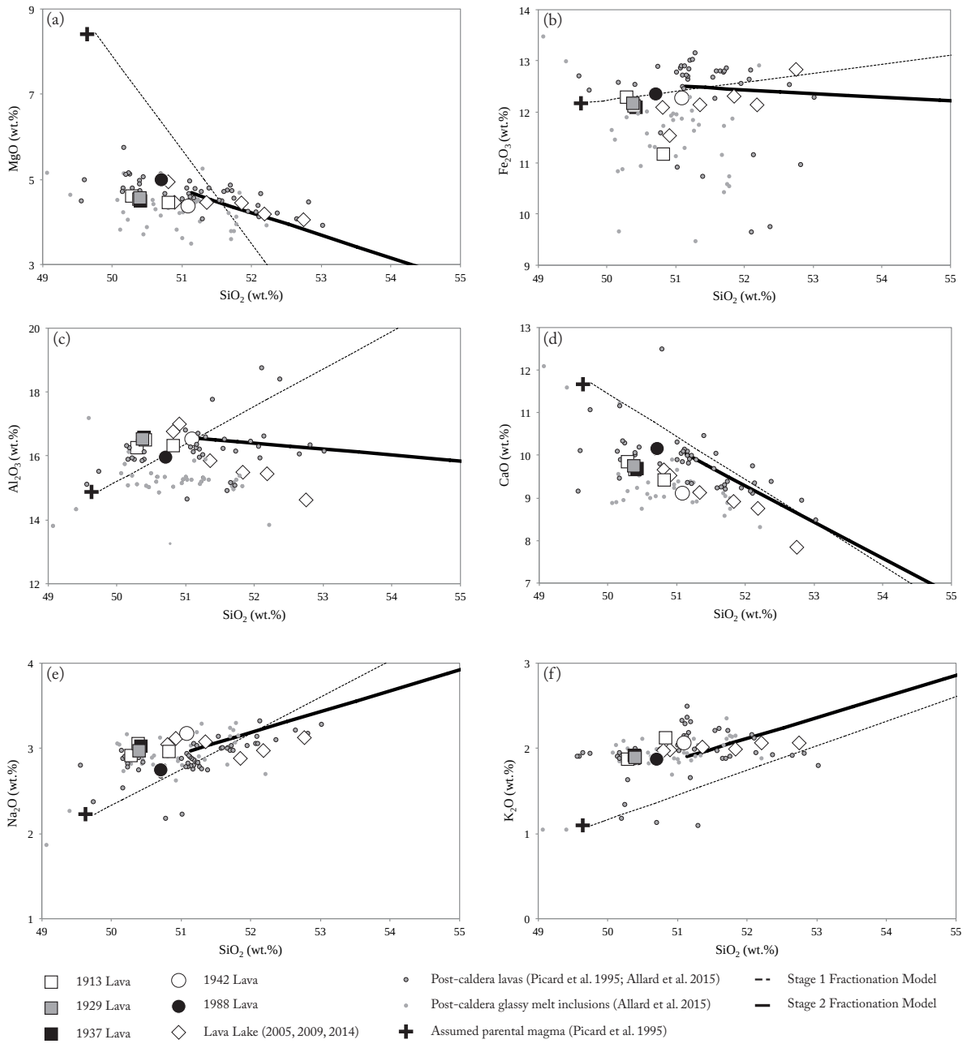

Fig. 4.4 Major element contents of Ambrym volcanic rocks plotted against SiO_2. Two predicted fractional crystallisation trends are also shown (see Table 4.7 for details). Errors are less than the size of the symbols.

Lava Lake Activity (2005, 2009 and 2014 samples)

The 2009 and 2014 samples differ from the remainder of the samples, having a glassy matrix (Fig. 4.2b) and larger vesicles. Both features are likely a consequence of the explosive, rather than effusive, eruption of these samples.

Plagioclase is the most abundant phenocryst phase (Table 4.1) and is present as large (>1 mm), euhedral grains, commonly accumulated into glomerocrysts. Plagioclase phenocrysts are less calcic (An_{60-75}) than those seen in the 1913, 1929 and 1937 lavas, and also display a

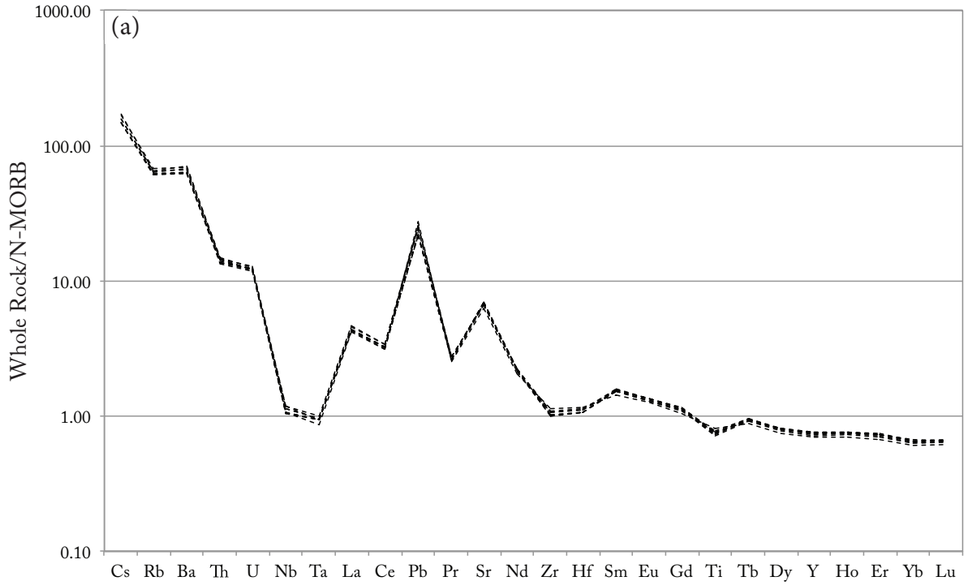

Fig. 4.5 a) N-MORB normalised trace element abundance diagram for historical volcanic rocks from Ambrym analysed in this study. Normalising values from Sun and McDonough (1989) b) Chondrite-normalised REE plot for historical volcanic rocks from Ambrym. Chondrite-normalising values from McDonough and Sun (1995).

Fig. 4.6 Trace element variation diagrams, showing the abundance of trace elements plotted against Zr (a-h) and Rb (i-j), with predicted fractional crystallisation trends also presented (Table 4.7). Errors are less than the size of the symbols.

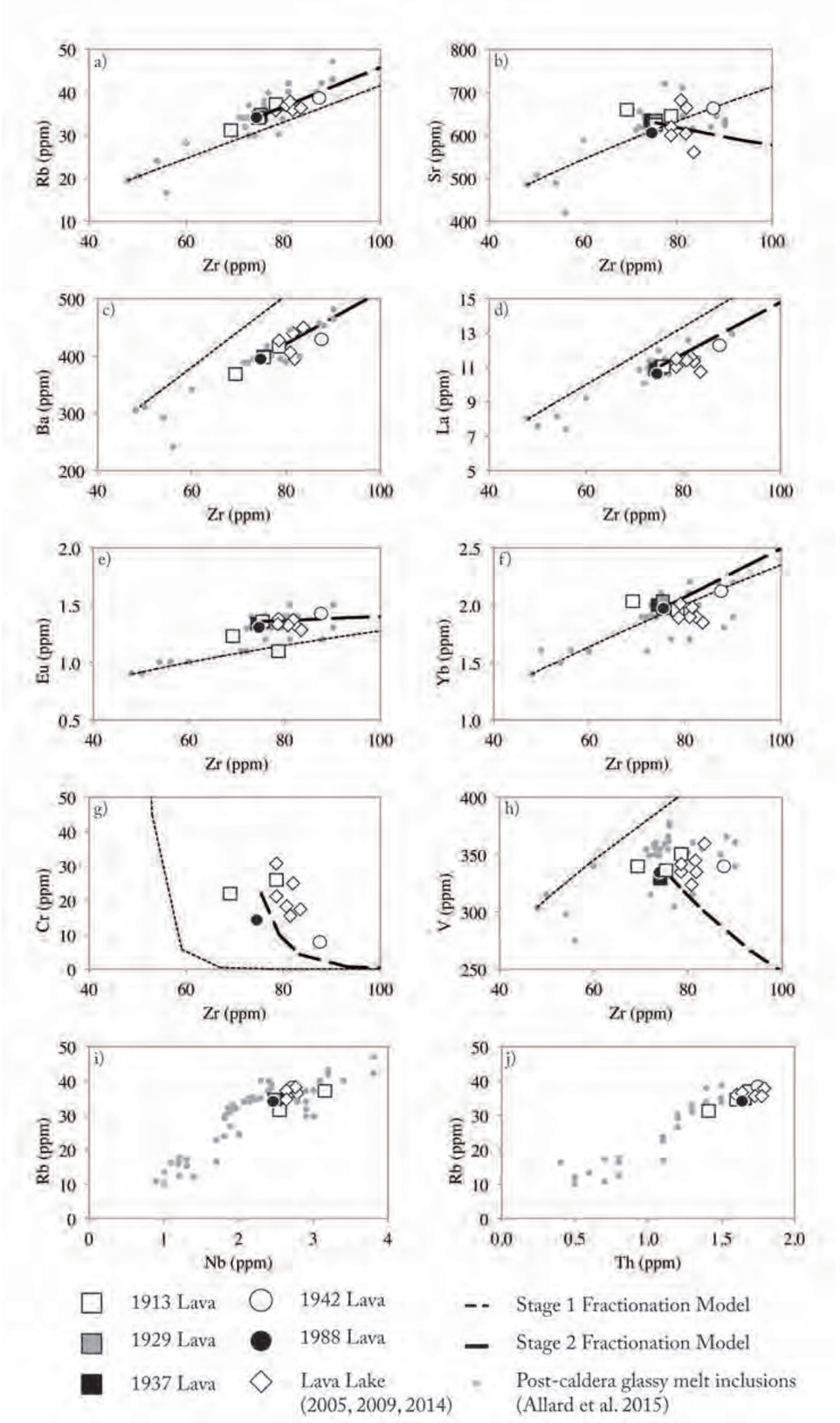

Table 4.3. Whole rock major and trace element and Sr and Nd isotope data for historical volcanic rocks from Ambrym

Sample	AMB 13	AR 15*	AR 23*	AMB 37	AMB 50	AMB 42	AMB 88
Eruption Year	1913	1913	1913	1929	1937	1942	1988
Eruption type	Flank	Flank	Flank	Flank	Flank	Intra-caldera	Intra-caldera
Rock type	Lava	Lava	Lava	Lava	Lava	Lava	Lava
Latitude	16°14’ 34.4’S			16°15’ 47.36”S	16°15’ 8”S	16°14’ 35.1”S	16°20’ 3.4”S
Longitude	167°58’ 48.4”E			167°55’ 25.62”E	167°59’ 1.6”E	168°8’ 13.6”E	168°7’ 22.0”E
SiO_2	50.40	50.29	50.82	50.41	50.38	51.08	50.71
TiO_2	0.93	0.94	0.96	0.94	0.95	0.95	0.92
Al_2O_3	16.50	16.28	16.34	16.60	16.54	16.52	15.94
Fe_2O_3	12.08	12.29	11.18	12.11	12.16	12.26	12.34
MnO	0.21	0.21	0.18	0.20	0.21	0.67	0.21
MgO	4.58	4.60	4.45	4.59	4.52	4.38	4.99
CaO	9.66	9.86	9.43	9.71	9.75	9.11	10.14
Na_2O	3.06	2.92	2.96	3.05	2.98	3.17	2.74
K_2O	1.88	1.87	2.12	1.88	1.90	2.07	1.87
P_2O_5	0.35	0.32	0.37	0.35	0.34	0.35	0.32
Total	99.65	99.58	98.82	99.84	99.73	100.55	100.18
Li	9.21	-	-	8.68	8.94	9.17	8.76
Be	1.00	-	-	0.98	0.96	1.04	0.94
Sc	30.13	31.36	28.67	29.92	29.27	28.18	34.36
Ti	5715.26	-	-	5676.50	5541.40	5828.82	5489.95
V	335.22	339.46	350.46	333.52	328.75	340.10	327.99
Cr	10.67	21.99	26.15	11.57	10.70	7.97	14.36
Mn	1604.89	-	-	1607.45	1574.49	1685.41	1590.12
Co	37.75	51.53	43.78	37.73	39.91	35.87	38.93
Ni	24.53	27.57	30.48	23.92	23.48	17.69	29.09
Cu	224.46	-	-	217.00	232.70	156.86	168.44
Zn	94.08	-	-	94.20	94.53	100.16	91.36
Ga	17.42	-	-	17.48	17.36	18.22	17.19
Rb	34.46	31.48	37.05	34.69	34.65	38.75	34.11
Sr	628.85	658.70	643.69	633.73	633.35	664.05	605.71
Y	21.13	18.35	17.31	21.26	20.84	23.36	20.62
Zr	75.39	69.17	78.53	75.36	74.28	87.55	74.62
Nb	2.50	2.56	3.16	2.48	2.45	2.72	2.47
Mo	1.20	-	-	1.20	1.16	1.22	1.20
Cd	0.06	-	-	0.06	0.05	0.09	0.06

Table 4.3. Whole rock major and trace element and Sr and Nd isotope data for historical volcanic rocks from Ambrym

AMB 05	AMB 09 I	AMB 09 II	AMB 09 III	AMB 09 IV	AMB 14	BHVO-2
2005	2009	2009	2009	2009	2014	
Lava lake	Lava lake	Lava lake	Lava lake	Lava lake	Lava lake	
Tephra	Scoria	Scoria	Scoria	Reticulite	Bomb	Standard
16°15’ 7.4”S	16°15’ 7”S	16°15’ 7”S	16°15’ 7”S	16°15’ 7”S	16°15’ 0.37”S	
168°8’ 17.6”E	168°8’ 1”E	168°8’ 1”E	168°8’ 1”E	168°8’ 1”E	168°7’ 57.68”E	
50.81	52.19	51.84	51.35	52.75	50.91	50.31
0.95	1.03	1.00	0.98	1.06	0.92	2.80
16.76	15.43	15.48	15.86	14.61	16.99	13.88
12.08	12.14	12.31	12.15	12.83	11.54	12.38
0.63	0.20	0.20	0.20	0.18	0.61	0.52
4.93	4.18	4.43	4.47	4.03	4.43	7.42
9.65	8.74	8.90	9.13	7.85	9.51	11.62
3.04	2.97	2.88	3.08	3.12	3.11	2.34
1.97	2.07	1.98	2.01	2.05	1.99	0.53
0.34	0.37	0.36	0.36	0.38	0.34	0.28
101.17	99.32	99.38	99.59	98.86	100.34	102.07
8.94	9.11	8.97	9.21	8.76	9.06	5.00
0.99	1.02	0.98	1.05	0.97	1.00	1.00
28.59	28.55	28.44	27.77	27.76	25.75	33.80
5601.73	5959.67	5801.17	5742.51	6179.30	5473.75	16561.00
335.47	342.60	342.53	334.75	359.06	323.05	320.91
24.83	15.86	30.33	20.83	17.26	18.14	277.60
1583.25	1520.72	1507.82	1555.32	1419.93	1527.45	1311.00
36.50	33.59	34.66	34.92	31.65	33.47	45.84
32.71	25.66	29.91	29.04	23.41	28.25	128.42
179.14	221.99	227.25	236.34	217.87	179.96	151.61
92.25	94.70	90.73	93.28	89.08	90.34	105.95
17.77	17.78	17.87	17.20	18.91	17.46	21.00
36.01	37.68	35.55	36.49	36.35	36.71	9.08
662.74	600.51	600.92	617.97	560.43	681.90	399.33
21.44	20.80	20.23	21.03	19.61	21.04	28.74
81.83	81.45	78.59	78.66	83.45	80.72	183.72
2.67	2.75	2.62	2.64	2.78	2.61	18.60
1.13	1.46	1.41	1.34	1.66	1.15	9.22
0.07	0.09	0.07	0.06	0.09	0.07	0.09

Table 4.3 (cont) Whole rock major and trace element and Sr and Nd isotope data for historical volcanic rocks from Ambrym

Sample	AMB 13	AR 15*	AR 23*	AMB 37	AMB 50	AMB 42	AMB 88
Eruption Year	1913	1913	1913	1929	1937	1942	1988
Cs	1.05	0.59	0.82	1.05	1.03	1.09	1.03
Ba	399.60	368.49	414.28	401.27	393.66	430.30	394.81
La	11.06	-	-	10.99	10.84	12.33	10.60
Ce	24.61	-	-	24.54	24.29	25.96	23.65
Pr	3.52	3.18	3.30	3.52	3.49	3.69	3.39
Nd	15.96	15.25	16.41	16.14	15.84	16.74	15.54
Sm	4.10	3.76	3.55	4.12	4.05	4.34	4.02
Eu	1.36	1.22	1.10	1.36	1.34	1.44	1.32
Tb	0.63	0.61	0.46	0.64	0.63	0.67	0.62
Gd	4.21	3.68	4.04	4.22	4.13	4.40	4.09
Dy	3.68	3.46	3.50	3.71	3.68	3.86	3.58
Ho	0.77	0.70	0.66	0.78	0.76	0.82	0.75
Er	2.15	2.07	1.79	2.18	2.18	2.32	2.11
Tm	1.18	0.30	0.30	1.20	1.19		1.17
Yb	1.97	2.04	1.96	2.04	2.00	2.12	1.94
Lu	0.30	0.30	0.31	0.30	0.30	0.32	0.29
Hf	2.18	2.25	2.14	2.19	2.17	2.36	2.20
Ta	0.12	0.20	0.21	0.12	0.12	0.16	0.11
Pb	6.54	12.20	9.29	6.67	6.53	7.74	6.51
Th	1.61	1.42	1.69	1.66	1.63	1.75	1.64
U	0.56	0.49	0.55	0.58	0.57	0.60	0.57
La/Yb	5.62	-	-	5.39	5.42	5.80	5.47
Rb/Th	21.44	22.21	21.91	20.88	21.20	22.14	20.74
Nb/Th	1.55	1.80	1.87	1.49	1.50	1.55	1.50
$^{87}Sr/^{86}Sr$	0.70437	0.704369	0.704433	0.70438	0.70433	-	0.70432
±	6.72E-6	3.40E-6	3.60E-6	9.08E-6	5.59E-6		5.53E-6
$^{143}Nd/^{144}Nd$	0.512905	0.512896	0.512893	0.512902	0.512901	-	0.512904
±	7.24E-6	4.20E-6	2.90E-6	8.13E-6	2.81E-6		3.09E-6

* Samples AR 15 and AR 23 were analysed at Auckland University - see methods in text.

marginally wider compositional range (Fig. 4.3a). Those in the 2014 lava bomb (An_{60-71}) display less calcic compositions than in the 2009 scoria (An_{74-76}). Some plagioclase phenocrysts in the 2009 samples display oscillatory zoning. This is accompanied by fluctuations in mineral chemistry of An_{68-72} (Fig. 4.3). Pyroxene and olivine phenocrysts are visually and compositionally similar to those from the 1913, 1929 and 1937 lavas, as are Fe-Ti oxides. The glassy matrix

Table 4.3 (cont)**.** Whole rock major and trace element and Sr and Nd isotope data for historical volcanic rocks from Ambrym

AMB 05	AMB 09 I	AMB 09 II	AMB 09 III	AMB 09 IV	AMB 14	BHVO-2
2005	2009	2009	2009	2009	2014	
1.01	1.18	1.10	1.10	1.19	1.03	0.10
396.19	437.33	424.50	421.70	448.89	403.48	132.00
11.39	11.56	11.03	11.44	10.72	11.44	16.05
24.19	25.42	24.15	25.75	23.58	24.56	39.21
3.42	3.61	3.45	3.61	3.32	3.43	5.45
15.40	16.30	15.73	16.42	15.12	15.43	26.06
3.99	4.10	3.98	4.17	3.79	3.96	6.57
1.33	1.37	1.32	1.37	1.28	1.33	2.11
0.61	0.64	0.61	0.63	0.59	0.61	0.96
4.05	4.19	4.02	4.26	3.84	4.03	6.29
3.53	3.64	3.53	3.73	3.39	3.50	5.25
0.74	0.76	0.74	0.78	0.71	0.74	1.01
2.08	2.16	2.08	2.21	1.99	2.08	2.59
	1.19	1.15	1.21	1.10		
1.90	1.98	1.92	2.00	1.86	1.90	2.09
0.29	0.30	0.29	0.30	0.28	0.29	0.28
2.14	2.34	2.27	2.29	2.39	2.18	4.58
0.16	0.13	0.13	0.13	0.12	0.16	1.14
7.03	7.75	7.52	7.30	8.23	7.20	3.00
1.61	1.78	1.73	1.76	1.76	1.64	1.33
0.56	0.60	0.57	0.61	0.57	0.57	0.43
6.01	5.83	5.73	5.71	5.78	6.04	
22.35	21.17	20.59	20.74	20.63	22.35	
1.66	1.54	1.52	1.50	1.58	1.59	
-	0.70437	-	-	-	-	0.70348
	3.31E-6					1.00E-6
-	0.512902	-	-	-	-	0.51298
	1.30E-6					4.82E-6

of both 2009 and 2014 samples is similar and almost identical to the whole-rock composition.

WHOLE-ROCK CHEMISTRY

Historically erupted lavas from Ambrym display a relatively restricted range in composition. All samples belong to the high potassium trend identified by Picard et al. (1995) and plot about the junction of the basalt, trachy-basalt and basaltic andesite fields on a total-

alkali silica (TAS) plot (not shown), having 50-53 wt.% SiO_2. Lava flows erupted during major flank and intra-caldera eruptions have the least evolved compositions, while the most evolved samples represent lava lake activity. The most evolved magma examined in this study (SiO_2 = 52.75 wt.%; AMB 09 IV) is a reticulite erupted during mild Strombolian activity in 2009 (Table 4.3). Major element variation diagrams (Fig. 4.4) show that CaO, MgO and Al_2O_3 decrease with increasing SiO_2, while Fe_2O_3, Na_2O and K_2O display sub-horizontal to slightly positive arrays. These diagrams also highlight that lavas erupted during the 1988 eruption have higher CaO, MgO and FeO and lower Al_2O_3 and Na_2O for a given SiO_2 value than lavas erupted during flank eruptions.

Normal mid-ocean ridge basalt (N-MORB) normalised trace element patterns for volcanic rocks from Ambrym are all parallel and conform with patterns previously determined for volcanoes in the centre of the Vanuatu Arc (Fig. 4.5a). Large ion lithophile elements (LILE) along with U, Th and Pb are highly enriched relative to N-MORB and produce positive arrays when plotted against an index of differentiation, such as SiO_2 or Zr (Fig. 4.6). Strontium is similarly enriched, however it displays a negative array when plotted against Zr (Fig. 4.6c). Pronounced positive linear arrays are also observed on co-variance plots for incompatible trace elements, such as Rb vs. Nb or Rb vs. Th (Fig. 4.6i and j). The light rare earth elements (REE) are enriched relative to the heavy REE. Chondrite-normalised REE patterns for Ambrym are unusual amongst high-K, calc-alkaline arc rocks, with a higher abundance of middle REE, producing a sigmoidal pattern (Fig. 4.5b). Rare earth elements, such as Eu and Yb display roughly horizontal arrays when plotted against Zr (Fig. 4.6g and h).

Strontium and neodymium isotope ratios for historical volcanic rocks from Ambrym are consistent with previously measured ratios for Ambrym (Peate et al. 1997; Turner et al. 1999) (Fig. 4.7). $^{87}Sr/^{86}Sr$ varies between 0.70432 and 0.70443, while $^{143}Nd/^{144}Nd$ ranges from 0.51289 to 0.51290 (Fig. 4.7a). Previous investigations (Briqueu et al. 1994; Crawford et al. 1995; Peate et al. 1997) have identified noticeable along-arc trends in Sr and Nd isotope ratios. The values presented here conform to these trends (Fig. 4.7b), showing Ambrym displays the highest $^{87}Sr/^{86}Sr$ found in the Vanuatu Arc. No noticeable correlation between Sr and Nd isotopes and indices of differentiation, such as SiO_2, are observed (Fig. 4.7c and d).

GLASS COMPOSITION

Matrix glass compositions were determined by EMP for two lava lake samples (from

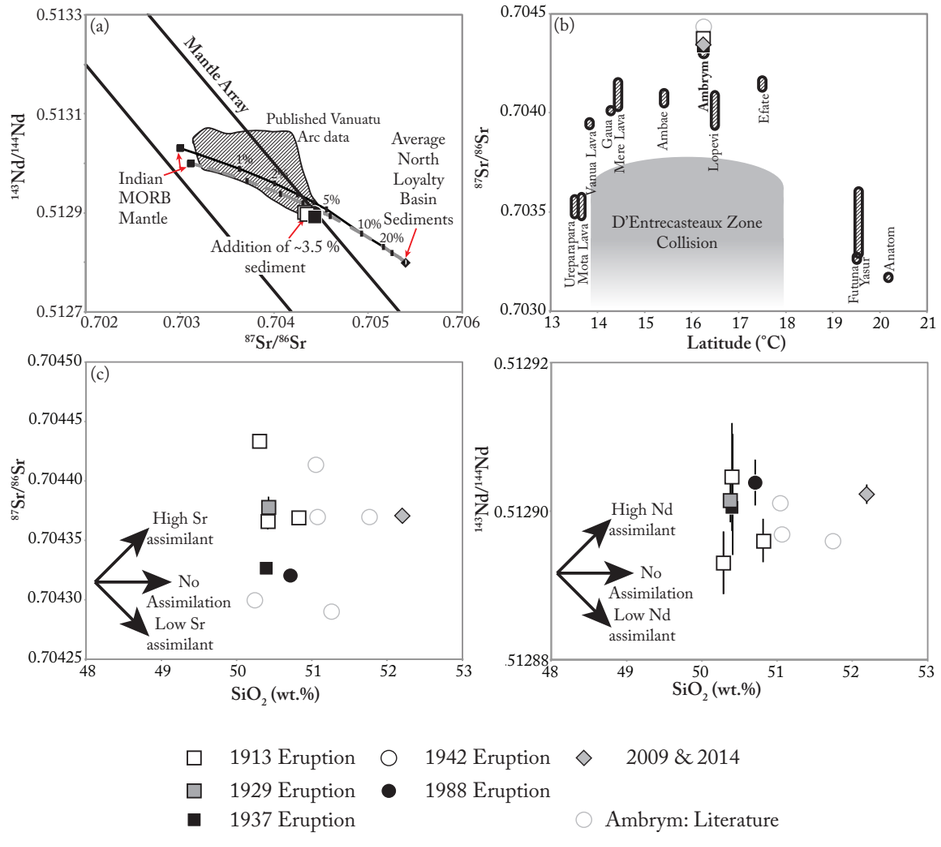

Fig. 4.7 a) Sr and Nd isotopic ratios for historical volcanic rocks from Ambrym. Two end-member bulk mixing curves show varying addition of sediment to a MORB source similar to that beneath Ambrym. I-MORB and basin sediment compositions are from White et al. (1987) and Peate et al. (1997). Previously published data from Peate et al. (1997); Turner et al. (1999); Handley et al. (2008), Beaumais et al. (2008). b) Variation in Sr isotopes with latitude along the Vanuatu Arc. Sr isotopes are highest adjacent to the D'Entrecasteaux Collision Zone, with Ambrym displaying the highest isotope ratios witnessed in the arc. c) Sr isotopes vs. SiO_2 for Ambrym lavas. Various potential assimilation trends are shown. Previously published data from Turner et al. (1999). Compare with similar plot for Lopevi in Handley et al. (2008) to see influence of crustal assimilation. d) Nd isotopes vs. SiO_2 for Ambrym lavas.

2009 and 2014). Both contain basaltic to basaltic-trachy-andesitic glass, comparable with the whole rock composition (Table 4.4; Fig. 4.6). SiO_2 ranges between 51.23-53.02 wt.%.

Accurate glass compositions could not be obtained for the remainder of the samples, as a result of their high microlite abundances. Nevertheless, glass compositions are estimated for these samples using mass balance equations. These rely upon the whole rock compositions (Table 4.3), mineral compositions (Table 4.1) and modal proportions (Table 4.2). Estimates for

Table 4.4 Analysed and estimated glass compositions of historically erupted samples from Ambrym

	SiO_2	TiO_2	Al_2O_3	FeO	MnO	MgO	CaO	Na_2O	K_2O
Analysed									
AMB 09*	51.41	1.15	14.03	11.71	0.22	4.45	8.45	2.99	2.41
AMB 14#	52.63	1.18	14.29	12.25	0.26	4.61	8.59	3.11	2.40
Estimated									
AMB 13	58.38	0.75	15.26	4.21	0.25	4.31	9.21	3.68	2.84
AR 15	53.44	1.41	13.32	15.28	0.30	2.68	5.05	3.82	3.32
AMB 37	52.83	1.33	10.04	14.69	0.32	6.45	7.23	3.12	3.08
AMB 50	59.42	1.17	9.48	7.66	0.37	5.94	7.29	3.34	3.92
AMB 42	62.58	0.21	8.51	6.44	1.38	6.91	6.26	3.84	4.32
AMB 88	60.95	0.37	7.49	10.36	0.33	7.58	5.46	2.80	4.27
AMB 09	52.72	1.22	12.74	14.14	0.23	4.74	7.48	3.05	2.42
AMB 14	52.27	1.39	9.48	17.01	0.93	6.41	5.92	3.62	2.95

* n=2

n=4

both the 2009 and 2014 samples compare favourably with measured glass compositions (Table 4.4). Estimates of matrix glass composition for the 1929 lava and one of the 1913 lavas (AR 15) are also similar to that of the analysed lava lake samples. The other 1913 lava (AMB 13) and the 1937 lava both return significantly more evolved glass estimates, with 58.4-59.4 wt.% SiO_2. Trachy-andesitic to trachytic glass compositions are estimated for the intra-caldera lavas (Table 4.4).

THERMOBAROMETRY

A range of methods to estimate the pressure and temperature of mineral crystallisation have been developed to accommodate different phase assemblages (see Putirka 2008 for a review). Methods involving clinopyroxene and plagioclase compositions are used here. Calculations for both minerals use mineral-melt pairs, as this minimises the possibility of erroneous results due to the presence of xenocrysts or zoned crystals, which are not in equilibrium with the melt. Analysed glass compositions from the lava lake samples are used as the liquid component for both plagioclase and clinopyroxene calculations. Estimated glass compositions are explored as an alternative melt component when analysed glass is shown to be out of equilibrium with the minerals. All calculations assume an H_2O content for the melt component of 1.2 wt.%, based upon melt inclusions from scoria erupted in the 1913 eruption (Allard et al. 2015).

Allard et al. (2015) show that water content varies little, with H_2O only exsolving from the melt at shallow levels (<50 MPa). Reduction of the melt water content by 1 wt.% induces a shift in clinopyroxene-based pressure and temperature estimates of ~60 MPa and 15°C, forcing estimates to shallower pressures and lower temperatures. The change in estimates remain within the SEE of the original calculations.

The plagioclase-melt thermometer (equation 24a: Putirka 2008) returns temperature estimates with an error of ±36°C. Mineral-melt equilibrium can be determined using the ratio of the partitioning coefficients of anorthite and albite, K_D $(An\text{-}Ab)^{pl\text{-}liq}$, which should equal 0.27±0.11, for temperature estimates >1050°C (Putirka 2008). The plagioclase-melt thermometer is sensitive to the input liquid composition, so calculations were run using five different liquid components, which represent different degrees of magmatic differentiation. The most evolved was the analysed glass composition of the 2014 lava lake sample. Three different melt inclusion compositions analysed from the 1913 eruption (Allard et al. 2015) were also used, as was a primitive melt inclusion from an undated scoria clast collected from the flanks of Benbow (Allard et al. 2015). The liquid component returning a K_D value closest to 0.27 was chosen for each plagioclase grain (Table 4.5). Plagioclase crystallisation temperatures range from 1080-1141°C. Temperatures below 1113°C are restricted to the intra-caldera lavas, with the exception of one grain from the 2014 lava lake sample. These estimates require more evolved melt compositions. Higher anorthite plagioclase ($An_{>74}$) requires the most primitive melt compositions and returns temperature estimates of 1139-1141°C. The majority of plagioclase from the flank lavas, as well as isolated grains from the intra-caldera lavas fall in this category. A number of grains from the 1988 lava ($An_{<55}$) were not in equilibrium with any of the tested liquid compositions. Their K_D values point towards crystallisation from a more evolved liquid component. The estimated glass composition of the 1988 lava was explored as an equilibrium melt, but failed the equilibrium test, as it required less calcic plagioclase than was observed. Plagioclase-melt barometers are not used here, as they can randomly return poor results from certain datasets (Putirka 2008).

The clinopyroxene-melt thermobarometer relies upon the Jadeite-Diopside/Hedenbergite exchange between mineral and coexisting melt (equations 30 and 33: Putirka 2008). Errors of ±45°C and ±160 MPa are reported for these equations (Putirka 2008). Mineral-melt equilibrium can be tested by Fe-Mg exchange coefficient, K_D $(Fe\text{-}Mg)^{cpx\text{-}liq}$, which should fall within the range 0.28±0.08 (Putirka 2008). Other equilibrium tests include comparison of predicted and

Table 4.5 Plagioclase thermometry results for Ambrym

Eruption	Number	An (mol.%)	K_d	T (°C)	Eq. Liq.*
1913	13Pl2	81.7	0.28	1140	1
	13Pl3	79.4	0.33	1139	1
	AMB13Ol5	82.8	0.26	1140	1
	13Pl4a	82.3	0.27	1140	1
	13Pl4b	78.0	0.35	1139	1
	13Pl5	80.9	0.30	1140	1
	13Pl6	78.8	0.34	1139	1
	13Pl7	80.5	0.30	1140	1
	13Pl8a	79.8	0.32	1140	1
	13Pl8b	78.2	0.35	1139	1
	13Pl8c	81.3	0.29	1140	1
	AR15P1	83.4	0.25	1141	1
	AR15P2	69.3	0.29	1125	2
	AR15P3	82.2	0.27	1140	1
	AR15P4	81.9	0.27	1140	1
	AR15P5	69.8	0.28	1126	2
1929	37Pl2	84.6	0.23	1141	1
	37Pl3	80.0	0.31	1140	1
	37Pl4	82.8	0.26	1141	1
	37Pl5	84.5	0.23	1141	1
	37Pl1a	83.7	0.24	1141	1
	37Pl1b	77.3	0.36	1139	1
	37Pl1c	84.2	0.23	1141	1
1937	50Pl4	78.9	0.33	1139	1
	50Pl5	80.2	0.31	1140	1
	50Pl6	82.4	0.27	1140	1
	50Pl7	83.1	0.26	1140	1
	50Pl9	79.1	0.33	1139	1
1942	AMB42.4	60.6	0.29	1089	5
	AMB42.5	84.7	0.22	1141	1
	AMB42.6	83.4	0.25	1141	1
	AMB42.7	63.4	0.27	1099	4
	AMB42.8	60.3	0.30	1089	5
	AMB42.11	84.7	0.22	1141	1
	AMB42.13	84.9	0.22	1141	1
1988	88lath1	68.8	0.29	1125	2
	88lath2	64.5	0.28	1109	3
	88Pl3	84.9	0.22	1141	1
	88lat3	60.5	0.27	1104	4
	88Pl4	59.6	0.32	1085	5
	88Pl5	59.0	0.34	1081	5
	88Pl6	59.7	0.32	1085	5
	88lath4	65.4	0.27	1109	3
	88Pl7	64.9	0.25	1113	3
	88Pl10a	57.3	0.35	1083	5
	88Pl10b	61.0	0.30	1087	5
	88Pl10c	64.7	0.28	1107	3
	88Pl10d	55.5	0.37	1080	5
	AMB 88	61.5	0.29	1088	5
	AMB 88	64.0	0.26	1100	4
	AMB 88	83.7	0.24	1141	1
2009	09Pl4	73.8	0.23	1128	2
	09Pl6	75.9	0.20	1129	2
2014	AMB14.1	60.3	0.30	1089	5
	AMB 14.11	71.1	0.26	1126	2

*Equilibrium liquids:
1 - Ol12 (SiO_2 = 45.8 wt.% Allard et al. 2015)
2 - Ol7a (SiO_2 = 48.7 wt.% Allard et al. 2015)
3- Ol3a-b (SiO_2 = 50.6 wt.% Allard et al. 2015)
4 - 2a (SiO_2 = 51.3 wt.% Allard et al 2009)
5 - AMB 14 Glass (SiO_2 = 53.0 wt.%)

observed Di-Hd components (Fig. 4.8a) and comparison between liquid and crystal Mg#. Clinopyroxene-based calculations rely on the same liquid components used for the plagioclase-based calculations. Calculations using clinopyroxene are far less sensitive to changes in the melt composition and results vary little with different liquid components, so for this reason all results presented here use the lava lake glass analysis (AMB 14 - Table 4.4). This returns pressures of ~210-590 MPa and temperatures of 1062-1128°C are obtained (Fig. 4.8b; Table 4.6). One grain from the 1929 eruption returned a pressure of 1000 MPa and temperature of 1170°C, while a number of grains from the 1988 eruption returned negative pressures and temperatures of 1044-1077°C. Given the shared melt component in all pressure/temperature calculations, estimates form a linear array in Fig. 4.8. Pressure and temperature estimates for all samples roughly overlap, however the 1988 lava displays the greatest range. Within the flank lavas, clinopyroxene from the 1913 and 1929 eruptions more commonly require shallower pressures and lower temperatures, while the opposite can be said for the 1937 lava. Lava lake samples conform with the earlier flank eruptions.

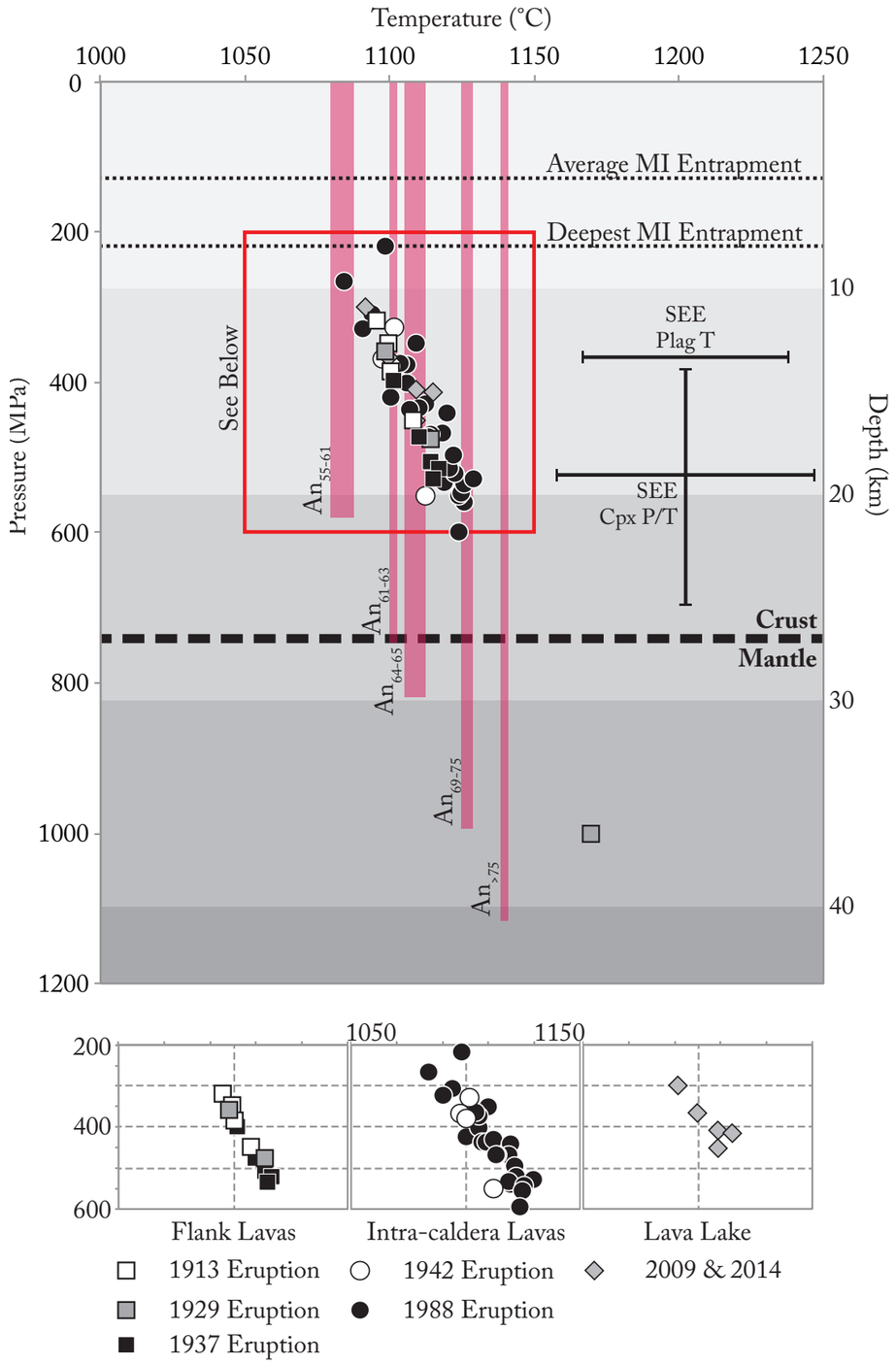

Fig. 4.8 Pressure and temperature estimates of clinopyroxene crystallisation at Ambrym. Sub-panels clarify data based on eruption style. Depth is estimated on the right of the diagram, assuming crustal densities of 2800 kg m^{-3}. Error bar shows the standard error of estimate (SEE) as reported by Putirka (2008). Plagioclase temperature estimates are shown as vertical, red bars, with corresponding anorthite content noted. Melt inclusion entrapment pessures for Ambrym (Allard et al. 2015) are also shown, as is the infered crustal depth (Coudert et al. 1984).

DISCUSSION

Primary Magmas

All historically erupted samples from Ambrym display strong linear trends when incompatible trace element pairs are plotted, demonstrating that they belong to a single magmatic differentiation series and are derived from a shared primary melt. Fig. 4.6 shows that historically erupted rocks analysed by Allard et al. (2015), as well as primitive melt inclusions (Sorbadere et al. 2013) conform with the same trends. Sr and Nd isotope ratios vary little when plotted against an index of differentiation, such as SiO_2 (Fig. 4.7c and d), suggesting they are unaffected by crustal processes and can be used to understand the primary melt composition. Further support for a shared primary melt comes from $^{143}Nd/^{144}Nd$. All historical lavas fall within error of each other for this isotope ratio (Fig. 4.7d). The only evidence against shared primary melts at Ambrym come from Sr isotopes (Fig. 4.7c), with certain samples from the flank eruptions plotting towards higher or lower $^{87}Sr/^{86}Sr$. Much of this variation is restricted to samples from a single eruption (1913 eruption – Table 4.3), suggesting variable primary magmas are not the cause of this disparity. These variations in Sr isotopes do not correlate with other geochemical indicators, such as SiO_2 and thus their cause remains uncertain. The remainder of evidence supports a shared primary melt between historical lavas from Ambrym, however.

Previous studies have shown that magmas erupted from Ambrym are produced by melting of an Indian-MORB source with small contributions from a subduction component (e.g. Peate et al. 1997). Indian-MORB signatures, which can be identified from Sr-Nd-Hf-Pb-U-Th isotopes (Briqueu et al. 1994; Crawford et al. 1995; Peate et al. 1997; Turner et al. 1999; Pearce et al. 2007) are only observed at volcanoes in the centre of the Vanuatu Arc, such as Ambrym, Lopevi and Ambae (Fig. 4.7b). These volcanoes display elevated $^{87}Sr/^{86}Sr$ and lower $^{143}Nd/^{144}Nd$, reflecting source mantle values (Fig. 4.7a). Volcanoes at the peripheries of the arc display Pacific-MORB signatures. Of the volcanoes displaying an Indian-MORB signature, Ambrym records the highest $^{87}Sr/^{86}Sr$ and lowest $^{143}Nd/^{144}Nd$. Two component mixing models suggest this is a product of increased incorporation of sediment from the subducted slab (Fig. 4.7a). Models for Ambrym suggest incorporation of ~3.5% sediment explains the witnessed isotope ratios. Volcanoes such as Lopevi and Ambae require addition of only 2-2.5% sediment. Sediment addition explains a number of geochemical features witnessed in Ambrym lavas, such as the negative Nb and Ta anomalies in Fig. 4.5a and the negative Ce anomaly in Fig. 4.5b.

Table 4.6 Clinopyroxene thermobarometry results for Ambrym

Eruption	Number	K_d	P (Mpa)	T (°C)
1913	AR15.1	0.27	386	1100
	AR15.2	0.27	451	1108
	AR15.3	0.27	320	1095
1929	37Px22	0.27	476	1114
	37Px18	0.28	1000	1170
	37Px23a	0.27	358	1098
1937	50Px3	0.27	515	1117
	50Px3b	0.27	396	1102
	50Px2	0.27	505	1114
	50Px2b	0.27	472	1110
	50Px2c	0.27	529	1115
1942	42.14	0.27	368	1098
	42.15	0.27	550	1112
	42.4	0.27	329	1102
	42.6	0.27	380	1101
1988	88Px13	0.27	536	1119
	88Px11	0.27	521	1122
	88Px10	0.27	371	1105
	88Px9	0.27	557	1125
	88Px8	0.27	600	1124
	88Px5	0.27	420	1100
	88Px3	0.27	473	1113
	88Pxfrag1	0.27	533	1119
	88Px4	0.27	437	1107
	88Px1	0.27	513	1120
	AMB 88	0.27	309	1094
	AMB 88	0.27	376	1104
	AMB 88	0.27	471	1114
	AMB 88	0.27	442	1120
	AMB 88	0.27	400	1106
	AMB 88	0.27	530	1129
	AMB 88	0.27	497	1122
	AMB 88	0.26	219	1098
	AMB 88	0.27	548	1124
	AMB 88	0.27	375	1106
	AMB 88	0.27	433	1110
	AMB 88	0.27	471	1119
	AMB 88	0.27	349	1109
	AMB 88	0.26	265	1084
	AMB 88	0.27	327	1091
	AMB 88	0.27	537	1126

Table 4.6 (cont) Clinopyroxene thermobarometry results for Ambrym

Eruption	Number	K_d	P (Mpa)	T (°C)
	AMB 88	0.27	429	1113
2009	09Px1	0.27	410	1108
	09Px5	0.27	300	1091
	09Px6	0.27	367	1099
2014	AMB14.2	0.27	413	1115
	AMB14.3	0.27	452	1109

Table 4.7. Inputs and results of fractional crystallisation models for Ambrym

					% Phases Removed				
Stage	**Initial Magma**	**Final Magma**	**Δ SiO_2 (wt.%)**	**ΣR²**	**Plag.**	**Cpx.**	**Ol.**	**Spinel**	**Total**
1	67*	AMB 50	0.74	0.10	-8.28	-16.12	-7.35	-0.19	-31.94
2	AMB 13	AMB 09I	1.79	0.19	-14.79	-3.00	-1.78	-1.58	-21.15

*Data from Picard et al. (1995)

These anomalies mirror anomalies in the composition of subducted sediment (Peate et al. 1997; Plank and Langmuir 1998).

Picard et al. (1995) showed that post-caldera magmas from Ambrym result from ~21% melting of a spinel lherzolite at pressures of 1000-1500 MPa, equivalent to a depth of 30-45 km. This is supported by REE patterns presented here (Fig. 4.5), which imply melting above the garnet stability field. Such melting produces a high-MgO (>10-11 wt.%) basaltic liquid (Picard et al. 1995).

Differentiation and Crystallisation

All historically erupted lavas are more evolved than the primary magma discussed by Picard et al. (1995). These authors highlighted the role of fractional crystallisation in producing the array of magma compositions seen at Ambrym. Strong linear trends when element abundances are plotted against an index of differentiation (Fig. 4.4 and 4.6) are apparent amongst historical lavas examined in this study, further supporting the operation of fractional crystallisation.

Lavas erupted during both flank and intra-caldera eruptions display similar major element compositions, with SiO_2 between 50.3 and 51.1 wt.% and MgO ranging from 4.38 to 4.99 wt.%

(Fig. 4.4). These compositions are consistent with other, previously determined, compositions for historically erupted lavas (Robin et al. 1993; Allard et al. 2015) and tephras from Ambrym (Taylor 1956; Nemeth and Cronin 2010). The flank lavas all share common mineral chemistry, with restricted variations in the compositions all phenocryst phases. A selection of phenocrysts from both intra-caldera lavas also preserve comparable compositions. This relative uniformity in mineral compositions suggests all lavas experienced similar crystallisation processes.

The derivation of these magmas from a shared parental liquid is explored using the XLFRAC least-squares major element modelling program (Stormer and Nicholls 1978). The most primitive post-caldera lava (Picard et al. 1995) is used as the starting composition, while the 1937 lava is chosen as the derivative magma (Table 4.7; Fig. 4.4 - Model 1). Given the relative homogeneity of flank eruption lavas, those of the 1913 or 1929 eruptions could be substituted for the final magma with little change to the model. The most statistically robust model (ΣR^2 <0.1) requires ~32% fractionation, primarily of clinopyroxene alongside olivine and plagioclase (Table 4.7). The fractionating assemblage predicted by this model is consistent with previous modelling by Picard et al. (1995), however they suggest a lower degree of fractionation.

To further test the validity of this model (Table 4.7 – Model 1), forward modelling of trace elements using the Rayleigh Fractionation Equation was performed, with results presented on Figure 4.6. Elements such as Rb, Sr and Yb offer strong support for the model. Trends predicted for Ba, La and V suggest these elements should be acting more incompatibly than they appear to be. Nevertheless, variations between predicted and real values are minimal and potentially result from poorly constrained partition coefficients. Similarly, Eu abundances are slightly underestimated during forward modelling. While this may indicate a lesser involvement of plagioclase, such a scenario is inconsistent with the Ba and Sr trends. Chromium is highly compatible with this crystallising assemblage, so is predicted to rapidly decrease in abundance. While Cr does act compatibly, it is present in abundances higher than those predicted. This potentially suggests that magma replenishment may be occurring within the magma reservoir. Processes of replenishment and fractionation operate against each other to buffer compositions at a point between the compositions of the replenishment magma and that produced by fractionation (O'Hara 1977; Albarede 1985). Lee et al. (2014) modelled compositions of such magma chambers, showing that elements with high partition coefficients, such as Cr, require the least number of overturns to attain a steady-state composition. This explains why replenishment

is evident in Cr compositions, but not those of more incompatible elements also shown in Figure 4.6.

As clinopyroxene is the dominant phenocryst phase predicted for this phase of fractional crystallisation, clinopyroxene-based pressure and temperature estimates give some indication of the conditions experienced during this phase of crystallisation. The clinopyroxene thermometer suggests crystallisation occurred at temperatures of ~1080-1130°C. Plagioclase thermometers suggest high-anorthite plagioclase ($An_{>75}$), such as that seen in the flank lavas, crystallised at temperatures >1139°C. These estimates remain within error of the clinopyroxene estimates (Fig. 4.8b). Nevertheless, higher temperatures of plagioclase crystallisation are consistent with the petrology of these lavas, where clinopyroxene commonly surrounds euhedral plagioclase phenocrysts.

The clinopyroxene barometer suggests crystallisation at pressures of ~210-590 MPa. Such estimates are deeper than depths of crystallisation inferred from melt inclusions, which suggest pressures of <220 MPa (Allard et al. 2015). Many of the melt inclusion derived pressure estimates remain within error of the shallower clinopyroxene pressure estimates, however. Combined, this data points towards magma crystallisation at pressures >100 MPa, but potentially as deep as 600 MPa. This is equivalent to a depth of ~4-20 km, assuming an average crustal density of 2800 g cm^{-3}. The shallower end of this depth range also overlaps with the source of very long-period tremors (3.9-4.1 km below the vents), which have been interpreted to represent a magma reservoir (Legrand et al. 2005). Within clinopyroxene pressure/temperature estimates significant clusters or breaks cannot be discerned. This raises the possibility that magmas did not stagnate for significant periods of time, but rather crystallised as they rose somewhat steadily through the crust (c.f. Armienti et al. 2013), however this cannot be confirmed, given the significant errors associated with pressure estimates. Nevertheless, if this is the case, the absence of pressure indicators from <100 MPa suggests more rapid magma rise from this depth during major eruptions.

Lava lake samples can be discriminated from flank and intra-caldera lavas by their more evolved whole rock compositions, with noticeably lower CaO and Al_2O_3. Similarly, plagioclase compositions in these samples are consistent with growth from a more evolved liquid than that of the remainder of the samples. Both features are consistent with these samples having undergone additional differentiation. Nevertheless, these samples diverge considerably from fractionation trends predicted above. Lava lake samples produce pronounced negative arrays of

Al_2O_3 and Sr when plotted an index of differentiation (Fig. 4.4b, 4.6b) suggesting a greater role of plagioclase crystallisation.

Potential fractionation trends are modelled using least-squares major element modelling. The most statistically robust model for this second stage of crystallisation suggests these magmas evolved through ~21% fractionation from a magma with a composition similar to that of the 1913 lava (Table 4.7; Figs. 4.4 and 4.6 – Model 2). The fractionation assemblage is dominated by plagioclase alongside clinopyroxene, spinel and limited amounts of olivine.

Fractionation models are consistent with observed variations in trace elements including Rb, Ba and Eu, (Fig. 4.6d, e, g). Elements such as V, Sr and Yb prove harder to reconcile with the models, however (Fig. 4.6b, c, h). Strontium concentrations vary widely between the lava lake samples. Such variations are linked to the abundance of plagioclase, which is the dominant phenocryst phase in all lava lake samples. Of the four 2009 samples, the reticulite (AMB 09IV –Table 4.3) displays the lowest Sr concentration, due to its negligible plagioclase content. This sample plots toward lower Sr than that predicted for the melt, suggesting plagioclase is under-represented in this fractionation model.

Variations in Yb are harder to decipher, as it is predicted to act incompatibly, however, displays a slightly negative array when plotted against Zr (Fig. 4.6h). Brophy (2008) explained constant HREE patterns with increasing differentiation in intermediate to felsic island arc rocks through processes including partial melting of amphibolite and low-mid crustal hornblende-bearing basalt fractionation. While such a scenario could be invoked to explain the pattern seen here, it is inconsistent with the models of earlier fractionation discussed above. Similarly addition of amphibole to the fractionating assembalge could explain the observed Yb trend, however the proportions required are inconsitent with both the petrology of the rocks and the observed variations in other elements. Furthermore, while the lava lake data presented here display a decreasing trend when plotted against Zr, examination of a wider dataset from Ambrym, (Robin et al. 1993; Picard et al. 1995) shows a positive array (Fig. 4.6f). The reticulite sample (AMB 09 IV) displays the highest Zr and lowest Yb, raising the possibility that variation in Yb amongst the lava lake samples is controlled by crystal content, with higher clinopyroxene abundances contributing greater Yb.

These limitations in trace element models for stage 2 crystallisation suggest that differentiation may not solely account for the compositional variations amongst these samples. The persistence of active lava lakes during periods of relative quiescence places Ambrym

amongst a select group of volcanoes to host such features. Persistent lava lakes require a heat source to inhibit cooling and crystallisation, and are envisaged to be continually replenished from a magma reservoir via an open conduit (Harris et al. 1999; Oppenheimer et al. 2004; Witter et al. 2004). In this way, lava lakes typically exhibit steady-state conditions, in which factors such as magma replenishment, crystallisation, heat loss and removal through eruption or intrusion are in equilibrium, effectively buffering the magma composition (O'Hara 1977; Albarede 1985). This is apparent amongst lavas from many lava lakes, including Villarica (Witter et al. 2004) and Erebus (Kelley et al. 2008). Trends for elements including Cr, V and the REE, as well as Na_2O and K_2O, are flatter than those predicted by forward modelling, raising the possibility that these elements are buffered by replenishment processes. Pronounced positive linear trends for TiO_2, and negative linear trends for Al_2O_3 and CaO suggest differentiation processes continue despite replenishment. Depletion of CaO and Al_2O_3 are consistent with plagioclase crystallisation, which is readily reconciled with the plagioclase microlites observed in these samples. Nevertheless, temporal fluctuations in these elements since 2005 suggest that differentiation has not proceeded in a closed system. The most evolved compositions were erupted in 2009, however even these display significant variations in chemistry. The distinctive chemistry of the crystal-free reticulite (AMB 09IV) again highlights the influence of crystals, showing that at least some of this variation in whole rock chemistry can be attributed to variations in mineral abundances (Table 4.2).

Clinopyroxene pressure and temperature estimates for the lava lake samples overlap with those from major flank and intra-caldera lavas. Nevertheless, fractionation models predict clinopyroxene is only a minor component of the assemblage crystallised to produce the lava lake samples. As such, clinopyroxene in these samples may represent antecrysts that have been entrained from greater depths and are associated with Stage I fractionation. Temperatures of plagioclase crystallisation are lower for the lava lake samples, albeit still within error of those from the major eruptions. Melt entrapment pressures calculated for melt inclusions in scoria samples from Benbow return a suite of shallower estimates (70-90 MPa) than those from the 1913 lava (Allard et al. 2015). This raises the possibility that a series of vertically dispersed magma reservoirs are present beneath Ambrym, with lava lake magmas potentially stored at shallower levels.

The high microlite abundance in numerous lava samples (Table 4.1) attests to late-stage crystallisation of plagioclase and spinel. This explains the significant disparity between whole

rock and estimated glass compositions for some samples. Groundmass plagioclase compositions were only analysed in the 1988 lava, where they were significantly less calcic than remaining plagioclase crystals, consistent with growth from a more evolved liquid. Crystallisation temperatures of <1088°C are estimated for these crystals. This stage of crystallisation was most likely driven by H_2O exsolution just prior to or during eruption (e.g. Cashman 2004). Allard et al. (2015) suggest H_2O primarily exsolves at shallow pressures (<<100 MPa) at Ambrym, on the basis of melt inclusion studies. As such, this exsolution most likely drives final microlite crystallisation.

Assimilation, mixing and recycling

While intra-oceanic arcs are commonly thought to be spared from most crustal contamination, a growing body of evidence suggests it is not uncommon. Lavas from Ambrym's southerly neighbour, Lopevi, (~35 km away), display significant evidence for crustal assimilation, with ascending magmas interacting with mafic oceanic crust, forcing magmas to less radiogenic Sr and more radiogenic Nd compositions (Handley et al. 2008; Beaumais et al. 2013). Recent findings from Buys et al. (2014) identified inherited zircons in Miocene basalts from Espirito Santo, to Ambrym's west, suggesting the incorporation of continental crustal material from the basement of the Vanuatu arc in these magmas. In contrast, magmas from Ambae, to the north, display primitive, picritic compositions that exhibit no evidence for crustal interaction (Eggins 1993; Sorbadere et al. 2011). Samples from Ambrym produce scattered, horizontal trends when Sr and Nd isotopes are plotted against an index of differentiation, such as SiO_2 (Fig. 4.7c and d). This suggests they display negligible contamination by isotopically distinct crustal material. Both Ambrym and Ambae sit astride axes of compressive stress resulting from subduction of the D'Etrecasteaux Ridge (Collot et al. 1985) and in both cases the volcanoes are elongated parallel to these axes, as a result of fissure-fed lava extrusion (e.g. Németh and Cronin 2009; 2010). These volcanoes are also the two most voluminous in the Vanuatu Arc (Bani et al. 2012), suggesting high rates of magma extrusion. These features raise the possibility that magma ascent from the zone of initial melting is facilitated by fractures associated with the axes of compressive stress at both Ambrym and Ambae. If this is the case, magmas are potentially inhibited less as they rise through the crust, presenting less opportunity for crustal assimilation and other differentiation processes. This potentially explains why assimilation dominates differentiation at Lopevi, but is limited at Ambrym.

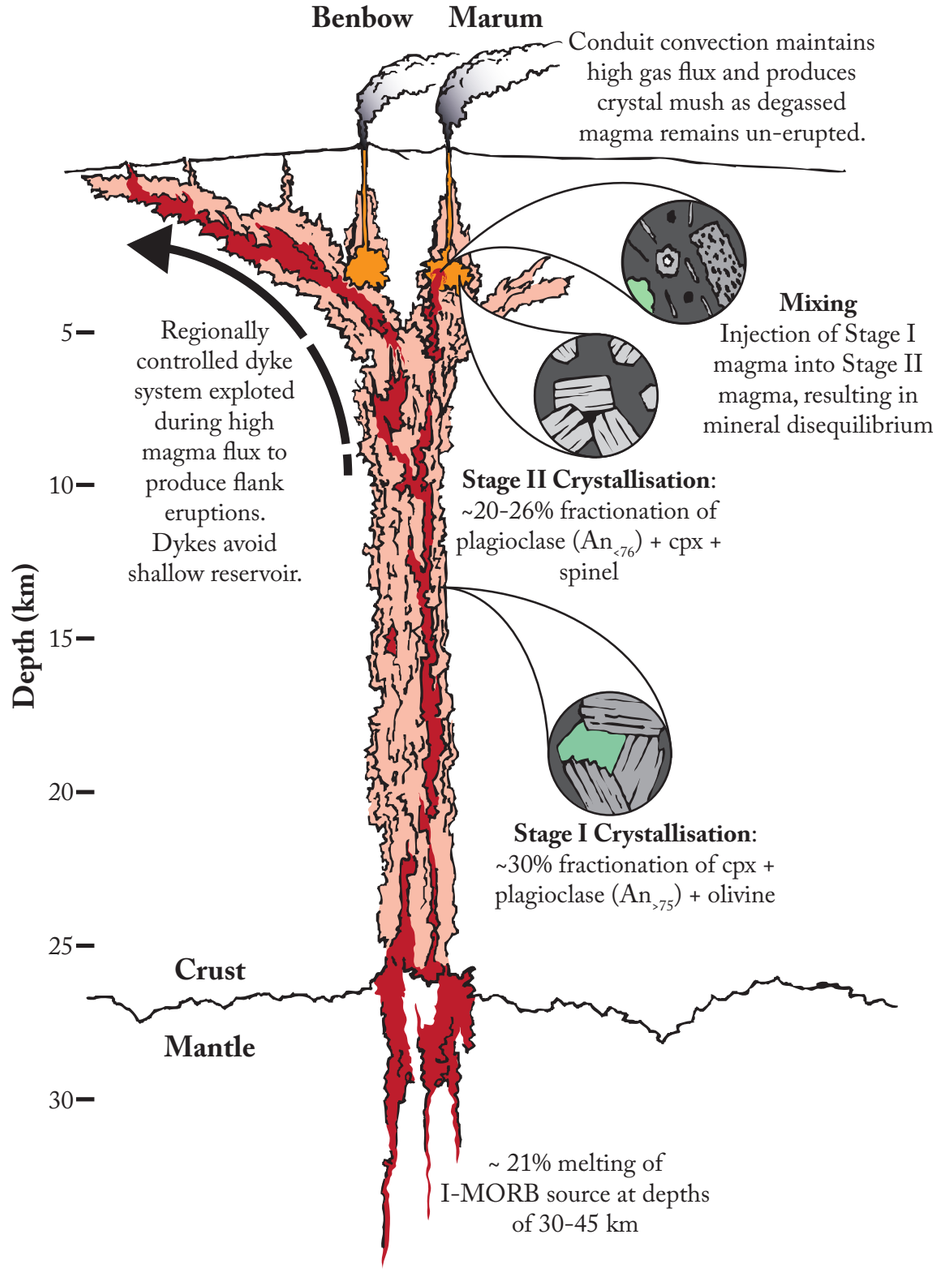

Fig. 4.9 Schematic cross-section showing the inferred plumbing system beneath Ambrym, with various storage zone and processes shown. Petrological textures resulting from major magmatic processes are shown within circles. Crust/Mantle boundary depth is based on seismic data from Coudert et al. 1984.

Whilst contamination with a geochemically distinct assimilant is unlikely at Ambrym, the petrology and mineralogical diversity seen within the intra-caldera lavas implies magma

mixing has played a significant role in their formation. A number of plagioclase crystals ($An_{>75}$) and the majority of clinopyroxene crystals are chemically similar to minerals found in the flank lavas and lava lake samples, recording shared processes of fractionation from a parental magma. In contrast with the flank and lava lake samples, where these minerals appear to be in equilibrium with their host liquid, plagioclase and clinopyroxene phenocrysts in the intra-caldera lavas commonly display resobrtion textures, as well as overgrowth rims. Such textures are most commonly associated with magma mixing (e.g. Murphy et al. 2000; Browne et al. 2006; Armienti et al. 2007; Streck 2008), but have also been linked with rapid decompression (Nelson and Montana 1992). Reverse zoning in less calcic plagioclase grains from the 1988 lava adds weight to magma mixing as the dominant process governing disequilibrium textures in this lava. Intra-grain fluctuations in anorthite are also noticed in plagioclase grains within the 2009 scoria, however this and other lava lake samples lack the full range of disequilibrium textures witnessed in the intra-caldera lavas. These features within the lava lake samples potentially result from recycling of plagioclase crystals within the volcanic conduit during lava lake activity. Elevated gas fluxes, such as those seen at Ambrym (Allard et al. 2015), have been linked with conduit convection, in which gas exsolution drives a density change in the ascending magma, causing it to sink back down the conduit (Kazahaya et al. 1994; Stevenson and Blake 1998; Burton et al. 2007). Mixing between degassed and un-degassed magma within the volcanic conduit has been postulated for Ambrym on the basis of vesicle textures (Polacci et al. 2012) and gas fluxes (Allard et al. 2015). Such processes of mixing, recycling and gas exsolution induce variations in melt composition, resulting in fluctuations in the anorthite content of crystallising plagioclase (e.g. Landi et al. 2004; Francalanci et al. 2005; Armienti et al. 2007; Burton et al. 2007).

The lack of resorbed phenocrysts in the lava lake samples suggests that processes of magma mixing are different in the intra-caldera lavas, where these crystals are an obvious part of the petrology. The presence of resorbed phenocrysts (or, more correctly, antecrysts) suggests that mixing prior to the intra-caldera eruptions involved addition of crystals from one or both magmas. Geochemical similarity between plagioclase antecrysts in these lavas and phenocrysts from the flank lavas, suggests a mafic recharge magma, such as that involved with the flank lavas most likely constitutes one of the mixing components and provided the high anorthite plagioclase. The other mixing component is harder to identify. The major and trace element and isotope compositions of intra-caldera lavas do not diverge significantly from those of flank lavas, opposing mixing with a geochemically distinct component. Instead, the mixing component is

more likely to have been produced from the same liquid line of decent, however reverse zoning in some plagioclase grains requires it to have been more evolved than the recharge magma. Resident or residual magma associated with lava lake activity is the most likely contender for this component. Under such a scenario, a pulse of recharge magma ascended from the deeper magma reservoir and was injected beneath Marum, where it mixed with more evolved magma associated with lava lake activity. Alternatively, Significant discrepancies between degassing rates and magma output have been identified at Ambrym, suggesting that at most ~5% of degassed magma is erupted (Polacci et al. 2012; Allard et al. 2015). This is a common observation at persistently degassing volcanoes (Allard et al. 2008; Métrich et al. 2011) and potentially indicates that the remaining magma is stored within the shallow plumbing system of the volcano (e.g. Francis et al. 1993; Bragagni et al. 2014). Intra-caldera lavas may record interaction of recharge magma with this stored component. Remobilisation of stored magma by mafic recharge has been invoked to explain eruptions at other arc volcanoes, including Ruapehu (Kilgour et al. 2013) and Soufriere Hills (Murphy et al. 2000). Interestingly, the 1988 lava records elevated ($^{230}Th/^{232}Th$), compared with the remainder of the samples, potentially indicating incorporation of an older component (Handley et al. in prep).

PETROGENETIC MODEL: CONTROLS ON ERUPTION STYLE

Reconciliation of the above observations into a petrogenetic model has important implications for understanding the controls on styles of eruption at Ambrym.

Primary melt composition has been linked with variation in eruption style at Kilauea, with melting of an heterogeneous mantle source supplying magmas of varying volatile content (Sides et al. 2014). Comparable primary melt compositions amongst samples from Ambrym indicate this is unlikely to be a significant factor governing eruption style at this volcano. This is corroborated by Allard et al. (2015), who find no evidence of varying volatile content amongst inferred primary magmas.

By contrast, the variations in petrology and geochemistry indicate significant differences in magma storage and ascent between samples from the different styles of eruption. All historical magmas appear to have undergone a common stage of fractional crystallisation from a parental basalt composition at depths between ~4-20 km (Fig. 4.9). Lavas erupted during both flank and intra-caldera eruptions appear to tap this magma, however evidence for additional mixing with magma stored higher in the magmatic system is observed amongst intra-caldera lavas

(Fig. 4.9). By contrast, flank eruptions, which are fed by dykes that diverge from the main plumbing system, show no evidence for mixing. This may suggest dykes diverge from the main magmatic system significant depths (potentially >5 km), as envisaged for Mt Etna (Acocella and Neri 2003). Alternatively, dykes may diverge at shallower depths, with rapid magma ascent restricting interaction and crystal transfer between these magmas and the crystal mush.

The dynamics of dyke propagation during flank eruptions at Ambrym remain largely unknown, however similarities in eruption dynamics between the 1913 eruption (Frater 1917; Gregory 1917; Németh and Cronin 2011) and the 2001 eruption of Etna (e.g. Acocella and Neri 2003; Corsaro et al. 2007) suggest the latter may be used as an analogue for flank eruptions on Ambrym. Here a fresh input of magma was emplaced as a dyke that exploited a regionally controlled N-S trending stress field. Propagation of the dyke at shallow levels opened fractures that decompressed magma stored within the summit vents, inducing summit activity during the opening phases of eruption. This was compositionally distinct from magma erupted directly from the dykes on the volcano's flanks (Corsaro et al. 2007). Similar eruption dynamics were reported for flank eruptions at Ambrym, with opening sub-Plinian activity at Benbow, followed by propagation of flank activity towards the western tip of Ambrym Island (Frater 1917; Gregory 1917). Unfortunately no material erupted from Benbow during the 1913, 1929 or 1937 eruptions has been collected for examination.

Benbow lies astride the ~N 105° oriented fissure system that transects Ambrym, while Marum is offset from it, by ~1.5 km (Fig. 4.1). This may indicate that Benbow is more closely linked with the dyke system that exploits these fissures, a feature reinforced by the absence of fissure activity during the 1942 and 1988 eruptions centred on Marum. Historical reports commonly state that one vent was noticeably more active than the other (e.g. Mallick 1968; Monzier and Charley 1989) raising the possibility that while Marum and Benbow are fed by the same magmatic system, their shallow plumbing networks diverge (Fig. 4.9). This is corroborated by Allard et al. (2015), who show that volcanic gases from Marum and Benbow represent degassing of a single magma body through different pathways. Nevertheless, the presence of active lava lakes in both vents and commonality of magma compositions erupted from both lava lakes (c.f. Allard et al. 2015) suggests both vents are readily supplied with magma.

CONCLUSION

Ambrym volcano has displayed a range of eruptive behaviours throughout the historical

record. Examination of the geochemistry, mineralogy and petrology of the lavas produced shows that such variations are intrinsically linked with subsurface processes of magma replenishment, storage, differentiation and ascent. Hazardous flank eruptions of the early 20th century appear linked with replenishment from a mid-crustal storage area. Replenishment magmas exploited regional faults, propagating through dykes to erupt on the volcano's flanks as fluid lava flows. Effusive, intra-caldera eruptions were similarly associated with magma replenishment, however ascending magma interacted with stored magma in the shallow plumbing system of the volcano, producing the crystal-rich textures and diversity of mineral compositions seen in these lavas. The stored magma component feeds lava lake activity, which is a continuing feature of this volcano.

Gas drifts from Yasur’s crater during a brief moment of quiet on the volcano

Theme 3:

Modelling Peristent Eruption Processes

4. Understanding drivers of persistent volcanic activity and their timescales using gas flux measurements and uranium-series isotopes

Chris Firth[1*], Simon Turner[1], Michael Turner[1], Shane Cronin[2] and Heather Handley[1]

[1] Department of Earth and Planetary Sciences, Macquarie University, Sydney, NSW 2109, Australia

[2] School of Environment, The University of Auckland, Private Bag 92019, Auckland

The geometry of the shallow plumbing and details of the magmatic processes occurring within it are explored at Yasur, a persistently-active volcano in the Vanuatu Arc, using a suite of physical and geochemical models. These rely on gas flux data, uranium-series isotopes and thermal cooling of the magma chamber. In particular, these models are used to understand rates of magma replenishment that sustain persistent activity. Results vary widely between these models, suggesting replenishment intervals of years to tens of thousands of years. These estimates can be reconciled by a scenario in which magma replenishment occurs on timescales of years to decades, with uranium-series isotopes recording mixing between replenishment magma and an older component that potentially represents a crystal mush. Comparison between degassing rates and magma output rates indicates large volumes of magma have accumulated beneath Yasur, explaining the presence of such a component. Comparison between Yasur and other persistently-active volcanoes, such as Stromboli, Erebus and Villarrica, shows that magma replenishment and degassing processes are broadly similar amongst this type of volcano. In detail, however, each volcano displays eruptive behaviour that is a feature of the individual shallow plumbing system and magma composition.

INTRODUCTION

A number of volcanoes display persistent eruptive behaviour lasting years to centuries. Prominent examples include Stromboli (e.g. Rosi et al. 2000), Erebus (e.g. Kelley et al. 2008), Villarrica (e.g. Witter et al. 2004) and Yasur (e.g. Firth et al. 2014). Ongoing eruptions can be represented by active lava lakes, regular Strombolian explosions, or persistent elevated gas fluxes. This behaviour contrasts strongly with the typical volcanic cycle, in which variable intervals of dormancy are interrupted by sudden, mostly short-lived, eruptions. The distinctions between these two styles of activity can result from differences in magma supply, ascent and degassing. Persistent eruptions lasting decades or longer are of great interest to understanding the dynamics of “open” magmatic systems and offer an opportunity to test a range of models regarding magma rise and eruption processes.

Persistently erupting volcanoes are considered to have relatively benign activity, however, sudden upsurges in eruption violence can cause loss of life, while elevated gas fluxes may cause chronic agricultural and health impacts (Allibone et al. 2012) as well as producing high, point-source greenhouse gas emissions (Bani et al., 2009). In addition, some of these volcanoes, such as Yasur, are intimately related to larger volcanic systems that produce rare, but catastrophic caldera-forming eruptions (Allen 2005).

A number of theoretical physical and geochemical models, relying on gas flux and

whole rock trace element and isotope compositions have been developed to evaluate processes operating in a magma chamber (e.g. O'Hara 1977; Albarède 1985), or conduit (e.g. Stevenson and Blake 1998). Application of these models to real-world scenarios has largely been restricted to understanding degassing processes and constraining conduit conditions (e.g. Witter et al. 2004; Stix 2007). A number of the models (e.g. Hughes and Hawkesworth 1999), however, remain largely untested against volcanic datasets. In this work, a suite of these theoretical models are applied to Yasur, a persistently-active scoria cone in the Vanuatu Arc, with the aim of better understanding the processes driving persistent activity and clarifying the timescales over which they operate. Further datasets from the literature are also examined and compared with the findings from Yasur.

Current understanding of persistent volcanic activity

To maintain ongoing magma and volatile fluxes, which are a defining feature of persistently-active volcanoes, reservoirs must either be very large, or experience regular replenishment with new magma. In contrast to magmas that feed brief eruptions, processes of replenishment, tapping (through eruption and intrusion) and fractionation are envisaged to operate near simultaneously, creating a system that is in 'steady-state'. Such RTF (replenished, tapped and fractionating) magma chambers have been the focus of much geochemical modelling (O'Hara 1977; Albarède 1985; Pyle 1992; Albarède 1993; Hughes and Hawkesworth 1999; O'Neill and Jenner 2012; Lee et al. 2014). These models show that equilibrium between RTF processes effectively buffers the magma composition, while regular replenishment slows cooling and crystallisation rates (Lee et al. 2014).

Persistent eruptive behaviour is accompanied by high rates of degassing (Stevenson and Blake 1998), with average SO_2 fluxes commonly exceeding 100 tons day^{-1} (e.g. Allard et al. 2008; Sawyer et al. 2008; Oppenheimer et al. 2011; Sawyer et al. 2011; Bani et al. 2012). Such prolonged and elevated volatile fluxes require an open system in which magma at depth is connected with the Earth's surface, allowing for continued magma renewal. This connection is commonly envisaged as a conduit, in which convective overturn of magma occurs. Buoyant, volatile-rich magma ascends through the conduit before volatile exsolution and crystallisation increase its density, causing it to sink (Kazahaya et al. 1994; Stevenson and Blake 1998; Burton et al. 2007; Palma et al. 2011; Beckett et al. 2014). Typical volatile fluxes indicate large volumes of magma are degassed, however these are usually irreconcilable with the volume of magma

erupted at such volcanoes, suggesting that significant volumes of magma remain stored beneath these volcanoes (Francis et al. 1993; Métrich et al. 2011; Witham 2011). The fate of this stored magma remains a point of speculation (Harris et al. 1999), however Bragagni et al. (2014) suggest that it is preserved within the magmatic system as a crystal mush.

Yasur volcano

Yasur, one of two of persistently-active volcanoes in the Vanuatu island arc (the other being Ambrym, located to the north), has been continually erupting for 600-800 years (Fig. 5.1) (Firth et al. 2014). Activity includes regular Strombolian eruptions, at intervals of seconds to minutes, accompanied by persistent degassing, with SO_2 fluxes averaging 633 tons day^{-1} (Bani et al. 2012). Yasur is a prime candidate to investigate processes driving persistent volcanic activity due to the presence of easily sampled, high temporal resolution tephra sequences, which span its most recent eruptive epoch. These show that the volcano has erupted magmas of an essentially invariant basalt-trachyandesitic composition, at a roughly constant rate of ~410-480 m^3 day^{-1} (Firth et al. 2014), supporting the presence of an RTF magma chamber feeding this activity. An earlier eruptive phase, which lasted for ~600 years, produced higher magnitude, lower frequency eruptions (Firth et al. 2014). Both episodes of activity have been accompanied by rapid uplift (>156 mm yr^{-1}) of an adjacent block/dome (Yenkahe Resurgent Dome – Fig. 5.1) (Chen et al. 1995; Merle et al. 2013). Such rapid uplift rates have been interpreted as evidence for continued replenishment or even growth of an underlying magma reservoir (Chen et al. 1995; Métrich et al. 2011). Based on the dimensions of the dome, its uplift would potentially accommodate a volume of ~4.5 km^3. Uplift rates (Chen et al. 1995) suggest this volume may have been vacated within the last ~2 kyr.

Yasur sits within the wider Yenkahe Caldera (Fig. 5.1) (Nairn et al. 1988), which has been formed through repeated ignimbrite-producing eruptions over the past 45 kyr (Fig. 5.1) (Allen 2005; Firth et al. in review). The most recent of these emplaced the Siwi Ignimbrite, which has been linked with a trachy-andesitic magma that is more evolved than current eruptive products from Yasur (Métrich et al. 2011). Nevertheless, both styles of activity have been connected to the same magmatic system (Métrich et al. 2011), allowing reliable comparison between persistent activity and older, low frequency/high magnitude eruptions.

In this paper, SO_2 gas flux data is presented along-side whole rock uranium-series isotope analyses of products from Yasur and the older Siwi Ignimbrite. A suite of geochemical models

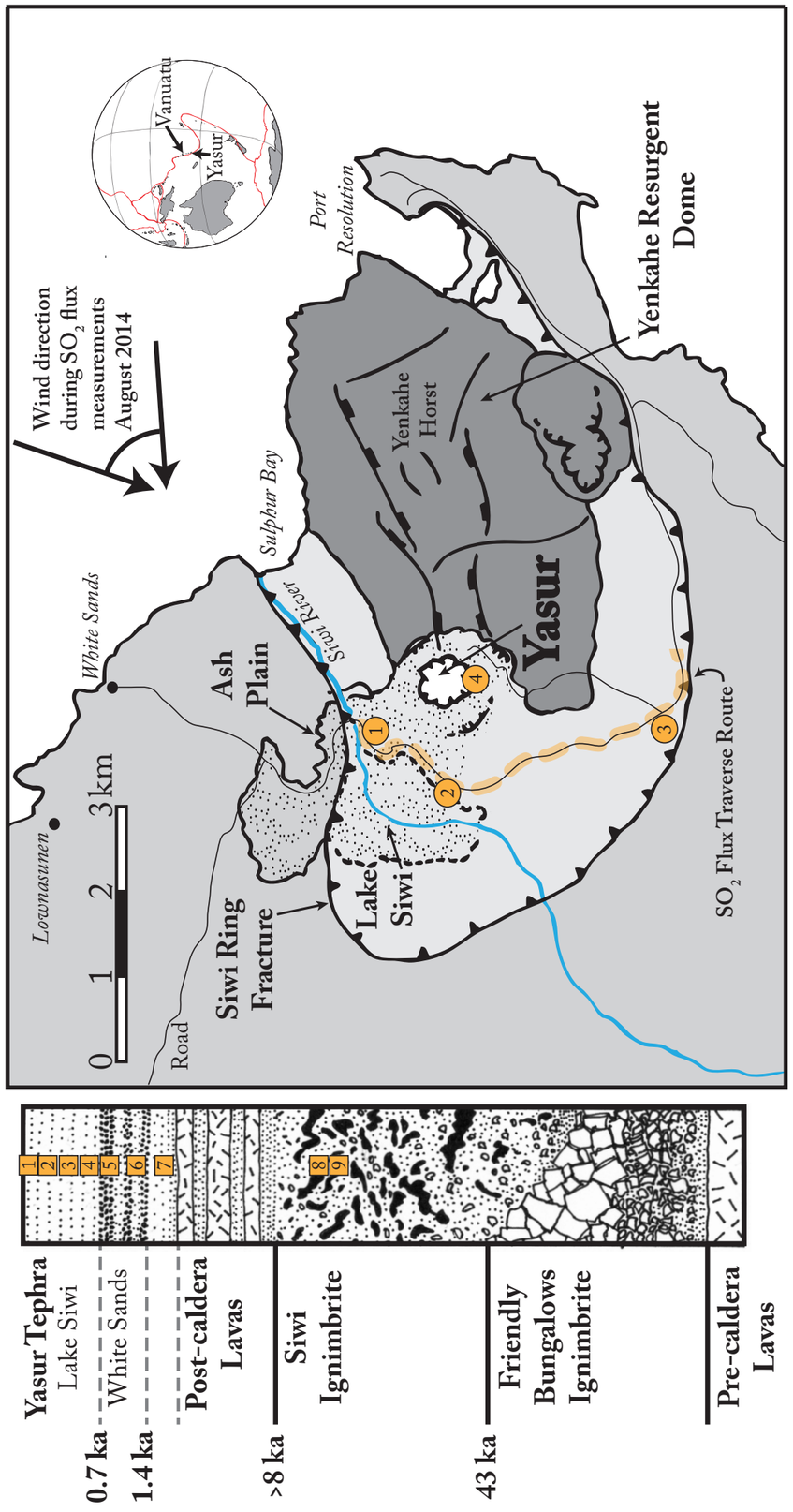

are applied to this data, together with a thermodynamic model, to understand magma chamber and conduit processes that sustain persistent eruption, the timescales over which they operate and their relation to higher-magnitude eruptions.

RESULTS

SO_2 Flux

SO_2 flux measurements (Table 5.1) were collected between the 25th and 30th of August 2014 (Table 5.1) using a FLYSPEC ultraviolet spectrometer (Horton et al. 2006) (For full methods see Appendix). This data adds to the work of Bani and Lardy (2007) and Bani et al. (2012), who recorded SO_2 flux at Yasur between 2004 and 2008 (Fig. 5.2). Three traverses beneath the gas plume at Yasur over a four-day period indicate a mean gas flux of ~1350 tons day^{-1} (t d^{-1}), with a maximum recorded flux of 1647 t d^{-1}. Five 2-3 hour long scans through the plume conducted over the same time period using a rotating mirror system on the FLYSPEC (see Appendix) yielded consistently lower results, with an average of ~850 t d^{-1} and a maximum of 1057 t d^{-1}. Additional scans completed from the crater rim show generally higher SO_2 fluxes (1261-2903 t d^{-1}), with significantly great variability (Table 5.1; Fig. 5.2) showing the pulsing nature of gas output (that is later homogenised in the downwind plume).

Measurements of SO_2 flux were also recorded for Ambrym volcano, which hosts two open-vent craters: Marum and Benbow. Walking traverses beneath the plume from Marum crater suggested a flux of ~3000 t d^{-1}, a figure corroborated by traverses conducted by boat on

Fig. 5.1 Map of Yasur and surrounding area, showing main landmarks and location of gas flux measurements, including both scan sites (circles) and traverse route (dashed line). The scan site numbers correspond with locations mentioned in Table 5.1. The area shaded light grey is the Yenkahe Caldera, which is surrounded by the Siwi Ring Fracture, while the darkest grey shaded area is the Yenkahe Resurgent Dome. A representative stratigraphic column for the area (after Firth et al. 2014 and Firth et al. review) is shown to the left, with known and inferred ages marked. Samples analysed for uranium-series isotopes are marked as squares, with numbers corresponding to samples in Table 5.2. Sample 1 is a lava flow erupted in 1920 (Firth et al. 2014). Samples 2-4 were collected from the Lake Siwi deposit (Firth et al. 2014) and represent the current episode of persistent activity. Samples 4-6 were collected at the White Sands deposit (Firth et al. 2014), with 4 and 5 representing an episode of higher-magnitude eruptions, and sample 6 an earlier episode of variable eruption frequency/magnitude. Samples 7 and 8 were collected from coastal exposures between White Sands and Sulphur Bay and represent the Siwi Ignimbrite (Firth et al. in review).

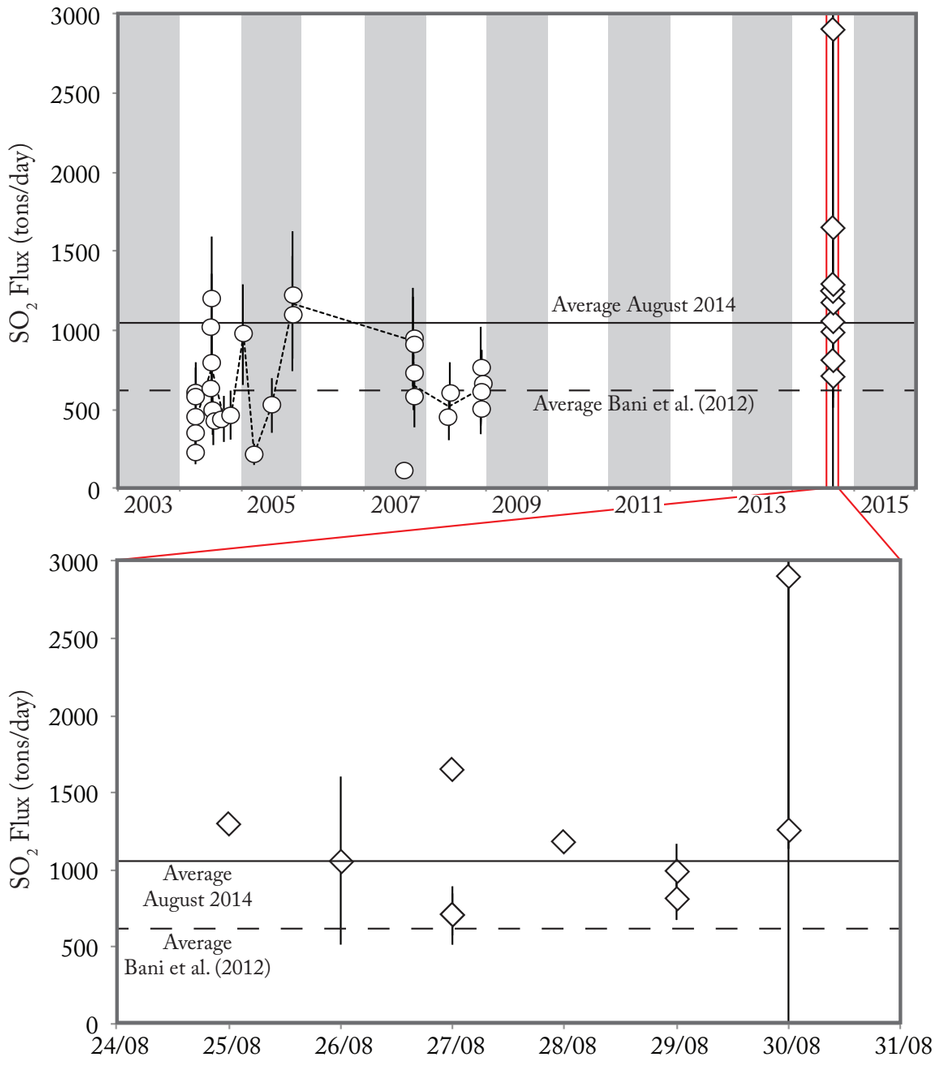

Fig. 5.2 Fluctuations in SO_2 flux at Yasur since 2003. Diamonds represent analyses from this study, while circles represent data from Bani et al. (2012). Averages of SO_2 flux from both studies are shown as horizontal lines (see Table 5.1). Temporal fluctuations apparent in the dataset from Bani et al. (2013) are shown by the dotted line.

later days (Table 5.1). Boat traverses also enabled the SO_2 flux from Benbow to be measured, suggesting the two vents both contribute to the total SO_2 flux of 6000-7000 t d^{-1} for Ambrym.

U-Th-Ra Isotopes

Full analytical procedures for U-Th-Ra isotope analysis are presented in Appendix 1. U-Th-Ra isotopes were analysed on nine samples (Table 5.2), including prehistoric tephra from Yasur and pre-Yasur activity, as well as the Siwi Ignimbrite (Fig. 5.1). These represent

Table 5.1 SO_2 flux data for Yasur and Ambrym volcanoes, Vanuatu

	Date	Type	Scan Location	Wind Speed (m/s)	Wind Direction (°)	SO_2 Flux (t/d)	±	Cycles
Yasur								
	25 Aug. 2014	Traverse	-	5	55	1296	-	-
	26 Aug. 2014	Scan	Site 3	8	22	1057	543	38
	27 Aug. 2014	Traverse	-	9	66	1647	-	-
		Scan	Site 1	8	35	712	138	65
		Scan	Site 2	8	35	702	190	36
	28 Aug. 2014	Traverse	-	5	40	1181	-	-
	29 Aug. 2014	Scan	Site 2	8	35	986	179	89
		Scan	Site 2	8	35	809	140	213
	30 Aug. 2014	Scan	Site 4	10	85	2902	1767	22
		Scan	Site 4	10	85	1261	2475	55
Ambrym								
	19 Aug. 2014	Traverse - Marum Only		6	22	2980	-	-
		Traverse - Marum Only		6	22	3016	-	-
	20 Aug. 2014	Boat Traverse - Whole Plume		10	104	5949	-	-
		Boat Traverse - Benbow Plume		10	97	3784	-	-
Yasur Average (Bani et al. 2012)						633		
Ambrym Average (Bani et al. 2012)						5440		

a subset of samples analysed for major and trace elements by Firth et al. (2014; in review) and complement the uranium-series isotope dataset compiled for recent (post 1975) Yasur lava bombs (Turner et al. 1999; Turner et al. 2001; Handley et al. in prep.).

The majority of samples record ($^{234}U/^{238}U$) within error of one, suggesting they are unaltered. They plot to the right of the equiline (Fig. 5.3a), in the area of ^{238}U excess. Prehistoric

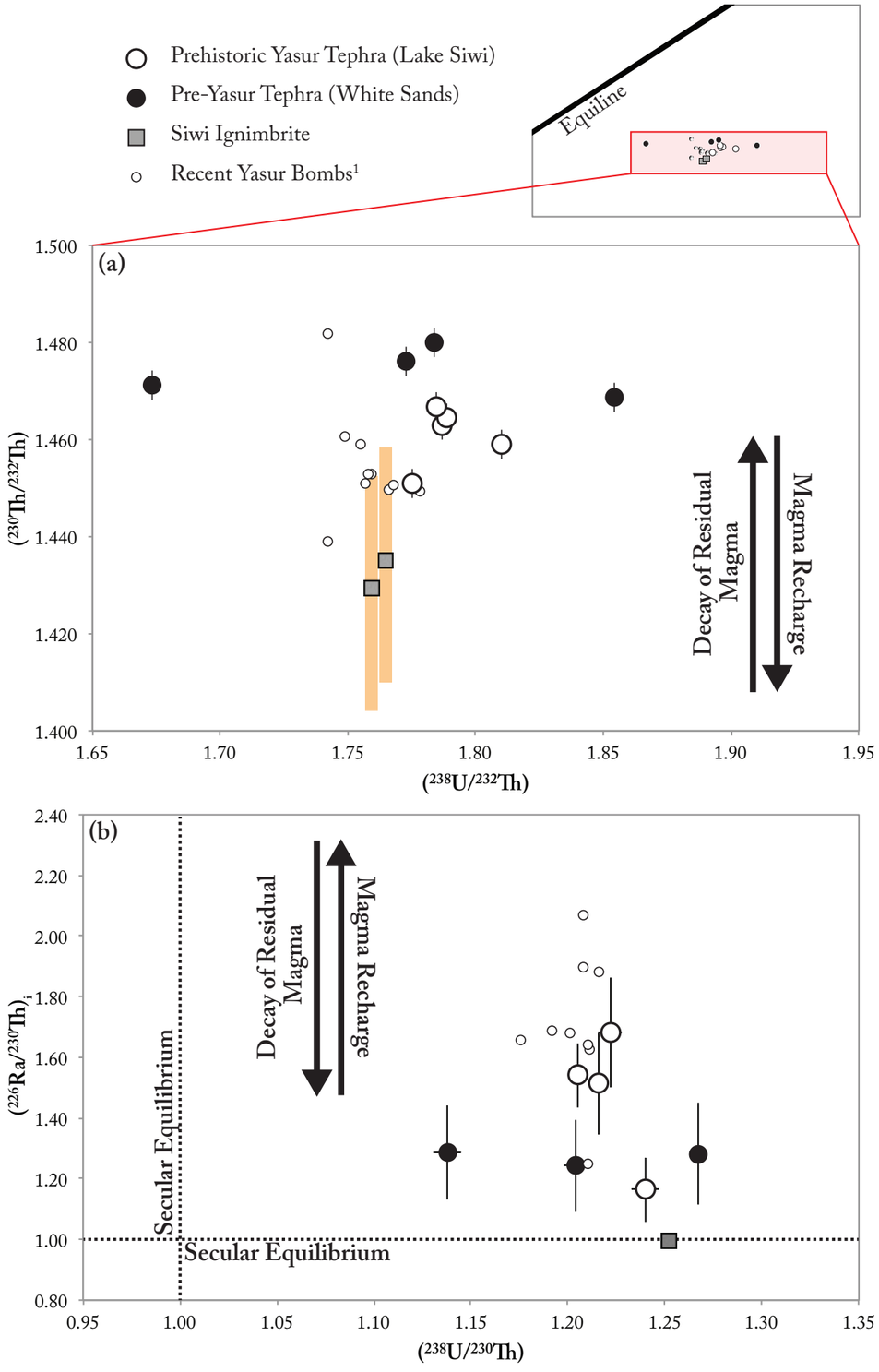

Yasur tephras display a range in ($^{230}Th/^{232}Th$) of between 1.452 and 1.482. Samples erupted during the current episode of persistent activity display lower ($^{230}Th/^{232}Th$) than those erupted during earlier eruptive episodes. Similarly these samples display a much narrower range in ($^{238}U/^{232}Th$) (1.775 to 1.81, compared with 1.673 to 1.855 for the older samples – Table 5.2). All prehistoric samples from Yasur display ($^{226}Ra/^{230}Th$) excesses, ranging from 1.165-1.758 (Fig. 5.3b), with samples erupted during the current eruptive episode displaying the greatest variation.

The age of the Siwi Ignimbrite remains uncertain, making accurate age corrections difficult. A lack of ($^{226}Ra/^{230}Th$) disequilibrium in one sample from this unit (Table 5.2) suggests an age >8 kyr. Given the uncertainty in age, corrections are made for various ages between 8 and 24 kyr (Fig. 5.3a). The latter age is based upon the inferred average recurrence interval of ignimbrite eruptions in the caldera (Firth et al. in review). A younger age draws ($^{230}Th/^{232}Th$) towards that of post-ignimbrite samples, with ages <12 kyr yielding ($^{230}Th/^{232}Th$) overlapping that of prehistoric Yasur samples (Fig. 5.3a). ($^{238}U/^{232}Th$) in both ignimbrite samples is comparable with the more recently erupted volcanic rocks.

DISCUSSION

Degassing and conduit geometry

While gas flux measurements from Yasur are sporadic and only date from the last decade, intermittent historical reports, such as those of Captain James Cook in 1774 (Cook 1777) suggest degassing has persisted over several hundred years, at least. Measurements collected in August 2014 suggest a mean SO_2 flux for Yasur of 1048 t d^{-1}. This is higher than the average of 633 t d^{-1} measured over 293 traverses of the plume between 2004 and 2008 by Bani et al. (2012) (Fig. 5.2). By contrast, data presented here was collected over a period of one week. Combined, both datasets show that Yasur exhibits significant fluctuations about the mean gas flux.

Fig. 5.3. a) U-Th Equiline Diagram, showing samples from Yasur. These plot below the equiline (see top). The variation in ($^{230}Th/^{232}Th$) as a result of uncertainties in age for the Siwi Ignimbrite (8-24 ka) are shown by shaded rectangles. Standard errors for the remainder of the samples are shown by error bars. b) Plot of $(^{226}Ra/^{230}Th)_i$ versus ($^{238}U/^{230}Th$), showing samples from Yasur. The effects of radioactive decay and magma recharge are shown on both diagrams. [1]Recent Yasur Bombs represent data from Turner et al. (1999), Turner et al. (2001) and Handley et al. (in prep.).

Table 5.2 Uranium-series data for prehistoric Yasur and Siwi Ignimbrite samples

Number	**1**	**2**	**2 *repl***	**3**	**4**	**5**	**5 *repl***	**6**	**7**	**8**	**9**	**TML**	**TML**
Sample No.	**1920R**	**3.23**	**3.23**	**3.35**	**3.44**	**2.2**	**2.2**	**2.6**	**2.11**	**WS6**	**WS3**	**TML**	**TML**
Type*	Lava	Tephra	Tephra	Tephra	Tephra	Tephra	Tephra	Tephra	Tephra	Ig.	Ig.	Standard	Standard
Sample Age (yr B.P.)	94	64	64	111	229	744	744	1314	1814	16000	16000	-	-
U (ppm)	0.98	1.21	1.53	1.57	0.94	1.18	1.18	1.22	1.37	1.66	1.63	9.75	10.55
±	1.24E-3	1.39E-3	0.00	2.67E-3	8.98E-4	1.34E-3	2.21E-3	1.96E-3	1.42E-3	1.35E-3	1.51E-3	7.38E-3	1.65E-2
Th (ppm)	1.67	2.05	2.66	2.63	1.61	2.02	2.01	2.22	2.24	2.87	2.81	26.98	29.09
±	2.68E-11	7.50E-12	3.06E-11	3.17E-12	4.80E-12	5.77E-12	6.73E-12	4.53E-12	4.52E-12	8.97E-12	1.24E-11	3.07E-11	1.29E-11
Ra (fg/g)	415.35	-	667.1	497.5	443.14	-	414.84	469.47	473.49	-	464.23	3463.08	-
±		-			50.9	-	9.37	8.76	9.71	-		92.7	-
($^{234}U/^{238}U$)	1.011	1.005	1.011	1.002	1.001	1.001	1.001	1.004	1.001	1.009	1.014	0.998	1.016
±	0.002	0.002	0.002	0.003	0.002	0.002	0.003	0.003	0.002	0.001	0.002	0.002	0.003
($^{238}U/^{232}Th$)	1.785	1.787	1.789	1.810	1.775	1.773	1.784	1.673	1.855	1.759	1.765	1.097	1.085
±	0.002	0.002	0.001	0.003	0.002	0.002	0.003	0.003	0.002	0.001	0.002	0.001	0.002
($^{230}Th/^{232}Th$)	1.467	1.463	1.464	1.459	1.452	1.478	1.482	1.472	1.469	1.474	1.480	1.072	1.065
±	0.003	0.004	0.003	0.005	0.005	0.005	0.004	0.005	0.003	0.003	0.002	0.005	0.003
($^{238}U/^{230}Th$)	1.217	1.222	1.206	1.240	1.223	1.201	1.205	1.139	1.268	1.253	1.252	1.023	1.014
±	0.004	0.005	0.004	0.007	0.006	0.005	0.006	0.006	0.004	0.003	0.003	0.005	0.004
($^{226}Ra/^{230}Th$)	1.515	-	1.542	1.157	1.686	-	1.243	1.283	1.281	-	0.997	1.067	-
±	0.018	-	0.025	0.017	0.155	-	0.022	0.019	0.021	-		0.023	-
$(^{230}Th/^{232}Th)_i$	1.467	1.463	1.464	1.459	1.451	1.476	1.480	1.469	1.463	1.429	1.435	-	-
$(^{226}Ra/^{230}Th)_i$	1.537	-	1.557	1.165	1.758	-	1.336	1.500	1.617	-	-	-	-

repl = replicate analysis; Ig = Ignimbrite; Samples: 1-5 - Persistent Activity; 6-7 - Higher Magnitude/Lower Frequency Eruptions; 8-9 - Siwi Ignimbrite

Differences in results between traverse and scan data collected in 2014 are a function of the differing methods of each procedure (see Appendix). The higher variability of scan passes reflects the highly pulsatory nature of Yasur's gas emissions, which are thought to result from bubble bursts associated with Strombolian explosions (Oppenheimer et al. 2006; Bani et al. 2013). This is most strongly seen in data collected from the crater rim, which records individual bursts and subsequent lulls in gas emission. A combination of traverse and scanning data, especially a few km downwind of the volcano (e.g. Sites 1 and 2), thus represent the most reliable average gas flux.

Based upon SO_2 flux estimates and pre-eruptive sulphur contents, deduced from melt inclusions, Métrich et al. (2011) estimated a bulk magma degassing rate (Q) for Yasur of ~4100 kg s^{-1}. Following the model of Stevenson and Blake (1998), this can be used to estimate the

$$R = \left(\frac{Q.\mu_d}{\pi(R^*)^2.Ps.g.\Delta\rho}\right)^{1/4} \quad (1)$$

where μ_d is the viscosity of the degassed magma; R^* is the dimensionless radius of upwelling magma, found by Stevenson and Blake (1998) to equal 0.6; Ps is the Poiseuille Number, again constrained by Stevenson and Blake (1998) at 0.64; g is gravitational acceleration; and $\Delta\rho$ is the change in density between the volatile-rich and degassed, volatile-poor magma. The viscosity of the degassed magma at Yasur is estimated at 18260 Pa s, calculated from glass compositions using the equations of Giordano et al. (2008), assuming ≥94 % water loss (Métrich et al. 2011) and temperatures of 1050°C (based upon minimum clinopyroxene crystallisation temperatures - Firth et al. 2014). A density difference of 60 kg m^{-3} is used, following calculations using the method of Bottinga and Weill (1970), assuming a pre-degassing magmatic H_2O content of 1.0 wt.% (Métrich et al. 2011) and almost complete volatile loss during degassing. Accordingly a conduit radius of ~5.5 m is estimated for Yasur. Within Yasur's crater, three main vents are active, representing the upper openings of conduits that supply magma from depth (Oppenheimer et al. 2006). Assuming an equal output from each vent, conduit radii of ~4.2 m are estimated (Table 5.3). This is consistent with visual observations of the vents made in August 2014.

For comparison, Stevenson and Blake (1998) estimated a conduit radius of 4-10 m for Stromboli. This result was based upon flux of H_2O rather than SO_2, however. Recalculation using an average SO_2 flux of 3-9 kg s^{-1} (Allard et al. 1994; 2008) and melt inclusion compositions

from Métrich et al. (2010) suggests a potentially narrower conduit radius for Stromboli, in the order of ~1.2 m (Table 5.3). Previous SO_2-based calculations for the Villarrica lava lake suggest it is supplied through a conduit of 2.2-2.7 m radius (Witter et al. 2004), while calculations by Stix (2007) suggest a 2-6 m conduit radius for Masaya. Conduit radius estimates using literature values for a number of other persistently-active volcanoes are presented in Table 5.3. Lava lakes on both Ambrym and Erebus (Antarctica) are thought to be fed by conduits with radii of 3.5-4.5 m. Visual observation of the conduit following draining of the lava lake at Erebus suggest a width of 5 – 10 m (Dibble et al. 2008). These observations suggest that conduit radius is similar between persistently-active volcanoes, regardless of their eruptive style. By comparison, Stevenson and Blake (1998) estimate a conduit radius >20 m for Mt St Helens, following its paroxysmal 1980 eruption.

Gas fluxes at persistently-active volcanoes fluctuate over timescales of minutes to years (Allard et al. 2008; Sweeney et al. 2008). Day-to-day fluctuations in SO_2 flux at Yasur are apparent within the dataset of Bani et al. (2012). Day-to-day fluctuations in the dataset presented here are less apparent, however the large errors on some analyses may mask smaller fluctuations. Bani and Lardy (2007) identified a correlation between SO_2 flux and eruptive behaviour, as recorded by seismic events, with peak gas fluxes accompanying the highest number of seismic events. This coincidence may reflect a relationship between elevated gas fluxes and more intense eruptive behaviour, although greater attention to the specific changes in frequency and magnitude of explosions is needed to confirm this. Palma et al. (2011) examined similar fluctuations from Villarrica, where SO_2 fluxes have been found to vary by ~690 t d^{-1} over a few days. They show that SO_2 flux is a function of conduit radius, sulphur loss and the change in magma density driven by degassing. The latter two variables are intrinsically linked and were favoured as the most-likely driver of short-term fluctuations in gas fluxes at Villarrica (Palma et al. 2011). Similarly, significant visual changes in conduit geometry have not been observed at Yasur over recent years, suggesting little change to the conduit radius over this period. A dichotomous degassing regime has previously been identified at Yasur, with background degassing maintained by regular bursting of small bubbles with low SO_2/HCl (~2), compared with less frequent, high-energy bursts that release SO_2-rich gas (SO_2/HCl ~30) (Oppenheimer et al. 2006; Bani et al. 2013). The latter may have a deeper derivation and are thought to represent gas slugs formed by foam collapse (Bani et al. 2013). Heightened daily SO_2 fluxes potentially represent a higher proportion of high-energy, high-SO_2 bursts. Thus, like Villarrica, fluctuations

Table 5.3 Comparison of calculated degssing budget and conduit radius between persistently active volcanoes

	Ambrym						
	Yasur	Marum	Benbow	Stromboli	Erebus	Villarrica	Masaya
SO_2 Flux (t/d)	633 [3]	3000	3000	259 [6]	61 [8]	460 [12]	800 [13]
ΔS (ppm)	969 [1]	1500 [4]	1500 [4]	2000 [7]	600 [9]	820 [12]	410 [14,15]
Degassing Budget (m^3/s)	**2.09**	**6.15**	**6.15**	**0.4**	**0.08**	**1.75**	**6.09**
Density Difference (kg/m^3)*	60 [1,2]	70 [5]	70 [5]	90 [7]	90 [10,11]	100 [12]	110 [15]
Viscosity (Pa s)^	18260 [1,2]	3487 [5]	3487 [5]	871 [7]	116570 [10,11]	1780 [12]	4716 [15]
Conduit Radius (m)	**4.16#**	**4.55**	**4.56**	**1.26**	**3.52**	**2.73**	**3.32**

* Calculated from references below using equations from Bottinga and Weil (1970).

^ Calculated from references below using equations from Giordano et al. (2008)

Assuming three condiuts of equal radius

References: [1] Metrich et al. (2011); [2] Firth et al. (2014); [3] Bani et al. (2012); [4] Allard et al. (2009); [5] Chapter 3; [6] Allard et al. (2008); [7] Metrich et al. (2010); [8] Sweeney et al. (2008); [9] Oppenheimer et al. (2009); [10] Kelley et al. (2008); [11] Oppenheimer et al. (2009); [12] Witter et al. (2004); [13] Mather et al. (2006); [14] Sadofsky et al. (2008); [15] Wehrmann et al. (2011)

in the SO_2 flux at Yasur are linked to variations in the initial volatile content of the magma contributed to the conduit, or differences in the volume of magma supplied. As such, gas flux variability potentially reflects overturn of the magma supplying volatiles, signifying the occurrence of regular magma replenishment.

Constraining magma replenishment using uranium-series isotopes

Equilibrium between RTF processes is expected to buffer the chemical composition of a magma chamber, both in terms of elements (e.g. O'Hara 1977; Albarède 1985; O'Neill and Jenner 2012; Lee et al. 2014) and isotopes (Pyle 1992; Hughes and Hawkesworth 1999). The uranium-series isotopes have relatively short half-lives, ranging from seconds to tens of thousands of years (Bourdon et al. 2003). Radioactive decay of these isotopes pushes them towards secular equilibrium, while magma replenishment operates in the other direction, returning them towards the starting composition (Fig. 5.3). When recharge operates at a similar rate to radioactive decay, the activity ratio becomes buffered. This was investigated theoretically by Hughes and Hawkesworth (1999), who showed that ^{238}U-^{230}Th disequilibria

can be maintained for significantly greater periods in an RTF system than would be expected if closed-system radioactive decay is assumed. This highlights a limitation in the traditional use of uranium-series isotopes to investigate magmatic processes, yet offers a unique means of quantifying magma replenishment rates if a system is known to be regularly replenished. In the case of Yasur, the constant magma output rate, constant composition of its erupted products (Firth et al. 2014) and persistent gas flux are all strong indicators of regular replenishment.

Samples erupted from Yasur during its latest episode of persistent eruption, (600-800 years; Firth et al. 2014) have (^{230}Th/^{232}Th) ratios that range from 1.452-1.467. This is a limited data spread, with values almost within error of each other (Table 5.2). Values presented here are consistent with recent (post 2005) volcanic bombs from the volcano, which extend the range in (^{230}Th/^{232}Th) to 1.449 (Handley et al. in prep.). Historical (1975 and 1993) volcanic bombs from Yasur analysed by Turner et al. (1999) display a wider range in (^{230}Th/^{232}Th) (1.439-1.482). Age corrected (^{226}Ra/^{230}Th) for samples erupted from Yasur in the last ~800 years range from 1.165 to 1.758. This overlaps with the lower bounds of the range in (^{226}Ra/^{230}Th) for historical bombs from Yasur (1.250-2.069) (Turner et al. 2001; Handley et al. in prep). Thus (^{230}Th/^{232}Th) shows relatively little variation in magmas from Yasur, while (^{226}Ra/^{230}Th) varies considerably. This observation suggests that processes that buffer uranium-series isotopes, such as magma recharge, operate on timescales that are significant with respect to the half-life of ^{226}Ra (~1.6 kyr), but not that of ^{230}Th (~75 kyr).

The Hughes and Hawkesworth (1999) model further constrains rates of magma replenishment. This model replicates RTF processes through two stages, with chamber evolution (radioactive decay and fractional crystallisation) extending for a set period of time (*t*), followed by replenishment and binary mixing between chamber and replenishment magmas. This follows the RTF model of O'Hara (1977), in which mixing occurs at the end of the cycle, prior to chamber evacuation. Albarède (1985) offered a variation to this scenario, in which mixing occurs at the beginning of the cycle. This increases the role of fractionation in the model, meaning that mixed liquid is fractionated, instead of the recharge magma. The Albarède (1985) scenario seems more realistic, especially if recharge is restricted to proportionally small volumes of magma, relative to the total chamber volume. The equations governing each individual process are unchanged from Hughes and Hawkesworth (1999), however, the order of chamber evolution followed by mixing is reversed.

The equation for mixing is:

$$\left(\frac{x}{y}\right) = \frac{\lambda_x \cdot \left(\frac{[x]_c.V_c + [x]_i.V_i}{M_x}\right)}{\lambda_y \cdot \left(\frac{[y]_c.V_c + [y]_i.V_i}{M_y}\right)} \qquad (2)$$

where (*x/y*) is the activity ratio of isotopes *x* and *y*; $[x]_c$ and $[x]_i$ are the concentrations of isotope *x* in the residing chamber magma and the incoming magma respectively; V_c and V_i are the volumes of chamber and incoming magma; λ_x is the decay constant for isotope x; and M_x is the atomic masses of isotope x.

During chamber evolution, the magma composition is influenced by radioactive decay:

$$(d) = (d)_O.e^{-\lambda t} + (p).(1 - e^{-\lambda t}) \qquad (3)$$

and fractional crystallisation:

$$X = X_O.(1 - f)^{(D-1)} \qquad (4)$$

where (p) and (d) are the activity ratios of the parent and daughter respectively; $(d)_O$ is the initial activity ratio of the daughter; λ is the decay constant of the daughter isotope; *t* is the recharge interval; X_O and *X* are the initial and final concentrations of the daughter element; *f* is the degree of fractionation; and *D* is the partition coefficient for element *X*.

To investigate the recharge interval, four variables remain to be constrained. Samples plotting furthest from secular equilibrium (i.e. lowest (^{230}Th/^{232}Th) and highest (^{226}Ra/^{230}Th)) are assumed to have undergone the least amount of radioactive decay, so are used as a starting composition. Trace element modelling suggests f = 0.3-0.35, consistent with estimates by Métrich et al. (2011) for fractionation in the upper plumbing system. Partition coefficients between melt and crystals were calculated for Yasur (D_U = 0.0003; D_{Th} = 0.001; D_{Ra} = 0.007) following methods described by Blundy and Wood (2003) and Fabrizzio et al. (2009), using average mineral and glass compositions (Firth et al. 2014). The volumes V_c and V_i are expressed as a proportion of the total chamber volume. If the chamber is completely evacuated to make way for the next recharge event, V_i = 1 and V_c = 0. Values for V_c and V_i are unknown, so a suite of solutions using different values have been generated. Models in which V_i <0.7 cross secular equilibrium for (^{226}Ra/^{230}Th), taking predictions into the area of ^{226}Ra deficit (Fig. 5.4a). This is

inconsistent with samples from Yasur, so such models have been discarded.

Models are presented graphically in Figure 5.4, with panel (d) showing an ideal scenario, in which the recharge interval explains the full range in (^{230}Th/^{232}Th) and (^{226}Ra/^{230}Th). Given the half-lives of ^{230}Th and ^{226}Ra replenishment intervals of 100 years require both (^{230}Th/^{232}Th) and (^{226}Ra/^{230}Th) to be extensively buffered. This is corroborated by the model which predicts (^{230}Th/^{232}Th) to be invariant with such recharge intervals (Fig. 5.4a). Some variation is apparent in (^{226}Ra/^{230}Th) with lower V_i, as a result of mixing with increasing proportions of the fractionated chamber component, however the predicted ratios do not correlate well with data from Yasur. Shorter recharge intervals would further buffer (^{230}Th/^{232}Th) and (^{226}Ra/^{230}Th). As the recharge interval increases the variability in (^{230}Th/^{232}Th) and (^{226}Ra/^{230}Th) similarly increases (Fig. 5.4c,d). Recharge intervals of 5000 years account for a much greater proportion of the data from Yasur (Fig. 5.4c), however still cannot explain the full range in (^{230}Th/^{232}Th) and (^{226}Ra/^{230}Th). A recharge interval of 11,000 years, with $V_i = 0.8$, returns the best approximation of data from Yasur (Fig. 5.4d).

While this provides a solution to explain recharge rates at Yasur, it seems unrealistic given the history of the volcano. A number of successive recharge events are required to buffer the system and achieve a steady-state composition (Hughes and Hawkesworth 1999). As the recharge interval increases, the time taken to achieve this steady-state composition also grows. Thus an 11,000 year recharge interval requires that the system has been buffered for substantially longer than this amount of time. At least two catastrophic, caldera-forming eruptions have completely evacuated the magma chamber within the last ~45 kyr (Firth et al. in review), meaning that a steady-state composition could not have been achieved with a recharge interval of this magnitude. Furthermore, tephra records suggest a constant magma output, which can be interpreted as a proxy for steady-state conditions, have only been maintained for 800 years or less (Firth et al. 2014). Additionally, the high V_i required by these models is inconsistent with observed activity at Yasur, which is more easily reconciled with smaller

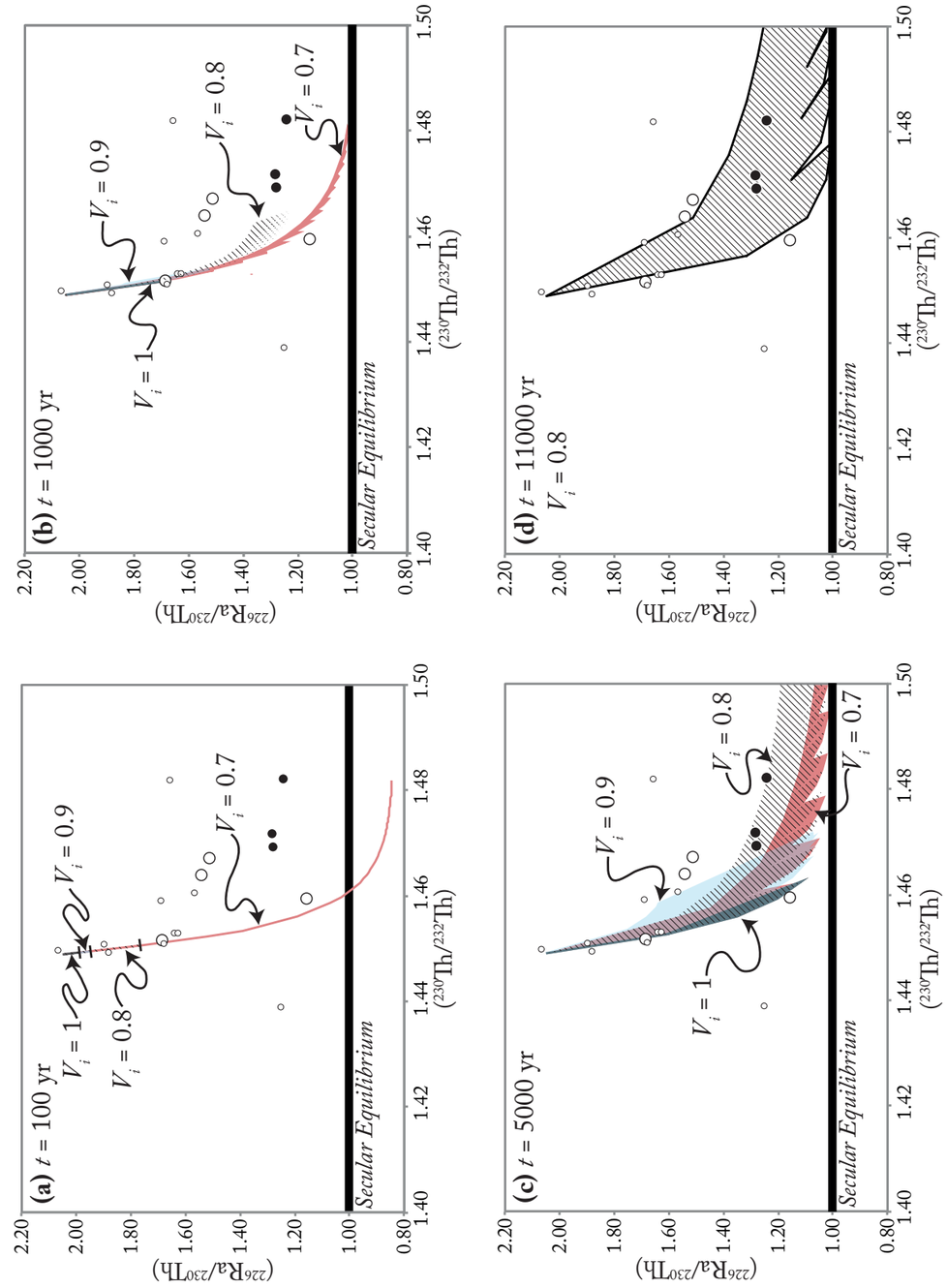

Fig. 5.4 Uranium-series models assuming different replenishment intervals (a – 100 years; b – 1,000 years; c – 5,000 years; d – 11,000 years) and replenishment volumes overlaid on plots of (^{226}Ra/^{230}Th) versus (^{230}Th/^{232}Th). The model best predicting the data from Yasur is shown in panel *d*. Different recharge volumes ranging from $V_i = 0.7$ to $V_i = 1$ are shown in panels *a*, *b*, and *c*. In panel *a* all models overlap, as this recharge interval produces negligible variation in (^{230}Th/^{232}Th). Tick marks show the end of models for $V_i = 1$, $V_i = 0.9$ and $V_i = 0.8$.

batches of magma (relative to the total reservoir volume) added regularly, rather than episodes of complete evacuation and re-filling.

An alternative approach: thermal models

The recharge rate can alternatively be estimated using thermal numerical models, which can calculate the minimum volume of magma required to sustain a magma reservoir in an eruptible state (Annen et al. 2008). This is typically interpreted as having >40-60% melt (Lejeune and Richet 1995), as crystals create a rigid framework, inhibiting melt movement at lower melt fractions. The simplest numerical solution, which involves cooling of a spherical magma body undergoing recharge and tapping at steady-state, is given by:

$$q_{in}(t) = \frac{4\pi kR(T_{cr}-T_\infty)}{\rho(c_p(T_{inj}-T_{cr})+fL}\, erfc\left(\frac{R}{2}\sqrt{\frac{\rho c_p}{kt}}\right)^{-1} \qquad (5)$$

where q_{in} (t) represents the magma flux (m^3/s); k is thermal conductivity (2.24 W/m K); R is the chamber radius; T_{cr} is the critical temperature above which magma remains eruptible; T_∞ is the far-field temperature of the country rock, assumed to be an infinite medium; T_{inj} is the temperature of the replenishment magma; ρ is the magma density; c_p is the magma heat capacity (1000 J/kg K); L is latent heat ($3x10^5$ J kg^{-1}); t is the time over which the magma body remains eruptible and f is the degree of crystallisation (Annen et al. 2008). From this, a recharge interval (t_R; years) can be calculated as:

$$t_R = \frac{t}{\left(\frac{q_{in}}{V}\right)} \qquad (6)$$

where V is the chamber volume equivalent to radius R.

A number of variables required for this model are poorly constrained for the Yasur system, however a range of likely values are used in order to generate a suit of potential solutions. Here, the model is used to constrain magma replenishment intervals sustaining the current episode of eruptive activity, so t = 600 years. Magma density is estimated at 2650 kg m^{-3} based upon the method of Bottinga and Weill (1970), using average glass compositions from Yasur (Métrich et al. 2011; Firth et al. 2014). The value for f is set at 0.3, as for the uranium-series model. The temperature of the replenishment magma (T_{inj}) is conservatively estimated at 1100°C, based upon the maximum temperature of mineral crystallisation estimated for Yasur (Firth et al. 2014).

Country rock temperature (T_∞) is a function of magma chamber depth. Métrich et al. (2011) suggest magma storage at depths of <1.8 km for Yasur, equivalent with T_∞ = 36°C, assuming a geothermal gradient of 20°C km^{-1}. The critical temperature is the most poorly constrained variable, and for this reason, a suite of solutions were calculated for varying T_{cr} (800-1100°C) (Fig. 5.5). T_{cr} must be <1000°C, as magma temperatures of this magnitude were recorded by thermal imaging within the crater. The magma chamber radius is also poorly constrained. Solutions are provided for a range of radii, equivalent to chamber volumes of 0.1-1 km^3 (Fig. 5.5). Greater chamber volumes return rapid recharge intervals of less than a year. This suite of input parameters suggest a magma flux of 0.058-75 m^3 s^{-1}, equivalent to recharge intervals of <50 years (Fig. 5.5).

Comparison between the magma flux calculated in Equation 5 and the degassing budget calculated by Métrich et al. (2011) suggests a recharge interval of between 3 and 7 years is required to provide the volume of magma necessary to sustain SO_2 fluxes seen at Yasur. Longer recharge intervals are unlikely to provide sufficient magma for degassing, while shorter recharge intervals require higher gas fluxes than those observed. The most likely scenario at Yasur thus involves recharge intervals of ~5 years, with a chamber volume of 0.4-0.5 km^3 (Fig. 5.5). This recharge interval is of a similar order of magnitude to observed fluctuations in both eruptive intensity and gas output (Bani and Lardy 2007), which may be taken as evidence for magma replenishment.

The thermal model presented here assumes a spherical magma chamber, however, Marsh (1989) notes that chambers may vary widely in shape and Annen et al. (2008) suggest that sills are the most common chamber shape in arc settings. Nevertheless, persistently-active volcanoes are commonly associated with structural features, such as local or regional faults. Yasur sits at the intersection of two local faults within the Yenkahe Caldera (Merle et al. 2014). Open-vent volcanoes including Villarrica and Ambrym are located on regional lineaments associated with tectonic stresses (Callot et al. 1985; Bohm et al. 2002). Similarly, Tibaldi (2001) suggests that a NE-trending weakness zone dissects Stromboli. Cigolini et al. (2008) argue that this is exploited by an ellipsoidal magma chamber or a dyke that is concordant with the regional stress. Such chamber shapes have an aspect ratio (diameter/thickness) <1, and have been shown by Dosseto et al. (2008) to behave similarly to spherical magma chambers. Thus, the calculations presented offer a reliable approximation of the magma flux required to sustain the Yasur chamber in an eruptible state.

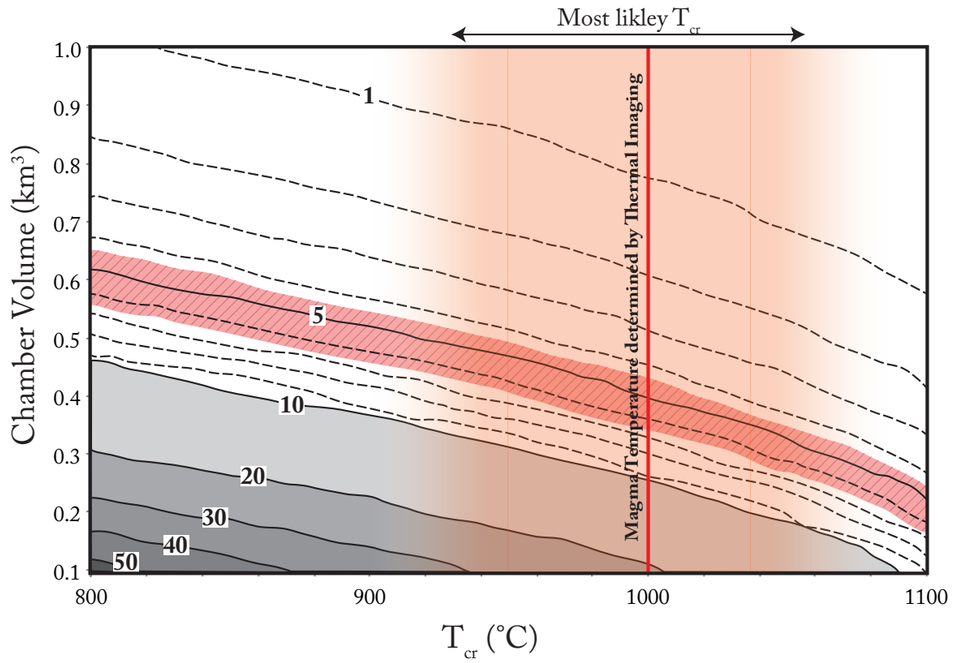

Fig. 5.5 Contoured plot showing the recharge interval, in years, required to sustain Yasur's magma chamber in an eruptible state during the most recent eruptive episode (600 years), as a function of T_{cr} and chamber volume. These two variables are chosen, as they are the least well-constrained variables used in the thermal model. The red shaded area shows the most likely values of T_{cr}, with magma temperature during eruption shown. The striped area represents the overlap between the magma flux predicted by the thermal model and the magma flux required to sustain the degassing budget at Yasur (Table 5.3). As such, this marks the most likely solutions for recharge intervals at Yasur.

Explaining uranium-series variation

The thermal model, in concert with degassing information, favours rapid magma replenishment rates for Yasur, while the uranium-series model cannot replicate data from Yasur using a feasible recharge interval. Estimations of magma chamber residence times for persistently-active volcanoes such as Stromboli (Pyle 1992; Francalanci et al. 1999; Gauthier et al. 2000; Bragagni et al. 2014) and Piton de la Fournaise (Sigmarsson et al. 2005) are compatible with the replenishment intervals suggested by the thermal model for Yasur. Thermal modelling by Giberti et al. (1992) and Harris and Stevenson (1997) suggests activity at Stromboli is maintained by magma fluxes of 200-1300 kg s^{-1}. Assuming a chamber volume of 0.001-0.1 km^3 (Giberti et al. 1992; Gauthier and Condomines 1999; Francalanci et al. 1999), Equation 6 requires recharge intervals of 0.07-42 years to have sustained these fluxes over the 1300 years of Stromboli's most recent eruptive episode. Such figures are comparable with those estimated

for Yasur by thermal modelling. Additional support for recharge intervals of this magnitude is provided by mineral zoning patterns from Stromboli (Landi et al. 2004; Armienti et al. 2007) and Arenal (Streck et al. 2002), which are indicative of magma recharge and mixing during crystal growth. Recharge intervals of 6-32 years are estimated for Stromboli, assuming crystal growth rates of $1x10^{-10}$-$2x10^{-11}$ cm s^{-1} and mineral zone widths of ~200 µm (Armienti et al. 2007). As such, recharge intervals of years to tens of years are favoured for Stromboli and other persistently-active volcanoes, supporting thermal model estimates of recharge interval for Yasur.

Why then do uranium-series isotopes not record magma replenishment on these timescales? Comparison with uranium-series data from other persistently-active volcanoes (Sigmarsson et al. 2005; Tepley et al. 2006; Sims et al. 2013; Bragagni et al. 2014) shows Yasur is not unique in displaying a wider variation in these isotopes than predicted for recharge intervals of <100 years by the uranium-series model. These volcanoes display a similar or greater range in ($^{230}Th/^{232}Th$) to Yasur, however many have a smaller range in ($^{226}Ra/^{230}Th$). The uranium-series model cannot replicate these datasets, as variations seen in ($^{230}Th/^{232}Th$) and ($^{226}Ra/^{230}Th$) require magma addition on different timescales. Recharge intervals of tens of thousands of years are needed to produce variation seen in ($^{230}Th/^{232}Th$), while ($^{226}Ra/^{230}Th$) requires recharge intervals of hundreds to thousands of years.

Volcanoes such as Stromboli, Arenal and Piton de la Fournasie, display consistent trends in ($^{230}Th/^{232}Th$) or ($^{226}Ra/^{230}Th$) when plotted in time-series (Bragagni et al. 2014; Tepley et al. 2006; Sigmarsson et al. 2005). These show repeated variation in both isotope pairs over timescales of tens of years, and have been interpreted to represent replenishment events followed by subsequent mixing (Sigmarsson et al. 2005; Tepley et al. 2006; Bragagni et al. 2014). Nevertheless, such variations cannot be reconciled with trends predicted by uranium-series models, which require both isotope ratios to be invariant for recharge intervals of this magnitude (Fig. 5.6a). Thus, simple RTF processes, as envisaged by Hughes and Hawkesworth (1999) cannot be reconciled with uranium-series isotope datasets from these volcanoes, and instead call for a more complex scenario.

One possibility is that RTF processes are operating, but are not behaving as predicted by Hughes and Hawkesworth (1999). Variability in either the timing of recharge or the composition of the recharge magma might occur. Gauthier et al. (2000) used ^{210}Pb, ^{210}Po and ^{210}Bi isotopes to show that the recharge interval at Stromboli varies between 75 and 213 days. These figures

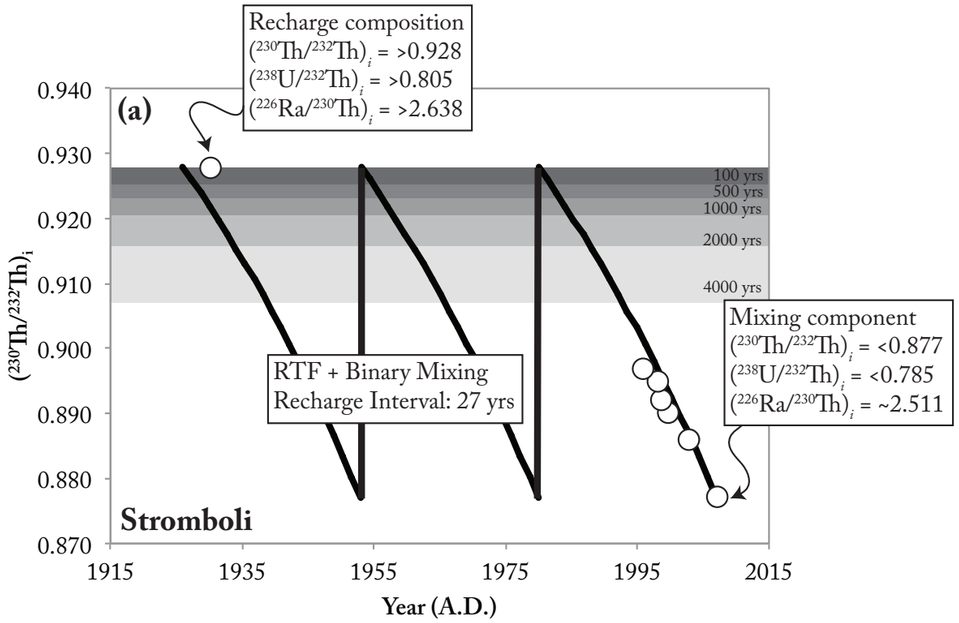

Fig. 5.6 Variation in ($^{230}Th/^{232}Th$) with eruption age at Stromboli (a) (after Bragagni et al. 2014) and Yasur (b). Potential mixing scenarios between recharge magmas and an older crystal mush component are shown for both volcanoes. Grey shaded contours also show the predictions of the Hughes and Hawkesworth (1999) model for a range of recharge intervals. Data from Stromboli and Yasur plot on different sides of the equiline, hence recharge and decay operate in different directions on each panel.

represent recharge to the volcanic conduit, rather than the wider shallow plumbing system, however their variability is potentially mirrored by the larger system. Nevertheless, variation of hundreds and thousands of years is still required to explain the Th and Ra isotopes at Yasur and many other persistently-active volcanoes. Similarly, the recharge interval might remain constant, whilst the recharge magma varies in composition between each recharge event. During short recharge intervals (i.e. <100 years) predicted by thermal modelling, however, the activity ratio is almost unaffected by radioactive decay, meaning that model predictions effectively form a mixing array between various recharge compositions. Again, this cannot explain data from Yasur or other persistently-active volcanoes.

Another possibility is that RTF processes are operating as originally envisaged, but are overprinted by other crustal processes, such as mixing or assimilation. Assimilation with a geochemically distinct crustal component is unlikely at Yasur given the negligible variation noted in long-lived isotopes, such as Sr, Nd and Hf (Firth et al. in review; Handley et al. in prep.). Nevertheless, assimilation with geochemically similar, but older, material cannot be ruled out. Magma output rates at persistently-active volcanoes and their bulk magma degassing rates, support the presence of large volumes of residual magma beneath these volcanoes. Métrich et al. (2011) suggest that if Yasur has maintained its current degassing regime through the past millennium, >25 km^3 of magma has degassed. By comparison, tephra records suggest that <0.2 km^3 of magma was erupted during this period (Firth et al. 2014). Further north in the Vanuatu Arc, Ambrym volcano is responsible for some of the highest rates of passive degassing worldwide (Bani et al. 2012; Oppenheimer et al. 2011). Here, average gas fluxes require degassing of >17 km^3 of magma (Table 5.3) over the last 50 years. Throughout this time lava lakes have been active at the volcano (e.g. Mallick 1970; GVN Bulletin 1997; Nemeth and Cronin 2008), however only one major effusive eruption occurred (1988-89), which was responsible for eruption of 0.001 km^3 of magma (Monzier and Charley 1989). Thus >16 km^3 of magma has degassed but not been erupted at Ambrym in the past half century. Similar discrepancies between volumes of degassed and erupted magma have been noted at Villarrica (Witter et al. 2004) and Stromboli, where only 0.3-7% of degassed magma is erupted during normal activity (Gauthier et al. 2000; Allard et al. 2008). All these cases indicate that vast quantities of magma may be stored beneath persistently-active volcanoes, either as intrusions or crystal mushes. Recycling of this material, or its interaction with recharging magmas is thus highly likely in such systems (Cooper and Kent 2014).

Bragagni et al. (2014) proposed that U-Th-Ra isotopes at Stromboli are modified by interaction with the residual liquid from a crystal mush that resides beneath the volcano. The residual liquid, or *antemelt*, in this model is enriched in U and Th as a result of fractionation, while having lower ^{226}Ra excesses, because it is older. Varying interaction with this component explains the different uranium-series isotope ratios of the normal '*hp*' lavas, which are sourced from high within the plumbing system, and the paroxysmal '*lp*' lavas, which ascend rapidly from greater depths, avoiding assimilation with the antemelt (Bragagni et al. 2014).

Such a scenario, involving mixing between components with distinct U-Th-Ra isotopes, readily explains the temporal variations in Th-Ra isotopes at volcanoes such as Stromboli. Replenishment magmas most likely form one component in this mixing scenario, suggesting that RTF processes are operating, and, indeed even at timescales consistent with the thermal model. Instead of mixing with a resident magma derived from an earlier iteration of recharge, as modelled by Hughes and Hawkesworth (1999), magmas mix with a crystal mush or antemelt with distinct U-Th-Ra isotopes, as proposed by Bragagni et al. (2014). In the case of Stromboli, this is modelled using Equation 2 (Fig. 5.6a) to show that recharge and subsequent mixing with a distinct component at intervals of ~27 years explains the variation in (^{230}Th/^{232}Th) amongst '*lp*' magmas. Such a scenario also explains temporal variations other uranium-series isotope ratios at Stromboli. Sigmarsson et al. (2005) invoke a similar scenario to explain temporal variations in (^{226}Ra/^{230}Th) at Piton de la Fournaise.

While this offers strong support for mixing between replenishment magmas and an older component, such as an antemelt, at Stromboli and Piton de la Fournaise, direct application of this scenario to Yasur is hampered by a lack of obvious temporal trends in uranium-series isotopes. This results from the poor time resolution of samples presented here. A potential mixing scenario for Yasur, assuming replenishment intervals of 10 years, is shown in Fig. 5.6b. The mixing component is derived from the same parental composition as the recharge magma, however has undergone ~5000 years of radioactive decay. While not definitive, this highlights the possibility that uranium-series isotopes at Yasur are affected by recharge and mixing with older material, as at many other persistently-active volcanoes.

In summary, regular magma replenishment can be envisaged for persistently-active volcanoes, with recharge operating on timescales of years to tens of years, consistent with thermal modelling and degassing rates. In this scenario, the variability in uranium-series isotopes represents additional mixing between recharge magmas and another, older component, that may represent magma or a crystal mush stored within the system. At basaltic volcanoes such mixing is easily achieved given the magma viscosity, however with more evolved magmas, higher viscosity inhibits homogenisation, masking temporal trends.

Comparison with higher magnitude eruptions

While Yasur's current eruptive activity is long-lived and small in volume, the magmatic system that feeds it has also been responsible for larger and much more violent eruptions. At least two caldera-forming, ignimbrite-producing eruptions have occurred in the past ~43 kyr (Firth et al. in review). Similar high-magnitude, mafic, Plinian eruptions occurred at Villarrica (Lohmar et al. 2012) and Masaya (Wehrmann et al. 2006). Pre-historic ignimbrite-producing eruptions at both Yasur and Villarrica were linked to rejuvenation of a crystalline magma following replenishment by fresh, hot, mafic magma (Lohmar et al. 2012; Firth et al. in review). Comparable Sr and Nd isotope ratios between the Siwi Ignimbrite and more recent Yasur eruptives suggest both are derived from similar parental magmas (Firth et al. in review). This is supported by comparable (^{238}U/^{232}Th) ratios presented here. While accurate age-corrected (^{230}Th/^{232}Th) activity ratios are not available for the Siwi Ignimbrite, given the uncertainty in its age, estimates suggest they are lower than those of material erupted from Yasur (Fig. 5.3), with older ages providing lower (^{230}Th/^{232}Th). Low (^{230}Th/^{232}Th) is consistent with a recharge magma, thus potentially implicating the involvement of a batch of fresh magma. Nevertheless, the whole rock composition of the Siwi Ignimbrite is more evolved than any other eruptive products from Yasur (Métrich et al. 2011), suggesting that fresh, recharge magma cannot solely account for the composition of the ignimbrite. A growing body of evidence supports the remobilisation of a crystal mush by mafic recharge as a key trigger for major caldera eruptions (Pallister et al. 1992; Murphy et al. 2000; Burgisser and Bergantz 2011; Cooper and Kent 2014). The likely presence of crystal mush bodies beneath persistently-active volcanoes has already been shown. Instead of small-scale mixing between recharge magma and the crystal mush, as invoked for persistent volcanic activity, the crystal mush may undergo occasional wholesale remobilisation to produce low frequency, catastrophic eruptions. Mineral-melt disequilibrium textures identified within the Lican Ignimbrite at Villarrica (Lohmar et al. 2012), and also the Siwi Ignimbrite (Firth et al. in review), support such a scenario.

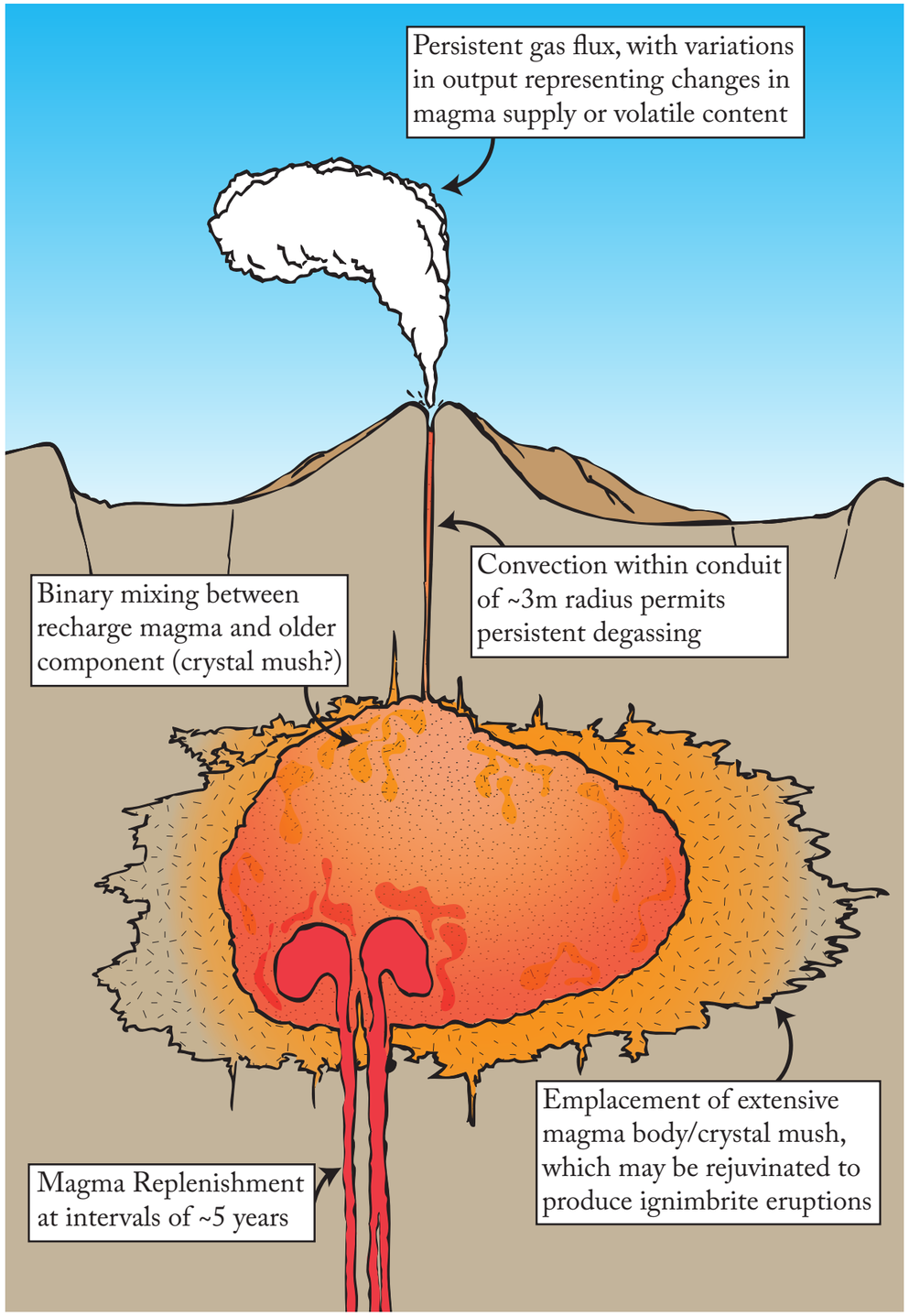

Fig. 5.7 A cartoon summarising the processes governing persistent volcanic activity at Yasur volcano.

CONCLUSIONS

Elevated gas fluxes and ongoing, low-magnitude eruptive activity define a group of volcanoes that are persistently-active for periods of years to millennia. Comparison of gas flux data between these volcanoes shows that conduit geometry and dynamics are similar, with all displaying comparable conduit radius regardless of their eruptive style. Models relying on uranium-series isotopes and thermal cooling of a magma chamber return disparate rates of magma replenishment for these volcanoes, which differ by orders of magnitude. They are reconciled by a scenario in which magma replenishment occurs on timescales of years to decades, with uranium-series isotopes reflecting mixing between fresh replenishment magma and an older component that may represent a resident antemelt or crystal mush (Fig. 5.7). The latter accords with degassing models that suggest large volumes of magma are degassed and stall at shallow levels, relative to the small volume of magma that is actually erupted. While small-scale mixing or assimilation of these bodies is the norm during typical, low-magnitude eruptions, large-scale rejuvenation may also occur, initiating catastrophic, caldera-forming eruptions that could potentially be overlooked in hazard plans.

Afternoon sunlight filters through the gas plume from Marum’s crater

Future Directions
and
Conclusions

FUTURE DIRECTIONS

As is always the case in science, the answer to one question opens the avenue for another, and the research presented here is no exception. It has highlighted a number of deficiencies in knowledge, both on the specific volcanoes of Yasur and Ambrym, but also about persistently active volcanoes more generally.

At Yasur, geochemical studies, such as this thesis, would benefit from further geophysical investigations of both the caldera structure and current plumbing system (e.g. Finlayson et al. 2003; Chiarabba et al. 2004). To date geophysical studies at Yasur have largely investigated the dynamics of Strombolian explosions (e.g. Nabyl et al. 1997) or uplift of the Yenkahe Dome (e.g. Merle et al. 2013; Brothelande et al in press). Geophysical investigation of the caldera structure would assist with interpretation of eruption dynamics during ignimbrite eruptions, while also offering valuable hazard information. Exploration of the currently active shallow plumbing system by geophysical means would also prove invaluable, offering a companion to thermobarometry estimates and, more importantly, providing valuable constrains for numerical models, such as those presented in Chapter 4.

The great gap in knowledge at Ambrym is the volcano's past. As noted in the introduction of Chapter 3, debate continues as to whether Ambrym's 12 km-wide caldera is the product of violent eruption, or non-explosive subsidence. Given the potential link between persistent activity, crystal mushes and ignimbrite eruptions shown in Chapter 2, and the high rates of passive degassing seen at Ambrym (Chapter 5; Bani et al. 2012; Allard et al. 2015), a similar scenario to the Yenkahe Ignimbrites is not unfeasible at Ambrym. To clarify the importance of caldera collapse within the Ambrym volcanic system, better exploration of the caldera is needed, together with re-examination and re-analysis of the deposits described by Robin et al. (1993) and Picard et al. (1995) and linked with caldera formation.

Given the brevity of historical records at all the volcanoes in the Vanuatu Arc, elucidation of the volcanic record beyond the beginning of the 20th century is important. At Ambrym the intervening period between caldera collapse (postulated at ~ 2ka: McCall et al. 1969) and the 1896 eruption remains almost completely unknown. Tephrostratigraphic studies, such as that completed for Yasur in Chapter 1 would greatly benefit understanding of eruptive behaviour at Ambrym and other volcanoes within the Vanuatu Arc. Tephra deposits suitable for such studies

were observed within the caldera at Ambrym in 2014, but detailed examination was not possible given time constraints.

This study has highlighted the role of magma mixing at both Ambrym and Yasur, as well as invoking the potential for remobilisation of crystal mushes. Further insight on these processes might be gained from application of crystal-scale techniques, such as mineral diffusion profiles (e.g. Costa et al. 2008; Costa and Morgan 2010) and uranium-series crystal ages (e.g. Cooper and Reid 2008) to samples from both volcanoes. Similarly, degassing plays a major role in driving persistent eruption at both Ambrym and Yasur. While gas fluxes and degassing processes have been well studied at both volcanoes (e.g Oppenhiemer et al. 2006; Métrich et al. 2011; Bani et al. 2012; Allard et al. 2015), timescales of degassing remain poorly constrained. By using (^{226}Ra/^{210}Pb) disequilibria, degassing process, and the timescales over which they operate, may be further elucidated (e.g. Berlo and Turner 2010; Turner et al. 2012; Turner et al. 2013). Such data would offer valuable contributions to understanding of magmatic processes driving persistent eruptive activity.

Lastly, both Ambrym and Yasur (and the volcanoes they have been compared with throughout this thesis) are ideal examples of persistently active volcanoes. The transition from persistent activity towards eruptions with lower frequency and higher magnitude is far from clear-cut, however. On which side of this divide does continued lava dome growth sit, for instance? Or the monthly to yearly occurrence of vulcanian blasts? These variations in eruptive behaviour may result from differences in degassing processes, magma viscosity, conduit geometry or fundamental differences in magma composition. A comparative study, using similar models to those presented in Chapter four, however expanding the dataset to include marginally-persistently active volcanoes like Montserrat, Merapi, Sakurajima and Colima would potentially identify magmatic controls on eruption dynamics at these different volcanoes.

CONCLUSIONS

Within the Vanuatu Arc, a number of volcanoes have displayed persistent eruptive activity with long-lived gas and magma fluxes from open conduits. They offer an unparalleled opportunity to investigate magmatic processes that sustain persistent eruptive behaviour, the duration of such behaviour and its importance in the wider magmatic system.

Examination of the stratigraphy at Yasur has clarified much about the volcano's history. Tephra records preserved in Lake Siwi suggest that the current episode of persistent eruption has continued, much like today, for 600-800 years. In this way Yasur rivals Stromboli for one of the longest-lived eruptive episodes currently occurring around the world. Throughout this period variations in eruptive behaviour, magma output and magma chemistry have been minimal, marking Yasur as a true steady-state volcano. Nevertheless, observed variations in geochemical parameters, such as uranium-series isotope ratios, while still minimal, cannot be reconciled with traditional models of replenished, tapped and fractionating magma reservoirs. While magma recharge remains the dominant process influencing persistent eruptive activity, models of steady-state behaviour appear too simplistic to explain the full suite of magmatic processes that sustain such behaviour. Fluctuations in the major element content of glass shards can be explained by temporal variations in degassing regime, while differences in uranium-series isotope ratios require cryptic interaction with an older residual magma or crystal mush. Pronounced disparity between degassing regimes and magma output rates at Yasur, Ambrym and other persistently active volcanoes, suggests that significant volumes of magma are degassed, but remain un-erupted at these volcanoes, potentially producing this crystal mush component.

Earlier eruptions at Yasur involved stronger Vulcanian to sub-Plinian blasts, as well as lava extrusion, from Yasur or another-pre-Yasur cone. Such activity appears to be have been a repeated feature during repose intervals between large ignimbrite eruptions at the Yenkahe Caldera. Volcanic rocks erupted during such repose intervals are all geochemically similar, with comparable compositions to those erupted from Yasur today. The occurrence of eruptive cones along faults within the caldera, such as Yasur, which sits on the margin of the uplifting Yenkahe Resurgent Dome, suggests magma exploits pre-existing structural weaknesses during ascent. Similar structural controls are evident at other persistently active volcanoes, like Ambrym, potentially linking such activity with un-impeded magma ascent.

From a hazard perspective, one of the most significant discoveries within this thesis is the realisation that the Yenkahe Caldera has hosted at least two catastrophic ignimbrite-producing eruptions. As such, large, Plinian-style eruptions are a repeated feature of this volcanic system. Juvenile material from both ignimbrite deposits offers significant petrological evidence for magma mixing and/or crystal mush rejuvenation, with glassy enclaves, skeletal and resorbed phenocrysts and crystal clusters. These features suggest that residual crystal mush produced by low-magnitude, persistent activity during repose intervals was rejuvenated to provide the volumes of magma required for these large eruptions. In this way, the two distinct styles of activity witnessed at Yasur are shown to be a direct consequence of each other. This Jekyll and Hyde personality is also seen at other persistently active volcanoes, like Villarrica, suggesting it may be common amongst volcanoes hosting this style of activity.

Similar mineral disequilibria textures are identified in certain, intra-caldera lavas at Ambrym, however the erupted volumes and frequency/magnitude relationships of these eruptions differ significantly from the ignimbrite-producing blasts of the Yenkahe Caldera. These textures represent mixing of residual magma feeding persistent activity with intrusions of fresh, replenishment magma, however show no evidence for wholesale crystal mush remobilisation. The differences in frequency and dynamics of major eruptions between Ambrym and Yasur suggest significant inter-volcano disparity in the time intervals between major magma replenishment events and the volumes of magma they contribute. Similar disparities also explain the differences between persistent activity and higher magnitude eruptions that are evident at individual volcanoes, like Yasur and Ambrym.

APPENDIX 1 – ANALYTICAL METHODS

Glass and Mineral Chemistry

The major and trace element composition of glass shards and minerals was determined using in-situ methods with a high spatial resolution. Electron microprobe analysis (EMPA) was employed to analyse major element contents, while laser-ablation induced coupled plasma mass spectrometry (LA-ICP-MS) was used to measure trace element concentrations.

Glass shard (Tephra) preparation

Geochemical examination of tephra is most commonly achieved through glass shard analysis. By only analysing glass shards, impurities within bulk tephra samples, including xenocrysts, xenoliths and detrital grains, can be avoided (Shane 2000). Tephra samples were rinsed in deionised water to remove clays and fine organic material. Given the depositional environment of tephras examined in this study, samples were relatively clean and further methods of separating unwanted material, such as magnetic or density methods, as well as removing organic or weathered coatings from individual shards, such as acid/alkali digestion (e.g. Shane 2000; Lowe 2011) were unnecessary. Samples were dry-sieved and a split of the 250-125 μm grain size fraction was collected. This grainsize fraction was chosen as shards were of sufficient size for EMPA and LA-ICP-MS analysis. Exclusion of smaller grainsize fractions also limited the accidental inclusion of clays that were not removed during rinsing. Samples were mounted in polished epoxy blocks following the method outlined in Lowe (2011). Sample maps were prepared by scanning electron microscope (SEM) so that individual shards could be targeted and recorded, allowing major and trace element analysis of the same grain using different techniques.

On a number of occasions glass compositions were also analysed from lava bomb samples which were prepared as thin sections. Mineral analyses were primarily undertaken using thin sections.

Glass Shard Major Elements (EMPA)

Electron microprobes use a focused beam of electrons fired at a point on the sample to excite X-rays. The energies and wavelengths of these x-rays relate to individual elements and their

intensity is a measure of elemental abundance. This technique is perfectly suited to analysis of glass shards and minerals due to its high spatial resolution (~1 μm), which allows the chemistry of individual grains to be analysed, rather than the bulk sample (e.g. Hayward 2011; Lowe 2011). Glass shard and mineral major element concentrations were analysed using a Cameca SX 100 electron microprobe at the Geochemical Analysis Unit (GAU) at Macquarie University.

All analyses were carried out with a beam energy of 15 keV and a beam current of 20 nA. Backscatter images were used to avoid visible microlites and other irregularities within the glass. Accuracy and precision were estimated from replicate analyses of appropriate synthetic and natural standards: $CaSiO_3$ for Si, TiO_2 for Ti, kyanite for Al, VG-A99 for Fe, MgO for Mg, wollastonite for Ca, jadeite for Na and orthoclase for K. Analyses with totals outside the range 100 ± 2 % were discarded as being unreliable.

A beam width of 1 μm was used for mineral analyses. Chemical modification of glass samples during EMP analysis is an often cited issue with this technique. Charging and heating within the sample by incident electrons can cause depletion of alkalis, especially Na, within the upper ~1 μm of the sample and enrichment in layer directly beneath this, leading to an overall under-reading of Na abundance. This issue is commonly overcome by using a wider, de-focused electron beam during glass shard analysis (Hunt and Hill 1993; Hayward 2011). To determine the effects of Na-loss in glass shard samples from Yasur initial analyses were conducted using a focused 1 μm beam, as well as defocused 10 μm and 20 μm beams. All beams returned similar results for Na content, with the 1 μm beam providing the most reliable overall major element analyses. As such, the 1 μm beam was chosen for further analyses. It is also favoured, as the narrower beam width is more likely to avoid micro-inclusions that may be present (*c.f.* Platz et al. 2007). A wider, defocussed 10 μm beam was used for glass analyses on samples from the Siwi and Old Tanna Ignimbrites and from Ambrym.

Glass Shard Trace Element (LA-ICP-MS)

LA-ICP-MS offers an in-situ technique for trace element analysis, with sub-ppm detection limits and high spatial resolution (Pearce et al. 1999). As such, it is well suited to analysis of glass shards. Selected trace elements (Sc, V, Rb, Sr, La, Yb) were analysed on a sub-set of glass shard samples using the same polished grainmounts as the major element analyses. Sample maps were used to target the same grains as were analysed by EMPA. All analyses were completed at the GAU. An excimer laser operating at 9.45 J cm^{-2} and 5 Hz, with a spot size of

50 μm was used for ablation. Trace element concentrations were measured on an Agilent 7700 ICP-MS. USGS reference glass BCR-2 was analysed as an unknown to assess accuracy. Data reduction was completed with the software package GLITTER (van Achterbergh et al. 2001), using NIST 610 glass and Ca as internal and external standards respectively.

Whole Rock Geochemistry

Whole rock samples were analysed for major and trace element chemistry, with sub-sets undergoing additional analysis of Sr, Nd, Hf and U-series isotopes.

Weathered edges were removed from whole rock samples before further preparation and all were examined for evidence of alteration. Samples were crushed using a hydraulic crusher and resulting rock chips were cleaned ultrasonically in deionised water and dried in an oven at ~70°C overnight. Samples were then milled in an agate mill at ~700 RPM for 15-20 minutes each. A small number of samples analysed for U-series isotopes involved small quantities of tephra, so were milled by hand using an agate mortar and pestle.

Whole Rock Major Elements (XRF)

Major elements were analysed using X-ray fluorescence spectrometry (XRF). This technique relies on the bombardment of a sample by X-rays to induce the emission of secondary radiation from the sample. This occurs as atoms within the sample are excited and electrons are shifted between energy shells. The secondary x-ray is detected and recorded, with peaks in intensity reflecting the presence of different elements. The magnitude of these peaks reflect the concentration of each element within the sample.

Samples were analysed in fused glass disks, which were created by mixing ~2.5 g of lithium borate Spectrachem 12:22 flux with ~0.4 g of powdered sample. These were combined in a crucible and then heated in a furnace, initially at 700°C for 30 minutes, then 1000°C for another 20 minutes. The samples were gently rocked in the furnace to homogenise them for a further half an hour. Ammonium Iodide tablet was added ~10 minutes prior to pouring of the sample, to decrease its viscosity and facilitate easier pouring of the molten sample. Samples were poured and gently pressed, then left to anneal on a hot plate for a three to four hours. They were then trimmed and placed in a desicator, prior to analysis.

Samples were analysed at both the GAU at Macquarie University (samples from Ambrym and Yasur – Chapters 2 and 4) and at the University of Auckland (samples from Yenkahe Caldera

ignimbrites – Chapter 3). Analyses undertaken at the GAU were completed on a Spectro XLAB 2000 polarising XRF spectrometer using the methods of Norrish & Chappell (1977). Accuracy and analytical precision were determined to be ~0.5% for major elements, based upon replicate analyses of USGS reference material BHVO-2. A Siemens SRS3000 X-ray spectrometer was used to analyse samples at the University of Auckland. Replicate analyses of USGS standards BCR-2 and AGV-2 suggest accuracy of < 1% for major elements (Except Fe_2O_3: ~3.5%).

Whole Rock Trace Elements (Solution and LA-ICP-MS)

Trace elements for whole rock samples were analysed by induced coupled plasma-mass spectrometry. The lower limits of detection (LLD) for ICP-MS are much lower than those for XRF. As such, ICP-MS is better suited to the analysis of less abundant elements, especially the REE, as it has sub-ppm resolution. Two methods of ICP-MS analysis were used, with differences relating to how the sample was passed into the plasma of the ICP-MS. Samples from Ambrym (Chapter 4) were dissolved, with the solution nebulised for analysis, while samples of Yenkahe caldera Ignimbrites (Chapter 3) were ablated by laser.

Solution ICP-MS involves more preparatory work, however potentially returns results with higher accuracy and precision. Approximately 0.1 g of sample was digested in an HF-HNO_3 mix in heated Teflon beakers. Fluorides were dissolved by repeatedly adding HCl or HNO_3 and then drying down the sample. H_3BO_3 was used to neutralise the HF. Once the sample was digested it was diluted with 2% HNO_3 to a ~1/1000 solution. A 5 mL aliquot was the taken for analysis. This was spiked with an internal standard that included known amounts of ^{6}Li, ^{75}As, ^{103}Rh, ^{115}In and ^{209}Bi in order to calibrate the machine. Samples were analysed on an Agilent 7500 ICP-MS at the GAU. International reference materials (BIR-1 and BHVO-2) were analysed to determine instrument accuracy. The results for these are compared with internationally accepted values in Table 3.1. Method blanks were also analysed to calibrate the instrument and determine accuracy.

In an alternate method, trace elements were analysed on the same glass discs used for XRF major element analysis by laser ablation ICP-MS. These analyses were carried out at the Research School of Earth Sciences, Australian National University using an Excimer LPX 120 laser coupled with an Agilent 7500 ICP-MS. The laser is arranged with a mask (Eggins et al. 1998) to allow changes to the spot size that are independent of the energy density delivered to the sample surface, allowing constant ablation conditions to be maintained. The laser is oper-

ated at a wavelength of 193 nm, with a pulse width of 20 ns and a spot size of 50 μm. Data reduction relied upon analyses of NIST 612 glass, which bracketed every 15 sample analyses, and Si, analysed by XRF, as internal and external standards respectively. Detection limits using this method are <1 ppb. Replicate analyses of USGS standards BCR-2 and AGV-2 suggest analytical errors <5% for reported trace elements. Furthermore, Brenna et al. (2012) show close correlation between selected trace element (V, Cr, Ni, Cu, Zn, Rb, Sr, Zr, Nb, Ba) abundances measured using this procedure and those analysed by XRF.

Whole Rock Sr, Nd, Hf Isotopes

All sample dissolution and column chemistry for Sr, Nd and Hf isotope ratios was conducted in the clean laboratory at Macquarie University. Sample digestion for Sr and Nd isotope ratio analysis used the same procedure as trace element digestion. Once digested, Sr and the REE were separated by passing the solution through a cationic column, followed by removal of Sm and Nd on an HDEHP column, using Ln.Spec resin. A ThermFinnigan Triton thermal ionisation mass spectrometer was used to analyse Sr and Nd isotope ratios at the GAU. Analyses were conducted on static mode, using degassed single and double Re filaments for Sr and Nd respectively. Mass fractionation was corrected for by normalizing Sr to $^{86}Sr/^{88}Sr = 0.1194$ and Nd to $^{146}Nd/^{144}Nd = 0.7219$.

To isolate Hf, the sample was dissolved in an HF:HNO_3 mixture, then dried, before being mixed with HF to remove REE, which were entrained in the fluoride salt. The solid is centrifuged out, evaporated and then taken up in a mixture of dilute HF and HCl before being passed through an anion exchange column (AG1-X8, 100-200 mesh). A second-stage cation exchange column (AG50W-X8 200-400 mesh) was used to separate Ti and Cr from Hf (Blichert-Toft et al. 1997). Hf isotopes were analysed in static mode on a Nu Intruments multi-collector, ICP-MS at the GAU. Data was normalised to $^{179}Hf/^{177}Hf = 0.7325$, using exponential correction for mass bias. Interferences on ^{176}Hf by ^{176}Lu and ^{176}Yb were corrected for by analysing interference-free isotopes of Lu and Yb and correcting based upon $^{176}Lu/^{175}Lu = 0.02669$ and $^{176}Yb/^{172}Yb = 0.5865$ (De Bievre and Taylor 1993; Griffin et al. 2000). Repeat analysis of JMC 475 and BHVO-2 were within 0.01% of accepted values (Nowell et al. 1988; Weis et al. 2005).

Whole Rock U-Th-Ra Isotopes

Uranium-series isotopes were analysed at the U-series Research Laboratory, within the

Geochemical Analysis Unit (GAU) at Macquarie University. One gram of sample was spiked with ^{236}U, ^{229}Th and ^{228}Ra, before being digested in a mix of HNO_3, HCl and HF. Conversion to chloride was achieved by adding 6N HCl, before HCl saturated with H_3BO_3 was added to remove residual fluorides and then converted to nitrate using 14N HNO_3. U and Th were purified by passing through a 4 ml anionic column. A Nu-Instruments multi collector ICP-MS at the GAU was used to analyse Th and U isotope ratios. ^{238}U and ^{235}U were analysed on Faraday cups, U mass bias estimated assuming $^{238}U/^{235}U = 137.88$. ^{236}U and ^{234}U were alternately collected on the ion counter IC0. Th isotope measurements were made using a dynamic routine with ^{232}Th collected on the Faraday cup and ^{230}Th and ^{229}Th alternating on IC0. Uranium isotope analyses were bracketed by measurements of standards U010 and U005A, while Th isotope analyses bracketed by measurement of Th'U'. These repeat analyses were used to assess accuracy and precision and also for calculation of Th mass bias. Replicate analyses of TML show ($^{230}Th/^{232}Th$) is within 0.5% of accepted values (Sims et al. 2008). Errors for ($^{234}U/^{238}U$) and ($^{238}U/^{232}Th$) are greater (1.6% and 4.8%).

Ra was collected during elution of the U-Th column and converted to chloride using 6N HCl. The resulting solution was then passed through an 8 ml cationic column, from which Ra was eluted. This process was repeated using a 0.6 ml column. The REE were removed using 0.1N HNO_3 in a 150 μl column containing Ln-spec resin. Finally Ra and Ba were separated by passing 3N HNO_3 through a 150 μl column containing Sr-spec resin. Samples were loaded onto single, degasseed Re filaments, using a Ta-HF-H_3PO_4 solution (Birck 1986). Ra was analysed on a ThermoFinnigan Triton TIMS at the GAU, using dynamic ion counting mode. Accuracy was assessed by replicate analyses of TML, with results falling within 6.5% of accepted values.

Gas Measurements

SO_2 Flux (Flyspec)

Analysis of SO_2 flux from Yasur and Ambrym was carried out using Massey University's FLYSPEC ultraviolet spectrometer (Horton et al. 2006). This is a compact and portable instrument (Fig. A1.1) that relies on the absorption of ultraviolet radiation from the sun by SO_2 (Horton et al. 2006; Oppenheimer 2010). A collimating lens directs UV radiation into the spectrometers' input aperture, resulting in a field of view of ~ 2.5° (Horton et al. 2006). The instrument was calibrated using internal calibration cells and background measurements were conducted

Fig. A1.1 The SO_2 monitoring set-up employed at Yasur during a stationary scan on the ash plain. Note the small size of the Flyspec, which is entirely housed within the black case in the centre of the image, and is connected to a small notebook computer for data capture. The gas plaume from Yasur is onvious in the upper right of the image.

on clear sky, away from the plume, before and after each analysis. Measurements of overhead SO_2 column were collected during traverses underneath the gas plume. These were made either on foot or in the back of a truck or boat, moving at a constant speed. Measurements were also conducted from a fixed location using a rotating mirror attached to the end of the collimating lens. This rotated through and arc of up to 180°, with analyses taken at 1° intervals. Such scans could be run for a number of hours, allowing better assessment of plume variability over time. These scans were completed either along the traverse route or on the crater rim. An anemometer was installed on the crater rim of the volcano to measure wind velocity and direction. These measurements are used during data processing, which was completed using the reduction program, Fluxcalc (K. Horton, Flyspec Inc.).

REFERENCE LIST

Acocella V, Neri M (2003) What makes flank eruptions? The 2001 Etna eruption and its possible triggering mechanisms. *Bulletin of Volcanology* **65**, 517-529

Aiuppa A, Bertagnini A, Metrich N, Moretti R, Di Muro A, Liuzzo M, Tamburello G (2010) A model of degassing for Stromboli volcano. *Earth and Planetary Science Letters* **295**, 195-204

Aiuppa A, Federico C, Giudice G, Gurrieri S, Liuzzo M, Shinohara H, Favara R, Valenza M (2006) Rates of carbon dioxide plume degassing from Mount Etna volcano. *Journal of Geophysical Research* **111**, doi:10.1029/2006JB004307

Albarède F (1985) Regime and trace-element evolution of open magma chambers. *Nature* **318**, 356-358

Albarède F (1993) Residence time analysis of geochemical fluctuations in volcanic series. *Geochimica et Cosmochimica Acta* **57**, 615-621

Albarède F, Tamagnan V, (1988) Modeling the Recent Geochemcial Evolution of the Piton de la Fournaise Volcano, Reunion Island 1931-1986. *Journal of Petrology* **29**, 997-1030

Allard P, Aiuppa A, Bani P, Metrich N, Bertagnini A, Gauthier P, Parello F, Sawyer GM, Shinohara H, Bagnato E, Mariet C, Garaebiti E, Pelletier B (2009) Ambrym Basaltic Volcano (Vanuatu Arc): Volatile fluxes, magma degassing rate and chamber depth. *American Geophysical Union Fall Meet.*

Allard P, Aiuppa A, Bani P, Métrich N, Bertagnini A, Gauthier P-J, Shinohara H, Sawyer GM, Parello F, Bagnato E, Pelletier B, Garaebiti E (2015) Prodigious emission rates and magma degassing budget of major, trace and radioactive volatile species from Ambrym basaltic volcano, Vanuatu island Arc. *Journal of Volcanology and Geothermal Research*, doi: 10.1016/j.jvolgeores.2015.08.022

Allard P, Aiuppa A, Burton M, Caltabiano T, Federico C, Salerno G, La Spina A (2008) Crater Gas Emissions and the Magma Feeding System of Stromboli Volcano. *American Geophysical Union Geophysical Monograph Series* **182**, 65-80

Allard P, Carbonelle J, Métrich N, Loyer H, Zettwoog P (1994) Sulphur output and magma budget of Stromboli volcano. *Nature* **368**, 326-329

Allen SR, (2004) Complex spatter- and pumice-rich pyroclastic deposits from an andesitic caldera-forming eruption: the Siwi pyroclastic sequence, Tanna, Vanuatu. *Bulletin of Volcanology* **67**, 27-41

Allibone R, Cronin SJ, Charley DT, Neall VE, Stewart RB, Oppenheimer C (2012) Dental fluorosis linked to degassing of Ambrym volcano, Vanuatu: a novel exposure pathway. *Environmental Geochemistry and Health* **34**, 155-170

Andronico D, Pistolesi M (2010) The Novermber 2009 paroxymal explosions at Stromboli. *Journal of Volcanology and Geothermal Research* **196**, 120-125

Annen C, Pichavant M, Bachmann O, Burgisser A (2008) Conditions for the growth of a long-lived shallow crustal magma chamber below Mount Pelee volcano (Martinique, Lesser Antilles Arc). *Journal of Geophysical Research* **113**, B07209 doi:10.1029/2007JB005049

Aramaki S (1984) Formation of the Aira Caldera, Southern Kyushu, ~22,00 Years Ago. *Journal of Geophysical Research* **89**, 8485-8501

Armienti P, Francalanci L, Landi P (2007) Textural effects of steady-state behaviour of the Stromboli feeding system. *Journal of Volcanology and Geothermal Research* **160**, 86-98

Armienti P, Perinelli C, Putirka K (2013) A New Model to Estimate Deep-level Magma Ascent Rates, with Applications to Mt. Etna (Sicily, Italy). *Journal of Petrology* **54**, 795-813.

Arrighi S, Principe C, Rosi M (2001) Violent Strombolian and sub-Plinian eruptions at Vesuvius during post-1631 activity. *Bulletin of Volcanology* **63**, 126-150

Bachmann O (2010) The petrologic evolution and pre-eruptive conditions of the rhyolitic Kos Plateau Tuff (Aegean Arc). *Central European Journal of Geoscience* **2**, 270-305

Bachmann O, Bergantz GW (2003) Rejuvenation of the Fish Canyon magma body: A window into the evolution of large-volume silicic magma systems. *Geology* **31**, 789-792

Bachmann O, Bergantz GW (2006) Gas percolation in upper-crustal silicic crystal mushes as a mechanism for upward heat advection and rejuvenation of near-solidus magma bodies. *Journal of Volcanology and Geothermal Research* **149**, 85-102

Bachmann O, Bergantz G (2008) The Magma Reservoirs That Feed Supereruptions. *Elements* **4**, 17-21

Bacon CR (1986) Magmatic Inclusions in Silicic and Intermediate Volcanic Rocks. *Journal of Geophysical Research* **91**, 6091-6112

Bani P, Harris AJL, Shinohara H, Donnadieu F (2013) Magma dynamics feeding Yasur's explosive activity observed using thermal infrared remote sensing. *Geophysical Research Letters* **40**, 3830-3835

Bani P, Lardy M (2007) Sulphur dioxide emission rates from Yasur volcano, Vanuatu archipelago. *Geophysical Research Letters* **34**, L20309, doi:10.1029/2007GL030411

Bani P, Oppenheimer C, Allard P, Shinohara H, Tsanev V, Carn S, Lardy M, Garaebiti E (2012) First estimate of volcanic SO_2 budget for Vanuatu island arc. *Journal of Volcanology and Geothermal Research* **211-212**, 36-46

Bani P, Oppenheimer C, Tsanev VI, Carn SA, Cronin SJ, Crimp R, Calkins JA, Charley D, Lardy M, Roberts TR (2009) Surge in sulphur and halogen degassing from Ambrym volcano, Vanuatu. *Bulletin of Volcanology* **71**, 1159-1168

Beaumais A, Chazot G, Dosso L, Bertrand H (2013) Temporal source evolution and crustal contamination at Lopevi Volcano, Vanuatu Island Arc. *Journal of Volcanology and Geothermal Research* **263**, 72-84

Beckett FM, Burton M, Mader HM, Phillips JC, Polacci M, Rust AC, Witham F (2014) Conduit convection driving persistent degassing at basaltic volcanoes. *Journal of Volcanology and Geothermal Research* **283**, 19-35

Benioff H (1949) Seismic evidence for the fault origin of oceanic deeps. *Bulletin of the Geological Society of America* **60**, 1837-1856

Beresford SW, Cole JW (2000) Kaingaroa Ignimbrite, Taupo Volcanic Zone, New Zealand:

evidence for asymmetric caldera subsidence of the Reporoa Caldera. *New Zealand Journal of Geology and Geophysics* **43**, 471-481

Berlo K, Turner S (2010) ^{210}Pb-^{226}Ra disequilibria in volcanic rocks. *Earth and Planetary Science Letters* **296**, 155-164

Bice DC (1985) Quaternary volcanic stratigraphy of Managua, Nicaragua: Correlation and source assignment for multiple overlapping Plinian deposits. *Geological Society of America Bulletin* **96**, 553-566

Birck JL (1986) K, Rb, Sr isotopic analysis: Application to Rb-Sr chronology. *Chemical Geology* **56**, 73-83

Blake S (1984) Volatile oversaturation during the eruption of silicic magma chambers as an eruption trigger. *Journal of Geophysical Research* **89**, 8237-8244

Blake S, Rogers N (2005) Magma differentiation rates from (^{226}Ra/^{230}Th) and the size and power output of magma chambers. *Earth and Planetary Science Letters* **236**, 654-669

Blichert-Toft J, Chauvel C, Albarède F (1997) Separation of Hf and Lu for high-precision isotope analysis of rock samples by magnetic sector-multiple collector ICP-MS. *Contributions to Mineralogy and Petrology* **127**, 248-260

Blundy J, Cashman K (2001) Ascent-driven crystallisation of dacite magmas at Mount St Helens, 1980-1986. *Contributions to Mineralogy and Petrology* **140**, 631-650

Blundy J, Cashman K (2008) Petrologic Reconstruction of Magmatic System Variables and Processes. *Reviews in Mineralogy and Geochemistry* **69**, 179-239.

Blundy J, Wood B (2003) Mineral-Melt Partitioning of Uranium, Thorium and their Daughters. *Reviews in Mineralogy and Geochemistry* **52**, 59-123

Bohm M, Lüth S, Echtler H, Asch, G, Bataille K Bruhn C, Rietbrock A, Wigger P (2002) The Southern Andes between 36° and 40°S latitude:seismicity and average seismic velocities. *Tectonophysics* **356**, 275-289

Bottinga Y, Weill DF (1970) Densities of liquid silicate systems calculated from partial molar volumes of oxide components. *American Journal of Science* **269**, 169-182

Bourdon B, Turner S, Henderson GM, Lundstrom CC (2003) Introduction to U-series Geochemistry. *Reviews in Mineralogy and Geochemistry* **52**, 1-19

Bouvet de Maisonneuve C, Dungan MA, Bachmann O, Burgisser A (2013) Petrological Insights into Shifts in Eruptive Styles at Volcán Llaima (Chile). *Journal of Petrology* **54**, 393-420.

Bowen NL (1915) Crystallisation – Differentiation in Silicate Liquids. *American Journal of Science* **39**, 175-191

Bowen NL (1928) The Evolution of Igneous Rocks. Princeton University Press, Princeton, New Jersey. 334 pp.

Boygle J, (1999) Variability of tephra in lake and catchment sediments, Svínavatn, Iceland. *Global Planetary Change* **21**, 129-149

Bragagni A, Avanzinelli R, Freymuth H, Francalanci L (2014) Recycling of crystal mush-derived melts and short magma residence times revealed by U-series disequilibria at Stromboli volcano. *Earth and Planetary Science Letters* **404**, 206-219

Branca S, Del Carlo P (2005) Types of eruptions of Etna volcano AD 1670-2003: implications for short-term eruptive behaviour. *Bulletin of Volcanology* **67**, 732-742.

Branney MJ, Kokelaar P (2002). Pyroclastic Density Currents and the Sedimentation of Ignimbrites. *Geological Society of London Memoir* **27**, 1-136

Brenna M, Cronin SJ, Smith IEM, Maas R, Sohn YK (2012) How Small-volume Basaltic Magmatic Systems Develop: a Case Study from the Jeju Island Volcanic Field, Korea. *Journal of Petrology* **53**, 985-1018

Briqueu L, Laporte C, Crawford AJ, Hasenaka T, Baker PE, Coltorti M (1994) Temporal magmatic evolution of the Aoba Bain, central New Hebrides island arc: Pb, Sr and Nd isotopic evidence for the coexistence of two mantle components beneath the arc. *Proceedings of the Ocean Drilling Program, Scientific Results* **134**, 393-401.

Brothelande E, Lenat J-F, Normier A, Bacri C, Peltier A, Paris R, Kelfoun K, Merle O, Finizola A, Garaebiti E (in press). Insights into the evolution of of the Yenkahe resurgent dome (Siwi caldera, Tanna Island, Vanuatu) inferred from aerial high-resolution photogrammetry. *Journal of Volcanology and Geothermal Research.*

Browne BL, Eichelberger JC, Patino LC, Vogel TA, Uto K, Hoshizumi H (2006) Magma mingling as indicated by texture and Sr/Ba ratios of plagioclase phenocrysts from Unzen volcano, SW Japan. *Journal of Volcanology and Geothermal Research* **154**, 103-116.

Bruins HJ, MacGillivrray JA, Synolakis CE, Benjamini C, Keller J, Kisch HJ, Klugel A, van der Plicht J (2008) Geoarchaeological tsunami deposits at Palaikastro (Crete) and the Late Minoan IA eruption of Santorini. *Journal of Archaeological Science* **35**, 191-212

Burgisser A, Bergantz GW (2011) A rapid mechanism to remobilize and homogenize highly crystalline magma bodies. *Nature* **471**, 212-215

Burnham CW, (1975) Water and magmas; a mixing model. *Geochimica et Cosmochimica Acta* **39**, 1077-1084

Burton MR, Mader HM, Polacci M (2007) The role of gas percolation in quiescent degassing of persistently active basaltic volcanoes. *Earth and Planetary Science Letters* **264**, 46-60

Buys J, Spandler C, Holm RJ, Richards SW (2014) Remnants of ancient Australia in Vanuatu: Implications for crustal evolution in island arcs and tectonic development of the southwest Pacific. *Geology* **42**, 939-942

Calkins J, Oppenheimer C, Kyle PR (2008) Ground-based thermal imaging of lava lakes at Erebus volcano, Antarctica. *Journal of Volcanology and Geothermal Research* **177**, 695-704

Callot JY, Daniel J, Burne RV (1985) Recent tectonics associated with the subduction/collision of the D'Entrecasteaux Zone in the central New Hebrides. *Tectonophysics* **112**, 325-356

Campbell FA, (1888) The active volcano on Tanna, New Hebrides, with some remarks on the cause of volcanic action. *Proceedings of the Royal Society of Victoria* **1**, 73-83.

Carey S, Sigurdsson H, Mandeville C, Bronto S (2000) Volcanic hazards from pyroclastic flow discharge into the sea: Examples from the 1883 eruption of Krakatau, Indonesia. *Geological Society of America Special Paper* **345**, 1-14

Carney JN, McFarlane A (1979) Geology of Tanna, Aneityum, Futuna and Aniwa. *New Hebrides Government Geological Survey*, pp 5-29

Carniel R, Di Cecca M, Rouland D (2003) Ambrym, Vanuatu (July-August 2000): spectral and dynamical transitions on the hours-to-days timescale. *Journal of Volcanology and Geothermal Research* **128**, 1-13

Cashman KV (2004) Volatile controls on Magma Ascent and Eruption. The State of the Planet: Frontiers and Challenges in Geophysics. *American Geophysical Union Geophysical Monograph Series* **150**, 109-124

Cashman K, Blundy J (2000) Degassing and crystallisation of ascending andesite and dacite. *Philosophical Transactions of the Royal Society of London A* **358**, 1487-1513

Cashman K, Blundy J (2013) Petrological cannibalism: the chemical and textural consequences of incremental magma body growth. *Contributions to Mineralogy and Petrology* **166**, 703-729

Cashman KV, Sparks RSJ (2013) How volcanoes work: A 25 year perspective. *Geological Society of America Bulletin* **125**, 664-690

Caulfield JT, Cronin SJ, Turner SP, Cooper LB (2011) Mafic Plinian volcanism and ignimbrite emplacement at Tofua volcano, Tonga. *Bulletin of Volcanology* **73**, 1259-1277

Charlier BLA, Wilson CJN, Lowenstern JB, Blake S, Van Valsteren PW, Davidson JP (2005) Magma Generation at a Large, Hyperactive Silicic Volcano (Taupo, New Zealand) Revealed by U-Th and U-Pb Systematics in Zircons. *Journal of Petrology* **46**, 3-32

Chen JK, Taylor FW, Edwards RL, Cheng H, Burr GS, (1995) Recent Emerged Reef Terraces of the Yenkahe Resurgent Block, Tanna, Vanuatu: Implications for Volcanic, Landslide and Tsunami Hazards. *Journal of Geology* **103**, 577-590

Chiarabba C, De Gori P, Patane D (2004) The Mt. Etna Plumbing System: The Contribution of Seismic Tomography. *American Geophysical Union Geophysical Monograph Series* **143**, 191-204

Cigolini C, Laiolo M, Bertolino S (2008) Probing Stromboli volcano from the mantle to paroxysmal eruptions. *Geological Society of London Special Publication* **304**, 33-70

Collot JY, Daniel J, Burne RV (1985) Recent tectonics associated with the subduction/collision of the D'Entrecasteaux Zone in the central New Hebrides. *Tectonophysics* **112**, 325-356

Coltelli M, Del Carlo P, Vezzoli L (1998) Discovery of a Plinian basaltic eruption of Roman age at Etna volcano, Italy. *Geology* **26**, 1095-1098

Cook J (1777) A voyage round the world, performed in His Britannic Majesty's ships the Resolution and Adventure, in the years 1772, 1773, 1774 and 1775. 523 pp

Cooper KM, Kent AJR (2014) Rapid remobilization of magmatic crystals kept in cold storage. *Nature* **506**, 480-483

Cooper KM, Reid MR (2008) Uranium-series Crystal Ages. *Reviews in Mineralogy and Geochemistry* **69**, 479-544

Corsaro, R.A., Miragila, L., Pompilio, M. (2007). Petrologic evidence of a complex plumbing system feeding the July-August 2001 eruption of Mt. Etna, Sicily, Italy. *Bulletin of Volcanology* **69**, 401-421.

Costa F, Dohmen R, Chakraborty S (2008) Time Scales of Magmatic Processes from Modelling the Zoning Patterns of Crystals. *Reviews in Mineralogy and Geochemistry* **69**, 545-594

Coudert E, Cardwell RK, Isacks BL, Chatelain JL (1984) P-wave velocity of the uppermost mantle and crustal thickness in the central Vanuatu Islands (New Hebrides Island Arc). *Bulletin of the Seismological Society of America* **74**, 913-924

Crawford AJ, Briqueu L, Laporte C, Hasenaka T (1995) Coexistence of Indian and Pacific Ocean Upper Mantle Reservoirs Beneath the Central New Hebrides Island Arc. *American Geophysical Union Geophysical Monograph* **88**, 199-217

Cronin SJ, Nemeth K (2005) Where are the giant tuff cones and ignimbrites of Ambrym? A more conventional story of mafic volcanism at Ambrym Volcano, Vanuatu. In: Pettinga J, Wandres AM (eds) Abstract Volume of the Geological Society of New Zealand 50th Annual Conference, Kaikoura, New Zealand. *Geological Society of NZ Miscellaneous Publication* **119A**, 21-22

Cronin SJ, Sharp DS (2002) Environmental impacts on health from continuous volcanic activity at Yasur (Tanna) and Ambrym, Vanuatu. *International Journal of Environmental Health Research* **12**, 109-123

Dahren B, Troll VR, Andersson UB, Chadwick JP, Gardner MF, Jaxybulatov K, Koulakov I (2012) Magma plumbing beneath Anak Krakatau volcano, Indonesia: evidence for multiple magma storage regions. *Contributions to Mineralogy and Petrology* **163**, 631-651

Davidson JP, Hora JM, Garrison JM, Dungan MA (2005) Crustal forensics in arc magmas. *Journal of Volcanology and Geothermal Research* **140**, 157-170

Davies AG, Calkins J, Scharenbroich L, Vaughn RG, Wright R, Kyle P, Castano R, Chien S, Tran D (2008) Multi-instrument remote and in situ observations of the Erebus Volcano (Antarctica) lava lake in 2005: A comparison with the Pele lava lake on the Jovian moon Io. *Journal of Volcanology and Geothermal Research* **177**, 705-724

De Bievre P, Taylor PDP (1993) Table of the isotopic composition of the elements. *International Journal of Mass Spectrometry and Ion Processes* **123**, 149

DePaolo DJ, Wasserburg GJ (1977) The source of island arcs as indicated by Nd and Sr isotopic studies. *Geophysical Research Letters* **4**, 465-468

Dibble RR, Kyle PR, Rowe CA (2008) Video and seismic observations of Strombolian eruptions at Erebus volcano, Antarctica. *Journal of Volcanology and Geothermal Research* **177**, 619-634

Dosseto A, Turner SP, Sandiford M, Davidson J (2008) Uranium-series isotope and thermal constraints on the rate and depth of silicic magma genesis. *Geological Society of London Special Publication* **304**, 169-181

Druitt TH, Costa F, Deloule E, Dungan M, Scaillet B (2012) Decadal to monthly timescales of magmatic transfer and reservoir growth at a caldera volcano. *Nature* **482**, 77-80

Druitt TH, Edwards L, Mellors RM, Pyle DM, Sparks RSJ, Lanphere M, Davies M, Barreirio B (1999) Santorini Volcano. *Geological Society of London Memoirs* **19**, 1-165

Druitt TH, Sparks RSJ (1984) On the formation of calderas during ignimbrite eruptions.

Nature **310**, 679-681

Dupre B, Allegre CJ (1983) Pb-Sr isotope variation in Indian Ocean basalts and mixing phenomena. *Nature* **303**, 142-146

Dupuy C, Dostal J, Marcelot G, Bougault H, Joron JL, Treuil M (1982) Geochemistry of basalts from central and southern New Hebrides arc: implications for their source rock composition. *Earth and Planetary Science Letters* **60**, 207-225

Edmonds M (2008) New geochemical insights into volcanic degassing. *Philosophical Transactions of the Royal Society A* **366**, 4559-4579

Eggins SM (1993) Origin and differentiation of picritic arc magmas, Ambae (Aoba), Vanuatu. *Contributions to Mineralogy and Petrology* **114**, 79-100

Eggins SM, Rudnick RL, McDonough WF (1998) The composition of peridotites and their minerals: a laser-ablation ICP-MS study. *Earth and Planetary Science Letters* **154**, 53-71

Eissen J, Blot C, Louat R (1991) Chronologie de l'activite volcanique historique de l'arc insulaier des Nouvelles-Hebrides de 1595 a 1991. ORSTOM Rep: 68 pp

Erfurt-Cooper P (2011) Geotourism in Volcanic and Geothermal Environments: Playing with Fire? *Geoheritage* **3**, 187-193

Fabbrizio A, Schmidt MW, Gunther D, Eikenberg J (2009) Experimental determination of Ra mineral/melt partitioning for feldspars and ^{226}Ra-disequilibrium crystallisation ages of plagioclase and alkali-feldspar. *Earth and Planetary Science Letters* **280**, 137-148

Favalli M, Chirico GD, Papale P, Pareschi MT, Boschi E (2009) Lava flow hazard at Nyiragongo volcano, DRC. *Bulletin of Volcanology* **71**, 363-374

Finlayson DM, Gudmundsson O, Itikarai I, Nishimura Y, Shinamura H (2003) Rabaul volcano, Papaua New Guinea: seismic tomographic imaging of an active caldera. *Journal of Volcanology and Geothermal Research* **124**, 153-171

Firth CW, Handley HK, Cronin SJ, Turner SP (2014) The eruptive history and chemical stratigraphy of a steady-state volcano: Yasur, Vanuatu. *Bulletin of Volcanology* **76**, 837 DOI 10.1007/s00445-014-0837-3

Forbes HO (1884) The volcanic eruption of Krakatau. *Proceedings of the Royal Geographical Society* **6**, 142-152

Francalanci L, Avanzinelli R, Nardini I, Tiepolo M, Davidson JP, Vannucci R (2012) Crystal recycling in the steady-state system of the active Stromboli volcano: a 2.5-ka story inferred from in situ Sr-isotope and trace element data. *Contributions to Mineralogy and Petrology* **163**, 109-131

Francalanci L, Davies GR, Lustenmhower W, Tommasini S, Mason P, Conticelli S (2005) Intra-grain Sr isotope evidence for crystal re-cycling and multiple magma reservoirs in the recent activity of Stromboli volcano, southern Italy. *Journal of Petrology* **46**, 1997–2005

Francalanci L, Tommasini S, Conticelli S, Davies GR (1999) Sr isotope evidence for short magma residence time for the 20th century activity at Stromboli volcano, Italy. *Earth and Planetary Science Letters* **167**, 61-69

Francalanci L, Tommasini S, Conticelli S (2004) The volcanic activity of Stromboli in the 1906-1998 AD period: mineralogical, geochemical and isotope data relevant to the understanding of the plumbing system. *Journal of Volcanology and Geothermal Research* **131**, 179-211

Francis P, Rothery D (2000) Remote Sensing of Active Volcanoes. *Annual Reviews in Earth and Planetary Science* **28**, 81-106

Francis P, Oppenheimer C, Stevenson D (1993) Endogenous growth of persistently active volcanoes. *Nature* **366**, 554-557

Frater M, (1917) The Volcanic Eruption of 1913 on Ambrym Island, New Hebrides. *Geological Magazine* **6**, 496-503

Froggatt PC, Wilson CJN, Walker GPL (1981) Orientation of logs in the Taupo Ignimbrite as an indicator of flow direction and vent position. *Geology* **9**, 109-111

Gao C, Robock A, Self S, Witter JB, Steffenson JP, Clausen HB, Siggaard-Andersen M, Johnsen S, Mayewski PA, Ammann C (2006) The 1452 or 1453 A.D. Kuwae eruption signal derived from multiple ice core records: Greatest volcanic sulphate event of the past 700 years. *Journal of Geophysical Research* **111**, doi:10.1029/2005JD006710

Gaudin D, Taddeucci J, Scarlato P, Moroni M, Freda C, Gaeta M, Palladino DM (2014) Pyroclast Tracking Velocimetry illuminates bomb ejection and explosion dynamics at Stromboli (Italy) and Yasur (Vanuatu) volcanoes. *Journal of Geophysical Research* **119**, 5384-5397

Gauthier P-J, Condomines M (1999) ^{210}Pb-^{226}Ra radioactive disequilibria in recent lavas and radon degassing: inferences on the magma chamber dynamics at Stromboli and Merapi volcanoes. *Earth and Planetary Science Letters* **172**, 11-126

Gauthier P-J, Le Cloarec M-F, Condomines M (2000) Degassing processes at Stromboli volcano inferred from short-lived disequilibria (^{210}Pb-^{210}Bi-^{210}Po) in volcanic gases. *Journal of Volcanology and Geothermal Research* **102**, 1-19

Gertisser R, Self S, Thomas LE, Handley HK, van Calstren P, Wolff JA (2012) Processes and Timescales of Magma Genesis and Differentiation Leading to the Great Tambora Eruption in 1815. *Journal of Petrology* **53**, 271-297

Ghiorso MS, Sack RO (1995) Chemical mass transfer in magmatic processes IV. A revised and internally consistent thermodynamic model for the interpretation and extrapolation of liquid-solid equilibria in magmatic systems at elevated temperatures and pressures. *Contributions to Mineralogy and Petrology* **119**, 197-212

Giberti G, Jaupert C, Sartoris G (1992) Steady-state operation of Stromboli volcano, Italy: constraints on the feeding system. *Bulletin of Volcanology* **54**, 535-541

Giggenbach WF (1975) A simple method for the collection and analysis of volcanic gas samples. *Bulletin of Volcanology* **39**, 132-145

Giordano D, Russell JK, Dingwell DB (2008) Viscosity of magmatic liquids: a model. *Earth and Planetary Science Letters* **271**, 123-134

Global Volcanism Program (1991) Report on Ambrym (Vanuatu). *Bulletin of the Global Volcanism Network* **16**, 7

Global Volcanism Program (1996) Report on Ambrym (Vanuatu). *Bulletin of the Global Volcanism Network* **21**, 9

Global Volcanism Program (1998) Report on Ambrym (Vanuatu). *Bulletin of the Global*

Volcanism Network **23**, 9

Global Volcanism Program (2009) Report on Ambrym (Vanuatu). *Bulletin of the Global Volcanism Network* **34**, 1

Global Volcanism Program (2015) Report on Villarrica (Chile) in: Sennert SK (ed.), *Weekly Volcanic Activity Report, 25 February-3 March 2015*. Smithsonian Institution and US Geological Survey.

Gorman MK, Quinn TM, Taylor FW, Partin JW, Cabioch G, Austin JA, Pelletier B, Ballu V, Maes C, Saustrup S, (2012) A coral-based reconstruction of sea surface salinity at Sabine Bank, Vanuatu from 1842 to 2007 CE. *Palaeooceanography*. doi:10.1029/2012PA002302

Gorton MP (1977) The geochemistry and origin of quaternary volcanism in the New Hebrides. *Geochimica et Cosmochimica Acta* **41**, 1257-1270

Gregory JW (1917) The Ambrym Eruptions of 1913-14. *Geological Magazine* **6**, 529-540

Griffin WL, Pearson NJ, Belousova E, Jackson SE, O'Reilly SY, van Achterberg E, Shee SR (2000) The Hf isotope composition of cratonic mantle: LAM-MC-ICPMS analysis of zircon megacrysts in kimberlites. *Geochimica et Cosmochimica Acta* **64**, 133-147

Grove RH, (2007) The Great El Niño of 1789-93 and its Global Consequences: Reconstructing an Extreme Climate Event in World Environmental History. *The Medieval History Journal* **10**, 75-98

Gurioli L, Colo L, Bollasina AJ, Harris AJL, Whittington SA, Rieppe M (2014) Dynamics of Strombolian explosions: Inferences from field and laboratory studies of erupted bombs from Stromboli volcano. *Journal of Geophysical Research Solid Earth* **119**, 319-345

GVN Bulletin (1990) *Global Volcanism Network Bull* **15** (11)

GVN Bulletin (1997) *Global Volcanism Network Bull* **22** (11)

GVN Bulletin (1999) *Global Volcanism Network Bull* **24** (07)

Halmer MM, Scvhmincke HU, Grfa, HF (2002) The annual volcanic gas input into the atmosphere, in particular into the stratosphere: a global data set for the past 100 years. *Journal of Volcanology and Geothermal Research* **115**, 511-528

Handley HK, Turner SP, Smith IEM, Stewart RB, Cronin SJ (2008) Rapid timescales of differentiation and evidence for crustal assimilation at intra-oceanic arcs: Geochemical and U-Th-Ra-Sr-Nd isotopic constraints from Lopevi Volcano, Vanuatu, SW Pacific. *Earth and Planetary Science Letters* **273**, 184-194

Hammer JE, Cashman KV, Hoblitt RP, Newman S (1999) Degassing and microlite crystallisation during pre-climactic events of the 1991 eruption of Mt. Pinatubo, Philippines. *Bulletin of Volcanology* **60**, 355-380

Hansen H, Grönvold K (2000) Plagioclase ultraphyric basalts in Iceland: the mush of the rift. *Journal of Volcanology and Geothermal Research* **98**, 1-32

Harris AJL, Stevenson DS (1997) Magma budgest and steady-state activity of Vulcano and Stromboli. *Geophysical Research Letters* **24**, 1043-1046

Harris AJL, Flynn LP, Rothery DA, Oppenheimer C, Sherman C (1999) Mass flux measurements at active lava lakes: Implications for magma recycling. *Journal of Geophysical Research* **104**, 7117-7136

Harrison DE, Luther DS, (1990) Surface Winds from Tropical Pacific Islands-Climatological Statistics. *Journal of Climate* **3**, 251-271

Hawkesworth C, George R, Turner S, Zellmer G (2004) Time scales of magmatic processes. *Earth and Planetary Science Letters* **218**, 1-16

Hayward C (2011) High spatial resolution electron probe microanalysis of tephras and melt inclusions without beam-induced chemical modification. *The Holocene* DOI:10.1177/0959683611409777

Heggie TW (2009) Geotourism and volcanoes: Health hazards facing tourists at volcanic and geothermal destinations. *Travel Medicine and Infectious Disease* **7**, 257-261

Heiken G (2013) From Kīlauea Iki 1959 to Eyjafjallajökull 2010: How volcanology has changed! *Geological Society of America Special Paper* **500**, 33-63

Hemming RF (1974) Geology and Petrology of Rabaul Caldera, Papua New Guinea. *Geological Society of America Bulletin* **85**, 1253-1264

Hendy EJ, Gagan MK, Albert CA, McCulloch MT, Lough JM, Isdale PJ, (2002) Abrupt decrease in tropical Pacific sea surface salinity at the end of Little Ice Age. *Science* **295**, 1511-1514

Hogg AG, Hua Q, Blackwell PG, Niu M, Buck CE, Guilderson TP, Heaton TJ, Palmer JG, Reimer PJ, Reimer RW, Turney CSM, Zimmerman SRH (2013) SHCAL13 Southern Hemisphere Calibration, 0-50,000 years cal BP. *Radiocarbon* **55**, 1889-1903

Horton KA, Williams-Jones G, Garbiel H, Elias T, Sutton AJ, Mouginis-Mark P, Porter JN, Clegg S (2006) Real-time measurement of volcanic SO_2 emissions: validation of a new UV correlation spectrometer (FLYSPEC). *Bulletin of Volcanology* **68**, 323-327

Houghton BF, Wilson CJN, Del Carlo P, Coltelli M, Sable JE, Carey R (2004) The influence of conduit processes on changes in style of basaltic Plinian eruptions: Tarawera 1886 and Etna 122 BC. *Journal of Volcanology and Geothermal Research* **137**, 1-14

Huber C, Bachmann O, Dufek J (2012) Crytsal-poor versus crystal-rich ignimbrites: A competition between stirring and reactivation. *Geology* **40**, 115-118

Hughes RD, Hawkesworth CJ (1999) The effects of magma replenishment processes on ^{238}U-^{232}Th disequilibrium. *Geochimica et Cosmochimica Acta* **63**, 4101-4110

Hunt JB, Hill PG (1993) Tephra geochemistry: a discussion of some persistent analytical problems. *The Holocene* **3**, 271-278

Hurles ME, Matisoo-Smith E, Gray RD, Penny D, (2003) Untangling Oceanic Settlement: the edge of the knowable. *TRENDS in Ecology and Evolution* **18**, 531-540

Ilanko T, Oppenheimer C, Burgisser A, Kyle P (2015) Cyclic degassing of Erebus volcano, Antarctica. *Bulletin of Volcanology* **77**, doi10.1007/s00445-015-0941-z

Jaupert C, Vergniolle S (1988) Laboratory models of Hawaiian and Strombolian eruptions. *Nature* **331**, 58-60

Jerram DA, Cheadle MJ, Philpotts AR (2003) Quantifying the Building Blocks of Igneous Rocks: Are Clustered Crystal Frameworks the Foundation? *Journal of Petrology* **44**, 2033-2051

Kanas T, Nango I, Fransser J, Morris, S, (2000). Lake Siwi to River Siwi. Vanuatu Department of Land Survey. 27 pp

Kazahaya K, Shinohara H, Saito G (1994) Excessive degassing of Izu-Oshima volcano: magma convection in a conduit. *Bulletin of Volcanology* **56**, 207-216

Keiding JK, Sigmarsson O (2012) Geothermobarometry of the 2010 Eyjafjalljökull eruption: New constraints on Icelandic magma plumbing systems. *Journal of Geophysical Research* **117**, doi: 10.1029/2011JB008829

Kelley JL (2008) Glassy tephra of Yasur Volcano, Vanuatu: A magnetic, petrographic and crystallographic study and implications for devitrification. MSc Thesis, Southern Illinois University

Kelley PJ, Kyle PR, Dunbar NW, Sims KWW (2008) Geochemistry and mineralogy of the phonolite lava lake, Erebus volcano, Antarctica: 1972-2004 and comparison with older lavas. *Journal of Volcanology and Geothermal Research* **177**, 589-605

Kilgour G, Blundy J, Cashman K, Mader HM (2013) Small volume andesite magmas and melt-mush interactions at Ruapehu, New Zealand: evidence from melt inclusions. *Contributions to Mineralogy and Petrology* **166**, 371-392

Kremers S, Lavallee Y, Hanson J, Hess K, Chevrel MO, Wassermann J, Dingwell DB (2012) Shallow magma-mingling-driven Strombolian eruptions at Mt. Yasur volcano, Vanuatu. *Geophysical Research Letters* **39**, doi:10.1029/2012GL053312

Kremers S, Wassermann J, Meier K, Pelties C, van Driel M, Vasseur J, Hort M (2013) Inverting the source mechanism of Strombolian explosions at Mt Yasur, Vanuatu, using a multi-parameter dataset. *Journal of Volcanology and Geothermal Research* **262**, 104-122

Labillardiere J (1800) Voyage in search of La Perouse. London 655 pp

Landi P, Corsaro RA, Francalanci L, Civetta L, Miraglia L, Pompilio M, Tesoro R, (2009) Magma dynamics during the 2007 Stromboli eruption (Aeolian Islands, Italy): Mineralogical, geochemical and isotopic data. *Journal of Volcanology and Geothermal Research* **182**, 255-268

Landi P, Métrich N, Bertagnini A, Rosi M (2004) Dynamics of magma mixing and degassing recorded in plagioclase at Stromboli (Aeolian Archipelago, Italy). *Contributions to Mineralogy and Petrology* 147:213-227.

Latter JH (1981) Tsunamis of Volcanic Origin: Summary of Causes, with Particular Reference to Krakatoa, 1883. *Bulletin of Volcanology* **44**, 467-490

Lawrie JH (1898) Corals and Coral Islands, with special reference to the New Hebrides Group. *Transactions of the Edinburgh Field Naturalists and Microscopical Society* **3**, 320-326

Le Guern F, Carbonelle J, Tazieff H (1979) Erta'Ale Lava Lake: Heat and gas transfer to the atmosphere. *Journal of Volcanology and Geothermal Research* **6**, 27-48

Lee CA, Lee TC, Wu C (2014) Modelling the compositional evolution of recharging, evacuating and fractionating (REFC) magma chambers: Implications for differentiation of arc magmas. *Geochimica et Cosmochimica Acta* **143**, 8-22

Legrand D, Rouland D, Frogneux M, Carniel R, Charley D, Roult G, Robin C (2005) Interpretation of very long period tremors at Ambrym volcano, Vanuatu, as quasi-static displacement field related to two distinct magmatic sources. *Geophysical Research Letters* **32**, L06314. doi:10.1029/2004GL021968

Lejeune A-M, Richet P (1995) Rheology of crystal-bearing silicate melts: An experimental study at high viscosities. *Journal of Geophysical Research* **100**, 4215-4229

Leonard GS, Cole JW, Nairn IA, Self S (2002) Basalt triggering of the c. AD 1305 Kaharoa rhyolite eruption, Tarawera Volcanic Complex, New Zealand. *Journal of Volcanology and Geothermal Research* **115**, 461-486

Lohmar S, Parada M, Guitérrez F, Robin C, Gerbe MC (2012) Mineralogical and numerical approaches to establish the pre-eruptive conditions of the mafic Licán Ignimbrite, Villarrica Volcano (Chilean Southern Andes). *Journal of Volcanology and Geothermal Research* **235-236**, 55-69

Lowder GG, Carmichael ISE (1970) The Volcanoes and Caldera of Talasea, New Britain: Geology and Petrology. *Geological Society of America Bulletin* **81**, 17-38

Lowe DJ, (2011) Tephrochronology and its application: A review. *Quaternary Geochronology* **6**, 107-153

McCall GJH, LaMaitre RW, Malahoff A, Robinson GP, Stephenson PJ (1969) The Geology and Geophysics of the Ambrym Caldera, New Hebrides. *Bulletin of Volcanology* **34**, 681-696

McCormick MP, Thomason LW, Trepte CR (1995) Atmospheric effects of the Mt Pinatubo eruption. *Nature* **373**, 399-404

McCoy FW, Heikern G (2000a) The Late-Bronze Age explosive eruption of Thera (Santorini), Greece: Regional and local effects. *Geological Society of America Special Paper* **345**, 43-70

McCoy FW, Heiken G (2000b) Tsunami Generated by the Late Bronze Age Eruption of Thera (Santorini), Greece. *Pure Applied Geophysics* **157**, 1227-1256

McDonough WF, Sun S (1995) The composition of the Earth. *Chemical Geology* **120**, 223-253

McGonigle AJS, Oppenheimer C, Tsanev VI, Saunders S, Mulina K, Tohui S, Bosco J, Nahou J, Kuduon J, Taranu F (2004) Sulphur dioxide fluxes from Papua New Guinea's volcanoes. *Geophysical Research Letters* **31**, L08606, doi:10.1029/2004GL019568.

McGuire WJ (1991) Monitoring active volcanoes. *Geology Today* **7**,181-187

McKee CO (2015) Tavui Volcano: neighbour of Rabaul and likely source of the Middle Holocene penultimate major eruption in the Rabaul area. *Bulletin of Volcanology* **77**, doi10.1007/s00445-0150968-1

McKee CO, Baillie MG, Reimer PJ (2015) A revised age of AD 667-699 for the latest major eruption at Rabaul. *Bulletin of Volcanology* **77**, doi10.1007/s00445-015-0954-7

Mallick DIJ (1970) Volcanology. *New Hebrides Geological Survey Annual Report* 1968

Marsh BD (1989) Magma Chambers. *Annual Reviews in Earth and Planetary Science* **17**, 439-474

Mastin LG, (2001) A simple calculator of ballistic trajectories for blocks ejected during volcanic eruptions. U.S. Geol Survey Open-File Report 01-45, U.S. Geological Survey.

Mastin LG, Witter JB (2000) The hazards of eruptions through lakes and seawater. *Journal of Volcanology and Geothermal Research* **97**, 195-214

Martin VM, Morgan DJ, Jerram DA, Caddick MJ, Prior DJ, Davidson JP (2008) Bang! Month-Scale Eruption Triggering at Santorini Volcano. *Science* **321**, 1178

Mather TA, Pyle DM, Tsanev VI, McGonigle AJS, Oppenheimer C, Allen AG (2006) A reassessment of current volcanic emissions from the Central American arc with specific examples from Nicaragua. *Journal of Volcanology and Geothermal Research* **149**, 297-311

Melchior, A.H., 1988, Rapport de Mission de Reconnaissance Volcanologique Ambrym (25-28 May 1988) et à Tanna (14 May 1988): Document ORSTOM, Nouméa, 10 p.

Mellors RA, Sparks RSJ (1991) Spatter-rich pyroclastic flow deposits on Santorini, Greece. *Bulletin of Volcanology* **53**, 327-342

Merle O, Brothelande E, Lenat JF, Bachelery P, Garaebiti E (2013) A structural outline of the Yenkahe volcanic resurgent dome (Tanna Island, Vanuatu Arc, South Pacific). *Journal of Volcanology and Geothermal Research* **268**, 64-72

Métrich N, Allard P, Aiuppa A, Bani P, Bertagnini A, Shinohara H, Parello F, Di Muro A, Garaebiti E, Belhadj O, Massare D, (2011) Magma and Volatile Supply to Post-collapse Volcanism and Block Resurgence in Siwi Caldera (Tanna Island, Vanuatu Arc). *Journal of Petrology* **52**, 1077-1105

Métrich N, Bertagnini A, Di Muro A, (2010) Conditions of Magma Storage, Degassing and Ascent at Stromboli: New Insights into the Volcano Plumbing System with Inferences on the Eruptive Dynamics. *Journal of Petrology* **51**, 603-626

Michon L, Ferrazzini V, Di Muro A, Villeneuve N, Famin V (2015) Rift zones and magma plumbing system of Piton de la Fournaise volcano: How do they differ from Hawaii and Etna? *Journal of Volcanology and Geothermal Research* **303**, 112-129

Monzier M, Charley D (1989) Rapport de mission a Ambrym (Vanuatu) du 26 au 30 septembre 1989. *Rapports de Missions, Science de la Terre, Geologie-Geophysique* **10**, 1-36

Monzier M, Robin C, Eissen J (1994) Kuwae (~1425 A.D.): the forgotten caldera. *Journal of Volcanology and Geothermal Research* **59**, 207-218

Moromoto N (1989) Nomenclature of Pyroxenes. *Canadian Mineralogist* **27**, 143-156

Murphy MD, Sparks RSJ, Barclay J, Carroll MR, Brewer TS (2000) Remobilisation of Andesite Magma by Intrusion of Mafic Magma at the Soufriere Hills Volcano, Montserrat, West Indies. *Journal of Petrology* **41**, 21-42

Nabyl A, Dorel J, Lardy M (1997) A comparative study of low-frequency seismic signals recorded at Stromboli volcano, Italy and Yasur volcano, Vanuatu. *New Zealand Journal of Geology and Geophysics* **40**, 549-558

Nairn IA, Scott BJ, Giggenbach WF, (1988) Yasur volcano investigations, Vanuatu, Sept 1988. *New Zealand Geological Survey Report G* **134**, 74 pp

Neef G, Zhao JX, Collerson KD, Zhang FS (2003) Late Quaternary uplift and subsidence of the west coast of Tanna, south Vanuatu, southwest Pacific: U-Th ages of raised coral reefs in the Median Sedimentary Basin. *Australian Journal of Earth Science* **50**, 39-48

Nelson ST, Montana A (1992) Sieve-textured plagioclase in volcanic rocks produced by rapid decompression. *American Mineralogist* **77**, 1242-1249

Németh K, Cronin SJ (2008) Volcanic craters, pit craters and high-level magma-feeding systems of a mafic island-arc volcano: Ambrym, Vanuatu, South Pacific. *Geological Society of London Special Publication* **302**, 87-102

Németh K, Cronin SJ (2009) Phreatomagmatic volcanic hazards where rift-systems meet the sea, a study from Ambae Island, Vanuatu. *Journal of Volcanology and Geothermal Research* **180**, 246-258

Németh K, Cronin SJ (2011) Drivers of explosivity and elevated hazard in basaltic fissure eruptions: The 1913 eruption of Ambrym Volcano, Vanuatu (SW Pacific). *Journal of Volcanology and Geothermal Research* **201**, 194-209

Newhall CG, Self S (1982) The Volcanic Explosivity Index (VEI): An estimate of Explosive Magnitude for Historical Volcanism. *Journal of Geophysical Research* **87**, 1231-1238

Nimis P (1995) A clinopyroxene geobarometer for basaltic systems based on crystal-structure modelling. *Contributions to Mineralogy and Petrology* **121**, 115-125

Norrish K, Chappell BW (1977) X-ray fluorescence spectrometry. In: Zussman J. (ed.) Physical Methods in Determinative Mineralogy. Academic Press, New York: 202-272.

Nowell GM, Kempton PD, Noble SR, Fitton JG, Saunders AD, Mahoney JJ, Taylor RN (1998) High precision Hf isotope measurements of MORB and OIB by thermal ionisation mass spectrometry: Insights into the depleted mantle. *Chemical Geology* **149**, 211-233

Nunn P (2007) Climate, Environment and Society in the Pacific During the Last Millennium. *Developments in Earth and Environmental Sciences* **6**

O'Hara MJ (1977) Geochemical evolution during fractional crystallisation of a periodically refilled magma chamber. *Nature* **266**, 503-507

O'Neill HC, Jenner FE (2012) The global pattern of trace-element distributions in ocean floor basalts. *Nature* **491**, 698-704

Oppenheimer C (2003) Climatic, environmental and human consequences of the largest known historic eruption: Tambora volcano (Indonesia) 1815. *Progress in Physical Geography* **27**, 230-259

Oppenheimer C (2010) Ultraviolet sensing of Volcanic Sulfur Emissions. *Elements* **6**, 87-92

Oppenheimer C, Yirgu G (2002) Thermal imaging of an active lava lake: Erta 'Ale volcano, Ethiopia. *International Journal of Remote Sensing* **23**, 4777-4782

Oppenheimer C, Bani P, Calkins JA, Burton MR, Sawyer GM (2006) Rapid FTIR sensing of volcanic gasses released by Strombolian explosions at Yasur volcano, Vanuatu. *Applied Physics B* **85**, 453-460

Oppenheimer C, Lomakina AS, Kyle PR, Kingsbury NG, Boichu M (2009) Pulsatory magma supply to a phonolite lava lake. *Earth and Planetary Science Letters* **284**, 392-398

Oppenheimer C, McGonigle AJS, Allard P, Wooster MJ, Tsanev V (2004) Sulphur, heat and magma budget of Erta 'Ale lava lake, Ethiopia. *Geology* **32**, 509-512

Oppenheimer C, Scaillet B, Martin RS (2011) Sulphur degassing from volcanoes: Source Conditions, Surveillance, Plume Chemistry and Earth System Impacts. *Reviews in Mineralogy and Geochemistry* **73**, 363-421

Pallister JS, Hoblitt RP, Reyes AG (1992) A basalt trigger for the 1991 eruptions of Pinatubo

volcano? *Nature* **356**, 426-428

Palma JL, Blake S, Calder ES (2011) Constraints on the rates of degassing and convection in basaltic open-vent volcanoes. *Geochemistry Geophysics Geosystems* **12**, Q11006, doi:10.1029/2011GC003715

Palma JL, Calder ES, Basualto D, Blake S, Rothery DA (2008) Correlations between SO_2 flux, seismicity, and outgassing activity at the open vent of Villarrica volcano, Chile. *Journal of Geophysical Research* **113**, B10201, doi: 10.1029/2008JB005577

Parmigiani A, Huber C, Bachmann O (2014) Much micropysics and the reactivation of crystal-rich magma reservoirs. *Journal of Geophysical Research* **119**, 6308-6322

Paton W (1937) The Ambrim eruption. *Walkabout* **4**, 59-61

Pearce JA, Peate DW (1995) Tectonic implications of the composition of volcanic arc magmas. *Annual Review of Earth and Planetary Science* **23**, 251-285

Pearce JA, Kempton PD, Gill JB (2007) Hf-Nd evidence for the origin and distribution of mantle domains in the SW Pacific. *Earth and Planetary Science Letters* **260**, 98-114

Pearce NJG, Westgate JA, Perkins WT, Eastwood WJ, Shane P (1999) The application of laser ablation ICP-MS to the analysis of volcanic glass shards from tephra deposits: bulk glass and single shard analysis. *Global Planetary Change* **21**, 151-171

Peate DW, Pearce JA, Hawkesworth CJ, Colley H, Edwards CM, Hirose K (1997) Geochemical Variations in Vanuatu Arc Lavas: the Role of Subducted material and a Variable Mantle Wedge Composition. *Journal of Petrology* **38**, 1331-1358.

Peltier A, Finizola A, Douillet GA, Brothelande E, Garaebiti E (2012) Structure of an active volcano associated with a resurgent block inferred from thermal mapping: The Yasur-Yenkahe volcanic complex (Vanuatu). *Journal of Volcanology and Geothermal Research* **243-244**, 59-68

Picard C, Monzier M, Eissen JP, Robin C (1995) Concomitant evolution of tectonic environment and magma geochemistry, Ambrym volcano (Vanuatu, New Hebrides arc). *Geological Society of London Special Publication* **81**, 135-154

Plank T, Langmuir CH (1993) Tracing trace elements from sediment input to volcanic output at subduction zones. *Nature* **362**, 739-742

Plank T, Langmuir CH (1998) The chemical composition of subducting sediment and its consequences for the crust and mantle. *Chemical Geology* **145**, 325-394

Platz T, Cronin SJ, Smith IEM, Turner MB, Stewart RB (2007) Improving the reliability of microprobe based analyses of andesitic glasses for tephra correlation. *The Holocene* **17**, 573-583

Polacci M, Baker DR, La Rue A, Mancini L, Allard P (2012) Degassing behaviour of vesiculated basaltic magmas: an example from Ambrym volcano, Vanuatu Arc. *Journal of Volcanology and Geothermal Research* **233-234**, 55-64

Polacci M, Corsaro RA, Andronico D (2006) Coupled textural and compositional characterisation of basaltic scoria: Insights into the transition from Strombolian to fire fountain activity at Mount Etna, Italy. *Geology* **34**, 201-204

Polacci M, Rosi M, Landi P, Di Muro A, Papale P (2005) Novel Interpretation for Shift Between Eruptive Styles in Some Volcanoes. *EOS Transactions American Geophysical Union* **86**, 333-336

Purey-Cust HE (1896) The Eruption of Ambrym Island, New Hebrides, South-West Pacific, 1894. *The Geographical Journal* **8**, 585-602

Putirka KD (2008) Thermometers and barometers for volcanic systems. *Reviews in Mineralogy and Geochemistry* **69**, 61-120

Pyle DM (1992) The volume and residence time of magma beneath active volcanoes determined by decay series equilibria methods. *Earth and Planetary Science Letters* **112**, 61-73

Quantain P (1978) Archipel des Nouvelles-Hébrides: Atlas des sols et de quelques données du milieu. Cartes pédologiques (1150.000 ou 11100.000), des formes du relief, géologiques et de la végétation (11100.000 ou 11250.000). ORSTOM.

Richardson JP, Waite GP, Palma JL (2014) Varying seismic-acoustic properties of the fluctuating lava lake at Villarrica volcano, Chile. *Journal of Geophysical Research* **119**, 5560-5573.

Ringwood AE (1974) The petrological evolution of island arc systems: Twenty-seventh William Smith Lecture. *Journal of the Geological Society* **130**, 183-204

Robin C, Eissen JP, Monzier M (1993) Giant tuff cone and 12-km-wide associated caldera at Ambrym Volcano (Vanuatu, New Hebrides Arc). *Journal of Volcanology and Geothermal Research* **55**, 225-238

Robin C, Eissen JP, Monzier M, (1994) Ignimbrites of basaltic andesite and andesite compositions from Tanna, New Hebrides Arc. *Bulletin of Volcanology* **56**, 10-22

Robin C, Eissen J, Monzier M (1995) Mafic pyroclastic flows at Santa Maria (Gaua) Volcano, Vanuatu: the caldera formation problem in mainly mafic island arc volcanoes. *Terra Nova* **7**, 436-443

Roggensack K, Hervig RL, McKnight SB, Williams SN (1997) Explosive Basaltic Volcanism from Cerro Negro Volcano: Influence of Volatiles on Eruptive Style. *Science* **277**, 1639-1642

Rose S, Ramsey M (2009) The 2005 eruption of Kliuchevskoi volcano: Chronology and processes derived from ASTER spaceborne and field-based data. *Journal of Volcanology and Geothermal Research* **184**, 367-380

Rosi M, Bertagnini A, Landi P, (2000) Onset of the persistent activity at Stromboli Volcano (Italy). *Bulletin of Volcanology* **62**, 294-300

Rosi M, Pistolesi M, Bertagnini A, Landi P, Pompillio M, Di Roberto A (2013) Stromboli volcano, Aeolian Islands (Italy): present eruptive activity and hazards. *Geological Society of London Memoirs* **37**, 473-490

Rouland D, Legrand D, Zhizhin M, Vergnolle S (2009) Automatic detection and discrimination of volcanic tremors and tectonic earthquakes: An application to Ambrym volcano, Vanuatu. *Journal of Volcanology and Geothermal Research* **181**, 196-206

Rymer H, van Wyk de Vries B, Stix J, Williams-Jones G (1998) Pit crater structure and processes governing persistent activity at Masaya Volcano, Nicaragua. *Bulletin of Volcanology* **59**, 345-355

Sadofsky SJ, Portnyagin M, Hoernle K, van den Bogaard P (2008) Subduction cycling of

volatiles and trace elements through the Central American volcanic arc: evidence from melt inclusions. *Contributions to Mineralogy and Petrology* **155**, 433-456

Sawyer GM, Carn SA, Tsanev VI, Oppenheimer C, Burton M (2008) Investigation into magma degassing at Nyiragongo volcano, Democratic Republic of the Congo. *Geochemistry Geophysics Geosystems* **9**, doi:10.1029/2007GC001829

Sawyer GM, Salerno GG, Le Blond JS, Martin RS, Spampinato L, Roberts TJ, Mather TA, Witt MLI, Tsanev VI, Oppenheimer C (2011) Gas and aerosol emissions from Villarrica volcano, Chile. *Journal of Volcanology and Geothermal Research* **203**, 62-75

Self S (1992) Krakatau Revisited: The Course of Events and Interpretations of the 1883 Eruption. *Geological Journal* **28**, 109-121

Self S, Rampino MR (1981) The 1883 eruption of Krakatau. *Nature* **294**, 699-704

Self S, Sparks RSJ (1978) Characteristics of Widespread Pyroclastic Deposits Formed by the Interaction of Silicic Magma and Water. *Bulletin of Volcanology* **41**, 196-212

Self S, Gertisser R, Thordarson T, Rampino MR, Wolff JA (2004) Magma volume, volatile emissions, and stratospheric aerosols from the 1815 eruption of Tambora. *Geophysical Research Letters* **31**, doi:10.1029/2004GL020925

Self S, Rampino MR, Newton MS, Wolff JA (1984) Volcanological study of the great Tambora eruption of 1815. *Geology* **12**, 659-663

Shane P (2000) Tephrochronology: a New Zealand case study. *Earth Science Reviews* **49**, 223-259

Shinohara H, Witter JB (2005) Volcanic gasses emitted during mild Strombolian activity of Villarrica volcano, Chile. *Geophysical Research Letters* **32**, L20308, doi:10.1029/2005GL024131

Sides IR, Edmonds M, Maclennan J, Swanson DA, Houghton BF (2014) Eruption style at Kilauea Volcano in Hawai'I linked to primary melt composition. *Nature Geoscience* DOI:10.1038/NGEO2140

Sigmarsson O, Condomines M, Bachelery P (2005) Magma residence times beneath the Piton de la Fournaise Volcano, Reunion Island, from U-series disequilibria. *Earth and Planetary Science Letters* **234**, 223-234

Silva Parejas C, Druitt TH, Robin C, Moreno H, Naranjo J-A (2010) The Holocene Pucon eruption of Volcan Villarrica, Chile: deposit architecture and eruption chronology. *Bulletin of Volcanology* **72**, 677-692

Sims KWW, Gill JB, Dosseto A, Hoffmann DL, Lundstrom CC, Williams RW, Ball L, Tollstrup D, Turner S, Prytulak J, Glessner JJG, Standish JJ, Elliot T (2008) An Inter-Laboratory Assessment of the Thorium Isotopic Composition of Synthetic and Rock Reference Materials. *Geostandards and Geoanalytical Research* **32**, 65-91

Sims KWW, Pichat S, Reagan MK, Kyle PR, Dulaiova H, Dunbar NW, Prytulak J, Sawyer G, Layne GD, Blichert-Toft J, Gauthier PJ, Charette MA, Elliot TR (2013) On the Time Scales of Magma Genesis, Melt Evolution, Crystal Growth Rates and Magma Degassing in the Erebus Volcano Magmatic System Using the ^{238}U, ^{235}U and ^{232}Th Decay Series. *Journal of Petrology* **54**, 235-271

Sorbadere F, Schiano P, Métrich N, Garaebiti E (2011) Insights into the origin of primitive silica-undersaturated arc magmas of Aoba volcano (Vanuatu arc). *Contributions to Mineralogy and Petrology* **162**, 995-1009

Sorbadere F, Schiano P, Métrich N (2013) Constraints on the Origin of Nepheline-Normative Primitive Magmas in Island Arcs Inferred from Olivine-hosted Melt Inclusion Compositions. *Journal of Petrology* **54**, 215-233

Smith IEM, Stewart RB, Price RC (2003) The petrology of a large intra-oceanic silicic eruption: the Sandy Bay Tephra, Kermadec Arc, Southwest Pacific. *Journal of Volcanology and Geothermal Research* **124**, 173-194

Sparks RJS, Self S, Walker GPL (1973) Products of Ignimbrite Eruptions. *Geology* **1**, 115-118.

Sparks RSJ, Sigurdsson H, Wilson L (1977) Magma mixing: a mechanism for triggering acid explosive eruptions. *Nature* **267**, 315-318

Stametelopoulou-Seymour K, Vlassopoulos D, Pearce TH, Rice C (1990) The record of magma chamber processes in plagioclase phenocrysts at Thera Volcano, Aegean Volcanic Arc, Greece. *Contributions to Mineralogy and Petrology* **104**, 73-84

Stevenson DS, Blake S (1998) Modelling the dynamics and thermodynamics of volcanic degassing. *Bulletin of Volcanology* **60**, 307-317

Stix J (2007) Stability and instability of quiescently active volcanoes: The case of Masaya, Nicaragua. *Geology* **35**, 535-538

Stix J, Kobayashi T (2008) Magma dynamics and collapse mechanisms during four historic caldera-forming events. *Journal of Geophysical Research* **113**, doi:10.1029/2007JB005073

Stormer JC, Nichols J (1978) XLFRAC: A program for the interactive testing of magmatic differentiation models. *Computers and Geoscience* **4**, 143-159

Stovall WK, Houghton BF, Harris AJL, Swanson DA (2009) Features of lava lake filling and draining and their implications for eruption dynamics. *Bulletin of Volcanology* **71**, 767-780

Streck MJ, Dungan MA, Malavassi E, Reagan MK, Bussy F (2002) The role of basalt replenishment in the generation of basaltic andesites of the ongoing activity at Arenal volcano, Costa Rica: evidence from clinopyroxene and spinel. *Bulletin of Volcanology* **64**, 316-327

Streck MJ (2008) Mineral Textures and Zoning as Evidence for Open System Processes. *Reviews in Mineralogy and Geochemistry* **69**, 695-622

Sweeney D, Kyle PR, Oppenheimer C (2008) Sulphur dioxide emissions and degassing behaviour of Erebus volcano, Antarctica. *Journal of Volcanology and Geothermal Research* **177**, 725-733

Sumner JM (1998) Formation of clastogenic lava flows during fissure eruption and scoria cone collapse: the 1986 eruption of Isu-Oshima Volcano, eastern Japan. *Bulletin of Volcanology* **60**, 195-212

Sumner JM, Blake S, Matela RJ, Wolff JA (2005) Spatter. *Journal of Volcanology and Geothermal Research* **142**, 49-65

Sun S, McDonough WF (1989) Chemical and isotopic systematics of oceanic basalts:

implications for mantle composition and processes. *Geological Society of London Special Publication* **42**, 313-345

Swanson DA, Rose TR, Fiske RS, McGeehin JP (2012) Keanakako'I Tephra produced by 300 years of explosive eruptions following collapse of Kilauea's caldera in about 1500 CE. *Journal of Volcanology and Geothermal Research* **215-216**, 8-25

Taddeucci J, Scarlato P, Capponi A, Del Bello E, Cimarelli C, Palladino DM, Kueppers U, (2012) High-speed imaging of Strombolian explosions: The ejection velocity of pyroclasts. *Geophysical Research Letters* **39**, doi:10.1029/2011GL050404

Taylor GA (1956) Review of Volcanic activity in the territory of Papua New Guinea, the Solomon and new Hebrides Islands 1951-53. *Bulletin of Volcanology* **18**, 25-37

Tazieff H (1977) An Exceptional Eruption: Mt Niragongo, Jan. 10th, 1977. *Bulletin of Volcanology* **40**, 189-200

Tazieff H (1994) Permanent lava lake: observed facts and induced mechanisms. *Journal of Volcanology and Geothermal Research* **63**, 3-11

Tepley III FJ, Lundstrom CC, Gill JB, Williams RW (2006) U-Th-Ra disequilibria and the time scale of fluid transfer and andesite differentiation at Arenal volcano, Cost Rica (1968-2003). *Journal of Volcanology and Geothermal Research* **157**, 147-165

Tibaldi A (2001) Multiple sector collapses at Stromboli volcano, Italy: how they work. *Bulletin of Volcanology* **63**, 112-125

Tilling RI (2008) The critical role of volcano monitoring in risk reduction. *Advances in Geoscience* **14b**, 3-11

Tsuchiyama A (1985) Dissolution kinetics of plagioclase in the melt system diopside-albite-anorthite, and the origin of dusty plagioclase in andesites. *Contributions to Mineralogy and Petrology* **89**, 1-16

Turner MB, Cronin SJ, Stewart RB, Bebbington M, Smith IEM (2008) Using titanomagnetite textures to elucidate volcanic eruption histories. *Geology* **36**, 31-34

Turner MB, Reagan MK, Turner SP, Sparks RJS, Handley HK, Girard G, Suh CE (2013) Timescales of magma degassing – Insights from U-series disequilibria, Mount Cameroon, West Africa. *Journal of Volcanology and Geothermal Research* **262**, 38-46

Turner SP, Beier C, Niu Y, Cook C (2011) U-Th-Ra disequilibria and the extent of off-axis volcanism across the East Pacific Rise at 9°30'N, 10°30'N, and 11°20'N. *Geochemistry Geophysics Geosystems* **12**, Q0AC12, doi:10.1029/2010GC003403

Turner S, Black S, Berlo K (2004) ^{210}Pb-^{226}Ra and ^{228}Ra-^{232}Th systematics in young arc lavas: implications for magma degassing and ascent rates. *Earth and Planetary Science Letters* **227**, 1-16

Turner S, Evans P, Hawkesworth C (2001) Ultrafast Source-to-Surface Movement of Melt at Island Arcs from ^{226}Ra-^{230Th} Systematics. *Science* **292**, 1363-1366

Turner SP, Peate DW, Hawkesworth CJ, Eggins SM, Crawford AJ (1999) Two mantle domains and the time scales of fluid transfer beneath the Vanuatu arc. *Geology* **27**, 963-966

Turner S, Reagan M, Vigier N, Bourdon B (2012) Origins of ^{210}Pb-^{226}Ra disequilibria in basalts: New insights from the 1978 Asal Rift eruption. *Geochemistry Geophysics Geosystems* **13**, doi:10.1029/2012GC004173

van Achterbergh E, Ryan CG, Jackson SE, Griffin WL, (2001) Data reduction software for LA-ICP-MS. In Laser-Ablation ICP-MS in the Earth Sciences: Principles and Applications, Sylvester P (ed.). *Mineralogical Association of Canada* **29**, 239-243

van Manen SM (2014) Perception of a chronic volcanic hazard: persistent degassing at Masaya volcano, Nicaragua. *Journal of Applied Volcanology* **3**, 1-16.

Valentine GA, Perry FV, WoldeGabriel G (2000) Field characteristics of deposits from spatter-rich pyroclastic density currents at Summer Coon volcano, Colorado. *Journal of Volcanology and Geothermal Research* **104**, 187-199

Vanderkluysen L, Harris AJL, Kelfoun K, Bonadonna C, Rieppe M, (2012) Bombs behaving badly: unexpected trajectories and cooling of volcanic projectiles. *Bulletin of Volcanology* **74**, 1849-1858

Verbeek RDM (1884) The Krakatoa Eruption. *Nature* **30(757)**:10-15

Vinkler AP, Cashman K, Giordano G, Groppelli G (2012) Evolution of the mafic Villa Senni caldera-forming eruption at Colli Albani volcano, Italy, indicated by textural analysis of juvenile fragments. *Journal of Volcanology and Geothermal Research* **235-236**, 37-54

Wadge G (1981) The magma budget of Volcan Arenal, Costa Rica from 1968-1980. *Journal of Volcanology and Geothermal Research* **19**, 281-302

Wadge G (1982) Steady-State Volcanism: Evidence from eruption histories of polygenetic volcanoes. *Journal of Geophysical Research* **87**, 4035-4049

Walker GPL (1973) Explosive volcanic eruptions – a new classification scheme. *Geologische Rundschau* **62**, 431-446

Walker GPL (1985) Origin of coarse lithic breccias near ignimbrite source vents. *Journal of Volcanology and Geothermal Research* **25**, 157-171

Wallace PJ (2004) Volatiles in subduction zone magmas: concentrations and fluxes based on melt inclusion and volcanic gas dat. *Journal of Volcanology and Geothermal Research* **140**, 217-240

Waythomas CF, Neal CA (1998) Tsunami generation by pyroclastic flow during the 3500-year B. P. caldera-forming eruption of Aniakchak Volcano, Alaska. *Bulletin of Volcanology* **60**, 110-124

Wegener A (1912) Die Entstehung der Kontinente. *Petermanns Geographische Mitteilungen* **58**, 185-195, 253-256, 305-309

Wehrmann H, Bonadonna C, Freundt A, Houghton BF, Kutterolf S (2006) Fontana Tephra: A basaltic Plinian eruption in Nicuragua. *Geological Society of America Special Paper* **412**, 209-223

Wehrmann H, Hoernle K, Portnyagin M, Wiedenbeck M, Heydolph K (2011) Volcanic CO_2 output at the Central American subduction zone inferred from melt inclusions in olivine crystals from mafic tephras. *Geochemistry Geophysics Geosystems* **12**, doi:1029/2010GC003412

White WM, Hofmann AW, Pulchelt H (1987) Isotope Geochemistry of Pacific Mid-Ocean Ridge Basalt. *Journal of Geophysical Research* **92**, 4881-4893

Wilson CJN (2008) Supereruptions and Supervolcanoes: Processes and Products. *Elements* **4**,

29-34

Wilson JT (1963) Hypothesis of Earth's Behaviour. *Nature* **198**, 925-929

Witham F (2011) Conduit convection, magma mixing, and melt inclusion trends at persistently degassing volcanoes. *Earth and Planetary Science Letters* **301**, 345-352

Witham F, Llewellin EW (2006) Stability of lava lakes. *Journal of Volcanology and Geothermal Research* **158**, 321-332

Witter JB, Kress VC, Delmelle P, Stix J (2004) Volatile degassing, petrology, and magma dynamics of the Villarrica Lava Lake, Southern Chile. *Journal of Volcanology and Geothermal Research* **134**, 303-337

Witter JB, Self S (2007) The Kuwae (Vanuatu) eruption of AD 1452: potential magnitude and volatile release. *Bulletin of Volcanology* **69**, 301-318

Woods AW, Koyaguchi T (1994) Transitions between explosive and effusive eruptions of silicic magmas. *Nature* **370**, 641-644

Wright JV, Walker GPL (1977) The ignimbrite source problem: Significance of a co-ignimbrite lag-fall deposit. *Geology* **5**, 729-732